Universidad de Cantabria
Departamento de Física Moderna

CSIC — Universidad de Cantabria
Instituto de Física de Cantabria

Espectroscopía de galaxias activas distantes detectadas con el observatorio XMM-Newton

Memoria presentada por la Licenciada

Silvia Mateos Ibáñez

para optar al título de Doctor en Ciencias Físicas

2006

Universidad de Cantabria
Departamento de Física Moderna

CSIC — Universidad de Cantabria
Instituto de Física de Cantabria

Espectroscopía de galaxias activas distantes detectadas con el observatorio XMM-Newton

Memoria presentada por la Licenciada

Silvia Mateos Ibáñez

para optar al título de Doctor en Ciencias Físicas

2006

Xavier Barcons Jáuregui, Profesor de Investigación del Consejo Superior de Investigaciones Científicas,

y

Francisco J. Carrera Troyano, Profesor Titular de la Universidad de Cantabria

CERTIFICAN que la presente memoria

Espectroscopía de galaxias activas distantes detectadas con el observatorio XMM-Newton

ha sido realizada por Silvia Mateos Ibáñez bajo nuestra dirección. Consideramos que esta memoria contiene aportaciones suficientes para constituir la Tesis Doctoral del interesado.

En Santander, a 9 de Octubre de 2006

Xavier Barcons Jáuregui　　　　Francisco J. Carrera Troyano

A mis padres

Resumen de la tesis en castellano

0.1 Objetivos de la investigación

La emisión de rayos X en el universo está asociada a los fenómenos más energéticos, por ejemplo partículas relativistas sometidas a intensos campos magnéticos, plasmas a temperaturas del orden de millones de grados ó intensos campos gravitacionales. Por lo tanto estudiar el cielo en rayos X significa estudiar el universo más violento y más caliente. Dentro de nuestra Galaxia, distintos tipos de fuentes emiten rayos X, como por ejemplo, estrellas aisladas o en sistemas binarios (enanas blancas, estrellas de neutrones) y remanentes de supernova. Entre los objetos extragalácticos emisores de rayos X se encuentran las galaxias, cúmulos de galaxias y los Núcleos Galácticos Activos (AGN).

El cielo en rayos X está dominado por una radiación difusa procedente de todas las direcciones, altamente isótropa. Esta emisión se conoce como el *fondo cósmico de rayos X* (FRX). Hoy en día sabemos que el origen del FRX es la emisión integrada de fuentes cósmicas extragalácticas. A energías por encima de $\sim$0.2 keV la emisión del FRX está dominada por AGN, la mayoría absorbidos por grandes cantidades de gas y polvo.

Los AGN son un tipo de galaxias emisoras de gran cantidad de energía, procedente de una región muy pequeña, conocida como el núcleo. La energía emitida por los AGN es muy superior a la emisión integrada de las galaxias que los contienen. Los AGN son los objetos persistentes más luminosos en el Universo. Tan solo los estallidos cósmicos de rayos gamma son capaces de sobrepasar el brillo de los AGN; sin embargo estos últimos tan solo tienen unos pocos segundos de duración. Es imposible explicar las altas luminosidades observadas en AGN como la emisión integrada de las estrellas de la galaxia que contiene el AGN o emisión del gas interestelar. El único fenómeno conocido capaz de explicar las luminosidades de estos objetos es la acreción de material en un agujero negro supermasivo.

De acuerdo con el modelo estándar, los AGN contienen agujeros negros supermasivos (con masas entre 10^6-10^9M$_\odot$[1]). En las regiones donde el campo gravitatorio del agujero negro domina sobre el producido por las estrellas ($\sim$10 parsecs para un agujero negro de masa $\sim 10^8$M$_\odot$), el agujero negro está acretando material de la galaxia (estrellas y gas). Como el material acretado tiene momento angular, el fenómeno de la acreción ocurre en forma de un disco de acreción en torno al agujero negro. El material en el disco de acreción se calienta debido a procesos de fricción y la influencia de fuertes campos magnéticos, alcanzando temperaturas del orden de 10^5-10^6 K y liberando energía en forma

---

[1] Las masas se dan en unidades de masa del Sol, M$_\odot$.

de radiación térmica emitida en el rango óptico-ultravioleta (UV). A pesar de que está generalmente aceptado que la fuente de energía en AGN es acreción de material en un agujero negro supermasivo, los detalles de como se produce la emisión en rayos X en estos objetos aún no están totalmente determinados.

Estudios de variabilidad muestran que los AGN son fuentes muy variables en todo el rango del espectro, aunque las mayores amplitudes de variabilidad se han detectado en rayos X. Las escalas más rápidas de variabilidad observadas en AGN, en torno a los minutos, se han detectado en rayos X, sugiriendo que la emisión en rayos X de estos objetos debe proceder de una región muy pequeña y cercana al agujero negro. Uno de los modelos más aceptados, capaces de explicar la emisión en rayos X en AGN, es el modelo de Comptonización [102]. Según este modelo, un plasma caliente de electrones-iones (y quizás pares electrón-positrón) rodea la zona del disco de acreción más cercana al agujero negro. Este plasma reprocesa a través de difusión Compton inversa los fotones ópticos/UV emitidos en el disco de acreción. Los fotones reprocesados son emitidos en rayos X. El proceso de Comptonización es capaz de producir un espectro de emisión en rayos X con forma ley de potencia, tal y como se observa en espectroscopía de rayos X.

Los AGN muestran una gran variedad de propiedades. Dependiendo de las propiedades observadas, los AGN se clasifican en distintas categorías. Una de las clasificaciones de AGN más extendidas, la cual hemos usado también para el trabajo presentado en esta tesis, está basada en las propiedades de los espectros ópticos de las fuentes: los AGN para los que se observan tanto líneas de emisión anchas (anchura a media altura, del inglés Full Width at Half Maximum FWHM$\geq 2000\,\mathrm{km\,s^{-1}}$) como estrechas en el espectro óptico/UV se clasifican como AGN de tipo 1, mientras que las fuentes para las que solo se observan líneas de emisión estrechas (FWHM$< 2000\,\mathrm{km\,s^{-1}}$) se clasifican como AGN de tipo 2.

Las líneas de emisión anchas se cree que se forman en nubes de gas denso ($\geq 10^8\,\mathrm{cm^{-3}}$) moviéndose a altas velocidades (entre 1000 y 10000 km $\mathrm{s^{-1}}$) en las proximidades del agujero negro (a distancias del orden de decenas de parsecs). Esta región se conoce como la región de líneas anchas. Las líneas de emisión estrechas son emitidas en nubes de gas menos densas ($\sim 10^3 - 10^4\,\mathrm{cm^{-3}}$) más alejadas de la región central del AGN (a distancias del orden de kilo-parsecs) moviéndose a velocidades más bajas (entre 100 y 1000 km $\mathrm{s^{-1}}$). Esta región se conoce como la región de líneas estrechas.

Otra componente, el gas molecular, probablemente en forma de "toroide" [5] [237], se encuentra situado a distancias intermedias entre la región de líneas anchas y la región de líneas estrechas del AGN. El material del "toroide" absorbe la radiación procedente del disco de acreción y la región de líneas anchas, oscureciendo el núcleo del AGN en ciertas líneas de visión. La radiación absorbida es reemitida en el infra-rojo (IR). Los modelos de unificación de AGN intentan explicar la presencia ó ausencia de líneas anchas en los espectros ópticos/UV de AGN como debidas a la anisotropía del material absorbente (el "toroide") en estas fuentes. Según estos modelos, las propiedades observadas en el óptico/UV/rayos X dependen de la visual con respecto al núcleo del AGN: los AGN de tipo 1 son fuentes en las que estamos observando directamente el núcleo, mientras que en los AGN de tipo 2 el material absorbente intercepta la línea de visión, oscureciendo el núcleo y la región donde se emiten las líneas anchas. Si estos modelos son correctos, debería existir una correlación entre las propiedades observadas en el óptico/UV y en rayos X: AGN de tipo 1 deberían verse no absorbidos en rayos X mientras que los de tipo 2 deberían estar absorbidos en rayos X. Estudios espectrales recientes de muestras de AGN, incluyendo los dos estudios presentados en los Capítulos 3 y 4 de esta tesis, han encontrado que la correlación oscurecimiento óptico-absorción en rayos X no se cumple en una fracción importante de AGN tanto de tipo 1 como de tipo 2 [152] [153]. Estos resultados cuestionan la validez universal del modelo unificado de AGN, al menos en su versión más simple.

Los AGN son emisores de radiación en todo el rango del espectro, desde el IR y radio hasta los rayos gamma, aunque la emisión en rayos X, que normalmente supone el 3-10% de la emisión total del AGN, es una propiedad común de los AGN. Los modelos de síntesis del fondo de rayos X (ver por ejemplo [44] [57] [84] [139] [155] [193]) intentan explicar la emisión del fondo de rayos X y la distribución en flujo de las fuentes como la superposición de AGN. Sin embargo para poder ajustar los resultados observacionales, estos modelos necesitan que una fracción importante de los AGN está absorbida por grandes cantidades de material. Es decir, los modelos predicen que la mayor parte de la emisión por acreción en el universo está oscurecida. Los rayos X más energéticos son capaces de atravesar importantes cantidades de material absorbente sin verse apenas afectados, proporcionando la única manera (salvo el infrarojo lejano FIR) de ver directamente la emisión procedente de las regiones más internas en AGN absorbidos. Por lo tanto la mejor manera de estudiar la estructura y mecanismos de emisión en las regiones de los AGN más cercanas al agujero negro es estudiando su emisión en rayos X.

La generación actual de observatorios de rayos X, *Chandra*, *XMM-Newton* y *Suzaku*, está proporcionando datos de calidad sin precendentes, que nos están permitiendo incrementar significativamente nuestro conocimiento acerca de la naturaleza de dichas fuentes. Sin embargo, sólo se pueden realizar estudios espectroscópicos detallados para los objetos más brillantes y cercanos. Las propiedades observadas para fuentes en el universo local no tienen por qué describir necesariamente las propiedades de las fuentes más débiles y más lejanas que, como hemos visto, dominan la emisión del FRX. Es más, no está clara la dependencia de los mecanismos de emisión en AGN con distintos parámetros de las fuentes como el flujo, luminosidad en rayos X y redshift. Por lo tanto, para entender la naturaleza y evolución de los AGN es necesario cuantificar estas dependencias. Uno de los métodos más eficientes para realizar este tipo de estudios es a través de análisis estadísticos de muestras amplias y representativas de fuentes. Nosotros hemos seguido este camino para realizar los estudios espectrales de fuentes presentados en esta tesis.

Algunos de los aspectos que nos hemos planteado abordar en nuestros estudios son los siguientes:

1. Estudiar las propiedades de emisión en rayos X de AGN débiles, a flujos donde la contribución de fuentes a la emisión del fondo extragaláctico de rayos X tiene su máximo, en especial las propiedades del continuo de emisión y la absorción. Como hemos visto, existen evidencias observacionales de que la mayoría de los AGN están absorbidos en rayos X por grandes cantidades de gas y polvo situado en las proximidades del agujero negro. Sin embargo, una de las mayores incertidumbres de los modelos de síntesis del FRX es la distribución de densidades columna entre distintos tipos de AGN, ya que hasta el momento esta distribución solo se ha podido medir

de forma fiable para fuentes cercanas.

2. ¿Existe alguna dependencia de las propiedades de la emisión de los AGN con la luminosidad intrínseca de estos objetos? ¿Han evolucionado las propiedades de emisión con el redshift cosmológico? Conocer la distribución de absorción en AGN y su dependencia con la luminosidad y el redshift de las fuentes es esencial para conocer la función de luminosidad de los AGN, y su evolución con el redshift, que es clave para los modelos de síntesis del FRX y por tanto la historia de acreción en el Universo.

3. Comprobar la validez del modelo unificado de AGN, utilizando los resultados de análisis espectrales: ¿tienen los AGN de tipo 1 y tipo 2 las mismas propiedades intrínsecas? ¿Puede la absorción intrínseca explicar las diferencias observacionales en el óptico/UV y en rayos X en estas fuentes? ¿En qué fracción de AGN el oscurecimiento en el óptico/absorción en rayos X no están correlacionados y cuál es el origen de esta discrepancia? ¿Es el modelo unificado de AGN todavía válido en estos casos?

4. ¿Cómo de frecuente es la variabilidad de AGN en rayos X en escalas temporales de meses-años? ¿Cuál es la amplitud de la variación? ¿Se observan las mismas propiedades de variabilidad en AGN de tipo 1 y tipo 2? ¿Cuál es la dependencia de la variabilidad con la energía? ¿Existe alguna correlación entre la variabilidad espectral y variabilidad en flujo como se ha observado en binarias de rayos X y AGN cercanos? ¿Dependen las propiedades de la variabilidad detectada de la luminosidad de las fuentes o el redshift?

0.2 Planteamiento y metodología

Las misiones *XMM-Newton* de la ESA y *Chandra* de la NASA son los observatorios de rayos X más potentes hasta la fecha. Ambos fueron lanzados en 1999. *Chandra* es principalmente un observatorio de imagen, es decir, *Chandra* está optimizado para obtener imágenes de alta resolución angular (precisión de $\sim 0.5''$), mientras que *XMM-Newton*, con resolución espacial moderada ($\sim 15''$ Half Energy Width HEW), tiene mayor área colectora, convirtiéndose en el observatorio ideal para realizar estudios de espectroscopía en rayos X. *XMM-Newton* lleva a bordo 3 instrumentos operando en paralelo: RGS que consta de dos espectrómetros de dispersión diseñados para realizar espectroscopía de alta resolución ($E/\Delta E \sim 100$-700) en el rango de energías 0.3-2.1 keV, tres cámaras de rayos X (European Photon Imaging Cameras-EPIC) llamadas MOS1, MOS2 y pn, y un monitor óptico. Las cámaras EPIC cubren un campo de visión de $30'$, y tienen resolución espectral moderada ($E/\Delta E \sim 20$-50). Todos los datos que se han utilizado para los estudios presentados en esta tesis fueron obtenidos con los detectores EPIC.

Para dar respuesta a las preguntas planteadas en la sección anterior, hemos realizado un análisis espectral detallado de las propiedades en rayos X de dos muestras de fuentes. La primera de las muestras que hemos utilizado fue extraída de 25 observaciones (algunos de los campos observados más de una vez) incluidas en el proyecto AXIS (An XMM-Newton International Survey). Las fuentes fueron detectadas sobre un ángulo sólido de $\sim 3.5\,\mathrm{deg}^2$ y tienen flujos $\sim 10^{-15} - 10^{-12}\,\mathrm{erg\,cm^{-2}\,s^{-1}}$. La mayoría de estas fuentes tienen flujos típicos de la población de fuentes donde la contribución a la emisión del FRX es máxima. AXIS es parte del programa de seguimiento e identificación de fuentes detectadas “al azar” con *XMM-Newton*. AXIS está liderado por el IFCA (Instituto de Física de Cantabria; investigador principal Xavier Barcons). Todas las observaciones incluidas en el proyecto tienen imagen multi-banda en el óptico. Para una fracción significativa de las fuentes en rayos X más brillantes también disponemos de espectroscopía óptica. Esto nos ha permitido realizar un análisis espectral detallado en una de las muestras de AGN de mayor tamaño hasta la fecha.

Las observaciones seleccionadas dentro del proyecto AXIS tienen tiempos de exposición típicos de ∼20 ks, y por tanto, teniendo en cuenta que la mayoría de las fuentes analizadas son débiles (la mayoría de las fuentes incluidas en nuestro análisis tienen espectros en rayos X con ∼100 cuentas), las incertidumbres en algunos de los resultados obtenidos de nuestro análisis espectral son importantes. Para conocer mejor la población de AGN a estos flujos, hay que incrementar sustancialmente el cociente señal ruido de los espectros, lo cual requiere realizar observaciones significativamente más largas. Sin embargo, los tiempos de integración que serían necesarios para poder obtener suficiente calidad espectral son demasiado altos, y sólo pueden realizarse en un número reducido de campos. Uno de estos campos es el *Lockman Hole* (R.A.:10:52:43, Dec:+57:28:48). Debido a que la absorción por la Galaxia es mínima ($\sim 5 \times 10^{19}\,\mathrm{cm}^{-2}$) en la dirección del *Lockman Hole*, se trata de una de las zonas del cielo mejor estudiadas a diferentes longitudes de onda. Es más, una gran fracción de las fuentes detectadas en rayos X en el *Lockman Hole* ya han sido identificadas espectroscópicamente. *XMM-Newton* ha realizado la observación más larga hasta la fecha sobre esta zona del cielo. Las observaciones de *XMM-Newton* en el *Lockman Hole* constan de 17 exposiciones diferentes con un tiempo de integración total de más de 600 ks con cada cámara EPIC. Para el segundo de los análisis espectrales presentados en esta tesis, hemos seleccionado las fuentes más brillantes detectadas por *XMM-Newton* en el *Lockman Hole*, todas ellas con suficiente señal en los espectros (más de 500 cuentas) como para poder realizar un estudio detallado de las propiedades de emisión de cada fuente individualmente. Como nuestro mayor interés es el estudio de las propiedades de emisión de la población de AGN, excluimos de la lista de fuentes seleccionadas todos los objetos no identificados como AGN, es decir estrellas y cúmulos de galaxias.

Los estudios de poblaciones de fuentes de rayos X requieren un laborioso proceso antes de comenzar el análisis de los datos. Una parte importante de este proceso es la identificación de las fuentes. En primer lugar hay que tomar imágenes en el óptico de la zona donde se detectan las fuentes en rayos X. Estas imágenes se utilizan para buscar las posibles contrapartidas ópticas de las fuentes de rayos X, es decir, fuentes ópticas cuya posición se encuentra próxima a la fuente en rayos X. Seguidamente hay que realizar espectroscopía en el óptico de las fuentes seleccionadas. Como hemos visto en la sección anterior, una fuente en la que se observan líneas de emisión anchas se clasifica como AGN de tipo 1 mientras que las fuentes donde sólo se observan líneas de emisión estrechas se clasifican como galaxias con líneas de emisión estrechas, del inglés NELG. No todas las NELG contienen necesariamente un AGN; en general la naturaleza de AGN se confirma con la luminosidad en rayos X de la fuente, o mediante diagnósticos de líneas de emisión ópticas. Si la luminosidad observada es $\geq 10^{43}\,\mathrm{erg\,s^{-1}}$ entonces se puede decir con gran seguridad que la fuente contiene un AGN, ya que no se conocen galaxias sin el fenómeno de acreción con tales luminosidades.

Antes de comenzar nuestros análisis espectrales de fuentes, realizamos los siguientes pasos para obtener las listas de fuentes de rayos X de AXIS y del *Lockman Hole*:

1. *Selección de observaciones*: En primer lugar hay que seleccionar observaciones de *XMM-Newton* de suficiente calidad como para realizar el estudio. Por ejemplo, las observaciones deben tener un mínimo de tiempo de exposición que garantize que, para las fuentes en las que estamos interesados y que son típicamente débiles, los espectros tendrán suficiente calidad como para permitir que realicemos los estudios en los que estamos interesados. Por otro lado, hay que evitar observaciones que contengan fuentes muy brillantes, en especial si las fuentes son además extensas, ya que estas fuentes reducen significativamente el área del campo de visión donde podemos detectar las fuentes en las que estamos interesados.

2. *Obtención de listas de fuentes para cada observación*: Para cada observación hay que obtener una lista de fuentes detectadas. La cadena de procesado de datos de *XMM-Newton* proporciona listas de fuentes para cada observación y cámara EPIC. Normalmente estas listas de fuentes son de suficiente calidad, así que en general no es necesario extraerlas nuevamente. Para el análisis de las fuentes de AXIS utilizamos los datos proporcionados por la cadena de reprocesado de *XMM-Newton*. Sin embargo, para extraer la lista de fuentes detectadas en la observación total del *Lockman Hole* tuvimos que hacer nuestra propia detección de fuentes, ya que hemos combinando datos de distintas observaciones. Para obtener la lista de fuentes detectadas por *XMM-Newton* en la exposición total, primero combinamos los datos de cada observación, y después ejecutamos el algoritmo de detección de fuentes de la cadena de reprocesado de *XMM-Newton* utilizando los datos combinados.

3. *Control de calidad de las listas de fuentes*: Hay que controlar la calidad de cada una de las listas de fuentes, eliminando detecciones espúreas, asociadas con detecciones en áreas de los detectores problemáticas, como por ejemplo detecciones en píxeles o columnas calientes. Parte de este proceso se puede automatizar. Sin embargo, los resultados de cada una de las observaciones tienen que ser comprobados individualmente.

4. *Extracción de espectros*: Para cada fuente, detector EPIC y observación (en AXIS como hemos visto anteriormente algunos de los campos han sido observados en más de una ocasión, mientras que en el *Lockman Hole*, aunque la detección de fuentes se realizó sobre los datos combinados, la extracción de espectros debe realizarse en cada observación por separado) hay que hacer la extracción de todos los productos necesarios para realizar el análisis espectral de las fuentes: espectro de la fuente y del fondo en el área donde se detectó la fuente, y matrices de calibración. Las matrices de calibración contienen información acerca del área efectiva de cada detector en función de la energía, y la conversión entre canales de detector y energías. Para realizar los ajustes espectrales el software que utilizamos para nuestros estudios necesita, a

parte de los espectros de las fuentes, la información que contienen estas matrices de calibración.

5. *Primer filtrado de calidad de espectros*: No queremos incluir en nuestros estudios fuentes detectadas con baja calidad en los espectros extraídos. Por tanto hemos realizado un "filtro de calidad" de los espectros extraídos para cada objeto: seleccionamos los espectros de fuentes detectadas fuera de las áreas problemáticas de los detectores.

6. *Suma de espectros*: En los casos donde tenemos más de un espectro disponible por fuente, combinamos todos los espectros de la fuente, es decir los espectros de la fuente+fondo, los espectros del fondo y las matrices de calibración. Para incrementar la calidad de los datos se combinaron los espectros obtenidos con los detectores EPIC MOS1 y MOS2, y que pasaron el primer "filtro de calidad". No combinamos estos con los del EPIC-pn ya que los detectores MOS y pn tienen respuestas diferentes. Al final tenemos para cada fuente un espectro promedio MOS y otro pn.

7. *Segundo filtrado de calidad de espectros*: Una fracción de las fuentes detectadas son demasiado débiles como para poder permitir un estudio espectral. Solo hemos utilizado en nuestros estudios espectros de fuentes con suficiente calidad (número de cajas, número de cuentas de la fuente). Por ejemplo, para las fuentes de AXIS seleccionamos aquellos espectros con más de 5 cajas. Para las fuentes del *Lockman Hole* no hizo falta aplicar el segundo "filtro de calidad", ya que todos los espectros de las fuentes seleccionadas pasaban el corte.

Para el análisis de los espectros combinados de cada fuente utilizamos el paquete de ajuste de espectros `Xspec`11.3.0 [7]. Para realizar el ajuste de los espectros hemos utilizado el test χ^2, ya que nos permite obtener la bondad de los ajustes. Para poder usar este test los datos tienen que seguir una distribución estadística gausiana, así que antes de realizar los ajustes espectrales tuvimos que agrupar los espectros de nuestras fuentes de manera que cada caja tenga suficientes cuentas para que la hipótesis de estadística gausiana fuera correcta. Para los espectros de AXIS, con menor número de cuentas, utilizamos 10 cuentas por caja. Para comprobar que con 10 cuentas por caja la hipótesis de estadística gausiana es correcta, comparamos las distribuciones de χ^2 obtenidas de nuestros ajustes con la distribución de χ^2 esperada. No hemos visto indicaciones de que nuestra distribución sea diferente de la esperada (por ejemplo que nuestra distribución tenga un exceso a valores bajos de χ^2), y por tanto concluimos que la hipótesis de estadística gausiana se cumple. Para los espectros del *Lockman Hole*, de mayor calidad, utilizamos un mínimo de 30 cuentas por caja.

Para obtener el ajuste que mejor reproduce la emisión de nuestras fuentes, utilizamos diferentes modelos espectrales a los que fuimos añadiendo nuevas componentes. Para aceptar la detección de componentes adicionales en los modelos utilizamos el test F, exigiendo que la significancia de la mejora al introducir un modelo adicional fuera mayor que el 95%.

Finalmente, para complementar los resultados de los análisis espectrales de las fuentes de AXIS y del *Lockman Hole*, hemos realizado un estudio detallado de la variabilidad en

flujo y espectral en escalas temporales de meses/años de las fuentes del *Lockman Hole* que fueron seleccionadas para el análisis espectral.
Para realizar el estudio de variabilidad en flujo fabricamos curvas de luz utilizando las tasas de contaje detectadas en cada observación. Como queremos comparar las propiedades de variabilidad de las fuentes con los resultados del análisis espectral utilizamos tasas de contaje en la misma banda de energía donde se extrajeron los espectros, 0.2-12 keV. Para realizar el estudio de variabilidad espectral de las fuentes no utilizamos los espectros de los objetos de cada observación, ya que las incertidumbres en los parametros obtenidos en los ajustes van a ser mayores que la amplitud de la variabilidad. Por lo tanto, definimos un "color" en rayos X para cada fuente, que no es más que la diferencia (normalizada) entre tasas de cuentas ó contajes medidos en dos bandas de energía: 0.5-2 keV y 2-12 keV. Las bandas de energía se definieron intentando separar mejor las distintas componentes espectrales que dominan la emisión de nuestras fuentes. Para buscar fuentes variables se utilizó el test χ^2, mientras que para cuantificar la amplitud de variabilidad en flujo detectada en cada fuente se utilizó un análisis bayesiano [3].

Muchos de los resultados de nuestros análisis spectrales y de variabilidad pueden estar afectados por sesgos presentes en nuestras muestras, por ejemplo relacionados con la forma en que las fuentes fueron seleccionadas, sesgos inherentes a la instrumentación utilizada para detectar las fuentes, o simplemente debido a la calidad de los datos. Todos estos efectos tienen que tenerse en cuenta a la hora de interpretar los resultados obtenidos. Sin embargo, en la mayoría de los casos, corregir los resultados por estos sesgos conlleva el realizar un gran número de simulaciones. Nosotros hemos realizado un gran número de simulaciones de distintos tipos para corregir algunos de los resultados obtenidos en el análisis espectral de las fuentes de AXIS, y en el análisis de variabilidad de las fuentes del *Lockman Hole*.

0.3 Aportaciones originales

Los estudios presentados en esta tesis han contribuido significativamente al conocimiento de las propiedades de emisión de los AGN, a flujos donde se origina la mayor parte de la emisión del FRX. El análisis espectral de las fuentes de AXIS es uno de los análisis más detallados sobre una de las muestras de AGN seleccionados en rayos X de mayor tamaño realizados hasta la fecha. Este análisis ha permitido estudiar las propiedades de emisión de AGN en un amplio rango de parámetros de las fuentes, estudiando la dependencia de las propiedades de emisión con respecto a estos parámetros. Por otro lado, el análisis detallado de la emisión de las fuentes detectadas en el *Lockman Hole* nos ha permitido estudiar las propiedades de emisión observadas en AGN, usando espectros de cociente señal ruido sin precedentes para fuentes de flujos intermedios.

Con estos estudios espectrales hemos podido, por ejemplo, cuantificar la importancia de las distintas componentes que contribuyen a la emisión en rayos X de AGN a las energías observadas. Hemos podido cuantificar tanto la forma del continuo de emisión de AGN, como la amplitud de su dispersión intrínseca. Hemos podido obtener las distribuciones de densidad de absorción, tanto para AGN de tipo 1 como para AGN de tipo 2. Hemos confirmado observacionalmente que el modelo unificado falla para una cierta fracción de fuentes de tipo 1 y tipo 2, y hemos podido cuantificar la fracción de AGN donde el modelo falla (∼10% AGN de tipo 1 y ∼20% AGN de tipo 2). Hemos podido comprobar algunas de las hipótesis que podrían explicar el desacuerdo entre las propiedades de estas fuentes observadas en el óptico y en rayos X, y que en principio no invalidarían el modelo unificado de AGN: por ejemplo, el efecto contraste AGN/galaxia anfitriona para explicar la no detección de líneas anchas en AGN de tipo 2 no absorbidos, la naturaleza opaca por difusión Compton de las fuentes para explicar la no detección de absorción en rayos X en algunos AGN de tipo 2, y finalmente la variabilidad espectral.

Finalmente hemos realizado un estudio detallado de la dependencia de las propiedades de emisión de las fuentes con el flujo observado. Para las fuentes identificadas como AGN, hemos podido realizar un estudio de la dependencia de las propiedades observadas con la luminosidad de las fuentes y con el redshift.

0.4 Conclusiones

Los resultados más importantes de nuestros análisis espectrales de las fuentes de AXIS y del *Lockman Hole* son los siguientes:

1. Los análisis espectrales previos de fuentes en rayos X han observado que el espectro promedio de las fuentes se hace más plano (más duro) para las fuentes con flujos más bajos. Este fenómeno es de esperar, ya que la suma de los espectros de todas las fuentes del Universo tiene que "ajustar" el espectro del FRX, más plano que el de las fuentes brillantes. Las dos hipótesis más extendidas que explican este efecto son por un lado un incremento en la absorción en rayos X en fuentes más débiles, que hace que el espectro de las fuentes parezca más plano. Por otro lado, la existencia de una población de fuentes a flujos débiles intrínsecamente más duras también podría explicar el efecto observado. Con los estudios espectrales presentados en esta tesis hemos podido confirmar la dependencia del espectro promedio de las fuentes con el flujo en rayos X, tanto para las fuentes de AXIS como para las fuentes del *Lockman Hole*. Sin embargo nuestros análisis espectrales muestran que este efecto no se debe a que las fuentes más débiles tengan espectros intrínsecamente más duros: la absorción en rayos X hace que las fuentes con flujos observados (es decir, sin corregir por el efecto de la absorción) más bajos parezcan más duras. **Una vez los datos se han corregido por el efecto de absorción**, observamos que **la forma del continuo de emisión de los AGN no cambia con el flujo.**

2. Utilizando flujos corregidos por absorción en vez de flujos observados, encontramos que **tanto la fracción de fuentes absorbidas en rayos X como la cantidad de absorción no varían con el flujo**. El resultado es el mismo independientemente de si se utilizan flujos en la banda 0.5-2 keV (donde el efecto de la absorción es más importante) o en la banda 2-10 keV.

3. La pendiente promedio del continuo de emisión a energías entre ∼0.2-12 keV es ∼1.9-2 (en fotones por unidad de banda de energía) tanto para AGN de tipo 1 como para

AGN de tipo 2. Si calculamos la forma del espectro promedio de las fuentes permitiendo una dispersión en los valores del continuo de emisión, **no encontramos evidencia de que los AGN de tipo 2 sean intrínsecamente más planos que los AGN de tipo 1,** como han sugerido análisis espectrales previos en distintas muestras de fuentes [4] [209]. Es más, **la amplitud de la dispersión intrínseca del continuo de emisión en AGN, del orden de 0.20, es similar en AGN de tipo 1 y tipo 2**. Para medir la amplitud de la dispersión intrínseca de pendientes del continuo de emisión es necesario tener suficiente señal en los datos, porque si no otras componentes espectrales no detectadas (por ejemplo absorción) aumentarán la dispersión. Este efecto es más evidente en las fuentes de AXIS donde encontramos un valor de la dispersión de 0.21 para los AGN de tipo 1 (menos afectados por absorción) y 0.36 para los AGN de tipo 2 (donde la absorción es mucho más importante). Para las fuentes del *Lockman Hole*, de mayor calidad espectral y donde los efectos de la absorción se pudieron "detectar" más eficazmente, el valor de la dispersión que encontramos fue de ~0.20 en ambas muestras de fuentes. Nuestros análisis espectrales muestran que **las diferencias en las propiedades del continuo de emisión observadas para AGN de tipo 1 y tipo 2** por algunos análisis espectrales previos, **son debidas a que ambas poblaciones de fuentes sufren distintas absorciones, y no a diferencias en las propiedades intrínsecas de las fuentes.**

4. **Una fracción importante de los AGN de tipo 1 en nuestras muestras de fuentes están absorbidos en rayos X**. Hemos detectado absorción en rayos X tanto en AGN de tipo 1 (~6% para fuentes de AXIS y 10% para las fuentes del *Lockman Hole*) como en AGN de tipo 2 (~40% para fuentes de AXIS y 77% para las fuentes del *Lockman Hole*). En ambas muestras encontramos que **la fracción de fuentes absorbidas es significativamente mayor en AGN de tipo 2 que en AGN de tipo 1 (en torno a un factor 4) tal y como esperamos si los modelos de unificacion de AGN son correctos**. Además, la distribución de densidades columna para las fuentes de tipo 1 parece estar sesgada a valores de absorción más bajos, lo que podría indicar que el material absorbente en estas fuentes es distinto del "toroide" responsable de la absorción en AGN de tipo 2. El material responsable de la absorción en los AGN de tipo 1 podría ser por ejemplo la propia galaxia que los alberga. Alternativamente, la detección de líneas anchas en el óptico y absorción en rayos X podría explicarse si el material responsable de la absorción en rayos X está formado por nubes de gas situadas dentro de la región de líneas anchas [206], es decir, mucho más cerca del agujero negro que el "toroide", o si el cociente gas-polvo del material absorbente es significativamente distinto del de la Galaxia [142]. Finalmente, debido a que las medidas en el óptico/rayos X de nuestras fuentes no se realizaron simultánemanete (como sucede en la gran mayoría de las campañas de identificación de fuentes seleccionadas en rayos X), no se puede descartar la hipótesis de que estos objetos hayan experimentado variabilidad espectral. Por ejemplo variaciones en la densidad columna ó en el estado de ionización del material absorbente. Variaciones del orden de $10^{21}\,\mathrm{cm}^{-2}$ en escalas temporales de meses-años parecen ser comunes tanto en AGN de tipo 1 como de tipo 2 [144].

5. **No todos los AGN de tipo 2 están absorbidos en rayos X**. Entre las fuentes de AXIS, sólo detectamos absorción en el ~40% de los AGN de tipo 2, mientras que en los datos del *Lockman Hole* la fracción de AGN de tipo 2 con absorción en rayos X detectada es del ~77%. Utilizando los resultados de nuestros análisis espectrales, hemos podido estudiar algunas de las hipótesis que explican la no detección de absorción en AGN de tipo 2. Por ejemplo, con los datos de AXIS pudimos estudiar si el efecto AGN/galaxia huésped puede explicarlo. Si estas fuentes son débiles la emisión en el óptico estará dominada por la emisión de la galaxia que los alberga, y por tanto en estos casos no podemos detectar líneas de emisión anchas en los espectros ópticos. Comparando la distribución de luminosidades en rayos X de los AGN de tipo 2 no absorbidos con la distribución para fuentes de tipo 1 en el mismo rango de redshifts (para evitar la correlación que existe entre luminosidad y redshift en muestreos de fuentes limitados en flujo) encontramos una probabilidad (utilizando el test de Kolmogorov-Smirnov) del ~99% de que la luminosidad promedio de los AGN de tipo 2 no absorbidos son intrínsecamente menos luminosos que los AGN de tipo 1. **Nuestros resultados parecen indicar que el efecto AGN/galaxia anfitriona podría explicar la no detección de absorción en los AGN de tipo 2 de AXIS**. El número de AGN de tipo 2 no absorbidos que encontramos en el *Lockman Hole* no es suficientemente grande como para poder comprobar si se obtiene el mismo resultado. Otra hipótesis que podría explicar la no detección de líneas de emisión anchas en estas fuentes es que la luminosidad del AGN no es suficientemente alta como para ionizar la región donde se emiten las líneas anchas. En este caso cabría esperar que la fracción de AGN de tipo 2 no absorbidos fuera mayor a luminosidades bajas; sin embargo no encontramos evidencia de este efecto en nuestros análisis: los AGN de tipo 2 no absorbidos en nuestras listas de fuentes no parecen tener luminosidades más bajas que los AGN de tipo 2 absorbidos. Otra hipótesis es que las fuentes sean opacas al efecto Compton: si la densidad columna de absorción es igual o mayor que el inverso de la sección eficaz de Thomson ($N_H \geq \sigma_T^{-1} \sim 1.5 \times 10^{24}\,\mathrm{cm}^{-2}$), entonces la profundidad óptica de dispersión Compton es 1 y ningún fotón con energía $\leq$10 keV escapa de la fuente. En estas fuentes la única emisión que se observa es radiación a energías más altas ($\geq$10 keV) dispersada a las energías observadas. Sin embargo si nuestras fuentes fueran opacas Compton, como la radiación nuclear estaría completamente bloqueada por el material absorbente, y por tanto el continuo en rayos X sería más débil, esperaríamos detectar mejor la línea de emisión de Fe Kα (mayor anchura equivalente). Sin embargo esta componente de emisión no se detecta en ninguno de los AGN de tipo 2 no absorbidos en el *Lockman Hole*. Por lo tanto, es improbable que nuestras fuentes sean opacas Compton.

6. El exceso blando es una componente de emisión común en el espectro de los AGN, que se pudo detectar en el ~7% de los AGN de AXIS y en el ~11% de los AGN de tipo 1 y 25% de los AGN de tipo 2 en el *Lockman Hole*. Nuestros análisis espectrales no muestran evidencia de que esta componente sea más común en AGN de tipo 1 o tipo 2. Ajustando esta componente con un modelo térmico de emisión (cuerpo negro) encontramos que la temperatura del exceso blando se encuentra en el rango

0.1-0.3 keV tanto para fuentes en AXIS como para las fuentes en el *Lockman Hole*, es decir, **la distribución de temperaturas del exceso blando varía muy poco entre unas fuentes y otras. Tampoco observamos una clara dependencia de las propiedades de esta componente, temperatura y luminosidad, con la luminosidad intrínseca de los AGN y el redshift**. La luminosidad en rayos X de brotes de formación estelar es del orden de $\sim 10^{41}\,\mathrm{erg\,s^{-1}}$ mientras que la mayoría de nuestros AGN tienen exceso blando con luminosidades $> 10^{43}\,\mathrm{erg\,s^{-1}}$. **Por lo tanto, las luminosidades típicas del exceso blando en nuestras fuentes son demasiado altas como para poder explicar su origen como emisión térmica de las galaxias que contienen los AGN únicamente**. Podría suceder que parte de la emisión procediera del AGN y parte de la galaxia. Sin embargo, la calidad de nuestros espectros no es suficiente como para poder separar ambas componentes. **Mientras que las luminosidades del exceso blando son similares tanto para AGN de tipo 1 como de tipo 2, la temperatura de esta componente en las fuentes del *Lockman Hole* parece ser mayor para fuentes de tipo 2 que de tipo 1, quizás debido a que en las fuentes de tipo 2 hay una componente reflejada mayor que en las de tipo 1**. No pudimos comprobar si se observa el mismo resultado para las fuentes de AXIS, ya que en esta muestra sólo tenemos dos fuentes de tipo 2 con exceso blando detectado. Mientras que en las fuentes de AXIS pudimos obtener un buen ajuste de los datos con un modelo térmico (probablemente debido a que la señal de los datos es más baja), para una fracción de las fuentes en el *Lockman Hole* el modelo térmico no fue capaz de ajustar los datos. En todos estos casos, un modelo donde sólo parte de la emisión del núcleo es absorbida fué capaz de proporcionar un buen ajuste de la emisión.

7. No está claro si las propiedades de emisión de los AGN dependen de la luminosidad de las fuentes o no. Por ejemplo, algunos autores han sugerido que la fracción de AGN absorbidos disminuye con la luminosidad de las fuentes [235]. **Nuestros análisis espectrales no muestran evidencia de que la forma del continuo de emisión y la cantidad de absorción en nuestras fuentes dependan de la luminosidad de los AGN. Por otro lado, hemos comparado las distribuciones de luminosidad de fuentes absorbidas y no absorbidas tanto para AGN de tipo 1 como de tipo 2. En ninguno de los casos encontramos que las distribuciones sean significativamente distintas.**

8. Análisis espectrales de fuentes detectadas con *ROSAT* [24] y *ASCA* [240] encontraron evidencias de que el continuo promedio de emisión de los AGN se hace más duro (más plano) a altos redshifts [20]. Sin embargo, estudios espectrales más recientes de fuentes de *XMM-Newton* y *Chandra* sugieren distintas evoluciones: algunos estudios han encontrado que el espectro promedio se hace más duro [20], mientras que en otros casos parece que se hace más blando [97]. Finalmente, algunos estudios sugieren que no hay evolución espectral significativa [239]. **En ninguno de nuestros análisis espectrales observamos evolución espectral en el continuo de emisión de nuestros AGN**. Tampoco hemos encontrado que la absorción en rayos X en AGN de tipo 1 ocurra preferentemente a ningún redshift. Finalmente, no se observó una

dependencia clara de la densidad columna de absorción con el redshift tanto para AGN de tipo 1 como de tipo 2.

9. Usando los resultados de la detección de absorción en la muestra de AGN de AXIS (número de fuentes con absorción detectada y distribuciones de densidad columna), hemos podido comprobar que **la gran mayoría de los modelos de síntesis del FRX predicen en torno a un factor ≥2 un mayor número de fuentes absorbidas que las que encontramos en nuestro análisis.** Incluso el modelo de Ueda et al.(2003) [235], que supone una dependencia de la absorción con la luminosidad de las fuentes (menos fuentes absorbidas a altas luminosidades), también predice un exceso de fuentes absorbidas, en especial a redshifts bajos, aunque está en mayor acuerdo con nuestros resultados.

Algunos de los resultados más importantes de nuestro estudio de las propiedades de variabilidad en rayos X de las fuentes más brillantes detectadas en el *Lockman Hole* son los siguientes:

1. **La mayoría de los AGN (posiblemente más del 80%) varían en flujo con amplitudes de variabilidad entre el 10-65% en escalas temporales de meses-años**. Amplitudes de variabilidad superiores al 65% no parecen ser muy comunes en nuestras fuentes, al menos en las escalas de tiempo que hemos estudiado. **Los AGN de tipo 1 y tipo 2 parecen poseer las mismas propiedades de variabilidad en flujo (amplitud y fracción de fuentes variables).** No encontramos dependencia de la amplitud de variabilidad en flujo con la luminosidad o el redshift de las fuentes. Esto último podría indicar que **las propiedades de variabilidad de nuestros AGN no dependen de la energía**, ya que nuestra muestra de fuentes de tipo 1 cubre un rango de redshifts hasta ~3.5, lo que supone que estamos estudiando variabilidad en distintas bandas de energía en el sistema de referencia de la fuente a distintos redshifts.

2. Utilizando colores de rayos X pudimos detectar variabilidad espectral en el 20% de las fuentes, aunque los resultados sugieren que **la fracción de fuentes en nuestra muestra con variabilidad espectral podría ser del orden del 40%**. Aunque la variabilidad espectral es más difícil de detectar que la variabilidad en flujo, este resultado parece indicar que **variabilidad espectral es menos común en los AGN que variabilidad en flujo, un resultado que puede explicarse si una única componente espectral es la que varía en flujo, por ejemplo el continuo de emisión**. Comparando los resultados de detección de variabilidad para las muestras de AGN, encontramos que **la variabilidad espectral parece ser más común en AGN de tipo 2 que de tipo 1**.

3. Los resultados de nuestro análisis sugieren que **para una gran parte de nuestras fuentes, la variabilidad en flujo y espectral no parecen estar correlacionadas**. Para las fuentes con variabilidad en flujo y espectral detectadas hemos comprobado si existe correlación entre el flujo y los colores en rayos X observados, con resultado negativo.

4. Para entender el origen de la variabilidad espectral observada agrupamos los espectros de las fuentes en cuatro períodos de tiempo, en función de los períodos de observación. De esta manera podemos estudiar la variabilidad espectral directamente en los espectros de las fuentes en escalas de tiempo similares a las que cubrimos con los colores en rayos X. Con este análisis detectamos variabilidad espectral en 8 fuentes de la muestra, 6 de ellas identificadas como fuentes de tipo 1 y una de tipo 2. Un análisis detallado de los espectros de estas fuentes nos ha permitido ver que en todos los casos **el origen de la variabilidad espectral en nuestras fuentes está asociado a cambios en la pendiente del continuo de emisión. En ninguna de las fuentes detectamos cambios significativos en otras componentes espectrales, como la densidad columna o el exceso blando**. Esto podría explicar por ejemplo, el resultado de que se detecta más variabilidad espectral en fuentes de tipo 2, ya que si gran parte del exceso blando en estas fuentes procede de una componente reflejada no debería variar, lo que haría que sólo una de las bandas del color en rayos X variara.

5. Solamente se detectó variabilidad espectral en uno de los 4 AGN de tipo 2 no absorbidos del *Lockman Hole*. Por lo tanto no parece probable que la variabilidad espectral sea el origen de la falta de correlación entre las propiedades observadas en el óptico y en rayos X para estas fuentes.

0.5 Futuras líneas de investigación

Cada observación de *XMM-Newton* detecta del orden de ~30-150 fuentes, la mayoría de ellas por primera vez. Todas las fuentes que han sido detectadas con *XMM-Newton* en ~4000 observaciones se van a unir para crear el segundo catálogo de fuentes detectadas con *XMM-Newton*, el *2XMM*. *2XMM* será publicado a comienzos de 2007, y va a ser el catálogo de rayos X de mayor tamaño hasta el momento (*2XMM* será 5 veces mayor que la versión anterior, *1XMM*, publicado en 2003). *2XMM* contendrá más de 250,000 fuentes de rayos X detectadas en ~600 deg^2 de las cuales ~150,000 serán detecciones únicas de fuentes.

Mi mayor interés es continuar con los estudios de la naturaleza y evolución de la población de AGN débiles. Fundamentalmente el estudio de la acreción oscurecida en el universo, y la interacción entre agujeros negros supermasivos y las galaxias que los contienen. Como hemos visto a lo largo de esta tesis, uno de los métodos más eficientes de detección de AGN es en rayos X (en torno al 80% de las fuentes detectadas en rayos X a latitudes galácticas altas son AGN, mientras que esta fracción se reduce a menos del 10% en el óptico, donde la contaminación por otras fuentes es mucho más importante). Por lo tanto, *2XMM* será la base de datos ideal para la selección de muestras de AGN utilizando las propiedades de emisión de estas fuentes en rayos X. *2XMM* permitirá realizar estudios de población de AGN en zonas del espacio de parámetros de las fuentes donde otros muestreos más profundos, como por ejemplo, las observaciones profundas de *XMM-Newton* en el *Lockman Hole*, no son capaces de obtener suficiente frecuencia de muestra. Un ejemplo es la búsqueda de fuentes con luminosidades/redshifts altos, ya que debido a la baja densidad de estas fuentes, se necesita cubrir un área de cielo importante para poder encontrarlas.

Los AGN son fuertes emisores en un ámplio rango del espectro electromagnético, de manera que entender la naturaleza de estas fuentes requiere estudios en todas las bandas. Por lo tanto una parte fundamental de este estudio viene de la correlación de *2XMM* con catálogos ya existentes en el óptico, como por ejemplo el SDSS (Sloan Digital Sky Survey). En torno a 24,000 fuentes del *2XMM* tendrán contrapartidas en SDSS. Los datos de *2XMM*/SDSS nos proporcionarán suficiente información para la clasificación de las fuentes, por ejemplo utilizando colores ópticos, morfología de las fuentes, y nos permitirán obtener redshifts fotométricos para fuentes aún no identificadas espectroscópicamente. Un complemento importante de este estudio será la información en el infrarojo cercano procedente de UKIDSS (UKIRT Infrared Deep Sky Survey). Se espera que en torno a ∼10,000 fuentes tendrán contrapartidas en SDSS y UKIDSS Large Sky Survey (LAS). Los datos en el IR proporcionados por UKIDSS nos permitirá ampliar la muestra de fuentes con redshifts fotométricos a redshifts más altos.

Universidad de Cantabria
Departamento de Física Moderna

CSIC — Universidad de Cantabria
Instituto de Física de Cantabria

X-ray spectroscopy of distant Active Galaxies with the XMM-Newton observatory

A disertation submitted in partial fulfillment of the requirements for
the degree of Doctor of Philosophy in Physics
by

Silvia Mateos Ibáñez

2006

The most exciting phrase to hear in science,
the one that heralds new discoveries,
is not 'Eureka!' but
'That's funny ...'

Isaac Asimov

Acknowledgements

Durante estos años han sido muchas las personas que han hecho posible el desarrollo de esta Tesis Doctoral y a las cuales deseo expresar mi más sincero agradecimiento.

En primer lugar, quisiera agradecerle a mi director de tesis, Xavier Barcons Jáuregui, la confianza que puso en mi al darme la oportunidad de adentrarme en el apasionante mundo de la astronomía de rayos-X.

Tambien quiero expresar mi más sincera gratitud a mi segundo director de tesis, Francisco Carrera Troyano, por la dedicación y interés que ha puesto en este trabajo y en especial por su inestimable ayuda en todos los aspectos de esta tesis. Gracias de nuevo a los dos por la supervisión durante el tiempo que ha llevado la tesis, por las discusiones, en algunos casos interminables, por los comentarios y sugerencias. Gracias por las ideas, siempre buenas y también por las críticas, de las cuales he aprendido mucho. Gracias por el apoyo incondicional en los buenos y malos momentos, en especial durante los comienzos de la tesis cuando las cosas no llegaban a salir y en los últimos meses, cuando la tesis parecia que no iba a acabarse nunca. Es muy difícil encontrar las palabras para agradecerles lo suficiente todo el tiempo que me han dedicado y todo el conocimiento que han compartido conmigo. A los dos me gustaría agradecerles también el enorme esfuerzo que han puesto en la revisión y correcciones del manuscrito final de esta tesis. Gracias a sus aportaciones, ha sido posible que esta tesis se hiciera realidad.

Gracias a Maria Teresa Ceballos por la ayuda que me ha prestado siempre que la he necesitado, por su apoyo tanto técnico como moral. Gracias por escucharme y por los buenos consejos.

No quisiera terminar sin darle las gracias a todos los compañeros del IFCA y a mis amigos. Gracias a aquellos que compartieron despacho conmigo por los buenos momentos, y a todos los compañeros con los que compartí edificio, por el apoyo y amistad que me han prestado siempre de manera desinteresada. Gracias a mi primer compañero de despacho, Jose Maria Diego, por ayudarme en mi primeros pasos de la tesis. Un especial agradecimiento a Aurora Ullán y Belen Barreiro por su apoyo y amistad, por sus buenos consejos y por estar ahí siempre que las necesitaba. Gracias tambien a Patricio Vielva y a Diego Herranz, tambien por su apoyo pero sobre todo por su buen humor, el cual me ha ayudado de una manera importante en los malos momentos.

Esta tesis no habría sido posible sin el apoyo incondicional de mi familia, mis padres y mi hermana, gracias por su cariño y por los buenos consejos. Mi más sincero agradecimiento a Sime, el cual ha sido un apoyo fundamental durante el tiempo de realización de esta tesis, pero sobre todo durante la escritura de la tesis, por estar siempre a mi lado apoyándome y dándome ánimos.

Finally I would like to express my gratitude to my "official" manager Mike Watson, who gave me the opportunity to continue my science career in the Survey Science Centre team in Leicester. I would like to thank all the members of the Survey Science Centre team in Leicester for all the support and help during the time I have spent in Leicester. Specially I would like to thank Jonathan Tedds for his unconditional help and for his friendship over the past two years.

Summary

Since its discovery 40 years ago, unveiling the origin and nature of the cosmic X-ray background emission (XRB) has been one of the major questions in X-ray astronomy. The deepest X-ray surveys conducted with the *Chandra* and *XMM-Newton* X-ray imaging observatories have resolved almost entirely the extragalactic X-ray emission from 0.1 to 10 keV, confirming the discrete origin of the XRB. Large campaigns of optical spectroscopic identifications of the sources detected in these surveys have shown that the dominant population of the X-ray sky is a mixture of unobscured and obscured Active Galactic Nuclei (AGN). Although the discrete nature of the XRB has been confirmed observationally, the nature and cosmic evolution of the sources that dominate the XRB emission is still rather uncertain, specially at X-ray fluxes $\sim 10^{-14}\,\mathrm{erg\,cm^{-2}\,s^{-1}}$ where the bulk of the XRB energy density resides. AGN are strong X-ray emitters, their luminosty is often several orders of magnitude larger than that of the host galaxy, and are believed to be powered by accretion onto a supermassive black hole. Significant X-ray variability on short time scales, often less than a day, has been detected in a number of AGN suggesting that the X-ray emission in these objects must originate in the inner most regions near the nuclear source.

Population synthesis models of the XRB explain the origin of this cosmic radiation as the superposition of AGN. According to these widely accepted models, the XRB is the "echo" of the growth of supermassive black holes in the centres of galaxies, mostly through accretion of matter. In order to reproduce the XRB intensity and spectrum, these models require most AGN to be photoelectrically absorbed. Absorption (and the most likely associated optical obscuration/reddening) suppresses severely optical/UV and soft X-ray photons. The absorbed radiation is reprocessed and re-emitted mostly in the IR. Radio waves can be used in principle to look deep inside the AGN, but this unfortunately only applies to a minority of them which are strong radio emitters. Hard X-rays and gamma rays can penetrate through large columns of gas and dust withougth being significantly affected, and hence, they provide a unique view of the central engine in these objects. Given the large sensitivity of current X-ray observatories, it is therefore clear that X-ray spectral analyses of AGN provide a unique tool to study the cosmic history of the accretion phenomenon in the Universe.

The aim of the work presented in this thesis is to provide further insight into the nature and cosmological evolution of the population of AGN that dominate the XRB emission at intermediate to faint X-ray fluxes and energies from ~ 0.1 to ~ 10 keV. In order to do that we carried out a detailed analysis of the X-ray spectral properties of one of the largest samples of X-ray sources analysed up to date, detected serendipitously with the *XMM-*

Newton observatory and included in the AXIS survey. This analysis allowed us to put observational constrains on the dominant X-ray emission properties of faint AGN, and on their dependence with different spectral parameters. We found the intrinsic emission properties of unabsorbed and absorbed AGN to be in good agreement. We explained the differences in their observed optical/X-ray emission properties as being due to a different amount of X-ray photoelectric absorption among different classes of AGN. We did not find the X-ray spectra of our AGN to depend on luminosity or redshift. In addition, the observed X-ray properties of our objects were found to be in good agreement with those of bright nearby AGN, which tend to be at lower redshifts and have lower X-ray luminosities, suggesting that the same physical process dominates the X-ray emission of AGN at low and high luminosities. Most results of our analysis were found to be in good agreement with AGN unification models and with synthesis models of the XRB. However for a number of AGN the existing correlation between their observed optical and X-ray properties was unclear. We provided possible explanations for the observed properties of these objects. To a first approximation the broad band X-ray spectra of our objects was well reproduced by a power law continuum and photoelectric absorption. It is also well known that other emission components are important in the X-ray spectra of AGN and if not well modelled they can affect the observed results. Unfortunately the signal-to-noise ratio of most objects detected in serendipitous surveys is not high enough to detect with enough significance these extra emission components.

In order to constrain the frequency and properties of the most important emission components in the X-ray spectra of faint AGN, we carried out an X-ray spectral analysis of a smaller sample of sources using the deepest observation carried out so far with *XMM-Newton* in the direction of the *Lockman Hole*. These sources had similar X-ray fluxes that our previous objects, but their spectra had much better signal-to-noise ratio and therefore a more detailed analysis of the emission properties of each individual source was possible. We were able to put strong observational constraints on the frequency and emission properties of the most important components of the X-ray spectra of faint AGN. The results of the two spectral analyses were found to be in good agreement.

While the study of the time averaged spectra of AGN can provide valuable information on the mechanisms of the X-ray emission in AGN, studies of the X-ray variability properties of the objects are an excellent complement to gain insight into the emission mechanisms. We carried out a variability analysis of our *Lockman Hole* sources, on long time scales, from months to years. We found a significant fraction of our objects to vary their X-ray flux with typical amplitudes of variability around $\sim 25\%$. The fraction of sources with detected spectral variability was found to be significantly lower, although this is probably due to the fact that spectral variability is much more difficult to detect than flux variability. The results of our study suggest that X-ray variability in our AGN is probably related with changes in the continuum shape most likely related to long-term variations in the accretion rate, while variability of other spectral components, e.g. X-ray absorbing column density, is unlikely to produce the variability properties of our objects. We did not find compelling evidence for a dependence of the variability properties of our AGN with luminosity or redshift.

Contents

List of Tables

List of Figures

Chapter 1

Introduction

X-ray emission is associated with very energetic phenomena (the energy of an X-ray photon being $\sim$1000 times that of optical photons): relativistic particles in strong magnetic fields, ionised plasmas at millions of degrees, strong gravitational fields... X-ray radiation is also very penetrating: it can pass through quantities of absorbing material which would completely obscure optical and ultraviolet photons. Therefore, X-ray astronomy provides a unique window to explore the hot (millions of degrees) and most violent and obscured universe.

Nowadays, many different astronomical sources are known to be X-ray emitters. For example, Galactic objects such as stars, compact objects in binary systems (e.g. cataclysmic variables, neutron stars, black holes), and supernova remnants. Many extragalactic sources are X-ray emitters, such as black holes in active galactic nuclei (AGN), and hot gas in galaxies and clusters of galaxies. The energy source of neutron stars and black holes is gravitational energy. In these objects, X-rays are emitted from gas that is heated while it is accreted onto the compact object. Some galaxies and most clusters of galaxies are massive enough as to confine gravitationally the hot (10^6-10^8 K) X-ray emitting gas that fills these objects (the intra-cluster medium in clusters of galaxies and the interstellar medium in galaxies). This gas emits X-rays through thermal bremsstrahlung, and line emission from metals. Even the coldest objects in the solar system, comets, are now known to emit X-rays, reflected from the solar X-ray emission.

The aim of the work presented in this thesis is to explore the physical properties of AGN through X-ray spectroscopy and variability analyses of samples of AGN.

1.1 Motivation

Cosmic X-rays cannot reach the Earth's surface as they are absorbed by the atmosphere. Therefore, in order to perform X-ray observations of astronomical sources, it is necessary to place X-ray instrumentation above the atmosphere. The study of astronomical objects in X-rays had to wait until rocket flights were available.

It is widely accepted that X-ray astronomy began in 1962 with the discovery, during a rocket flight designed to detect X-rays from the Moon, of the first extra-solar X-ray source, named Scorpio X-1 because it was the first X-ray source found in the constellation Scorpio (we now know it is a neutron star in a binary system). An isotropic X-ray flux coming from all sky directions was also detected [79]. This emission, known as the Cosmic X-ray background (XRB), was the first cosmological background to be discovered. Revealing the origin and nature of the XRB has been one of the most important goals of X-ray astronomy during the last 40 years.

Optical follow-up campaigns of sources detected in medium-deep *Chandra* and *XMM-Newton* surveys have confirmed that most of the energy density of the XRB originates in accretion of matter (gas and stars) onto supermassive black holes ($10^6 - 10^9\,\mathrm{M_\odot}$) at the centres of AGN. The accretion process occurs in the form of an accretion disc, which liberates most of the power due to dissipation within a few tens of gravitational radii. The XRB is therefore a “fossil” of the energy emitted by accretion in the Universe.

X-ray emission is a common property of AGN, with ~3-10% of their total energy being released at X-ray energies. In addition, timing studies have shown that AGN are strongly variable sources at all time scales, showing their fastest variability in X-rays. The most rapid variability observed in AGN is of the order of minutes, which can only be explained if the X-ray emitting region is small and therefore very close to the central engine.

In order to reproduce the XRB intensity and spectrum emission, and the observed flux distribution of sources, most AGN must be photoelectrically absorbed due to large quantities of gas. Hereafter we will refer to AGN with low intrinsic X-ray absorbing column densities, in the range $\mathrm{N_H} \sim 10^{22} - 3\times10^{24}\,\mathrm{cm^{-2}}$, as Compton-thin AGN and those with larger X-ray absorbing column densities, $\mathrm{N_H} \geq 3\times10^{24}\,\mathrm{cm^{-2}}$, as Compton-thick AGN. The typical X-ray spectrum of an unabsorbed AGN in the rest-frame energy range ~0.5-10 keV has a power law shape of slope $\Gamma\sim2$ (hereafter soft X-ray spectrum)[1]. Photoelectric absorption affects most optical-UV and soft X-rays, making the observed X-ray continuum of absorbed AGN to appear harder (Γ significantly lower than the typical value for unabsorbed AGN; hereafter hard spectrum). In Compton-thin AGN, even for moderate absorptions, the optical and UV emission are completely blocked, and therefore these sources cannot be distinguished from “normal” galaxies based on their optical colours alone. In addition, their IR emission is believed to originate as reprocessing of the nuclear radiation in the absorbing material. Radio waves can be used in principle to look deep inside the AGN, however only ~10% of optically and X-ray selected AGN are radio-loud. Hard X-rays and gamma rays can penetrate through large columns of obscuring gas without being significantly affected, providing a unique direct view of the central engine in these sources (unless they are extremely absorbed, i.e., Compton-thick).

Therefore X-ray spectroscopy of AGN provides a unique tool to investigate the physics and emission mechanisms of the objects that dominate the energy density of the XRB. In AGN the physical processes are associated with material under extreme conditions such as very high temperatures and strong gravitational fields, and therefore relativistic effects can become important.

---

[1] In general, the X-ray spectra of AGN are usually parameterised as power-laws in units of photon density: $\mathrm{N(E)} \propto \mathrm{E}^{-\Gamma}\,\mathrm{photons\,cm^{-2}\,s^{-1}\,keV^{-1}}$, where Γ is the photon index and α=Γ-1 is the spectral index.

1.2 History

Following the pioneering rocket flights in the 1960s, major advances in X-ray astronomy were obtained in the 1970s when orbiting X-ray observatories equipped with X-ray detectors, such as *UHURU* (USA), *Ariel 5* (UK), *SAS-3* (USA), *OSO-8* (USA) and *HEAO-1* (USA), proliferated. *UHURU* scanned the 2-20 keV X-ray sky for over 2 years producing the first all-sky survey. Among the most important discoveries of *UHURU* was the first detection of extended X-ray emission from clusters of galaxies. The observations with *UHURU* increased the number of known X-ray sources at the time to more than 400, showing that many X-ray sources were variable. The *UHURU* and *Ariel 5* X-ray catalogues provided important advances in the knowledge of the X-ray sky, showing that Seyfert galaxies (see Sec. 1.4.5) and clusters of galaxies represented a substantial fraction of the extragalactic sources at bright X-ray fluxes, while many of the most luminous Galactic sources were found to be in binary systems.

NASA launched three High Energy Astronomy Observatories in the 1970s. The first of them, *HEAO-1*, provided the only measurement of the XRB intensity spectrum from 10 to 100 keV up to date [150]. The data showed that the spectrum of the XRB in the 3-50 keV band exhibits a bell shape, with a broad peak at energies ~30-40 keV, where the bulk of the XRB energy density resides. In the 3-50 keV energy band, a good fit to the data was obtained with a thermal bremsstrahlung model -an optically thin, hot plasma- of temperature kT~40 keV [150]. The fact that the measured spectral shape of the XRB could be well fitted with a thermal model, prompted the hypothesis of a diffuse origin for a significant fraction of the XRB emission. This hypothesis however had to be finally ruled out when the *Cosmic Background Explorer* (COBE) satellite showed the Cosmic Microwave Background (CMB) emission spectrum to have a perfect black body spectrum, without any significant distortion due to Compton up-scattering of CMB photons by hot ($\sim 10^8$K) electrons [154]. These results left the theory of a discrete origin -the XRB being the integrated emission of discrete extragalactic sources- as the only possible explanation for the nature of the XRB.

The *Einstein* observatory (*HEAO-2*), launched in 1978, carried out the first large imaging X-ray telescope into orbit. With an angular resolution of several arcsec and a field of view (FOV[2]) of tens of arcmin, *Einstein* increased the number of detected X-ray sources to ~7000. In addition, *Einstein* performed, for the first time, deep imaging observations that allowed to resolve ~25% of the 1-3 keV XRB into discrete sources down to a flux of $\sim 3 \times 10^{-14}\,\mathrm{erg\,cm^{-2}\,s^{-1}}$ [78] [94] [103] [198]. A large fraction of these sources were optically identified as AGN [78] [94]. Thanks to its imaging capabilities, *Einstein* was able to map the distribution of hot gas in clusters of galaxies and produced X-ray images of many supernova remnants.

The German/USA/UK X-ray satellite *ROSAT* [229] launched in June 1990 conducted the first all-sky survey with an imaging telescope in the energy range 0.1-2.4 keV. The *ROSAT* all sky survey yielded a catalogue with more than 60,000 X-ray sources, while another similar number of objects were added from pointed observations during the lifetime

---

[2] The Field of View is the area of the sky visible from a telescope, i.e. it is the area of the sky that the detectors look at.

of the mission. The deepest observations carried out with *ROSAT* on the *Lockman Hole* region reached 0.5-2 keV fluxes of $\sim 10^{-15}\,\mathrm{erg\,cm^{-2}\,s^{-1}}$ and resolved ~70-80% of the XRB in this energy band into discrete sources [105] [107]. Optical spectroscopy of the brightest sources (with X-ray fluxes $\geq 5 \times 10^{-15}\,\mathrm{erg\,cm^{-2}\,s^{-1}}$) revealed the bulk of these objects to be type-1[3] AGN [130] [160] [216] [255]. These results provided a firm observational evidence that the bulk of the XRB from 0.5-2 keV is made up of accretion onto Supermassive Black Holes (SMBH) (the primary energy source of X-rays in AGN) integrated over cosmic time.

In the hard X-ray band ($\geq 2\,\mathrm{keV}$) where focusing of X-ray photons is more difficult (see Sec. 1.7.1), a wealth of new data were obtained after the launch of the Japanese/USA mission *ASCA* (Advanced Satellite for Cosmology and Astrophysics) in 1993. It was the first satellite using Charge Coupled Device (CCD) detectors (see Sec. 1.7.2) for X-ray astronomy. *ASCA* performed a number of medium-to-deep sky surveys in the energy band from 2 to 10 keV reaching limiting fluxes of $\sim 10^{-13} - 5 \times 10^{-14}\,\mathrm{erg\,cm^{-2}\,s^{-1}}$ [31] [73] [112] [236] that resolved ~35% of the XRB in this energy band [65] [70] [236]. These surveys discovered a population of discrete X-ray sources with significantly harder spectra than the AGN detected in surveys at softer X-ray energies. Optical spectroscopic identifications of the brightest objects detected with *ASCA* showed some of them to be X-ray absorbed AGN at low redshifts ($\leq$0.5) [2]. Thanks to the improved spectral resolution of the *ASCA* detectors, it was possible to detect for the first time broad Fe Kα fluorescence line emission in AGN, the shape of the line emission suggesting an origin in matter moving relativistically under a strong gravitational field (see Sec. 1.4.2).

The Italian Space Agency (ASI) in collaboration with SRON (NL) launched in 1996 *BeppoSAX* (Satellite per Astronomia X, "Beppo" in honor of Giuseppe Occhialini). The observations with *BeppoSAX* resolved 20-30% of the 5-10 keV XRB [43]. One of the major achievements of *BeppoSAX* was the detection of X-ray afterglows from gamma ray bursts, which are the most luminous sources in the Universe.

The most powerful X-ray observatories to date, NASA's *Chandra* [244] and ESA's *XMM-Newton* [113], were launched both in 1999. *Chandra* is mostly an imaging observatory, i.e., it has high angular resolution and reaches a positional accuracy of ~0.5 arcsec (ten times that of *ROSAT*), while *XMM-Newton*, with a modest angular resolution but larger throughput than *Chandra*, was designed for X-ray spectroscopy. *Chandra* and *XMM-Newton* deep pointed observations have reached X-ray fluxes ~100 times fainter than previous X-ray missions. The *Chandra* ultra-deep pointed observations in the directions of the Chandra Deep Field North (CDF-N; 2 Msec long) and Chandra Deep Field South (CDF-S; 1 Msec long) reached limiting fluxes of $\sim 2 \times 10^{-16}\,\mathrm{erg\,cm^{-2}\,s^{-1}}$ resolving 80-90% of the hard (~2-7 keV) XRB [27] [32] [81] [110] [162] [170] [210] [228]. On the other hand, the ongoing Deep *XMM-Newton*/Cosmos survey will cover $2\,\mathrm{deg}^2$ of a contiguous area of the Cosmos field, reaching in the 0.5-2 keV energy band a sensitivity of $\sim 5 \times 10^{-16}\,\mathrm{erg\,cm^{-2}\,s^{-1}}$ [129].

In a recent work using the 1-2 Msec *Chandra* deep fields, Bauer et al.(2004) [18] studied the contribution to the soft (0.5-2 keV) and hard (2-8 keV) XRB from different classes of

---

[3] Basically those AGN showing both narrow and broad (Full Width at Half Maximum FWHM $\geq 1500\,\mathrm{km\,s^{-1}}$) emission lines in their optical spectra are classified as type-1 AGN, while those showing only narrow (FWHM $< 1500\,\mathrm{km\,s^{-1}}$) emission lines are classified as type-2 AGN (see Sec. 1.4.5).

sources. They found the AGN population to make ~83% and ~95% of the fractions of XRB resolved in the soft and hard X-ray bands. In addition, the fraction of X-ray obscured AGN contributing to the XRB was found to increase at hard X-rays. Normal galaxies comprise ~5-15% and ~2-6% of the resolved soft and hard XRB.

Although the deepest surveys carried out by *Chandra* and *XMM-Newton* were able to resolve $\geq 90\%$ of the 2-10 keV XRB into discrete sources, there is a substantial decrease in the fraction of XRB resolved as we go to higher energies. This is due to the fact that X-ray telescopes have a large gradient in sensitivity across the 2-10 keV band. The effect of this on the fraction of XRB resolved has been studied by Worsley et al.(2004) [248] using the CDF-N, CDF-S and *XMM-Newton Lockman Hole* observations. Their study revealed that the fraction of XRB resolved drops from 80-90% at 2-6 keV to just 50-70% at 6-10 keV. They also found that the missing (unresolved) flux has the X-ray spectrum of highly absorbed AGN. Figure 1.1 shows the fraction of XRB resolved in the soft (0.5-2 keV) and hard (2-10 keV) bands as a function of X-ray flux obtained combining data from different *ROSAT*, *Chandra* and *XMM-Newton* surveys [167]. In the soft band, the integrated flux from discrete sources at $\sim 3 \times 10^{-18}\,\mathrm{erg\,cm^{-2}\,s^{-1}}$ can explain the entire XRB emission, while in the hard band it accounts for 93% of the emission at most, the missing flux probably originating from absorbed AGN still undetected.

In the 10-100 keV band where most of the XRB emission resides, only a small percentage has been resolved so far [121].

Thanks to its large FOV and large throughput, each *XMM-Newton* pointed observation detects serendipitously between ~30-150 sources, most of them being detected for the first time. All sources detected with *XMM-Newton* in ~600 pointed observations taken before May 2002 were put together in a catalogue named *1XMM* that was released in 2003 by the *XMM-Newton* Survey Science Centre (SSC)[4]. *1XMM* contains ~33,000 X-ray sources of which ~28,000 are unique[5]. A significantly larger catalogue of sources (it will be approximately 5 times the size of *1XMM*), *2XMM*, will be released at the beginning of 2007. *2XMM* will be the largest X-ray catalogue ever made. *2XMM* will contain data from ~4,000 *XMM-Newton* pointed observations covering a total sky area of ~600 deg^2 and will include ~250,000 X-ray detections, ~150,000 being unique X-ray sources.

1.3 The Cosmic X-ray background

The XRB emission extends from ~0.1 keV to several hundreds of keV. Figure 1.2 shows the energy spectrum of the XRB from soft X-rays to gamma-rays measured with different missions.

Over the energy range from 3 to 10 keV a good description of the spectrum is obtained with a power law of photon index Γ=1.4 (e.g., [150] from 3-15 keV; [71] from 1-10 keV; [165] from 1-10 keV; [238] from 1-8 keV). Note that a 40 keV bremsstrahlung spectrum (as measured by the *HEAO-1* mission, see Sec.1.2) is equivalent to a power law with photon

---

[4] `http://xmmssc-www.star.le.ac.uk/`

[5] There is a significant overlapping of *XMM-Newton* observations that implies that a significant fraction of X-ray sources have been detected more than once.

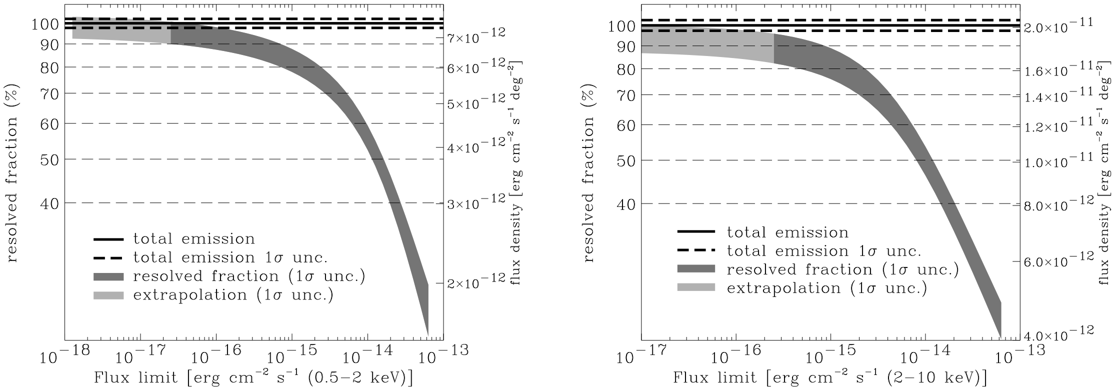

Figure 1.1: *Fraction of soft (0.5-2 keV; left) and hard (2-10 keV; right) XRB emission resolved into discrete sources (taken from [167]).*

spectral index Γ=1.4 in the 3-10 keV band. No indication of any other additional spectral features are observed in the spectrum of the XRB at these energies. Below ~2 keV the spectrum becomes steeper and can be well approximated with a power law of $\Gamma\sim$2.1 [104] although the Galaxy is mostly involved in this.

The nature of the XRB varies significantly over its energy range. At the softest energies, 0.1-0.3 keV, almost all observed emission originates as thermal emission from a hot ($\sim 10^6$ K) local plasma. One of the contributions is from a local bubble in the disc of the Galaxy that surrounds the Sun, known as the Local Hot Bubble. A second contribution comes from a thin plasma in the halo of our Galaxy [158]. From 0.5 to 1 keV, both the Galactic emission from hot plasma and extragalactic discrete sources, contribute to the emission of the XRB. Above ~3 keV, the XRB is observed to be highly isotropic (after the weak Galactic component and the dipole radiation field due to the motion of our Galaxy [58] are taken into account) and it is now known to be extragalactic in origin, being the integrated emission of unresolved sources.

None of the experiments that measured the spectrum of the XRB found any significant deviations in the measured spectral shape from $\Gamma\sim$1.4. However, the values obtained for its intensity (usually parameterised as the intensity -$I_{\rm XRB}$- at 1 keV in units of photons keV^{-1} cm^{-2} s^{-1} sr^{-1}) are found to be significantly different, sometimes among measurements taken with the same instrument, with variations as large as ~40%. This makes the value of the normalisation of the XRB intensity rather uncertain.

Above 2 keV, the *HEAO-1* background spectrum has been used for many years as the reference. However it appears to have a ~30% lower normalisation than several later background measurements. Even with the latest measurements of the XRB intensity, this discrepancy persists. For example, Kushino et al.(2002) [123], using 91 *ASCA*-GIS pointings covering a solid angle of 50 deg^2, found the XRB power law normalisation to be 9.66 ± 0.07 photons keV^{-1} cm^{-2} s^{-1} sr^{-1}, while Lumb et al.(2002) [135] using 8 *XMM-Newton* pointings measured a value of 11.1 ± 0.32 photons keV^{-1} cm^{-2} s^{-1} sr^{-1}. Recent

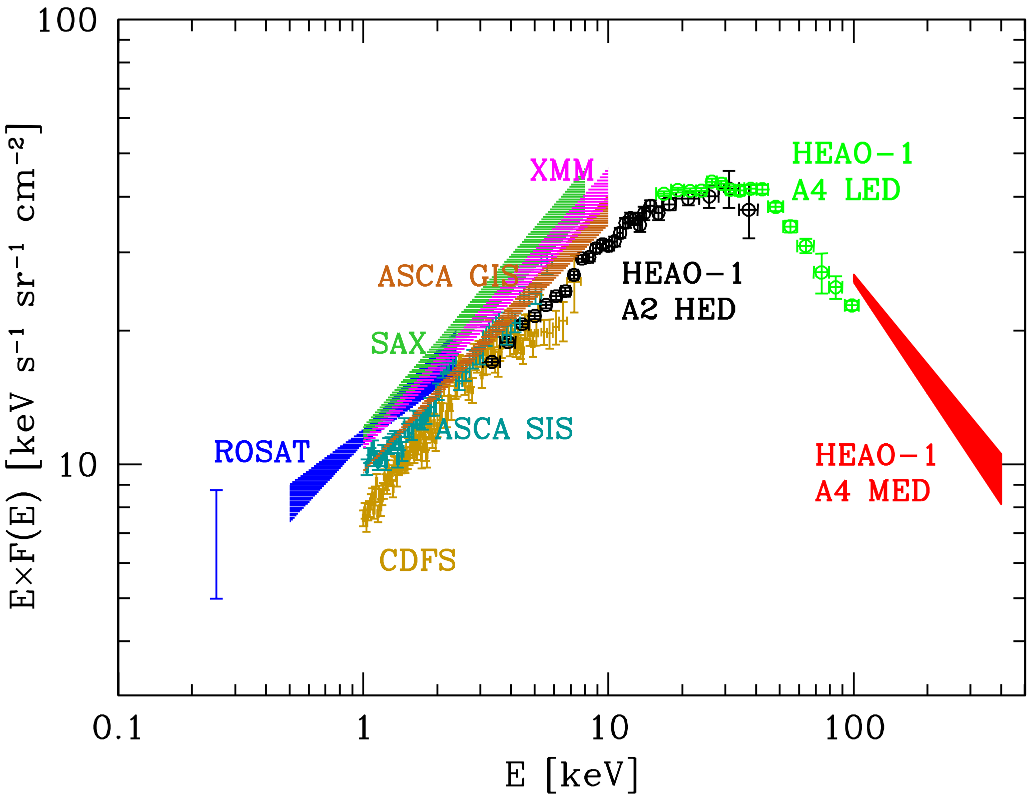

Figure 1.2: *Spectrum of the extragalactic X-ray background from 0.2 to 400 keV measured with different missions (taken from [83]): ROSAT 0.25 keV [242]; ROSAT [74]; HEAO-1 A2 HED+ A4 LED [95] [96]; HEAO-1 A4 MED [118]; SAX [238]; ASCA SIS [71]; ASCA GIS [123]; XMM-Newton [135]; Chandra Deep Field South [228].*

measurements of the XRB spectrum with the *Rossi X-ray Timing Explorer* (RXTE) mission [203] and *XMM-Newton* [48] confirm the 30% higher normalisation of the XRB with respect to the *HEAO-1* result. Different measurements of the intensity of the XRB emission are listed in Table 1.1.

We expect the discrete nature of the XRB to induce a *cosmic variance* in the measured value of the XRB intensity. The discrete nature of the XRB produces confusion noise, caused by unresolved sources in the images [9] [215]. Almost all measurements, except the one from the *HEAO-1*, were obtained from observations carried out over small solid angles (below ∼1 deg^2). Barcons et al.(2000) [12] showed that confusion noise can account for variations in the measured intensity of the XRB of ∼10% for measurements over solid angles under 1 deg^2. When *cosmic variance* is taken into account, measurements within the same mission but different instruments can be brought to consistency. However they found that *cosmic variance* alone cannot account for the observed discrepancies between missions, and hence, significant instrumental cross-calibration uncertainties between different

Table 1.1: *Measurements of the XRB intensity at 1 keV.* Ω_i *is the solid angle covered,* $I_{\rm i}$ *the measured intensity and* σ_i *the corresponding* 1σ *statistical uncertainty (taken from [12]).*

Mission (1)	*Field* (2)	$\Omega_{\rm i}$ (3)	$I_{\rm i}$ (4)	σ_i (5)	Reference (6)
ROSAT PSPC	QSF3	0.223	11.4	0.34	Chen et al. (1997) [37]
ASCA SIS	QSF3	0.134	10.0	0.37	Chen et al. (1997) [37]
ROSAT PSPC	GSGP4	0.283	11.8	0.44	Georgantopoulos et al. (1996) [74]
ROSAT PSPC	SGP2	0.283	12.0	0.61	Georgantopoulos et al. (1996) [74]
ROSAT PSPC	SGP3	0.283	12.0	0.68	Georgantopoulos et al. (1996) [74]
ROSAT PSPC	QSF1	0.283	9.9	0.65	Georgantopoulos et al. (1996) [74]
ASCA GIS	Lockman	0.165	10.9	0.61	Miyaji et al. (1998) [165]
ASCA GIS	Lynx	0.144	9.3	0.61	Miyaji et al. (1998) [165]
ROSAT PSPC	Lockman	0.165	10.0	0.30	Miyaji et al. (1998) [165]
ROSAT PSPC	Lynx	0.144	11.5	0.43	Miyaji et al. (1998) [165]
ASCA SIS	Various	0.538	8.9	0.50	Gendreau et al. (1995) [71]
ROSAT PSPC	Various	5.9	13.4	0.18	Hasinger et al. (1992) [104]
SAS LECS + MECS	Various	0.726	11.0	0.30	Vecchi et al. (1999) [238]
ASCA GIS	Various	50	9.66	0.07	Kushino et al. (2002) [123]
$XMM - Newton$	Various		11.1	0.32	Lumb et al. (2002) [135]

Columns are as follows: (1) instrument; (2) name of the field; (3) solid angle covered by the observations in deg^2; (4) and (5) measured value of the XRB intensity in units of photons keV^{-1} cm^{-2} s^{-1} sr^{-1} and the corresponding 1σ statistical error; (6) reference of the work.

instruments must still be present (see also [48]).

1.4 Active Galactic Nuclei

AGN were first discovered in the 1940s as galaxies characterised by extreme brightness in their centres (the luminosity of the centre can be from a few to thousands of times the luminosity of the underlying host galaxy), often appearing as a bright and highly variable point source in optical images. The suggested activity in their central region lead to the term Active Galactic Nuclei or AGN. These objects are the most luminous persistent[6] known objects in the Universe. Their bolometric luminosities span a broad

---

[6] Only gamma ray bursts can be brighter by a few orders of magnitude but they only last a few seconds.

range of values, from 10^{42} to $10^{48}\,\mathrm{erg\,s^{-1}}$ for the most luminous AGN, often referred as "quasars"[7]. With the improvement of sensitivity of X-ray detectors, the detection of activity has been possible in an increasing number of non-active galaxies, which blurs the existing division between active and non-active galaxies. There is compelling observational evidence that supermassive black holes are present in most, if not all, massive normal and active galaxies [21] [120], including the Milky Way [61] [77].

In this work, as customary in X-ray astronomy, we classify a galaxy as active if its X-ray luminosity is higher than $\sim 10^{42}\,\mathrm{erg\,s^{-1}}$.

1.4.1 Emission mechanisms in AGN

In this section I will give a brief description of the emission mechanisms that are believed to produce the observed emission in AGN at different wavelengths.

1. *Thermal black body emission:* A black body is defined as a body in thermal equilibrium with its surroundings, that is both a perfect absorber (and therefore it has very high optical depth) and a perfect emitter of radiation. None of the radiation reaching the black body is reflected. Real objects are not perfect black bodies, however the black body approximation works reasonably well in many cases. The spectrum emitted by a black body depends only on the temperature of the emitting object.

   Stars show thermal black body spectra at different temperatures. Thermal radiation by the gas in the accretion disc has been traditionally used to interpret the optical/UV emission in AGN. Typical AGN accretion discs are cool ($\sim 10^5 - 10^6$K) and therefore they produce relatively soft quasi-thermal spectra in the optical-UV energy range. Black body emission by dust heated by the optical/UV radiation field from the central source is believed to be responsible for the IR emission in radio quiet AGN (see Sec. 1.4.2).

2. *Inverse Compton scattering:* Photons can gain energy from interactions (scattering) with a population of charged particles, a process known as Compton scattering. Because the scattering cross-section of nuclei, σ_N, is much smaller than that of electrons, σ_e,

   $$\frac{\sigma_N}{\sigma_e} \sim \left(\frac{m_e}{m_N}\right)^2 \tag{1.1}$$

   where m_e and m_N are the masses of electrons and nuclei (protons and neutrons) respectively, Compton scattering by nuclei can be neglected. If the electrons are relativistic, photons gain energy from the electrons and the process is known as Inverse Compton scattering. The spectrum of the scattered radiation depends on the electron energy distribution.

---

[7] Originally the term "quasar" was used to refer to radio loud objects (quasi-stellar source) and QSO to radio quiet. More recently "quasar" has been frequently used to refer to all luminous AGN. We now know that AGN properties are similar for both low and high luminosity sources, and therefore we do not use the distinction AGN/quasar in this thesis and use the term AGN to refer to both low and high luminosity objects.

Inverse Compton scattering is believed to be responsible for the broad band continuum observed in the X-ray spectra of radio quiet AGN.

3. *Synchrotron radiation:* Electromagnetic radiation produced by relativistic charged particles accelerated in an external magnetic field is known as synchrotron radiation.

   Assuming a non-thermal particle distribution with a power law energy spectrum, the emitted spectrum is another power law with a spectral index α that is related to the power law index of the particle spectrum.

   Synchrotron radiation from a population of relativistic electrons located in jets is believed to be the emission mechanism responsible for the radio emission in radio loud AGN (see Sec. 1.4.2). It is unlikely that synchrotron radiation is an important contributor to the high energy spectra of most AGN, with the exception of radio loud AGN, which constitute only a small fraction of the population of AGN (see Sec. 1.4.2).

4. *Bremsstrahlung (free-free emission):* Bremsstrahlung means "braking radiation" and it is related to emission occurring in hot dense ionised plasmas. It is produced when free electrons loose energy, and therefore emit electromagnetic radiation, when they are accelerated by the electromagnetic fields of the ions. As free electrons can have a very large range of energies, the emission has a thermal continuum distribution.

   The emission mechanism on clusters of galaxies is believed to be thermal bremsstrahlung from hot $\sim 10^8\,\mathrm{K}$, low-density ($\sim 10^{-3}\,\mathrm{atoms\,cm^{-3}}$) gas.

1.4.2 Observational properties of AGN

All energies referred to in this section are in rest-frame, unless said otherwise. The broad band emission of AGN is very different to that of normal galaxies. It spans the whole electromagnetic spectrum from radio to gamma rays (see Fig. 1.3 top). The spectrum (defined hereafter $F(\nu) \propto \nu^{-\alpha}$) from the mid-infrared to hard X-rays is flat in $\nu\, F_\nu$ units, i.e. approximately the same luminosity is emitted at each decade (see Fig. 1.3 bottom), and usually has a peak in the far UV/soft X-ray range, where we do not have access at low redshift due to Galactic extinction:

1. *Radio emission*: Only ~10% of optically and X-ray selected AGN are strong radio emitters, although the emission in the radio band usually does not contribute more than 1% to their bolometric luminosity. The spectrum of AGN at radio wavelengths has a power law shape. The origin of the radio emission is believed to be synchrotron radiation in outflows of relativistic energetic particles (electrons) along the poles of a rotating black-hole.

2. *Infrared emission*: The IR continua of AGN rise continuously with a power law shape from the optical to the FIR/submillimeter wavelengths. The IR broad band spectra can be well reproduced by a model where a significant fraction of the nuclear emission is reprocessed by warm molecular gas that is surrounding the active nucleus and the broad line region (see Sec. 1.4.6) and with an axisymmetric torus-like

structure [87] [191] [192]. The gas absorbs the nuclear optical-UV radiation and reprocesses it thermally mostly into the rest-frame mid-IR range. Obscuration in a moderately thick gas (with optical depth[8] from 10 to 300 in the UV, and maximum distance to the black hole from tens to hundreds of pc) gives a good description of the broad-band IR spectra of AGN [88]. This hypothesis has now strong observational support from Hubble Space Telescope (HST) observations, which have resolved a torus structure (e.g. NGC 4261 [64]).

3. *Optical/UV*: The optical/UV continuum emission of AGN is dominated by a broad hump, known as the *Big Blue Bump* (BBB). The BBB is observed in the optical/UV range and peaks at ∼1000Å. The BBB is frequently interpreted as thermal emission from the accreting matter located in the innermost regions of the AGN in the form of an accretion disc. The optical/UV spectra of type-1 AGN (see Sec. 1.4.5) also show strong highly ionised broad permitted emission lines superimposed to the continuum, and narrow permitted and forbidden emission lines.

4. *X-rays*: AGN are very luminous X-ray sources. To a first approximation, the X-ray spectrum of AGN from ∼1 keV to ∼100 keV is continuum-dominated, and can be well described by a single power law with a typical slope $\Gamma \sim 1.9$. At gamma rays the spectra of AGN is also well reproduced with a power law but with a steeper slope than in X-rays. When the signal-to-noise ratio of the X-ray spectra of AGN is good enough, other prominent spectral features are often observed. The most common of these spectral features are shown in Fig. 1.4:

    (a) *Photoelectric absorption*: The strongest feature in the 0.1-100 keV spectra of a significant fraction of AGN is a photoelectric cut-off of the intrinsic power law at low energies due to absorption by a cold or partially ionised material in the line of sight to the nucleus. Photoelectric absorption by our Galaxy modifies the X-ray spectrum at observed energies below 0.6 keV. On the other hand, "local" OVII, OVIII, NVI, NVII, NeIX and CVI absorption lines have been detected in the X-ray spectra of bright AGN with the dispersive spectrometers onboard *Chandra* [177] and *XMM-Newton* [201]. A large fraction of this absorption is believed to be due to $10^5 - 10^7\,\mathrm{K}$ plasma outside our Galaxy, in the so-called *Warm-Hot Intergalactic Medium* (WHIM [36]). On top of that about 50% of Seyfert 1 galaxies [204] (see Sec. 1.4.5) show X-ray absorption by gas highly ionised by the intense nuclear UV/X-ray radiation [76] [204]. At low spectral resolution, the typical signatures of this gas, termed *warm absorber*, are K-shell deep absorption edges at low energies (<1 keV), the most frequently observed ones being OVII and OVIII [76] [204]. These absorption edges appear usually significantly blue-shifted, the majority showing velocities of the order of a few hundreds $\mathrm{km\,s^{-1}}$ [114] [115] suggesting that the absorbing material is moving away from the central source at these velocities.

---

[8] Optical depth, τ, is a measure of the transparency of a material and is the fraction of incident radiation that is scattered or absorbed before it reaches the observer.

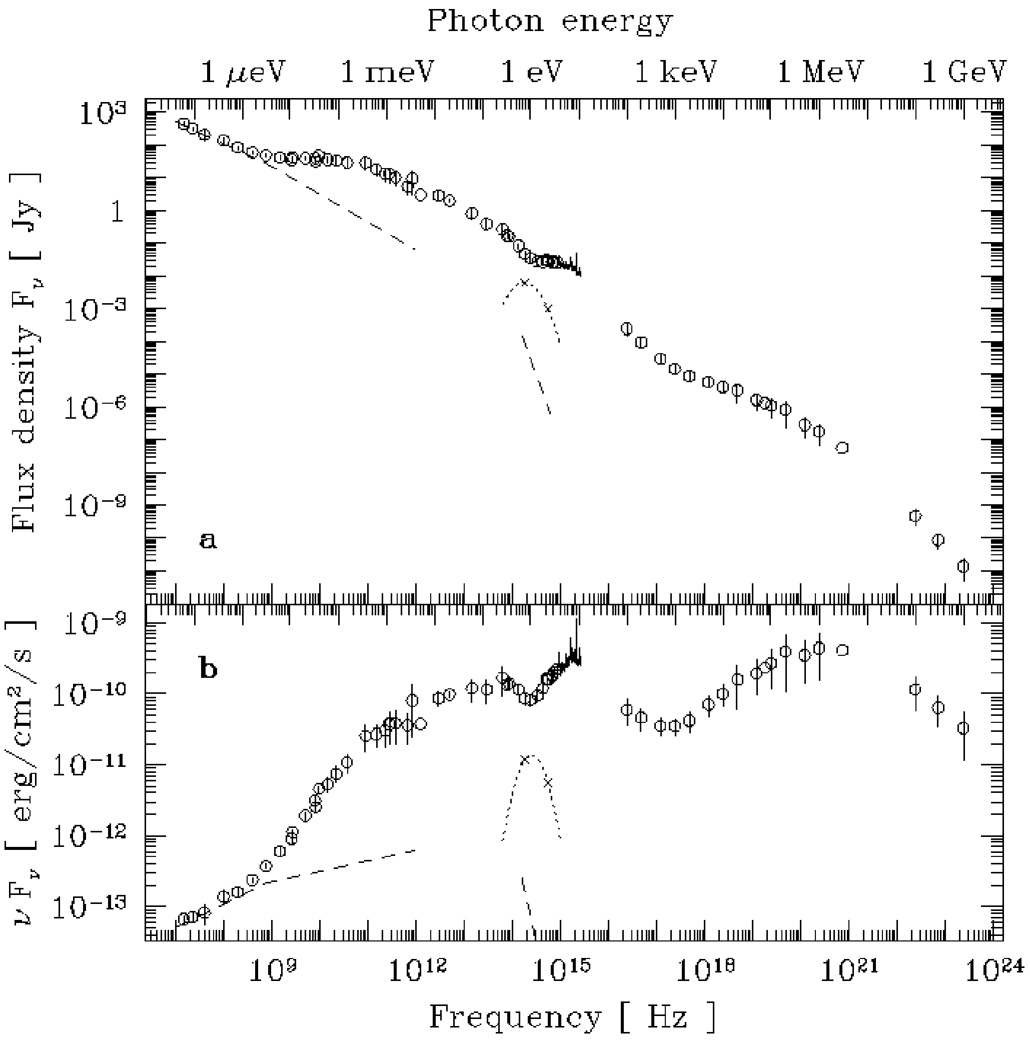

Figure 1.3: *Broad band mean spectrum of the quasar 3C 273 (taken from [230]) in* $\overline{\nu}$ *(top) and* $\overline{F_\nu}$ *(bottom) representations. The solid line centred at* $\sim 10^{15}$Hz *is the average IUE spectrum. The dashed line is the contribution from the jet (see Sec. 1.4.6). The dotted line is the contribution from the host galaxy.*

(b) *Soft excess* (SE): At low energies, below ~2 keV, the emission of a significant fraction of AGN (~30%) [234] shows a strong soft component superimposed over the hard X-ray continuum with a peak of emission in the Extreme Ultraviolet (EUV), generally termed as *soft excess* [246]. Soft excess emission was first reported by Arnaud et al. in 1985 [8]. The origin of this spectral component is not clear. It has been traditionally interpreted in the past as direct thermal emission from the hot, innermost region of the accretion disc [8] [47] [125] [196] [211], and therefore as the high energy tail extension to soft X-ray energies of the BBB. However the typical measured temperatures of the soft excess emission (>500 eV in some cases) are too high to explain it as thermal emission from the accretion disc (disc temperature $\leq$20 eV[9]). In addition, for AGN showing signatures of intrinsic photoelectric X-ray absorption (classified as type-2 AGN, see Sec. 1.4.5), it is hard to explain the soft excess component as emission from the accretion disc because, as we will see in Sec. 1.5, in type-2 AGN the nuclear emission is expected to be obscured by large amounts of gas.

There are several alternative models for the origin of the soft excess. One of them includes reflection of the hard X-rays by cold ($\leq 10^6$K) dense gas, either in the innermost regions of the accretion disc [101], or in the form of many clouds of gas surrounding the central hard source. The cold gas reprocesses the hard X-ray emission by Compton up-scattering of EUV accretion disc photons [194] and photoelectric absorption [99] [132]. Reflection models can only provide a good representation of the data in sources with weak excess, unless the primary continuum is hidden [38].

A partial covering of the X-ray source by cold dense material intercepting the line of sight, often provides a good representation of soft excess spectral signatures. In this model, a fraction of the X-ray photons (that can be as high as 98%), are absorbed by thick material while the rest are unaffected by absorption.

Gierlinski et al.(2004) [82] have recently proposed an alternative model to explain the soft excess emission in AGN. In their model, the observed spectral signatures of soft excess emission can be explained as an artifact due to ionised absorption of the primary continuum by a relativistic wind, moving at a bulk velocity of several thousand $\mathrm{km\,s^{-1}}$.

(c) *Fluorescent Fe Kα emission*: Emission lines at rest-frame energies ~6.4-6.7 keV are common in the X-ray spectra of AGN. Because iron is the most abundant heavy element, having large absorption cross-section at high energies and a large fluorescent yield, the observed line emission in X-rays has been generally attributed to fluorescence due to iron. The centre of the line gives an indication of the ionisation state of the emitting material. Most AGN with detected iron emission show the line peaking at ~6.4 keV, suggesting that the reflecting medium must be cold (kT<1 keV [173]), and therefore the emission originates in near neutral material. Fe Kα emission has been detected both in absorbed an unabsorbed AGN [169] [174] [195]. The material responsible for the line emission in type-2 objects is likely to be the molecular torus responsible for the X-ray absorption. In unabsorbed AGN the emission has been explained as originating in optically thick material out of the line of sight. This material has been associated with the accretion disc [60], with the molecular torus located farther away from the central source [5] [237], and with the broad line region (see Sec. 1.4.6) [206].

---

[9] The temperatures of the innermost part of the disc in a 'standard accretion disc model' (stationary, geometrically thin and optically thick disc, proposed by Shakura & Sunyaev in 1973 [219]) are ~60 eV for a black hole of mass $10^6\,M_\odot$ and ~10 eV for $10^9\,M_\odot$.

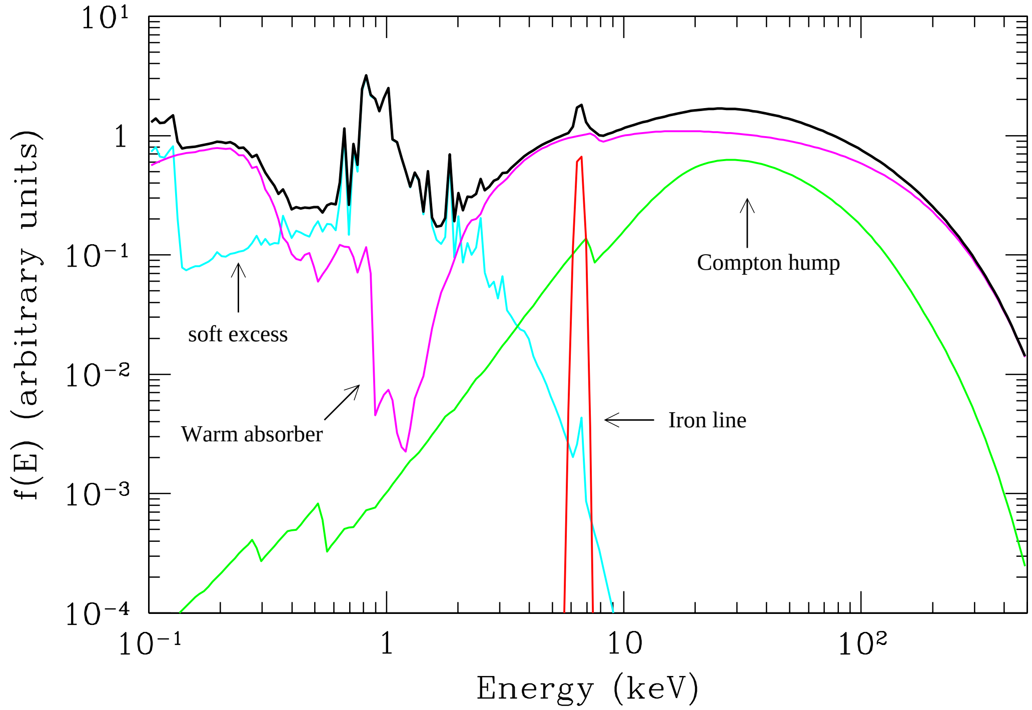

Figure 1.4: *Schematic diagram displaying the total spectrum (black solid line) and main spectral components in a Seyfert 1 X-ray spectrum (taken from [205]): Photoelectric absorption (pink), soft excess (cyan), Compton reflection (green) and fluorescent Fe Kα emission (red).*

Narrow iron lines (with rest-frame energy centroids ~6.4 keV) are expected to originate in neutral material in slow motion, and therefore must be farther away from the central source. On the other hand broad iron lines (with energy centroids ~6.7 keV) are expected to originate in highly ionised material moving at high velocities, which must be located in the innermost regions of the AGN, such as the accretion disc, where the line will be broadened due to the rotation of the accretion disc, transverse Doppler effect and gravitational redshift, producing a characteristically skewed line profile [60] [75] [126] [156] [157]. Both narrow and broad iron emission lines (in some cases the lines have been found to have both narrow and broad components) have been detected in a number of AGN, supporting the origin of the line emission in different regions of the AGN.

(d) *Compton reflection hump*: A broad bump above the power law continuum is observed in many AGN over the ~7-60 keV rest-frame energy range, peaking at a rest-frame energy of ~30 keV [175]. This spectral feature is often explained as reflection[10] of the hard X-ray photons in the accretion disc (e.g. [75] [99] [132]). X-ray photons with energies lower than ~2 keV are most probably photoelec-

---

[10] In this thesis we have used the term "reflection" to mean reprocessing and redirection of 2-10 keV radiation in material optically thick where there is no transmitted component. We will use "scattering"

trically absorbed and therefore only a few photons at these energies will be reflected. At higher energies, due to the decreasing abundance of elements with higher atomic number (Z) required for photoelectric absorption, most X-ray photons are reflected. Iron is the most abundant heavy element and absorbs the high energy photons giving an Fe absorption edge and Fe Kα fluorescent line emission (see (c)). At higher photon energies, the scattering cross-section reduces and Compton down-scattering becomes important decreasing the number of reflected photons. The overall effect is a broad band spectral hump that peaks at high energies.

(e) *Exponential cut-off*: At energies of several tens to hundreds of keV (from 60 to 300 keV) an exponential cut-off has been observed in the *BeppoSAX* spectra of a few AGN with a typical cut-off energy of a few hundreds of keV [98] [176] [184] [185]. The cut-off energy indicates the presence of a thermal hot corona around the accretion disc.

1.4.3 Origin of X-ray emission in AGN

AGN are cosmological sources that, because of their large bolometric luminosities, can be detected at very large distances. The large luminosities and compactness of these sources put very strong constraints on the emission mechanism that powers them. It is commonly accepted that the source of energy in AGN is the conversion of gravitational energy of accreting matter (gas and stars) in the region surrounding a supermassive central black hole with masses in the range $\sim 10^6 - 10^{10}\mathrm{M}_\odot$ into radiation. The efficiency of the accretion process can be of the order of ~10%, much higher than that of nuclear fusion (~0.7%), the power source in stars.

Although it is generally accepted that the energy source of AGN is accretion, the details on how X-rays are produced are still not clear and remain as one of the most challenging problems in AGN physics. As we have seen in Sec. 1.4.2, an optically thick accretion disc is not hot enough to form the soft excess emission often seen in the spectra of AGN and therefore, it cannot produce the higher energy hard X-ray emission.

On the basis of spectroscopic observations, the best model to date for the primary high energy (above 1 keV) X-ray emission in AGN is Compton up-scattering of optical-UV photons emitted thermally in the accretion disc by an optically thin hot plasma of thermal electrons that is surrounding the accretion disc. This plasma is commonly modelled as a Comptonizing corona. Comptonization can lead to a power law spectral shape that reproduces well the observed continuum emission of AGN in X-rays [47] [100] [101] [127] [212].

For the simplest geometry in the Comptonization model half of the X-ray radiation will be emitted towards the observer while the other half will be directed to the accretion disc, where it will be absorbed and re-emitted as optical-UV photons that will enter again the corona cooling the hot electrons. The spectral slope of the X-ray power law depends on the temperature and optical depth of the Comptonizing plasma. As the heating and cooling process are coupled, Comptonizing models predict a narrow range of power law shapes.

---

to mean reprocessing and redirection in the case of material that allows transmission of a large fraction of the incident 2-10 keV radiation (optical depth to electron scattering $0<\tau<1$).

This is in perfect agreement with observations that have found the typical dispersion on the X-ray continuum in AGN to be rather small ($\Delta\Gamma \sim 0.2$ [153]).

Thermal models for the corona predict a high energy cut-off at an energy that depends on the temperature of the Comptonizing plasma. A high energy cut-off (at energies >100 keV) has already been observed in the *BeppoSAX* spectra of a number of AGN [98] [176] [184] [185], lending strong observational support to the thermal models.

1.4.4 X-ray variability

All AGN appear to be strongly variable objects. Irregular variability at all wavelengths and time scales is a common phenomenon in AGN (see [188] for a review). However, the largest amplitudes of variability and shortest variability time scales have been detected in X-rays, which suggests that X-ray emission in AGN must originate in a small region close to the central supermassive ($10^6 - 10^9 M_\odot$) black hole [151] [171].

At time scales from minutes to years, the timescale of variability is correlated with the luminosity of the objects, i.e. AGN show stronger variability towards longer time scales, this effect being more important for higher luminosity objects [147] [173]. In addition it has been well established that X-ray variability amplitude on short [16] [128] [173] [233] and long time scales [147] when measured over a fixed temporal frequency correlates inversely with X-ray luminosity, i.e. lower variability amplitudes are detected for more luminous sources. However there are evidences that the strength of the anti-correlation decreases towards longer time scales [148].

All these findings are consistent with a scenario where more luminous sources, hosting more massive black holes, have larger X-ray emitting regions, and therefore the variability needs more time to propagate through the X-ray emitting region.

X-ray spectral variability studies have shown that most AGN tend to become softer with increasing source brightness (see e.g. [149] [173]) similar to the different states seen in black hole X-ray binaries (BHRXB) [159]. In addition, nearly all AGN exhibit stronger variability at the softest X-rays on all time scales [233].

Two phenomenological model parameterisations have been proposed to explain the variability patterns observed in AGN:

1. The *two-component spectral model*: It was proposed independently by M^{c}Hardy et al.(1998) [160] and Shih et al.(2002) [222]. In this model a softer continuum emission component of constant slope but variable flux (probably associated with the emission from the hot corona) is superimposed on a harder spectral component with constant flux (likely associated with the Compton reflection hump). This model does not require the form of the spectral components to vary, what varies is the relative contribution of the two spectral components with flux. When the source becomes brighter the soft component dominates the spectrum and the source becomes softer. In this model it is expected that as the sources become brighter their X-ray spectral slope will saturate to the slope of the soft component.

2. *Spectral pivoting model*: This alternative parameterisation was proposed to explain the observed variations in the underlying continuum spectrum of some sources for

which the *two-component spectral model* was not able to explain their observed variability properties (e.g. NGC 4151 see [186] [251] [252]). In this model flux-correlated changes in the continuum shape (coronal power law) are due to changes in a single variable component that becomes softer as the source brightens.

The mechanism producing X-ray variability in AGN is not fully defined. While long-term variability in AGN is probably caused by changes in the global accretion rate, rapid variability cannot arise in this manner as the viscous timescale in the accretion disc is much too long (~years). Several variability models have been proposed, involving the accretion disc, corona, and relativistic jet. For example, some models assume that the variability is caused by variations in the accretion rate propagating inwards [137]. In some cases variability has been attributed to variations in the obscuration of the nuclear engine. It is clear that X-ray variability studies of AGN can give us valuable information about the scale and structure of the innermost regions in AGN.

1.4.5 Classification of AGN

In previous sections the different observational properties of AGN have been described in detail. This broad range of observational properties is commonly used to classify AGN into different groups. We explain here the classification of AGN according to their observed emission properties at radio and optical/UV wavelengths (see Fig. 1.5), which is the scheme adopted for the work presented in this thesis.

AGN are classified into two broad categories according to their *radio-loudness*, defined as

$$R_L = log\left(\frac{f_{5\,GHz}}{f_B}\right) \tag{1.2}$$

where $f_{5\,GHz}$ is the radio flux at 5 GHz and f_B is the optical flux in the B band, centred at $\lambda = 4400\text{Å}$. Objects with $R_L \geq 10$ are termed *radio loud* AGN and those with $R_L < 10$ *radio quiet* AGN. The optical-UV emission line spectra and the infrared-soft X-ray continuum of both classes of objects are very similar [214]. However, *radio loud* AGN appear to have systematically flatter X-ray spectral slopes than *radio quiet* objects [220] [246]. *Radio loud* AGN constitute a small fraction (5-10%) of the X-ray and optically selected AGN population.

There is a second classification of AGN on the basis of their optical/UV spectral properties which is still valid for both *radio loud* and *radio quiet* AGN. Under this scheme AGN are classified into the following two broad categories:

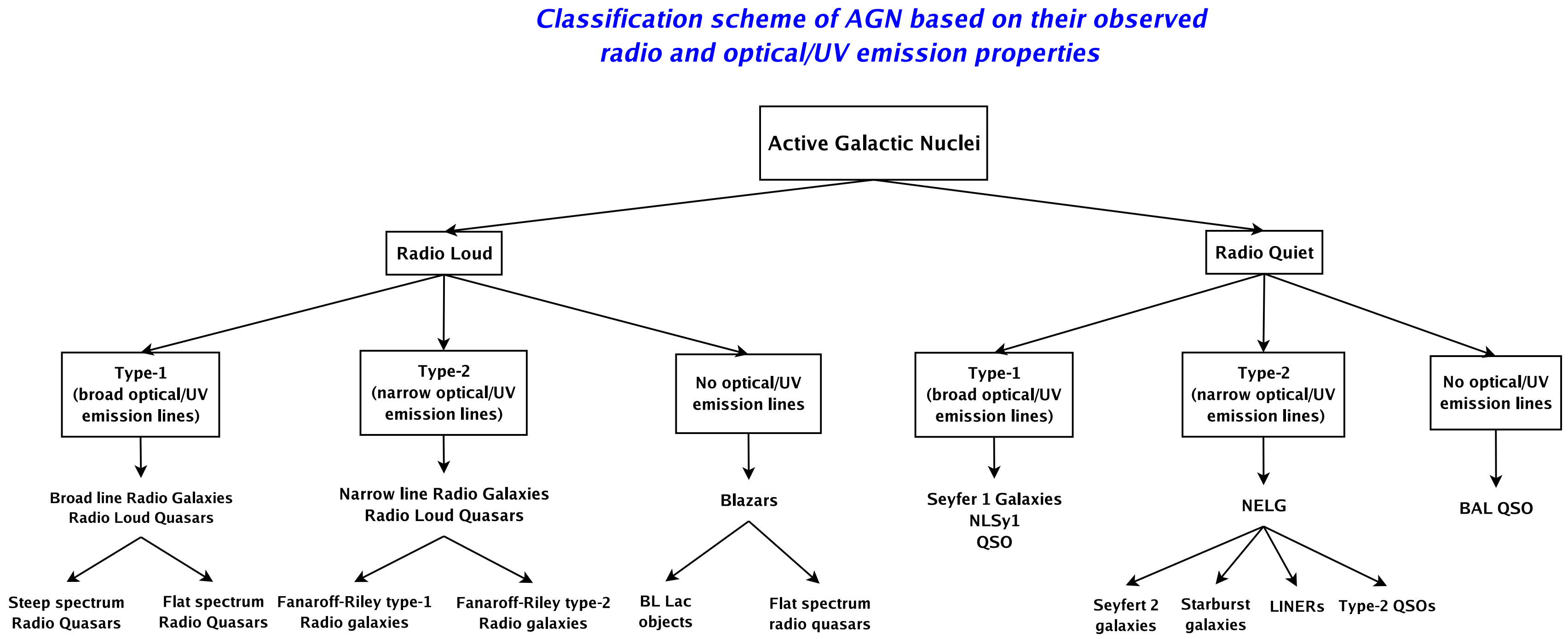

Figure 1.5: *Classification of AGN based on their observed radio and optical/UV emission properties. See Sec. 1.4.5 for an explanation of the different classes of objects.*

1. **Type-1 AGN (broad line AGN)**: The optical spectra of type-1 AGN show strong highly ionised broad permitted lines, mainly from hydrogen, although lines from HeI, HeII and FeII are also frequently detected (see Fig. 1.6 top). The typical line widths correspond to velocities from 2000-10,000 $\mathrm{km\,s^{-1}}$. Because of these properties these objects are often referred to as broad-line AGN (BLAGN). Type-1 AGN cover a broad range of redshifts (z$\sim$0-6[11]) and are the dominant X-ray source population at bright fluxes [227]. Most AGN in this group show no signs of obscuration at either X-ray or optical/UV wavelengths. However, there is recent observational evidence, mainly from X-ray surveys, that suggest that $\sim$10% of the sources in this group have X-ray absorption, although most of them with low (rest-frame absorption $< 10^{22}\,\mathrm{cm^{-2}}$) absorbing column densities. This is one of the results of the present work.

   The *radio quiet* objects in this class are usually sub-divided into low luminosity Seyfert 1 galaxies ($\leq 10^{44}\,\mathrm{erg\,s^{-1}}$ and therefore seen only nearby except in the deepest surveys) and the higher luminosity sources or QSO ($\geq 10^{44}\,\mathrm{erg\,s^{-1}}$) which appear as bright point like sources in optical and X-ray images. QSOs have a blue non-thermal optical continuum (their host galaxy is not visible) with the most prominent spectral feature being a broad optical-EUV bump, frequently attributed to thermal emission in the accretion disc [145] [221] (see also Sec. 1.4.2). Although Seyfert 1 galaxies also show a strong non-stellar optical continuum, the host galaxy is still visible in these objects. There is an important group of Seyfert 1 galaxies showing extreme properties, termed Narrow-Line Seyfert 1 galaxies (NLSy1). NLSy1 were first classified by Osterbrock & Pogge in 1985 [179] as a separate class of Seyfert 1, based on their observed relatively narrow permitted emission lines (FWHM $\leq 2000\,\mathrm{km\,s^{-1}}$), strong optical Fe II emission relative to Hβ, and weak [OIII]λ5007. NLSy1 show extreme X-ray properties: steep strong soft excess emission [26] [200], rapid and large-amplitude of variability [131] and steep ($\Gamma \geq$2.5) power-law continua [247]. NLSy1 are believed to have less massive black holes than Seyfert 1, accreting at higher Eddington ratios, suggesting that they might be in the early stage of AGN evolution [23].

   The *radio loud* type-1 AGN are classified into Broad Line Radio Galaxies at low luminosities, and Radio Loud Quasars (RLQ) at high luminosities. RLQ are usually separated into Steep Spectrum Radio Quasars (SSRQ) if their radio spectral index $\alpha_{\mathrm{r(3GHz)}} > 0.5$ and Flat Spectrum Radio Quasars (FSRQ) if their radio spectral index $\alpha_{\mathrm{r(3GHz)}} < 0.5$.

2. **Type-2 AGN (narrow line AGN)**: These sources have optical continua with superimposed permitted and forbidden lines. However, all observed lines in type-2 AGN are narrow ($\leq 1500\,\mathrm{km\,s^{-1}}$) although with widths similar to the narrow lines found in type-1 AGN (see Fig. 1.6 middle). Their optical spectra continuum is dominated by starlight and therefore they have very weak non thermal optical-UV continua, with little evidence for the optical-EUV bump typical of type-1 AGN. The X-ray spectra of type-2 AGN usually shows signatures of X-ray absorption, with a wide range of absorbing column densities. X-ray absorption in type-2 AGN tends

---

[11] The currently highest redshift QSO is at z=6.43 [62].

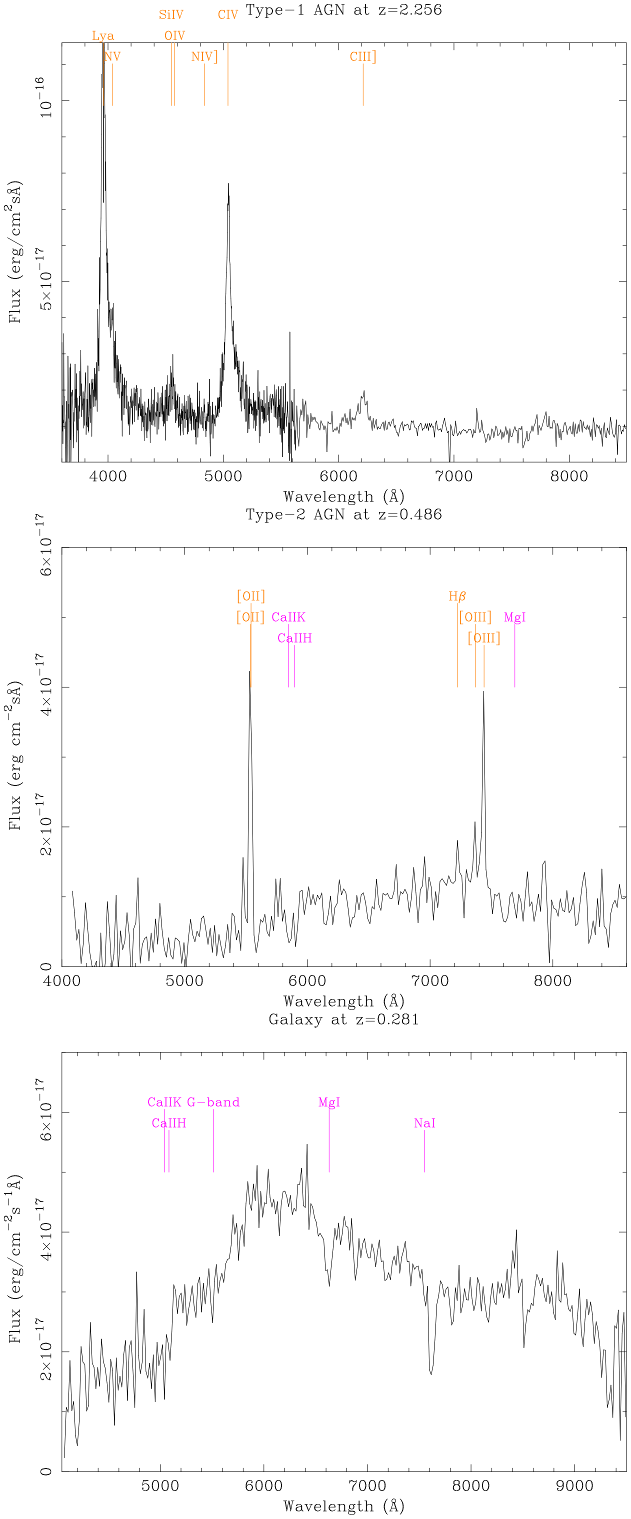

Figure 1.6: *Typical optical spectra of different classes of AGN based on their observed optical/UV emission properties. See Sec. 1.4.5 for an explanation of the different classes of objects. Top: Type-1 AGN showing both broad and narrow emission lines. Middle: Type-2 AGN showing only narrow emission lines. Bottom: ALG showing only absorption lines. The spectra were obtained from the AXIS project (see Sec. 2.7).*

to be systematically higher than in type-1 AGN, and therefore they are fainter soft X-ray sources, detected preferentially at z$\leq$ 1.5 in current X-ray surveys [13].

Type-2 *radio quiet* AGN are referred as Seyfert 2 galaxies at low luminosities ($\leq 10^{44}$ erg s^{-1}), and as type-2 QSO at high luminosities ($\geq 10^{44}$ erg s^{-1}). A general name used for all galaxies which only show narrow emission lines in their optical/UV spectra is Narrow Emission Line Galaxies (NELG) [169]. This category includes Seyfert 2 galaxies, LINERs, starburst galaxies and type-2 QSOs. The relative intensity of the optical/UV emission lines allows a detailed classification [178].

Radio loud type-2 AGN are usually termed Narrow Line Radio Galaxies (NLRG). NLRG are subdivided into two categories according to their morphological type: low luminosity *Fanaroff-Riley type-1 radio galaxies* (FRI) and the high luminosity *Fanaroff-Riley type-2 radio galaxies* (FRII) [63]. Radio emission in FRI sources is found to be core dominated, i.e. it peaks near the nucleus. FRI show weak optical emission. On the other hand, FRII show strong optical emission and their radio emission is lobe dominated.

The optical/UV spectra of a small number of AGN is characterised by the absence of emission lines (see Fig. 1.6 bottom).

The *radio loud* sources in this group include BL Lacertae (BL Lac) objects, *Optically Violently Variable Quasars* (OVV), *Highly Polarised Quasars* (HPQ) and *Core Dominated Quasars* (CDQ). All these subclasses are characterised by rapid variability in flux on very short time scales (>0.1 mag in a day). The objects in this group are frequently termed *blazars*. Emission in *blazars* is thought to be beamed.

One of the most surprising findings of medium-deep *Chandra* and *XMM-Newton* surveys was the discovery of X-ray luminous sources ($\geq 10^{42}$ erg s^{-1}) in the nuclei of optically normal galaxies [15] [42] [66] [80] [111] [170]. These sources which display an optical spectrum typical of an absorption line galaxy (ALG), have been given a variety of names such as *optically dull galaxies* [56], *passive galaxies* [92], *X-ray bright optically normal galaxies* (XBONG, [42]) and *elusive active galactic nuclei* [141]. In this thesis we have adopted the name XBONG. The objects in this group have X-ray spectra and X-ray/optical flux ratios that suggest AGN activity [42]. However XBONG are found to have the optical spectra of apparently normal galaxies, i.e., without clear evidence for AGN emission lines or non-stellar continua. At the faintest 0.5-2 keV flux levels of the *Chandra* deep X-ray surveys, a significant fraction of the X-ray source population ($\geq$40%) has been optically identified as ALG at z$\sim$0.1-1.5 [18] [109]. The flux distribution of the sources as well as models for the population of X-ray binaries in galaxies [93] [245] suggest that ALG will become the major contributor to the 0.5-2 keV XRB emission at fluxes of $\sim 10^{-18}$ erg cm^{-2} s^{-1}.

It is still rather uncertain why we do not see AGN signatures in the optical spectra of these sources. Some XBONG show absorbed X-ray spectra with column densities $\geq 10^{24}$ cm^{-2} [141] which is highly suggestive that these sources host luminous AGN and that their peculiar X-ray and optical properties are related to heavy obscuration. The nuclear emission in these objects must be completely obscured in all directions preventing the formation of the narrow emission line region. However not all XBONG show signatures of absorption in their X-ray spectrum. It has been claimed that some XBONG may be "normal" AGN with their optical signatures diluted by starlight from their host-galaxy [166] [218], although this model cannot provide a good explanation for all nearby XBONG for which good quality optical spectra are available and therefore the contribution from the AGN and its host galaxy can be separated.

XBONG are preferentially found at low redshifts, z$\sim$0.05-1 and have typical X-ray luminosities of $\sim 10^{41} - 10^{43}\,\mathrm{erg\,s^{-1}}$, relatively lower than those of standard AGN. In addition XBONG appear to have weaker intrinsic optical and UV continuum (and therefore they are expected to have weaker emission line luminosities) [218]. Based on these findings Yuan et al.(2004) [253] proposed a model in which XBONG are AGN that lack an optically thick accretion disc at small radii, having instead a radiatively inefficient accretion flow or advection dominated accretion flow (ADAF) [253]. Because of the lack of an accretion disc at small radii, these sources are expected to have fainter optical/UV continuum and optical/UV emission line spectra than standard AGN.

Finally, the detection at radio wavelengths of some XBONG suggests that some of these objects could be BL Lac-like AGN, in which most of the X-ray and radio emission comes from a highly relativistic and beamed flow towards our line of sight [29]. Although it is still not clear whether XBONG constitute a homogeneous population, all the models we have described have been able to explain the X-ray and optical properties of subsamples of XBONG. It is unlikely, however, that any of the models can be applied to the XBONG population as a whole.

1.4.6 The AGN model

As we have seen in previous sections, the large diversity of observational properties of AGN makes a detailed understanding of their physics very complex. However the approximate structure of AGN is believed to be as illustrated in Fig. 1.7. It is widely accepted that all active galaxies have the same fundamental ingredients:

1. A supermassive black hole ($10^6 - 10^{10}\,\mathrm{M_\odot}$) accreting matter is at the centre.

2. The accreting material is expected to have significant angular momentum and therefore the accretion cannot be radial, but forms a planar disc accretion geometry [219] of optically thick plasma that surrounds the black hole. The accreting matter is probably heated by magnetic and/or viscous processes to temperatures of the order of $10^5 - 10^6\,\mathrm{K}$ and emits thermally in the optical/UV and probably soft X-rays. The characteristic radius of an active nucleus is generally parameterised in terms of the radius of a non-rotating Schwarzschild black hole horizon, $\mathrm{R_{Schw}} = 2\,\mathrm{GM/c^2} \sim 3 \times 10^5$ $\mathrm{M\,/M_\odot}$ cm. For a black hole of mass $10^8\,\mathrm{M_\odot}$, $\mathrm{R_{Schw}} = 10^{14}\,\mathrm{cm}$ (midway between the orbits of Jupiter and Saturn) or 1 light-hour.

3. A quasi-spherical cloud of hot (electrons and ions) optically thin plasma surrounds or perhaps it is mixed with the inner parts of the accretion disc. The hot electrons Compton up-scatter the cooler photons thermally emitted in the accretion disc to medium and hard energy X-rays, resulting in the non thermal power law spectra observed at X-rays in AGN.

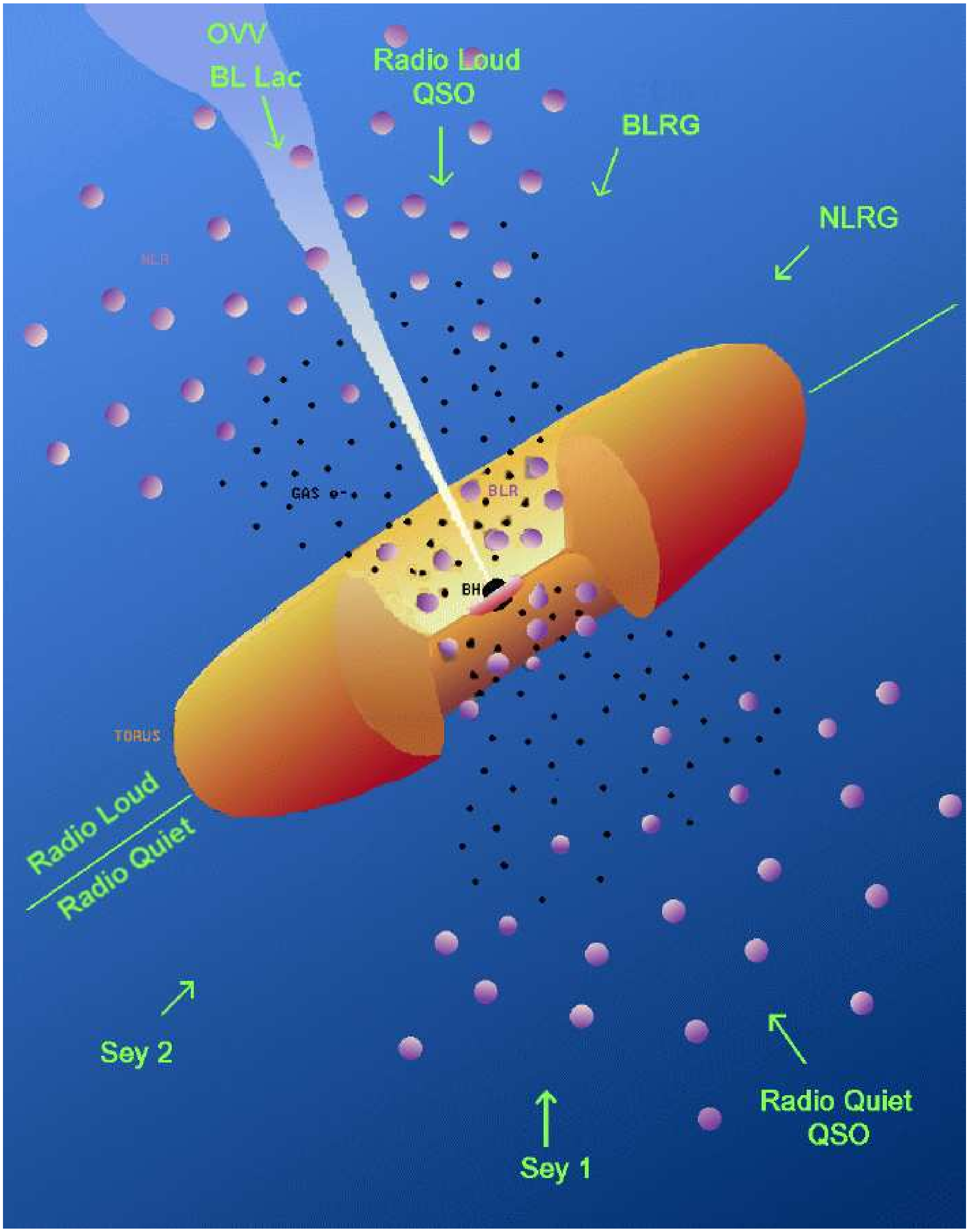

Figure 1.7: *Schematic diagram of the current unified theory of AGN adapted from [237] (*`http://www.asdc.asi.it/bepposax/calendar/`*). The torus is not drawn to scale, since the half-opening angle is believed to be in the range* 30°-60°.

4. Further out, at distances of about 100 light days from the central source, are located clouds of high density ($10^7 - 10^{10}\,\mathrm{cm}^{-3}$) gas moving at high velocity (a few thousand $\mathrm{km\,s}^{-1}$), which are responsible for the strong highly ionised Doppler-broadened optical and UV emission lines observed in the optical/UV spectra of many AGN. This region is known as the broad line region (BLR)[12]. The centroids and widths of the emission lines imply that the emitting clouds must be highly ionised (by the nuclear radiation) and moving at high velocities.

5. Still further out, at parsec (light years) distances from the central source [122] [191] [192] and at distances intermediate between the broad and narrow line regions, there is a region of thick cold material of gas and dust with a toroidal geometry in a similar plane as the accretion disc. The torus (or other geometrical form) absorbs and scatters the nuclear radiation and partially covers the central source, blocking the BLR and accretion disc from certain lines of sight. It is not clear whether the torus geometry depends on luminosity, but the apparent lack of cross-correlation of the amount of absorption with the host galaxy inclination angle, even for AGN of the same optical type [144], suggests that its orientation should be random with respect to the host galaxy.

6. Further out at distances from a few tens of parsecs to kilo-parsecs are low velocity clouds of gas excited by the ionising nuclear radiation emitted along the polar axis of the torus and that therefore escapes the absorbing material. This region (known as the narrow line region, NLR) is responsible for the narrow optical and UV emission lines. As the NLR lies outside the region affected by the high gas column density, optical narrow emission lines will suffer only moderate amounts of dust obscuration. Cone-shaped region of clouds illuminated by the nuclear emission from the AGN has been observed in a number of type-2 AGN, supporting the torus model, as the NLR should be "seeing" directly the nuclear light [41]. The detection of strong forbidden narrow lines implies that the density of the material in the NLR cannot exceed the critical density for collisional de-excitation, and therefore it needs to be low, of the order of $10^4\,\mathrm{cm}^{-3}$ or less.

7. Powerful relativistic radio jets and ionisation cones flow from the central black hole and can extend to tens of kilo-parsecs. They are symmetric about the black hole and propagate in both directions perpendicular to the plane of the accretion disc. They are best seen in radio, thanks to synchrotron emission, but it is not clear how common are these jets in AGN.

1.5 AGN Unification Picture

Unification models try to unify all different classes of AGN, with only a few parameters giving rise to the whole observed variety of properties. The basis of the unification schemes

---

[12] Traditionally the BLR has been interpreted as a system of clouds, however it has been also explained as a disc wind [55] and as the outer regions of the accretion disc [40].

is that all AGN have intrinsically the same mechanism (they are powered by accretion onto a supermassive black-hole) and their different observational properties are mostly the result of the anisotropic distribution of the obscuring matter[13]. Unification models were first invoked to explain the results of spectropolarimetric observations that detected broad line components in the polarised optical/UV spectra of Seyfert 2 galaxies [6]. The lack of optical broad emission lines was explained as the BLR being blocked by an optically thick structure. If not all directions are completely obscured then broad lines could be detected with spectropolarimetry, because of the scattering of the BLR radiation into our line of sight by free electrons and/or dust particles above the nucleus. Further support to the unified model was obtained with the detection of broad permitted emission lines in the near-IR unpolarised spectra of optically type-2 AGN, with no signatures of a broad line region in their polarised spectra, because absorption is less effective in the IR than in the optical band [86] [208] [213].

In this scenario the different observational properties of type-1 and type-2 AGN are mainly due to different orientation angles of the obscuring matter. The absorbing matter would be located at distances intermediate between the BLR and the NLR but it should not be blocking completely the nuclear region. The simplest geometry used to describe the obscuring matter is a torus [5] [237], the clouds in the BLR, or material associated with the accretion disc [108]. The sources where we can see directly the nuclear emission and the broad line region will have unabsorbed X-ray spectra and will be optically classified as type-1 AGN. In the sources where the obscuring matter intercepts our line of sight, the central source and the BLR will be hidden. These sources will have an absorbed X-ray spectra and will be optically classified as type-2 AGN. Fig. 1.7 shows a schematic diagram of the classification of AGN for different orientations of the line of sight.

Unification schemes provide a simple description of the most general properties of AGN. X-ray observations show type-2 AGN to be systematically weaker sources in the soft X-ray band than type-1 AGN, as expected if their nuclear emission is obscured. However the number of observational results that cannot be explained by the standard unified model is increasing very rapidly. X-ray surveys of AGN are finding that not all X-ray obscured AGN have type-2 optical spectra, while not all type-1 AGN are X-ray unobscured [152] [153]. We have addressed this point in more detail in this work.

1.6 Synthesis models of the X-ray background

The most serious challenge to models that explain the XRB as the integrated emission from discrete sources was the so-called *spectral paradox*: when these models began to be developed in the 80s, no known class of X-ray emitting sources had a spectral shape that matched the measured spectrum of the XRB above 3 keV. The known candidates with strong X-ray emission were clusters of galaxies, high mass X-ray binaries in starburst

---

[13] A second orientation effect is used to explain *radio loud* sources. When the line of sight is close to the axis of the radio jets of the AGN, relativistic beaming amplifies the luminosity of the source and we will observe the properties of a *radio loud* AGN: super-luminal motion, rapid variability and intense power-law continua. Radio jets are absent in the unification scheme of *radio quiet* AGN, that relies in obscuration alone.

galaxies, and AGN. The data obtained with the *Einstein* observatory showed AGN to be the major contributors to the XRB from 1 to 2 keV, however the spectrum of the XRB above ~3 keV is significantly flatter than the typical spectra of the AGN known at that time [25].

One way the XRB could be explained as the integrated emission from AGN was if a new class of reflection-dominated AGN was present [59]. Advection dominated accretion discs (ADAFs) in AGN were also put forward [51]. A very different hypothesis was postulated by Setti & Woltjer in 1989 [217], when only a small fraction of the XRB was resolved into discrete sources. Using data from the *UHURU* catalogue, Setti & Woltjer proposed the existence of a new population of AGN with intrinsic properties similar to the observed AGN, but heavily absorbed, and hence their observed spectra would be flattened by the effect of photoelectric absorption. This hypothesis is the basis of the synthesis models of the XRB based on AGN unification schemes (e.g. [44] [69] [84] [217] [235]).

Since it was originally proposed new variants of the model have been developed [44] [57] [84] [139] [155] [193]. The basis of all these models is that the XRB is made by the integrated emission over cosmic time of a mixture of unobscured and obscured AGN. The strongest observational evidence for these models has come from X-ray surveys, that have resolved most of the extragalactic XRB into discrete objects. Optical identification campaigns of the X-ray sources detected in deep X-ray surveys are showing that most sources are AGN with different degrees of absorption [1] [216].

However, as we will see in Sec. 1.5, *Chandra* and *XMM-Newton* surveys are finding an increasing number of objects where the X-ray and optical properties of AGN appear uncorrelated, and hence the AGN unification model, which is the basis of synthesis models, fails for these sources. Another problem with the synthesis models of the XRB is the lack of observational information for some of the most relevant parameters. The evolution of X-ray absorption over cosmic time, and the dependence of absorption on the intrinsic luminosity of the objects are not clear yet. The X-ray luminosity function and its evolution are rather well known only for unobscured AGN [163]. Furthermore, the number ratio between obscured and unobscured AGN is only known for local objects (~4 [143]) and the same happens for the distribution of absorbing column densities in type-2 AGN [207]. In addition the observed absorption and redshift distributions of samples of hard X-ray sources detected with *Chandra* and *XMM-Newton* are poorly reproduced by current XRB models.

Because of the lack of observational constrains a number of assumptions need to be made by the models, specially on the properties of the population of absorbed AGN. It is frequently assumed that the column density distribution in type-2 objects is the same at all luminosities and redshifts. Absorbed objects are assumed to evolve more rapidly than unabsorbed ones, as the observed redshift distributions indicate. For example, in order to reproduce the observed number count distributions of *ASCA* and *BeppoSAX* in the hard X-ray band, the models require a population of luminous and obscured AGN (obscured AGN being ~4-10 times more numerous), the so-called QSO2s. However, QSO2s are found to be rare objects in X-ray surveys.

1.7 Modern instrumentation in X-ray astronomy

The sources that dominate the XRB emission are very faint, with typical fluxes of $\sim 10^{-14}$ $\mathrm{erg\,cm^{-2}\,s^{-1}}$. In order to study these objects, large area detectors with very high efficiency are required. The rocket that discovered the X-ray background in 1962 carried a small X-ray detector, a Geiger counter, an instrument that has very low spectral resolution and no imaging capabilities. The first X-ray orbiting observatories used mechanical collimators to limit the field of view covered by the detectors. This provided very rough angular resolutions, of the order of several degrees, which limited significantly the sensitivity of the observations because of confusion of the faintest sources.

Since then there have been major advances in instrumentation in X-ray astronomy, the most important one being the introduction of imaging X-ray optics. The first observatory that used an imaging telescope was *Einstein* in the 70s.

Proportional counter detectors have been extensively used in X-ray missions for several decades, until the advent of high resolution solid state charge coupled device (CCD) detectors. CCDs were first used as X-ray astronomy detectors in the Japanese *ASCA* Observatory and were able to produce X-ray images with photons of up to 10 keV. The spectral resolution of CCD detectors is an order of magnitude better than that of proportional counters. CCD detectors are now used in all modern missions and are on board *Chandra* and *XMM-Newton*.

1.7.1 X-ray telescopes

Focusing X-ray photons is not an easy task. In a standard reflecting optical telescope, photons are directed almost normally to the surface of the reflector and collected in the focal plane. Because of their high energy, normal incidence only leads to the absorption and scattering of X-rays, but they are virtually never reflected.

X-rays can only be focused in grazing incidence at very small angles. The angle for reflection is ~1 deg for X-rays of energies of ~1 keV and standard reflection metals (Au, Pt, Ir, Ni).

The German physicist Hans Wolter showed in 1952 that a system formed by two reflectors (the first one being a paraboloid followed by a cofocal and coaxial hyperboloid) can focus X-rays. This system, known as Wolter-1 configuration, is the configuration most frequently used for X-ray astronomy and has been used for the *XMM-Newton* X-ray telescopes. The light path in a Wolter-1 configuration is illustrated in Fig. 1.8.

The critical angle for reflection depends inversely on the energy of the incident photons (making reflection more difficult at higher photon energies) and increases with the density of free electrons in the reflecting material. Shorter focal length telescopes focus mostly softer X-rays. Thus, to focus harder photons longer focal lengths, and therefore longer telescopes are needed. The effective area of the X-ray telescopes is therefore a function of the energy of the incident photons but also of the off-axis angle [14]: the fraction of incident photons reaching the focal plane decreases with the off-axis angle. This effect is known as

---

[14] Distance to the centre of the optical system or optical axis.

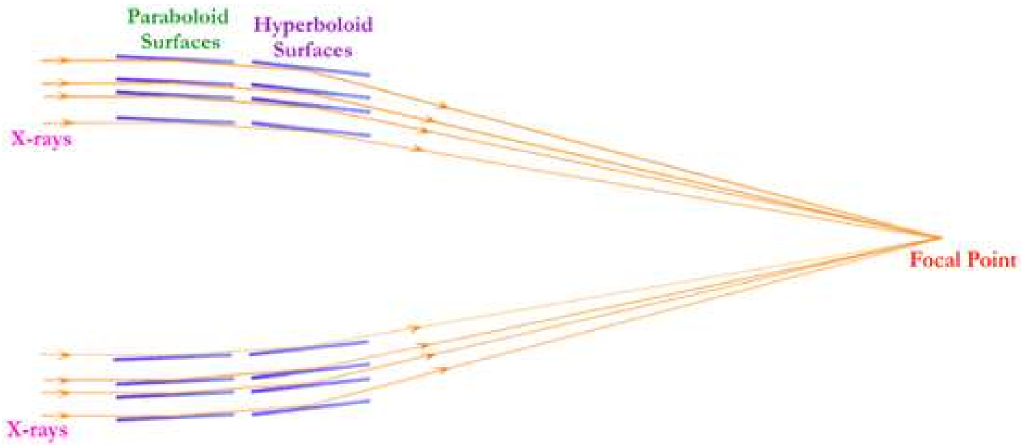

Figure 1.8: *Light path on an X-ray telescope with "type-1" Wolter configuration. Courtesy from* `http://chandra.harvard.edu/`.

vignetting and it is observed as a decline of the effective area of the X-ray telescopes at larger off-axis angles.

In grazing incidence, the effective area of the mirror seen by a photon is very small, and therefore a large number of mirrors are usually nested in order to significantly increase the collecting area of X-ray telescopes.

1.7.2 Imaging X-ray detectors

A variety of non-dispersive detectors have been used in X-ray astronomy, including Position Sensitive Proportional Counters (PSPC), Micro Channel Plates (MCP), Micro-calorimeters or Charge Coupled Devices (CCD). PSPCs have been used in a large number of X-ray missions including *Einstein* and *ROSAT*.

In this section I will concentrate on the description of CCDs as they are the detectors which have been used in this work. They were used in *ASCA* and are now on board *Chandra* and *XMM-Newton*. CCDs are imaging device arrays of pixels (charge collecting units or capacitors) with low noise and providing good energy resolution. The basic principle of CCD detectors is that when an X-ray photon hits a capacitor of the semiconductor material of the CCD, it produces multiple electron-hole pairs via the photoelectric effect. Visible photons only release a few electron-hole pairs and hence in order to collect enough signal longer exposures need to be accumulated. However an X-ray photon is able to produce hundreds of thousands of charged electrons, which makes possible to measure the energy of each photon individually, if the device is read often enough. CCD detectors in X-ray astronomy work as photon counting devices.

The charge carried by the cloud of excited electrons is proportional to the energy of the incident photon. To read the signal, the charge is transfered along the surface of the semiconductor from the capacitor which was struck by the X-ray photon to neighbouring capacitors. The last capacitor in the array will transfer its charge to an amplifier that converts the charge into a voltage, that can be recorded, making possible to recover the position of the incident photon and its energy.

The charge collected in a CCD is recovered in successive readouts that limit the time resolution of the observations to a few seconds. Detailed studies of rapid variability of astronomical sources require better time resolutions. CCDs can be operated in different observing modes, although in order to improve the time resolution of the observations it is necessary to reduce the read-out time of the CCD, which is only possible by limiting the area being read-out, and hence the field of view. Next generation CCDs for X-ray astronomy will be based on Active Pixel Sensors where each pixel is read individually.

1.7.3 The *XMM-Newton* observatory

All the data used in this thesis have been obtained with the X-ray detectors on board the *XMM-Newton* observatory. In the following I describe in detail the science instrumentation in *XMM-Newton*.

The *XMM-Newton* observatory[15] is the second cornerstore of the Horizon 2000 science programme of the European Space Agency (ESA). It was launched the 10th of December of 1999 on an Ariane 504 rocket from French Guiana. The satellite is in a 48-hour highly elliptical orbit allowing continuous monitoring of selected targets up to about 40 hours.

XMM-Newton carries six science instruments (see Figure 1.9). Three co-aligned X-ray telescopes (each with 58 nested Wolter-1 type mirrors) [113] focus X-ray photons into the X-ray instruments (CCD cameras) at the focal plane. Figure 1.10 shows the light path of the X-ray telescopes on board *XMM-Newton*. The telescopes have the largest effective area achieved so far (it is 3 to 10 times higher at 1 and 7 keV that *Chandra*'s, respectively).

Table 1.2 shows a comparison of the properties of the *XMM-Newton* X-ray instrumentation with those of other missions, while Fig. 1.11 compares the effective area of the mirrors with those of other recent observatories.

Table 1.2: *Comparison of XMM-Newton properties with those of Chandra, ROSAT and ASCA.*

Mission	Mirror PSF FWHM – HEW(arcsec)	energy range keV	mirror effective area at 1 keV cm^2
$XMM-Newton$	$6-15$	$0.15-15$	4650
$Chandra$	$0.2-0.5$	$0.1-10$	800
$ROSAT$	$3.5-7$	$0.1-2.4$	400
$ASCA$	$73-174$	$0.5-10$	350

Data taken from the Science Operations Centre webpage: `http://xmm.vilspa.esa.es`.

---

[15] `http://xmm.esac.esa.int`.

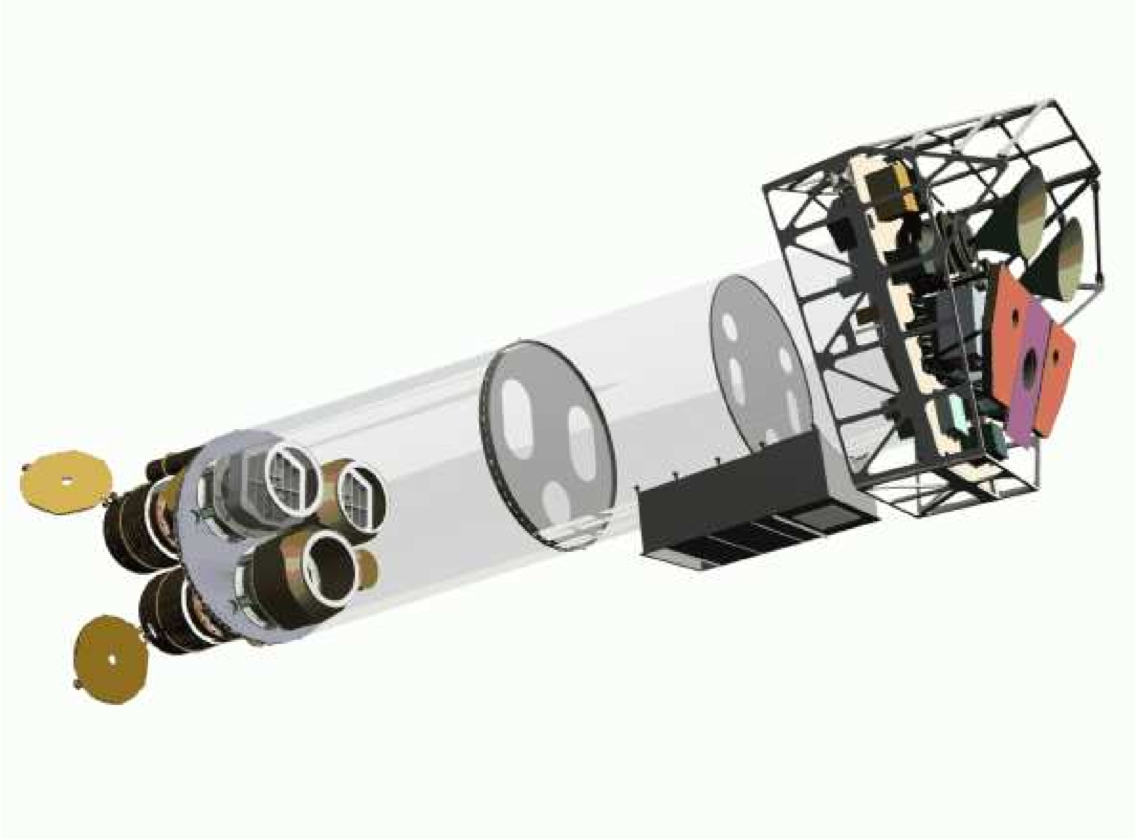

Figure 1.9: *Payload of the XMM-Newton observatory taken from [113]. At the lower left are located the X-ray telescopes (two with Reflection Grating Assemblies) and the optical monitor. At the right hand side are the focal instruments: the two EPIC-MOS cameras with their corresponding radiators (black/green "horns"), the radiator of the EPIC-pn camera (violet) and those of the RGS receivers (in orange).*

The peak effective area of the *XMM-Newton* mirrors is 0.15 m^2 at 1 keV and 0.05 m^2 at 5 keV. Each telescope has its own Point Spread Function (PSF)[16]. The PSF varies little with energy over a broad energy range (0.1-4 keV) but has a strong dependence with the off-axis angle (distance from the centre of the field of view) of the sources. Using the radius at which 90% of the total energy is encircled ($W90$) to quantify the width of the PSF, the values of $W90$ on-axis are ~42 arcsec for M1 and M2 mirrors (see below) and ~51 arcsec for pn (see below) at an energy of 1.5 keV. At an off-axis angle of 12 arcmin W90 increases to ~53 arcsec for M1 and M2, and ~65 arcsec for pn at the same energy.

On the focal plane of each telescope there is an European Photon Imaging Camera (EPIC) instrument. *XMM-Newton* carries two different technologies of CCD detec-

---

[16] The Point Spread Function of an optical device is the spatial distribution of light of a point like source in the focal plane. The PSF of a telescope is a measure of the quality of the optical system.

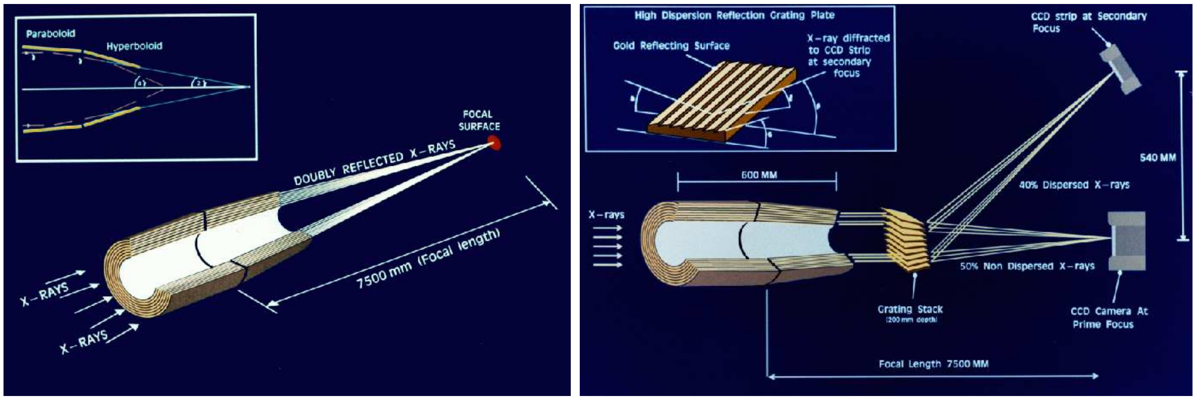

Figure 1.10: *Light path on the X-ray telescopes onborad XMM-Newton without grating assembly (left) and with grating assembly (right).*

tors. Two of the cameras contain 7 individual MOS (Metal-Oxide Semi-conductor) front-illuminated CCD arrays (600× 600 pixel each [231]) referred to as MOS1 and MOS2 (or M1 and M2) cameras respectively, while the last camera contains 12 pn (p-n-junction) back-illuminated CCDs (64× 200 pixel each [226]) and is referred as pn camera. The EPIC-pn camera was specially developed for *XMM-Newton*. The EPIC cameras can perform imaging over a field of view of 30 arcmin diameter (it is 2.5 times that of *Chandra*), are sensitive to photons with energies from 0.1 up to 15 keV and provide moderate energy resolution (E/ΔE ∼20-50). Because of the small sizes of the pixels of the EPIC cameras (1.1 and 4.1 arcsec on the sky for MOS and pn respectively), the angular resolution is determined by the PSF of their mirror modules. The FWHM of the PSF is 6 arcsec allowing to obtain X-ray source positions with accuracies of ∼1-3 arcsec (compared with the 0.3-1 arcsec positional accuracy achieved by *Chandra*). In *XMM-Newton* X-ray source confusion is not significant for observations with exposures ≤100-200 ksec.

The EPIC cameras can be operated in various observing modes [116] [117] [124]. The EPIC CCDs are sensitive to X-rays but also to IR, visible and UV photons. In order to reduce the contamination of the observations, each EPIC camera is equipped with three aluminised optical blocking filters with different thicknesses (named thick, medium and thin). It is also possible to perform observations in an open position, i.e. with no filter at all or in a closed position. However the later is only used for internal calibration purposes.

The telescopes with MOS cameras on their focal plane have a grating assembly (RGA, [50]) that diverts part (∼ 40%) of the incoming radiation focused by the telescopes to a Reflection Grating Spectrometer (RGS). About 44% of the incident light reaches the MOS cameras while the remaining 16% is absorbed by the supporting structures of the RGAs. The RGS instruments perform high resolution (resolving power of $\mathrm{E}/\Delta\mathrm{E} \sim 200-800$) dispersive spectroscopy of bright sources in the soft (from 0.3 to 2.1 keV) energy band.

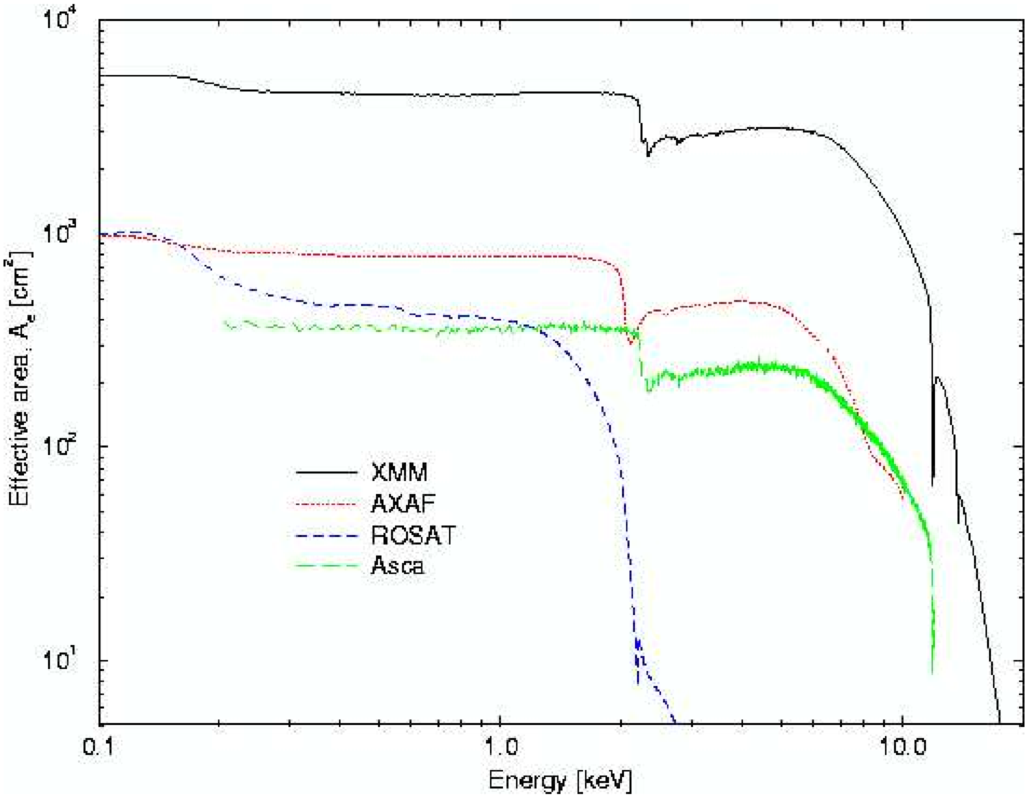

Figure 1.11: *Comparison of the mirror effective areas of recent observatories (taken from* `http : //heasarc.nasa.gov/docs/xmm/about_overview.html`. *It is very clear the greater effective area of the XMM-Newton mirrors over a broad range of energies compared with those of ROSAT, ASCA and even Chandra. Note that AXAF (Advanced X-ray Astrophysics Facility) was the original name for the Chandra observatory).*

1.7.4 Aim of this thesis

In previous sections a brief summary of our current understanding of the nature of the AGN and XRB emission has been given. We focused most of our description to our current knowledge of the nature of the population of AGN, that we now know dominate the XRB emission at medium X-ray fluxes, in particular to the X-ray properties of AGN, because as we have seen, X-rays in AGN are emitted in the innermost regions, close to the central supermassive black hole.

The aim of the work presented in this thesis is to give insight into the X-ray emission mechanisms in AGN. However, in order to do that it is necessary to constrain first observationally the overall X-ray spectral properties of AGN and their dependence with different spectral parameters. Most of our knowledge of the population of AGN is based on detailed studies of local bright objects. Important advances on the properties and cosmological evolution of the population of fainter AGN, which dominate the XRB emission, are being obtained now thanks to population studies of AGN using the latest generation of X-ray observatories, *Chandra* and *XMM-Newton*. However these studies have opened a number of questions on the X-ray properties and cosmological evolution of AGN, to which we will try to give some answers with the X-ray spectral and variability analyses presented in this thesis.

The typical AGN broad band continuum emission is known to have a shape of $\Gamma \sim 1.9$. However a strong dependence of this spectral parameter with X-ray flux has been found in several spectral analysis, including the study presented in Chapter 3. Possible interpretations of this effect are photoelectric absorption and the existence of a population of faint sources which are intrinsically different (flatter spectral slopes). In order to understand the origin of this dependence, which is fundamental to understand the evolution of AGN and the validity of the unified model of AGN, an analysis of a sample of objects with enough signal-to-noise ratio is required, such as the one presented in Chapter 4.

Most spectral analysis of samples of faint AGN are limited by the low signal-to-noise ratio of the data. Therefore it is common to make assumptions on some of the spectral properties of the objects, typically their continuum shape is fixed to the typical value found for type-1 AGN, in order to quantify the emission properties of other spectral components, for example the amount of X-ray absorption. However there are some evidences for the existence of an intrinsic dispersion in the broad band continuum shape of type-1 and type-2 AGN, and we confirm this with the analysis of Chapter 3. It is important to quantify the magnitude of this intrinsic dispersion, as it could be affecting the results of analysis where the continuum shape is fixed during the spectral fitting. However as we will see in Chapter 3, it is difficult to quantify it, as undetected spectral components, such as photoelectric absorption and soft excess emission, can make a significant contribution to the measured dispersion. Thanks to the unprecedented spectral quality of the *Lockman Hole* sources, we can constrain the mean value of the broad band continuum shape and its intrinsic dispersion for faint AGN.

Standard unified models of AGN assume that both type-1 and type-2 AGN are intrinsically the same objects, and that their observed differences are due to absorption. However some spectral analyses suggest that type-2 AGN tend to have flatter continuum slopes than type-1 AGN. Although the effect is believed to be mostly due to photoelectric absorption, a statistical comparison of the overall spectral properties of samples of type-1 and type-2 AGN is required to confirm the origin of the effect, and to test the validity of unified models of AGN.

In the standard unified model of AGN the observed emission properties of AGN, such as the broad band continuum shape and absorption, are not expected to depend on X-ray luminosity and redshift. In order to understand the cosmic evolution of AGN it is also important to understand whether the X-ray spectral properties of AGN evolve with cosmic time. This is also fundamental for the synthesis models of the XRB, the majority of which do not assume spectral cosmic evolution of both type-1 and type-2 AGN populations.

Absorbed AGN are believed to dominate the AGN population at faint fluxes, however the distribution of absorbing column densities, which is an essential ingredient of unification models of AGN, is still not well constrained.

Population studies of AGN are finding a significant fraction of type-1 and type-2 AGN for which the existing correlation between their observed optical and X-ray properties fails. It is important to understand the nature of these sources to test the validity of the unified model of AGN. We use the results of our spectral analyses to quantify the fraction of these objects among type-1 and type-2 objects, and provide further insight into the origin of the observed discrepancies from the analysis of their X-ray emission properties.

We have seen in previous sections that the origin of other spectral components, specially soft excess emission, is still controversial. We will try to give insight into the origin of this spectral component in faint AGN, constraining its emission properties in our samples of AGN.

A complementary way to study the intrinsic properties of both type-1 and type-2 AGN comes from X-ray variability studies of samples of sources. We have carried out a variability study of the *Lockman Hole* objects and compared the flux and variability properties of AGN. We then have tested whether they depend on the X-ray luminosity of the sources and redshift, and whether the same variability properties are observed for type-1 and type-2 AGN populations.

Chapter 2

AGN surveys with the *XMM-Newton* observatory

We have argued in the previous chapter that X-ray population studies are necessary in order to understand the overall X-ray emission properties and cosmic evolution of AGN. The main requirement for these studies is to collect a large enough number of objects. Population and evolutionary studies can be done by combining wide field shallow surveys and deep surveys.

In order to conduct population studies of samples of sources, there is a significant amount of work that must be done before the scientific analysis of the data starts. As all the work presented in this thesis has been obtained using *XMM-Newton* data, I will start this chapter with a detailed description of data from *XMM-Newton*. After that, I will describe the work involved in the reduction and preparation of the data to carry out X-ray surveys of AGN. Then I will describe the techniques and spectral models used to carry out the spectral analyses presented in this thesis. Finally I will describe in detail the AXIS wide field survey and the *Lockman Hole* deep survey, whose data have been used to carry out the population studies presented in the following chapters.

2.1 Reduction of *XMM-Newton* data: the Science Analysis Software

The most relevant "raw" products from an *XMM-Newton* observation which an observer receives and which are archived, are the observation data files (ODF), instrument housekeeping files, radiation monitor files and spacecraft files. A typical ODF contains uncalibrated event files (counts detected in the instruments, with information on their time of arrival, energy and angular position in the sky) from all *XMM-Newton* detectors that were operating during the observation (EPIC cameras, Reflection Grating Spectrometer, Optical Monitor). However ODFs cannot be directly used for scientific data analysis.

The Science Analysis Software (SAS; [68] [85]) is a package that has been developed specifically for the reduction and scientific analysis of *XMM-Newton* data. The SAS has been developed jointly by ESA's *XMM-Newton* Science Operations Centre (SOC)[1] and the *XMM-Newton* Survey Science Centre (SSC)[2]. An important application within the SAS is the reduction pipeline or Processing Pipeline Subsystem (PPS), a set of meta-tasks that, using the latest *XMM-Newton* calibration and ODF files, produces calibrated and cleaned event files, and data products suitable for scientific analysis of the observation.

The SAS tasks are continuously being updated, both due to improvements in their functionality, and on the calibration of the data, and therefore new versions of the software are frequently released (about once per year in 2006). The version of the SAS used for the analysis presented in this thesis were SASv5.3.3 for the work presented in Chapter 3, and SASv5.4 for the work presented in Chapter 4 and Chapter 5.

2.2 EPIC science data

The scientific analysis of EPIC data starts with the calibrated event files (one per EPIC camera) generated by the *XMM-Newton* reduction pipeline. The event files contain all the information about each X-ray count detected by the EPIC detectors during the observation. In general, unless there have been changes in the calibration between the time of the pipeline processing and the time of the analysis, users do not need to create new calibrated event files. We used event files from the reduction pipeline for our studies.

All the data used in this thesis have been obtained with the EPIC cameras operating in imaging mode, i.e. two dimensional angular information is available for the data[3], hence in the following I will describe the information included in the event files of observations taken with the EPIC cameras in imaging mode. This information is organised in columns. EPIC M1 and M2 event files contain 12 columns while pn event files contain 14 columns. The most relevant information included in these files is listed in Table 2.1.

In order to create science products, calibrated event files must be filtered first. The filtering of these files is done on an event-by-event basis. Events with patterns outside the recommended values[4], and artifacts (spurious noise events not created by X-rays) still present in the calibrated event files and for which standard filtering expressions are available need to be filtered out.

A fraction of the observations are affected by periods of high particle background, probably due to soft protons with energies up to 300 keV, scattered by the *XMM-Newton* mirrors and that fall into the X-ray detectors, creating events. They can reduce the Charge Transfer Efficiency (CTE) of the CCDs and degrade their energy resolution. The problem

---

[1] `http://xmm.vilspa.esa.es`

[2] `http://xmmssc-www.star.le.ac.uk`

[3] In timing mode images are made only in one dimension to increase the time resolution of the observation. The EPIC-pn camera can also be used in burst mode, which allows to obtain very high time resolution. The only difference between burst and timing mode is that in the former the source position is not read out.

[4] More than 90% of the detected photons are described as single or double events (see Table 2.1). For observations with the EPIC cameras operating in imaging mode, events with PATTERN$\leq$12 for M1 and M2 (i.e. only single, double, triple and quadruple events) and with PATTERN$\leq$4 for pn (i.e. singles and doubles) are the canonical set of valid X-ray events as they are well calibrated. Events with higher PATTERN codes are highly contaminated by cosmic rays.

Table 2.1: *Description of the most relevant information of each detected event included in an XMM-Newton event file when the EPIC cameras are operating in imaging mode.*

Column Name	Description
TIME	Arrival time (seconds)
RAWX/RAWY	Raw CCD pixel coordinates
DETX/DETY	Position in the focal plane in detector coordinates[a]
X/Y	Position in the tangential plane in the sky relative to the nominal pointing position[b]
PHA	Pulse height analyser or uncorrected event energy channel
PI	Energy[c]
FLAG	Quality flag of the event[d]
PATTERN	Type of event[e]

[a] In units of 0.05 arcsec.

[b] In units of 0.05 arcsec. X/Y are corrected for movements of the satellite during the observation.

[c] PIs are charge transfer efficiency (CTE) corrected and recombined. One PI channel is approximately equivalent to 1 eV.

[d] A value of zero is used for the events with best quality. Events with flags greater than zero are events detected at the edge of a CCD or at the edge of a bad pixel/column. These events may loose part of their charge into these undefined regions and hence their collected charge and energy may be wrong.

[e] This column describes how the charge produced by a photon is distributed over contiguous pixels. If the photon energy is released in one CCD pixel only, the events are described as single and have PATTERN value of zero. If more than one pixel is involved, events can be double (two contiguous pixels), triple (three contiguous pixels) and so on and have PATTERN values above zero.

of background flares is more serious in front illuminated CCDs like those used in the two MOS cameras. During periods of high background the filter wheel is put in a "closed" position to protect the EPIC detectors. Time intervals affected by high background are easy to identify as they are characterised by a large and variable background rate. In order to identify them, light curves (histograms of counts as a function of time) need to be created for each observation and EPIC camera. It is recommended to use only single events with energies above 10 keV to minimise the contribution from bright (and perhaps variable) sources, to guarantee that only the time behaviour of the background of the observation is studied. The light curves are then inspected to search for time intervals with high flaring background. Only periods with constant low count rates should be used.

The recommended values of count rate thresholds above which events are significantly contaminated are 0.35 cts $\sec^{-1}$ for the M1 and M2 data and 1 cts $\sec^{-1}$ for pn data. These have been thoroughly adapted in the data used in this work.

2.3 The *XMM-Newton* standard source detection algorithm

Once calibrated event files are properly cleaned, they can be used to build a list of sources detected in the observation. The SAS contains a standard source detection algorithm for detection of objects on EPIC datasets. This algorithm has been adopted to search for sources in the *XMM-Newton* data used in this work. We describe now the process of source detection in more detail.

X-ray source populations have different observed X-ray spectral properties, specially if their emission comes from different physical processes. Stars and clusters of galaxies for example, have typically soft X-ray spectra and hence both populations are best detected at soft X-rays. Even within the same class of objects a large variety of spectral shapes can be observed as it is the case for AGN: unabsorbed AGN and sources with strong soft excess emission will be best detected at soft X-ray energies, while absorbed AGN, for which their soft X-ray spectra is significantly reduced by photoelectric absorption, will have typically hard X-ray spectra and will be best detected at higher X-ray energies, if they have enough signal. The observed spectrum also depends on the redshift of the sources. For example, signatures of soft excess emission or absorption are more difficult to detect if the objects are at high redshift, because most of the spectral signatures from these components will be shifted outside the spectral window where EPIC is sensitive.

The standard *XMM-Newton* source detection algorithm implemented in the reduction pipeline performs source detection simultaneously on the EPIC data splitted into five energy bands, 0.2-0.5 keV, 0.5-2 keV, 2-4.5 keV, 4.5-7.5 keV and 7.5-12.0 keV. Conducting source detection on narrow energy bands improves significantly the sensitivity of source detection, specially for faint objects that are detected only in one of the energy bands, because for these sources the background level in the broad band (i.e. 0.2-12 keV) increases more rapidly than the signal, thus reducing the contrast of the source with respect to the background. In addition, doing source detection simultaneously in all bands increases the sensitivity of detection on each band and specially in the hard bands, where the effective area of the X-ray telescopes is much lower, because we get information for sources in energy bands where they are not formally detected.

However, although the *XMM-Newton* detectors are sensitive to photons over a broad energy range, the effective area of the X-ray telescopes is a strong function of energy, and decreases significantly above $\sim$4.5 keV. This means that we will detect better objects with X-ray spectra peaking within this interval of energy, and therefore we expect our samples of sources to be biased in favour to AGN with low X-ray photoelectric absorption. This needs to be taken into account when interpreting the results of populations studies of sources detected with *XMM-Newton*.

At the moment, the *XMM-Newton* pipeline carries out source detection on each EPIC camera separately, although the process is exactly the same for each camera. A flow chart

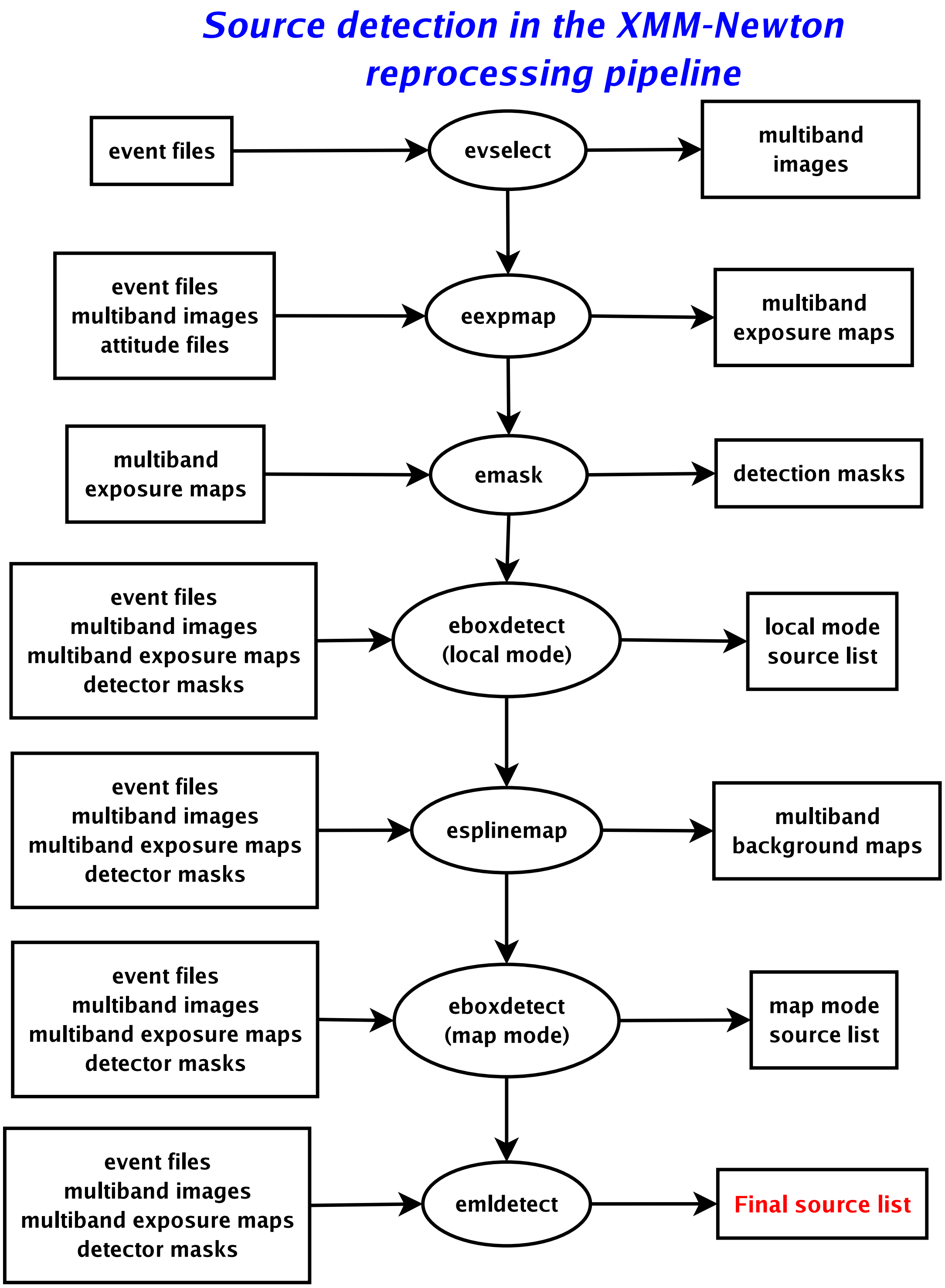

Figure 2.1: *Flow chart showing the standard SAS XMM-Newton source detection algorithm on EPIC data. Source detection produces a list of objects detected on each observation on each camera (see Sec. 2.3 for more details).*

showing the pipeline EPIC source detection is shown in Fig. 2.1:

1. *Multiband X-ray images*: X-ray images on the five *XMM-Newton* standard energy bands are created with the SAS task `evselect`. It is customary to create images with a pixel size of 4 arcsec×4 arcsec.

2. *Multiband exposure maps*: Exposure maps are images in which each pixel holds the effective exposure time at that detector point, corrected by relative efficiency, which includes vignetting, bad pixels and columns, inter-CCD areas, etc. They are created with the SAS task `eexpmap` using the latest calibration information on the spatial quantum efficiency, filter transmission, mirror vignetting (decrease of the effective area of the *XMM-Newton* X-ray telescopes, see Sec. 1.7.1) and FOV. As some of the effects are energy dependent (e.g. the mirror vignetting) one exposure map needs to be created for each image.

3. *Detection masks*: Sometimes we do not want to perform source detection in some areas of the detector (e.g. areas at the edge of the FOV, where the effective exposure is very low, CCD gaps, bad pixels). It is possible to define the area of the images where sources are searched for using the SAS task `emask`. `Emask` creates a detector map, indicating which pixels should be used by source detection.

4. *Sliding box source detection* (local mode): The source detection process starts with the SAS task `eboxdetect`. `Eboxdetect` performs sliding box cell detection (i.e. it searches for regions in the images with high signal-to-noise ratio) in the areas defined by the detector maps. `Eboxdetect` has two different operation modes: local and map detection. The first time `eboxdetect` is ran in local mode. The purpose of the local detection is to provide a list of sources to the next SAS task in the source detection chain, `esplinemap`. `Eboxdetect` gives the significance of detection of a source in terms of a detection likelihood (one per energy band and total), $\mathcal{L} = -\ln p$, where p is the probability of a Poissonian random fluctuation of the background to have caused the observed number of counts in the detection cell. In the standard processing pipeline all sources with total (0.2-12 keV band) detection likelihood[5] above 8 are accepted as positive detections. A detection likelihood of 8 corresponds to a probability of being a random background fluctuation of 3.3×10^{-4}.

5. *Multiband background maps*: Multiband background maps are created for each camera using the SAS task `esplinemap`. `Esplinemap` removes from the input images (using a source brightness dependent cut-out radius) sources detected by `eboxdetect` in local mode. Then it performs a spline fit over the source-free regions to create a background map. `Esplinemap` uses the exposure maps to remove gradients due to spatial variations in the exposure that could cause problems to the spline fits.

---

[5] Total detection likelihoods are obtained by `eboxdetect` using the expression $L = P(n, \sum L_i)$, where P is the incomplete Gamma function, L_i are the likelihoods for each energy band and n is the number of energy bands.

6. *Sliding box source detection* (map mode): `Eboxdetect` is ran a second time in map mode. This time the task searches for sources using the background maps created by `esplinemap`. This improves significantly the source detection sensitivity as compared to the local detection step. All sources with total (0.2-12 keV) detection likelihood above 8 are included in the list of sources produced by `eboxdetect`.

7. *Maximum likelihood fitting*: The final list of sources is obtained with the SAS task `emldetect`. `Emldetect` performs simultaneous maximum likelihood PSF fits to the distribution of counts of the sources detected by `eboxdetect` on each energy band. Free parameters of the fits are the source position and extent[6], count rates and detection likelihoods (one per energy band and total). If source detection is performed in more than one energy band simultaneously, X-ray colours (normalised difference of counts from two energy bands) are calculated for each object. The location is constrained to be the same in all energy bands, while the count rates are the best fit values on each energy band. Source lists produced by `emldetect` contain for each source an identification number and sky position (Right Ascension R.A. and Declination Dec) and error on sky position, and for each energy band (and total band, 0.2-12 keV) counts, count rates and fluxes[7]. The detection likelihoods given by `emldetect` are in the form of "equivalent" detection likelihoods, L_2, in order to allow comparison between source detection runs with different numbers of free parameters. `Emldetect` "equivalent" detection likelihoods are defined as $L_2 = -\ln(1 - P(\frac{\nu}{2}, L'))$ where P is the incomplete Gamma function, n is the number of energy bands (n=1 as only one energy band is involved), ν is the number of degrees of freedom of the fit ($\nu = 2 + n$ if we do not search for extension) and $L' = \sum_{i=1}^{n} L_i$ where $L_i = C_i/2$ and C as given by Cash [35]. For a description of the application of Maximum Likelihood analysis to detection of sources see [46]. All sources with `emldetect` 0.2-12 keV detection likelihoods ≥ 10 are included in the final source list[8].

`Emldetect` does not perform source detection, it only obtains parameters for each object detected by `eboxdetect` using a maximum likelihood fit. However the source detection likelihoods given by `emldetect` "clean" the lists of sources produced by `eboxdetect` from spurious detections. Therefore, as `eboxdetect` is the task that provides the source list of the observation, it is recommended to select a lower detection likelihood threshold in `eboxdetect` to get a source list as complete as possible, and to be sure that it is only `emldetect` the task that filters the source list.

---

[6] At the time of this analysis the SAS processing pipeline was not searching for extended sources.

[7] Count rates are converted to fluxes assuming that all sources have the same spectral shape in the 0.2-12 keV energy band, an absorbed power law with continuum slope Γ=1.7 and absorption $N_H = 3 \times 10^{20}$ cm^{-2}. The conversion factors are different for each EPIC camera and depend on the energy band, the observation mode and the blocking filter used during the observation.

[8] `Emldetect` "equivalent" detection likelihoods in the 0.2-12 keV energy band are obtained from $L_2 = -ln(1 - P(\nu/2, \sum_i L^i))$, where ν is the number of degrees of freedom (number of energy bands+2, i.e. 5+2 for the 0.2-12 keV band) and P is the incomplete Gamma function. The detection likelihoods, L^i, are obtained as explained in Sec. 2.3.

2.4 Building X-ray source lists

The SAS processing pipeline performs source detection separately on each EPIC camera, which means that we usually have three (one per EPIC camera) different source lists for each *XMM-Newton* observation. The geometrical shadowing of half of the sky X-ray emission received by M1 and M2 detectors (deviated to the RGS gratings) makes the observations with the pn camera a factor of two more sensitive than the ones with the MOS cameras overall. Therefore, to optimise the sensitivity of our surveys, we used the pipeline EPIC-pn source lists. For the AXIS survey (see Sec. 2.7) we had sometimes more than one observation for the same field. In these cases we used the EPIC-pn source list from the observation with the longest exposure time. In the case of the *Lockman Hole*, as we will see in more detail in Sec. 2.8, we added the data from each observation (images, background maps and exposure maps) and then we ran source detection on the combined data.

Once we have the source list for each individual observation, we have to inspect individually all of them in order to remove spurious detections still present in the data, in areas of the FOV contaminated by the emission of bright or extended sources (after a careful check we found most detections in such areas to be spurious). As we will see in the next chapters, we are mainly interested in studying the properties of serendipitously detected X-ray sources, hence we also need to exclude from the source lists the targets of the observations. In order to remove these objects we defined circular regions (with radius between 16 to 160 arcsec depending on the brightness and extension of the target) centred on the positions of the targets, and removed from the source lists all sources detected within these regions.

If sources are detected near CCD gaps, the uncertainties in their coordinates and flux may be larger than the statistical uncertainties as given by the pipeline products. In order to get rid of these sources with somewhat uncertain source parameters, we have excluded all sources detected in zones near CCD gaps, by widening the gaps, defined by the detector masks (Sec. 2.3), in size up to the radius that contains 80% of the PSF on each detector point.

EPIC-pn events registered during the readout of the CCDs are known as Out of Time (OoT) events. OoTs have wrong RAWY (raw CCD pixel coordinates, see Table 2.1) values and also wrong energy corrections (the correction for charge transfer inefficiency CTI depends on the distance from the readout node). The effect of OoT on pn images is a bright column along the RAWY direction. At the time of this analysis the source detection process was not accounting for OoTs in the background maps, resulting in a large number of spurious detections in OoT columns. We masked out the area of the images affected by OoTs, when present.

For each field and observation, we examined the images searching for remaining spurious sources, such as detections in hot pixels or bright segments. Hot or bad pixels are pixels with abnormal behaviour, they tend to mimic a signal or yield no signal. They need to be masked out as they might affect the science quality. The visual screening process removed ~10% of the objects from the original source lists in unmasked areas. An example of the results of “cleaning” of the source lists is shown in Fig. 2.2 (top) where a colour codding has been used to show the screening results. Fig. 2.2 (bottom) shows an example of an EPIC-pn detector mask that we used for authomatic screening of sources.

2.5 Extraction of X-ray spectral products

Spectral products need to be extracted for each object, EPIC camera (M1, M2 and pn) and observation. We did the extraction of X-ray spectral products automatically using different SAS tasks. The SAS task `region` provides optimised source and background extraction regions. The source regions were defined as circles centred on the source coordinates with typical radius ~14-30 arcsec depending on the source position within the detector, which corresponds to 70-80% PSF encircled energy radius. The internal background varies over the EPIC detectors, therefore in order to get a good representation of the background on the area where a source is detected, the background spectra should be extracted in a position close to the source. For M1 and M2 data it is recommended to extract background regions at the same off-axis angle as the source positions, and for pn data at the same RAWY positions on the chip. Therefore background regions were defined as annuli centred at the source position with inner radius equal to the source extraction radius[9] and outer radius three times the inner radius. In the cases where there is overlapping of the source extraction regions with nearby sources, then `region` reduces the size of the region in order to eliminate the overlapping. The same process is done if the extraction regions extend outside the FOV. In addition, if nearby sources fall inside the background region they are masked out.

The SAS task `evselect` is used to extract the events within the defined regions. Apart from the spatial filtering, only single and double pn events and single to quadruple MOS

---

[9] Using background extraction regions with inner radius equal to the size of the source extraction region we expect some of the emission of the sources to fall within the background region. In these cases the background flux will be overestimated and therefore the corresponding source count rates given by `Xspec` will be underestimated. We have quantified the magnitude of the effect as follows: let's assume that A_T and A_B are the areas of the source and background extraction regions and that f_T and f_B are the fractions of source counts that fall within each of the extraction regions. If N is the real count rate of the source and b the background count rate per pixel, assuming that the source and background exposure times are the same, the observed count rates within A_T and A_B, T and B are

$$T = b \times A_T + N \times f_T \tag{2.1}$$

and

$$B = b \times A_B + N \times (f_B - f_T) \tag{2.2}$$

The count rate given by `Xspec` within the area of the source is

$$S = T - B \times \frac{A_T}{A_B} = N \times f_T + N \times \frac{A_T}{A_B}(f_T - f_B) \tag{2.3}$$

and the source count rate estimated by `Xspec` will be

$$CR = N \times \left[1 - \frac{A_T}{A_B} \times \left(\frac{f_B}{f_T} - 1\right)\right] \tag{2.4}$$

For a source extraction region r_1=14 arcsec, the on-axis PSF encircled energy fractions are f_T=85% and f_B=97% for an energy of 1.5 keV. In this case the source count rate estimated by `Xspec` will be $CR = 0.98N$. For a value of r_1=30 arcsec, f_T=95.4% and f_B=99.3% and $CR = 0.995N$.

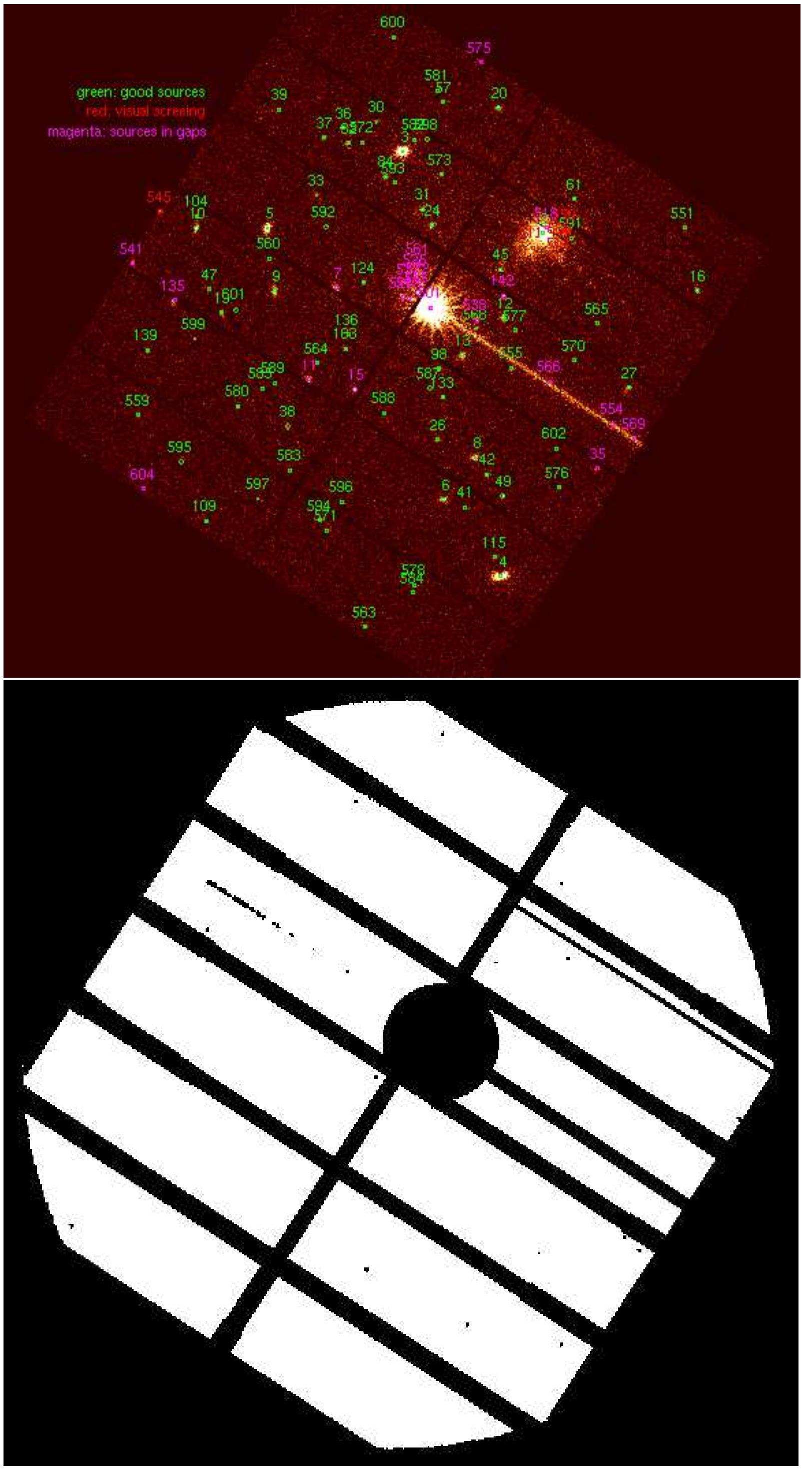

Figure 2.2: *Top: An example of the results of source detection from the SAS reprocessing pipeline. A colour codding has been used to show the results of the screening: green for good sources; magenta for sources falling in bad areas defined in the detector masks; red sources visually screened. Bottom: An example of an EPIC-pn detector mask used for automatic screening of sources with wider CCD chip gaps and the areas affected by the emission from the target (central circle) and OoT events being masked.*

events have been be used. Only events with the highest spectral quality (`FLAG=0`) for EPIC-pn data, and with energies from 0.2 to 12 keV have been used, as this is the energy range where the data is best calibrated. The SAS task `backscale` is used to calculate the sky areas of the source and background extraction regions, because the background needs to be rescaled to the same area as the source when doing the spectral analysis. In order to calculate the areas, `backscale` corrects for overlapping of the regions with CCD gaps and bad pixels. For each source a redistribution matrix file (RMF) and an ancillary response file (ARF) have been computed. These files provide a characterisation of the EPIC detector response necessary for the spectral fitting with `Xspec`. RMF files are created with the SAS task `rmfgen`, and contain the correspondence between detector channels and photon energies. They are discrete functions giving the probability that an incoming photon of energy E is detected in a detector channel I. ARF files contain the effective area of the telescopes and detectors, correcting for counts lost outside the extraction region. They are created with the SAS task `arfgen` that takes into account the effective area of the telescopes (it depends on the position of the source in the detector and energy), filter transmission, CCD quantum efficiency, region and pattern selections, fraction of the PSF encircled in the extraction region (including chip gaps, bad pixels and overlapping outside the field of view) and OoT events for pn data.

2.6 Spectral analysis

The spectral analysis of the X-ray sources presented in this thesis was conducted using the `Xspec` software package (version 11.2) [7]. `Xspec` needs three different files or spectral products: a source spectrum, a background spectrum, and the corresponding instrumental calibration files. The fitting technique that `Xspec` applies to the data requires information on the EPIC detector responses because `Xspec` computes output spectra as it would be seen by EPIC, given an input spectrum model, and compare them to the observed spectra.

The X-ray spectra, *C(I)* (background subtracted spectra), are defined as counts, C, on detector channels, I.

In order to do the fitting with `Xspec` a model spectrum needs to be defined, *f(E)*, that will be described with a set of parameters *f(E,p1,p2,...)*. `Xspec` tries to match this model spectrum to the observed data, *C(I)*, computing predicted count spectra, $C_p(I)$, varying the model parameters. Each predicted spectrum $C_p(I)$ is compared to the observed spectrum, *C(I)*, the comparison being quantified with a fit statistic. Different sets of parameters are tried until the best value fit statistic is obtained. The model parameters that give the best solution are referred as *best-fit parameters* and the corresponding model spectrum is the *best-fit model*. The fit statistic that we have used within `Xspec` is χ^2,

$$\chi^2 = \sum_I (C(I) - C_p(I))^2/(\sigma(I))^2 \tag{2.5}$$

where $\sigma(I)$ is the error in the counts detected in channel I (assuming no background $\sigma(I) = \sqrt{C(I)}$, however in general it is necessary to account for the background and the areas used to extract the source and background spectra). In order to use the χ^2 statistic (that assumes Gaussian statistics) we have to group first the X-ray spectra to be sure that each point in the data contains enough number of counts to ensure gaussianity.

The use of the χ^2 statistic for the spectral fitting allows to quantify the *goodness of fit* of the model that for the χ^2 is given by the incomplete Gamma function [197]. The best fit model corresponds to the minimum value of χ^2. As a rule-of-thumb, a reasonably good fit is achieved when $\chi^2_\nu \sim 1$ ($\chi^2_\nu \equiv \chi^2/\nu$ is the reduced χ^2, where ν is the number of degrees of freedom of the fit). We also want to obtain for each fitted parameter the interval where we know with a given confidence that the true value of the parameter lies. Confidence intervals are calculated for each parameter varying the value of the parameter until a desired $\Delta\chi^2$ is obtained (depending on the number of parameters on which we want to obtain a confidence region on, a value $\Delta\chi^2$ corresponds to a well defined confidence level).

The sources that we have studied are faint (with typical spectra with ~100 background subtracted counts in most cases) and therefore in order to maximise the signal-to-noise ratio of the data, we have combined M1 and M2 spectral products. Merged source and background spectra were obtained by adding the individual spectra. For the fields with more than one observation, we co-added all data from the same instrument, and further co-added all MOS data into single spectra (see Appendix D.1). MOS and pn data have not been merged because of their different response matrices[10].

The spectral analysis has been carried out by fitting simultaneously MOS and pn spectra, forcing the models to have the same parameters in both instruments, including the normalisation (given the quality level of our data we do not expect significant calibration mismatches between instruments to bias the results of the fits). We quantified the results of the spectral fits in terms of the null hypothesis probability P(χ^2) , i.e., the probability that the observed spectrum is derived from the model under scrutiny. We consider a model a bad fit if P(χ^2) is less than 5%.

2.6.1 Spectral models

In this Section I will describe the different spectral models that have been used to carry out the work presented in this thesis. A definition of the different composite models used for our spectral fitting is shown in Table 2.2, while the definition of spectral model components is shown in Table 2.3.

We started the analysis using a spectral model with one emission component, a power law (`powerlaw` model in `Xspec`) to fit the broad band continuum emission of our sources. To account for the effect of the Galactic absorption along the line of sight, a fixed photoelectric absorption component (`phabs` model in `Xspec`) has been included in this model, hereafter `model A`. This model has two free parameters, the normalisation and spectral slope of the continuum. The Galaxy H column density values for each field, N_H^{Gal}, were extracted from the HI map of Dickey & Lockman [52].

An indication of excess absorption above the Galactic value comes from obtaining a flat spectral slope when using `model A`. In order to search for sources with excess absorption, we defined a spectral model with two local absorbers, the first one, representing the Galactic

---

[10] For more details see *XMM-Newton* users handbook at `http://xmm.vilspa.esa.es`.

Table 2.2: *Definition of the spectral models used in this work.*

Model	`Xspec` definition
`model A`	`phabs` × (`powerlaw`)
`model B`	`phabs` × `phabs`(`powerlaw`)
`model C`	`phabs` × `zphabs`(`powerlaw`)
`model D`	`phabs` × (`zbbody` + `powerlaw`)
`model E`	`phabs` × (`zbbody` + `zphabs`(`powerlaw`))
`model F`	`phabs` × (`zpcfabs`(`powerlaw`))

`power law`: power law; `phabs`: photoelectric absorption; `zphabs`: photoelectric absorption at the sources' rest-frame; `zbbody`: black body emission at the sources' rest-frame; `zpcfabs`: partial covering at the sources' rest-frame.

absorption, having a fixed column density while the column density of the second absorber, N_H^{obs} is left free to vary. Hereafter we will refer to this model as `model B`. Note that, in broadly binned moderate signal-to-noise spectra like the ones used for our analysis, the term that quantifies the intrinsic absorption is essentially indistinguishable from an absorber with column density $\sim N_H^{obs}(1+z)^{2.7}$ [14] [134] at the redshift of the source, since absorption edges are not detected

`Model B` has three free parameters, the normalisation and spectral slope of the powerlaw continuum and the equivalent absorbing column at redshift zero, N_H^{obs}.

As an alternative, more physical parameterisation of the absorbing column for sources already identified (and therefore with known redshifts), we instead fitted the excess photoelectric absorption at the redshift of the sources (`zphabs` in `Xspec`). We will refer to this model as `model C` hereafter. This model has three free parameters, the normalisation, the continuum spectral slope, Γ, and the rest frame absorption, N_H^{intr}. The absorbing column densities, N_H^{Gal}, N_H^{obs} and N_H^{intr} are parameterised in terms of Hydrogen atoms per cm^2 integrated along the line of sight to the X-ray source.

Two different spectral models have been used to fit the observed signatures of soft excess emission. We first tried to fit the observed spectral signatures with a thermal black body spectrum (`zbbody` model in `Xspec`). We will refer to a model with a power law and black body components (the black body at the rest-frame of the source) both absorbed by the Galaxy as `model D`, while we will refer to a model with an absorbed (rest-frame) power law and a black body component all absorbed by the Galaxy, as `model E`. For all sources where the thermal model did not provide a good representation of the data, we obtained acceptable fits to the soft excess emission signatures with a partial covering model (`zpcfabs` model in `Xpsec`). We will refer to the model where soft excess emission is fitted with a partial covering model as `model F` (see Table 2.2).

Due to the limited spectral resolution of our data, signatures of line emission were fitted with a Gaussian line profile (`zgauss` model in `Xpsec`). However, the signal-to-noise ratio of

Table 2.3: *Definition of the emission model components*[a] *use for the spectral fits in this work.*

Model	Definition	Normalisation
Power law[b]	$A(E) = K\,(E/1\,\mathrm{keV})^{-\Gamma}$	$K[\mathrm{photons\,cm^{-2}\,s^{-1}\,keV^{-1}}]$
Phot. abs.[c]	$M(E) = e^{-\mathrm{N_H}\sigma(E)}$	*N/A*
Partial covering[d]	$M(E) = f\,e^{-\mathrm{N_H}\,\sigma(E(1+z))} + (1-f)$	*N/A*
Blackbody[e]	$A(E) \propto \frac{K\,(E(1+z))^2\,dE}{(kT)^4\,e^{(E(1+z)/kT)}-1)}$	$K = \frac{L_{39}}{D_{10}^2}[\mathrm{erg\,s^{-1}\,cm^{-2}}]$
Gaussian[f]	$A(E) = \frac{K}{\sqrt{2\,\pi\,\sigma^2}}\,e^{(\frac{E\,(1+z)-E_c}{\sqrt{2}\sigma})^2}$	$K[\mathrm{photons\,cm^{-2}\,s^{-1}}$ in the line]

[a] `Xspec` additive models, i.e. models representing sources of emission are represented as $A(E)$ while multiplicative models are represented as $M(E)$.
[b] We use the power law photon number index, Γ (dimensionless) to quantify the shape of the broad band continuum. Its relation with the energy index is $\alpha = \Gamma$-1.
[c] $\sigma(E)$ is the energy dependent photoelectric cross-section for photoelectric absorption of soft X-rays given by Morrison & McCammon [168] assuming solar abundance of metals; $\mathrm{N_H}$ is the neutral hydrogen column along the line of sight.
[d] $\sigma(E)$ is the energy dependent photo-electric cross-section, f is the covering fraction [11] ($0 < f \leq 1$) and $\mathrm{N_H}$ is the intrinsic absorption column density. [e] kT is the rest-frame temperature of the emitting plasma in units of keV; the normalisations K = L39/(D10)^2, where L39 is the source luminosity in units of $10^{39}\,\mathrm{erg\,s^{-1}}$ and $D10$ is the distance to the source in units of 10 kpc.
[f] E_c and σ are the centroid and width of the line in rest-frame units of keV and K is the intensity of the line in units of $\mathrm{photons\,cm^{-2}\,s^{-1}}$.
E refers to observed photon energies while $E(1+z)$ if used to refer to rest-frame energies.

most of the spectra analysed is not hight enough as to detected line emission signatures. In the few objects were this spectral component was detected, all sources from the *Lockman Hole* survey (see Sec. 4.5.4), the Gaussian model was added to the spectral modes A-F of Table 2.2.

The F-test[12] has been applied to test the significance of additional model compo-

---

[12] When additional spectral components are added to a model the quality of the fit improves. However we only accept the detection of additional spectral components if the improvement in the quality of the fit is significant. To search for these cases we used the F-test, that uses the statistic $F_\chi = [\chi^2(m) - \chi^2(m+1)]/[\chi^2(m)/N - m - 1]$, to compare the χ^2 of the fits corrected for the number of degrees of freedom of each fit and gives the probability of detection of the extra model component. N is the number of data points, m and $m+1$ are the free parameters of the fits and $\chi^2(m)$ and $\chi^2(m+1)$ are the corresponding values of the χ^2 statistic of the fits.

nents, with an adopted significance threshold of 95%. As it is shown in Protassov et al.(2002) [199], if the conditions to use the F-test statistic are not satisfied, the false positive rate might differ from the value expected for the selected confidence level. One of the conditions that must be satisfied is that the null values of the additional parameters should not be in the boundary of the set of possible values of the parameter. We are using the F-test to calculate the significance of detection of absorption (see Sec. 3.3.2), and one of the possible values of the absorbing column is zero. Hence, because one of the conditions for using the F-test are not satisfied, the fraction of false positives in our spectral fits might differ from the 5% expected from the selected confidence level. To calculate this fraction, we carried out simulations of unabsorbed spectra, and then calculated the number of cases where we detected absorption with a confidence level above 95%. We detected absorption in $\sim 2\%$ of the simulated spectra, a value consistent with the expected false positive rate.As the fraction of false positive rates obtained from the simulations is not significantly different from the expected value, we decided to be conservative, and hence, we continued assuming that 5% was still the expected false positive rate.

2.7 The AXIS (An *XMM-Newton* International Survey)

The first of the population studies presented in this thesis was carried out using data from the AXIS wide field medium survey.

Thanks to its large collecting area and large FOV every new *XMM-Newton* observation detects ~30-150 serendipitous sources, most of them being detected for the first time. The *XMM-Newton* Survey Science Centre (SSC) was appointed by *ESA* in 1996 for the scientific exploitation of the *XMM-Newton* serendipitous sky survey. The SSC is an international collaboration of 10 european institutions including the Instituto de Física de Cantabria (IFCA) and led by the University of Leicester. One of the main responsibilities of the SSC is the follow-up and identification (XID) programme [243] for the *XMM-Newton* serendipitous sky survey. The XID programme has two main components:

1. *Core programme*: To provide optical imaging and spectroscopic identifications of large enough well defined samples of sources with fluxes $\geq 10^{-13}\,\mathrm{erg\,cm^{-2}\,s^{-1}}$ (bright sample), $\geq 10^{-14}\,\mathrm{erg\,cm^{-2}\,s^{-1}}$ (medium sample) and $\geq 10^{-15}\,\mathrm{erg\,cm^{-2}\,s^{-1}}$ (faint sample) over a range of Galactic latitudes.

2. *Imaging programme*: Deep optical/IR imaging of a much larger fraction of objects, providing optical magnitudes and colours necessary for statistical identification of the sources.

An important fraction of the XID observing time was awarded by the AXIS programme (An XMM-Newton International Survey)[13] [11], led by IFCA (PI: X. Barcons), in two periods of time from 2000/2001 and 2001/2002 under the Canary Islands International Time Project (ITP) scheme. AXIS made use of the facilities of the Observatorio del Roque de los Muchachos.

---

[13] `http://venus.ifca.unican.es/~xray/AXIS/`

The AXIS survey is a large (total solid angle of $\sim 3.5\,\mathrm{deg}^2$) and medium to deep (0.5-10 keV flux in the range $\sim 10^{-15} - 10^{-12}\,\mathrm{erg\,cm^{-2}\,s^{-1}}$) survey, covering the fluxes where the dominant population of the cosmic X-ray background emission resides.

In order to carry out the first analysis presented on this thesis we selected 25 *XMM-Newton* observations from the AXIS project. This guarantees that all the observations have been followed-up in the optical, and therefore that we have enough optical spectroscopic identifications to obtain information on the spectral properties of representative samples of identified sources. I was an active participant in all aspects of the AXIS project including planning and execution of optical imaging and spectroscopy runs and in the reduction and analysis of the data. However my major contribution to the AXIS project was the compilation of "cleaned" X-ray source lists of the observations and the extraction of the X-ray spectral products of the sources.

The list of *XMM-Newton* selected observations is shown in Table 2.4 together with the details of each observation.

The final X-ray list of sources was built following the standard procedures described in previous sections. The spectral products of the selected sources were obtained following the recipe described in Sec. 2.5. The total number of sources detected in the 25 AXIS fields after the screening process (see Sec. 2.4) was 2145. In order to use the χ^2 minimisation technique during the spectral analysis we grouped the spectra, requiring a minimum of 10 counts per bin. As our sources are typically faint we imposed a minimum quality in the spectra: we used only sources having grouped spectra with a total number of bins (MOS+pn)$\geq$5 and a total number of background subtracted counts (MOS+pn)$\geq$50. We applied these quality filters to the spectra of our sources to ensure that we have data with enough quality for the spectral analysis. This reduced the sample of AXIS sources suitable for our analysis from 2145 to 1137.

2.7.1 Optical spectroscopic identification of AXIS sources

Because of the large number of objects involved in the AXIS survey, identification is an extensive effort. The 25 selected fields selected for our survey work have been followed-up in the optical band within the AXIS project, and continuing work at other ground based facilities, mainly the Centro Astronómico Hispano Alemán in Calar Alto and ESO's Very Large Telescope (VLT) in Chile and the Russian SAO 6-m telescope.

The optical observations consist of high quality multicolour imaging and optical spectra of the brightest sources. This is an ongoing process, whose first results were already presented by Watson et al.(2001) [243] and Barcons et al.(2002) [11]. The full catalogue of sources will be published in Carrera et al.(2006) [33] and the final identification list in Barcons et al.(2006) [13]. The full list of identified sources will be made available via the *XMM-Newton* Science Archive when completed down to a 0.5-4.5 keV flux of $2 \times 10^{-14}\,\mathrm{erg\,cm^{-2}\,s^{-1}}$ [13] [33]).

Table 2.4: Observational details of *XMM-Newton* selected fields.

Field (1)	R.A. (2)	Dec (3)	b (4)	N_H^{Gal} (5)	Rev/Obs Id (6)	Filter (7) M1/M2/pn	GTI (ksec) (8) M1/M2/pn	N_{tot} (9)	N_{good} (10)	N_{id} (11)
A2690	00:00:30.3	-25:07:30.0	-78.90	1.84	0088/0125310101	M/M/M	19/19/21	88	82	4/4
EQ Peg	23:31:50.0	+19:56:17.0	-39.14	4.25	0107/0112880301	Tck/Tck/Tck	14/14/12	41	37	10/7
CL0016+16	00:18:33.0	+16:26:18.0	-45.54	4.07	0194/0111000101	M/M/M	31/31/29	98	86	16/15
					0194/0111000201	M/M/M	5/5/3			
G133-69 pos 2	01:04:00.0	-06:42:00.0	-69.35	5.19	0104/0112650501	Th/M/Th	23/23/18	69	62	17/14
G133-69 pos 1	01:04:24.0	-06:24:00.0	-68.68	5.20	0188/0112650401	Th/M/Th	23/23/20	59	55	5/5
SDS-1b	02:18:00.0	-05:00:00.0	-59.75	2.47	0118/0112370101	Th/Th/Th	47/48/40	138	131	11/11
					0119/0112371001	Th/Th/Th	51/51/43			
SDS-3	02:18:48.0	-04:39:13.0	-59.35	2.54	0121/0112370401	Th/Th/Th	21/21/15	75	69	2/2
					0121/0112371501	Th/Th/Th	7/7/4			
SDS-2	02:19:36.0	-05:00:00.0	-58.91	2.54	0120/0112370301	Th/Th/Th	50/50/40	136	126	6/6
Mkn3	06:15:36.3	+71:02:15.0	22.72	8.82	0158/0111220201	M/M/M	54/54/44	125	106	21/20
MS0737	07:44:04.5	+74:33:49.5	29.57	3.51	0063/0123100101	Th/Th/Th	39/39/20	83	77	10/8
					0063/0123100201	Th/Th/Th	19/19/20			
CL0939+472	09:43:00.0	+46:59:30.0	48.88	1.24	0167/0106460101	Th/Th/Th	49/49/43	134	120	4/4
S5 0836+716	08:41:24.0	+70:53:41.0	34.43	2.98	0246/0112620101	M/M/M	4/4/25	98	70	10/8
B2 1028+31	10:30:59.1	+31:02:56.0	59.79	1.94	0182/0102040301	Th/Tck/Th	26/26/23	99	86	0/0
B2 1128+31	11:31:09.4	+31:14:07.0	72.03	2.00	0175/0102040201	Th/Tck/Th	19/23/13	65	58	13/12
Mkn205	12:21:44.0	+75:18:37.0	41.67	3.02	0075/0124110101	M/M/M	50/50/37	86	78	16/16
MS1229.2+6430	12:31:32.0	+64:14:21.0	53.05	1.98	0082/0124900101	Th/Th/Th	34/34/29	103	89	0/0
HD 117555	13:30:47.0	+24:13:59.0	80.67	1.16	0199/0100240101	M/M/M	29/29/25	139	127	11/11
					0205/0100240201	M/M/M	36/36/33			
UZ Lib	15:32:23.0	-08:32:05.0	36.57	8.97	0210/0100240801	M/M/M	23/23/23	61	55	5/5
PKS 2126-158	21:29:12.2	-15:38:41.0	-42.39	5.00	0255/0103060101	M/M/M	22/22/16	45	40	7/7
PKS 2135-147	21:37:45.2	-14:32:55.4	-43.85	4.70	0254/0092850201	M/M/M	15/16/28	88	77	14/11

Field (1)	R.A. (2)	Dec (3)	b (4)	N_H^{Gal} (5)	Rev/Obs Id (6)	Filter (7)	GTI (ksec) (8)	N_{tot} (9)	N_{good} (10)	N_{id} (11)
						M1/M2/pn	M1/M2/pn			
MS2137-23	21:40:15.2	-23:39:41.0	-47.50	3.50	0254/0008830101	Th/Th/Th	13/14/10	50	43	6/4
PB5062	22:05:09.8	-01:55:18.0	-43.28	6.17	0267/0012440301	Th/Th/Th	31/31/28	97	87	9/9
LBQS 2212-1759	22:15:31.6	-17:44:05.7	-52.92	2.39	0355/0106660401	Th/Th/-	33/33/-	199	177	10/10
					0355/0106660501	Th/Th/Th	8/5/8			
					0356/0106660601	Th/Th/Th	103/103/91			
PHL 5200	22:28:30.4	-05:18:55.0	-49.97	5.26	0269/0100440101	Tck/Tck/Tck	45/45/43	137	121	14/13
IRAS22491-18	22:51:49.4	-17:52:23.2	-61.42	2.71	0267/0081340901	M/M/M	22/22/20	92	86	1/1

Columns are as follows: (1)*XMM-Newton* field name. (2),(3) pointing coordinates of the fields in right ascension and declination (J2000). (4) Galactic latitude in degrees. (5) Galactic absorption in the direction of the field in units of $10^{20}\,\mathrm{cm}^{-2}$. (6)*XMM-Newton* revolution number and observation identifier. (7) M1/M2 and pn blocking filters[a] used for the observation. (8) M1/M2/pn good time intervals (GTI) after removal of periods of the observation affected by high background flares. (9) Number of sources detected in the FOV before screening. (10) Number of sources detected in the FOV after screening. (11) Number of sources after screening with optical identification/number of sources after screening with optical identifications and fulfilling the spectral quality filters.

[a] Blocking filters: Th: Thin at 40nm A1; M: Medium at 80nm A1; Tck: Thick at 200nm A1

The objects were classified using the criteria defined in Sec. 1.4.5. In this section we explained that AGN showing broad optical emission lines in their spectra are traditionally classified as type-1 AGN or broad line AGN. For the AXIS survey we used the term broad line AGN to refer to these sources; however for the *Lockman Hole* type-1 AGN was used. In this thesis we will use type-1 AGN to refer to both AXIS BLAGN and *Lockman Hole* type-1 AGN. As we will see in next chapter, where the X-ray spectral analysis of AXIS sources is presented, we found all sources classified as NELG to have X-ray luminosities (corrected for absorption) $\geq 10^{43}\,\mathrm{erg\,s^{-1}}$, and therefore X-rays confirm that they all harbour an AGN. In this thesis we will refer to them as type-2 AGN to use the same naming convention as for *Lockman Hole* type-2 AGN.

At the time of this analysis $\sim$11% (232) of the sources included in our initial X-ray source list were identified via optical spectroscopy[14] 149 ($\sim$64%) being BLAGN, 32 ($\sim$14%) NELG, 10 ($\sim$4%) ALG, 40($\sim$17%) Stars and 1 BL Lac. Two more identifications in one of the fields (*XMM-Newton* name A2690) were obtained from the literature [190].

Since the time when the analysis presented in this thesis was carried out, there have been a further optical identifications of AXIS sources. While the identifications of BLAGN and NELG have not changed, the optical identification of 9 out of the 10 sources initially classified as ALG has changed (most of them have turned out to be BLAGN). Therefore in Chapter 3 where we present the results of the analysis of AXIS objects, we have not included any results regarding the sample of ALG.

2.8 The *Lockman Hole* deep survey

The second population study presented in this thesis was carried out using the data from the *XMM-Newton* deep survey in the direction of the *Lockman Hole* field. Deep surveys are carried out by conducting very long observations over a small solid angle, and therefore these surveys are sometimes termed *pencil beam surveys*. Thanks to the much longer integration times involved, and because the density of sources in the X-ray sky increases as we go to fainter fluxes, these surveys can detect large number of objects over very small solid angles, providing better quality X-ray spectra. Deep surveys are usually carried out over sky regions with extensive coverage at other wavelengths. However, as these surveys are more efficient in detecting fainter objects, which will be also fainter in the optical, the identification of these objects is more difficult and requires larger optical telescopes.

The *Lockman Hole* field, centred on the sky position R.A.: 10:52:43 and DEC: +57:28:48 (J2000) (the Galactic absorbing column density in this direction is minimal $5.7\times10^{19}\mathrm{cm}^{-2}$ [133]) is one of the sky regions best studied over a very wide range of wavelengths including X-rays. It was selected for the deepest X-ray observations carried out by *ROSAT* in the soft band [107], and for the deepest observation carried out so far with *XMM-Newton*. The *XMM-Newton* deep survey in the *Lockman Hole* is made of 17 different observations obtained from 2000 to 2002. The observations give a total exposure time (after removal

---

[14] The fraction of sources with available optical identifications varied significantly among observations from $\sim$1.4% to $\sim$39% except for one field (*XMM-Newton* name MS1229) for which no optical identifications were available at the time of our analysis

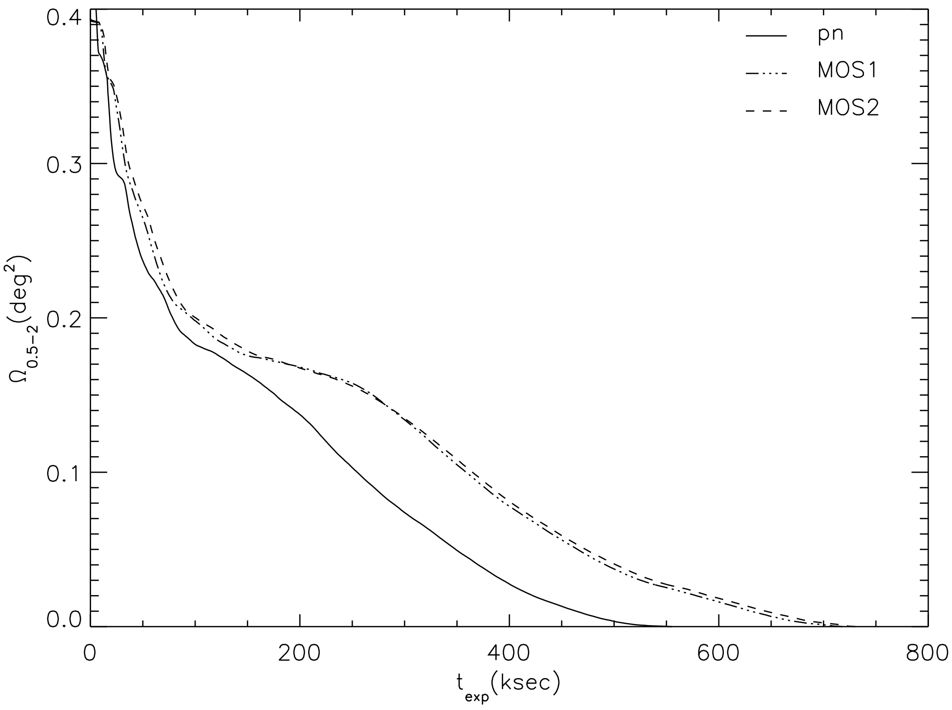

Figure 2.3: *Solid angle ($\Omega\,(t)$) in units of deg^2 covered by M1, M2 and pn detectors as a function of the exposure time (after removal of background flares) in the 0.5-2 keV band. $\Omega\,(t)$ was obtained using the 0.5-2 keV exposure maps of the total observation of each EPIC camera as is defined as the total area where the exposure $\geq$t.*

of periods of high background) of ~850 ksec for M1 and M2 data and ~650 ksec for pn data, that was accumulated during the science verification phase, First Announcement of Opportunity (AO1; PI: X. Barcons) and Second Announcement of Opportunity (AO2; PI: G. Hasinger). The solid angle of the total observation as a function of the exposure time[15] is plotted in Fig. 2.3.

Using the Science Verification Data, with a total integration time of 190 ksec, Hasinger et al.(2001) [106] presented the results of source detection and flux distribution of sources in different energy bands while Mainieri et al.(2002) [140] conducted an X-ray spectral analysis of the 98 objects in the field with more than 70 background subtracted counts in the 0.5-7 keV band. The sample included 38 type-1 AGN, 15 type-2 AGN and 34 unidentified sources. Worsley et al.(2004; 2005) [248] [249] used the total set of *XMM-Newton* observations to calculate the fraction of unresolved XRB in different energy bands. They found that the fraction of XRB resolved into discrete sources decreases significantly

---

[15] The solid angle for a value of t was obtained summing the number of pixels in the exposure maps of the total observation with a value $\geq$ t.

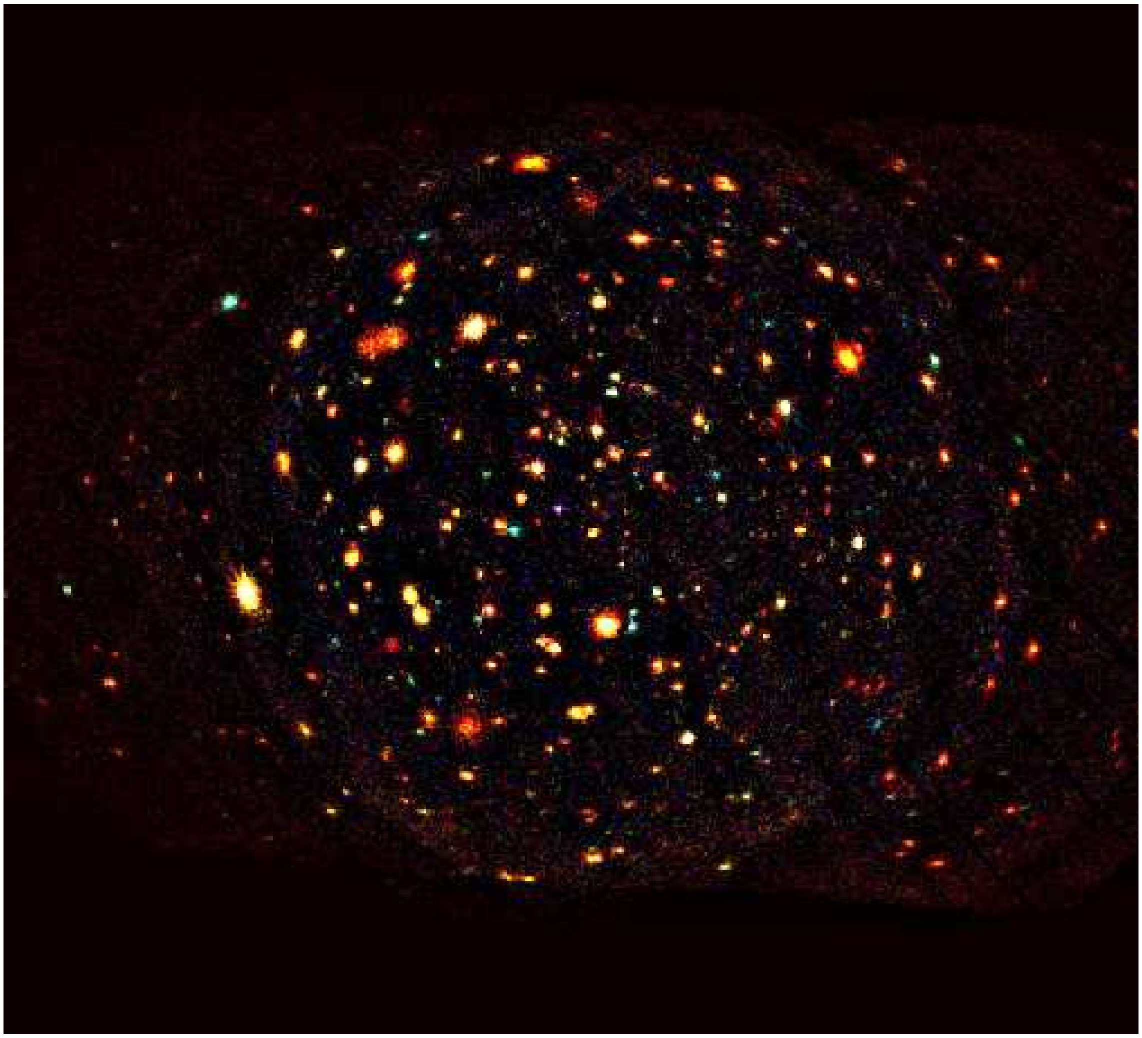

Figure 2.4: *Combining the images from all EPIC cameras, the XMM-Newton observations in the Lockman Hole provide the deepest X-ray survey of this region. Red, green and blue correspond to the 0.5-2, 2-4.5 and 4.5-10 keV energy bands, respectively. More than 60 new sources are detected in the 4.5-10 keV band alone (Image courtesy of G. Hasinger, MPE Garching, Germany and ESA).*

with energy and specially above 5 keV. Finally Streblyanska et al.(2005) [225] conducted a detailed study of the Fe Kα emission in the stacked spectra of sources identified as type-1 and type-2 AGN. They found indications of broad relativistic lines in the stacked spectrum of both type-1 and type-2 AGN. The results from this thesis on the spectral analysis of the brighter sources [153] and X-ray variability of the *Lockman Hole* will be presented in Chapters 4 and 5 respectively.

In order to build the X-ray list of sources for the total observation of the field, we had to follow a different method than the one used to build the AXIS X-ray source list, as

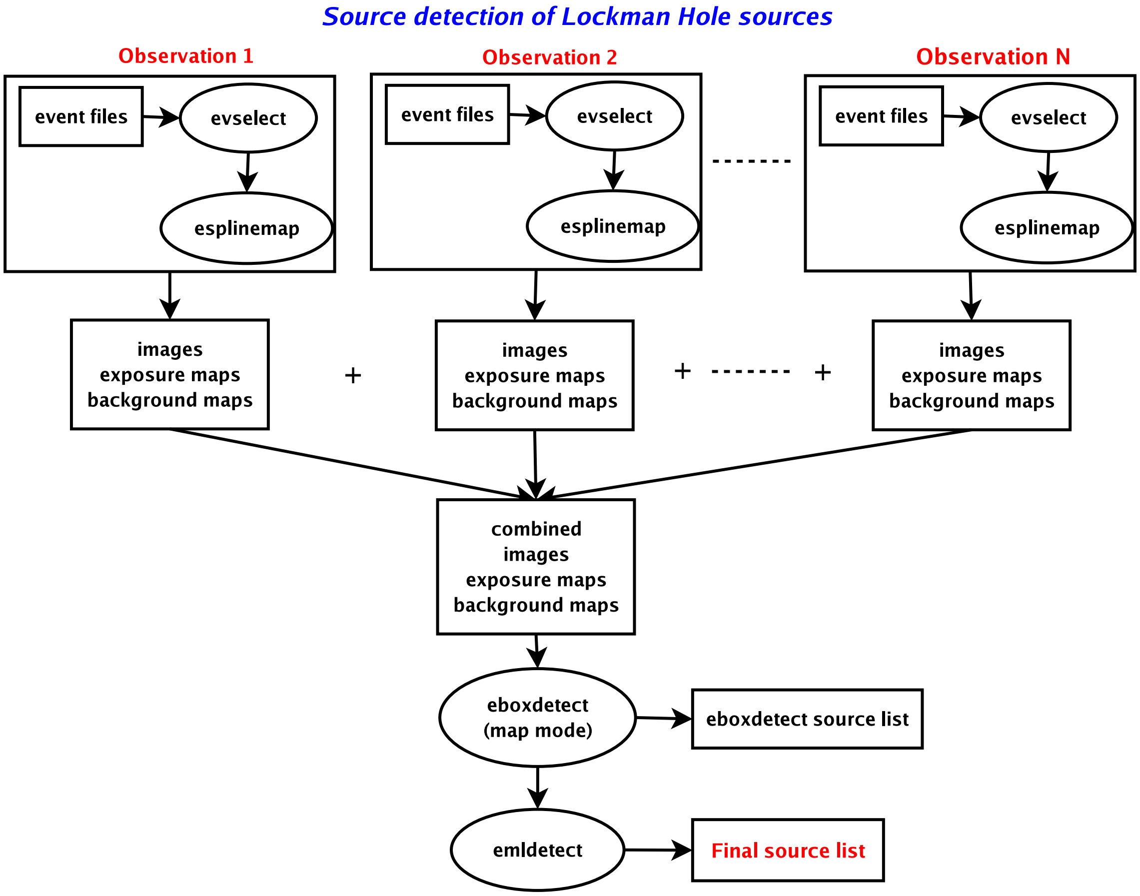

Figure 2.5: *Flow chart showing how we obtained the source list of the total XMM-Newton observation in the Lockman Hole. See Sec. 2.8 for more details.*

in this case all observations correspond to the same field. A flow chart showing source detection in the *Lockman Hole* is shown in Fig. 2.5.

The approach that we followed was to first extract images, exposure maps and background maps for each individual observation, EPIC detector and energy band. Then we combined the products to obtain images, exposure maps and background maps for the total observation for each detector and energy band. We ran `eboxdetect` in map mode to provide an initial list of objects and then `emldetect` to give a final list of sources. We carried out source detection independently on the data from each EPIC detector. However as pn data gave the deepest observation of the field we used the pn source list. We cross-correlated pn sources with the ones detected with each MOS detector and found that only one faint object was detected with M1 and M2 detectors but not with pn (probably because it was very close to a brighter object and was not resolved by source detection on pn data). We added this object to the X-ray source list. We then carried out a visual screening of the sources to remove spurious detections. The final (after visual screening) number of objects that we detected in the total *XMM-Newton* observation of the *Lockman Hole* was

268. A multicolour image of the *Lockman Hole* as seen by *XMM-Newton* combining all the data from the EPIC cameras is shown in Fig. 2.4.

We obtained MOS and pn co-added spectra[16] for each object following the method described in Appendix D.1. From the sample of sources we selected for our analysis the 123 brightest sources, all having more than 500 MOS+pn background subtracted counts in the 0.2-12 keV band. This allows to carry out a more detailed analysis of their X-ray emission properties.

2.8.1 Optical spectroscopic identification of *Lockman Hole* sources

A large fraction of the X-ray sources that were detected with the *ROSAT* satellite in the *Lockman Hole* have already been identified through optical spectroscopy [130] [216]. These sources were detected in the 0.5-2 keV energy range, and therefore the optical identification is expected to be biased against absorbed sources. These optical identifications go as deep as R$\sim$24. Because we are only studying the brightest sources in the field we do not expect the identifications in our sample to be significantly affected by the bias against absorbed sources.

The *XMM-Newton* observations cover a larger solid angle than *ROSAT* observations and find additional sources due to the superb high energy response of the EPIC detectors. Therefore we still do not have optical identifications for most of these newly detected *XMM-Newton* sources. However, for 8 of these objects optical spectra have been obtained with the LRIS and Deimos instruments at the Keck telescopes in 2001, 2003, and 2004 (PI: M. Schmidt and P. Henry).

To be consistent with the *ROSAT* optical spectroscopic identifications, the same criteria to differentiate between type-1 and type-2 AGN was used as described in detail by Schmidt et al.(1998) [216] and in Sec. 1.4.5. Classification of Narrow Line Seyfert 1 galaxies (NLSy1) was only possible for bright nearby objects. Hence, we cannot be sure that the optical classification criteria used to separate type-1 and type-2 AGN in our sample has excluded all NLSy1 from the sample of type-2 AGN. However, based on the observed X-ray properties of our sources, we do not expect this to affect the main conclusions of our study.

At the time of this analysis, 74 ($\sim$60%) of the selected sources in the *Lockman Hole* had optical spectroscopic identifications. Of these, 46 were classified as type-1 AGN and 28 as type-2 AGN.

2.9 Comparison of the AXIS and *Lockman Hole* surveys

One of the major differences between *wide field shallow surveys* and *deep surveys* is the signal-to-noise of the X-ray spectra of the sources. This is evident from Fig. 2.6 where we compare the distribution in 0.2-12 keV source counts (background subtracted) of the spectra of AXIS and *Lockman Hole* sources. For AXIS sources we only analysed spectra having (MOS+pn) total background subtracted counts above 50 while for *Lockman Hole* sources we used a threshold of 500 (MOS+pn) counts.

---

[16] Hereafter we use the term “co-added spectra“ to refer to the “time averaged spectra” of the sources.

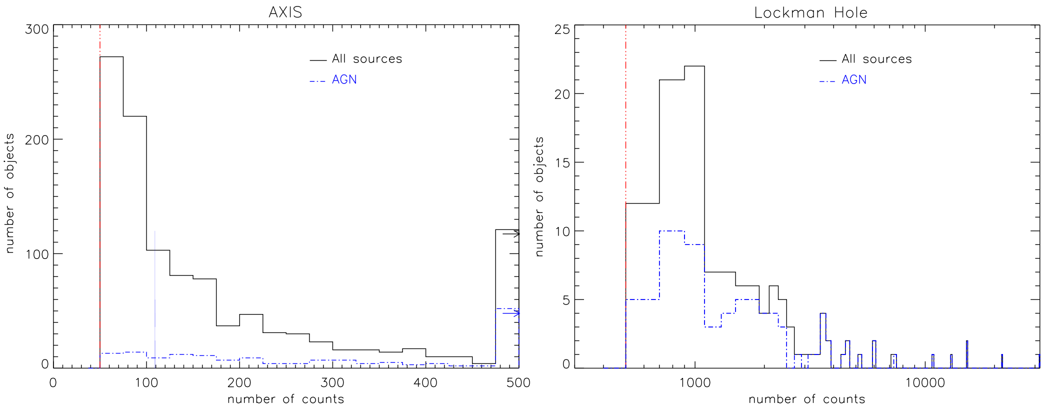

Figure 2.6: *Distributions of 0.2-12 keV background subtracted counts (MOS+pn) for AXIS (left) and Lockman Hole (right) sources. Solid histogram for all sources and dot-dashed histogram for AGN. The vertical line indicates the quality threshold applied to the X-ray spectra. We have studied AXIS sources if their spectra have more than 50 (MOS+pn) background subtracted counts and Lockman Hole sources with spectra having more than 500 (MOS+pn) background subtracted counts.*

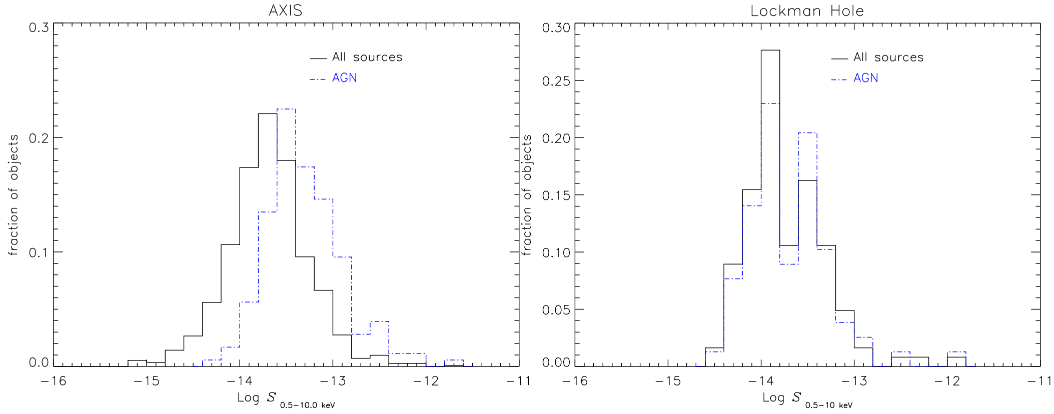

Figure 2.7: *AXIS (left) and Lockman Hole (right) $S_{0.2-12\,\mathrm{keV}}$ distributions for all sources (solid line) and for AGN (dashed-dot line). Fluxes were obtained from the best fit model of each object (see Sec. 4.5). Note that in [152] we showed the flux distribution of all identified objects, while here we show only the flux distribution of sources identified as type-1 or type-2 AGN.*

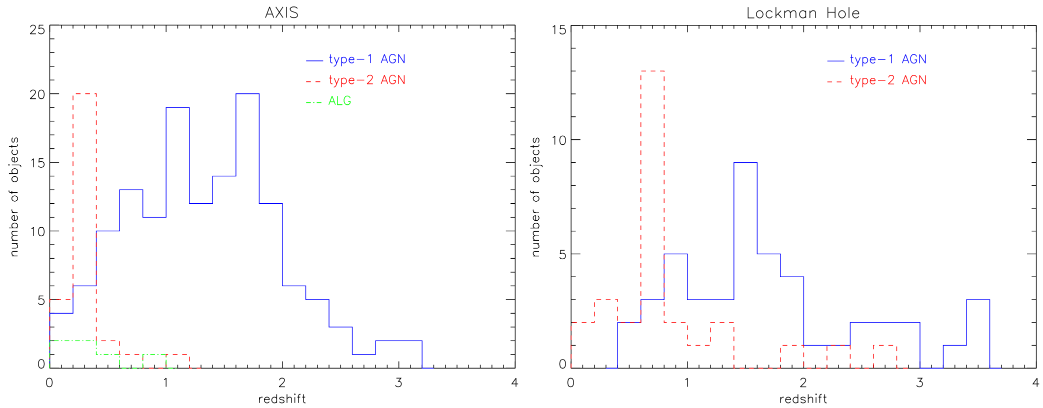

Figure 2.8: *Comparison of redshift distributions of type-1 and type-2 AGN in the AXIS (left) and Lockman Hole (right) samples. For AXIS we show the redshift distribution of objects that were identified as ALG at the time of the analysis. Because the optical identification of the ALG has now changed we do not show the results of the spectral analysis of these objects based on their initial optical identification.*

We see in Fig. 2.7 that both AXIS and *Lockman Hole* sources have similar flux distributions (we used the fluxes obtained from the best fit model of each object; see Sec. 3.3.4) and reach similar flux limits. We expect this as we are only using the brightest sources in the *Lockman Hole*. The reason why the flux distribution for *Lockman Hole* sources does not show a sharp end at low fluxes but a broadening of the distribution is that the effective exposure varies significantly across the FOV of the *Lockman Hole* observation, and hence a threshold in counts correspond to different thresholds in count rate (and flux) depending on the position of the source in the detector FOV. The same result is seen for AXIS sources at fluxes below $\sim 10^{-14}$ erg cm^{-2} s^{-1}, due to the selection of fields with a broad range of exposure times that results in a gradual reduction of the sky coverage as we go to fainter fluxes. The AXIS sample is likely to be representative of the dominant X-ray source population down to a flux of $\sim 10^{-14}\,\mathrm{erg\,cm^{-2}\,s^{-1}}$.

As both samples cover a similar range of fluxes we can do a direct comparison of the observed dependence of the spectral properties of AXIS and *Lockman Hole* sources with the X-ray flux.

Fig. 2.8 shows a comparison of the redshift distributions of the AGN in the two samples. The *Lockman Hole* survey is more efficient for detection of high redshift objects. However as the solid angle covered by the *Lockman Hole* survey is very small this survey is much less efficient for detection of low redshift AGN. The peak of the observed redshift distributions of type-1 AGN is located at z∼1.5 in both surveys while we see that the peak of the distribution for type-2 AGN is located at a redshift ∼0.3 for AXIS and z∼0.7 for *Lockman Hole* sources. However it is difficult to make a comparison of the observed

---

They were obtained by combining all MOS and pn spectra available for each source.

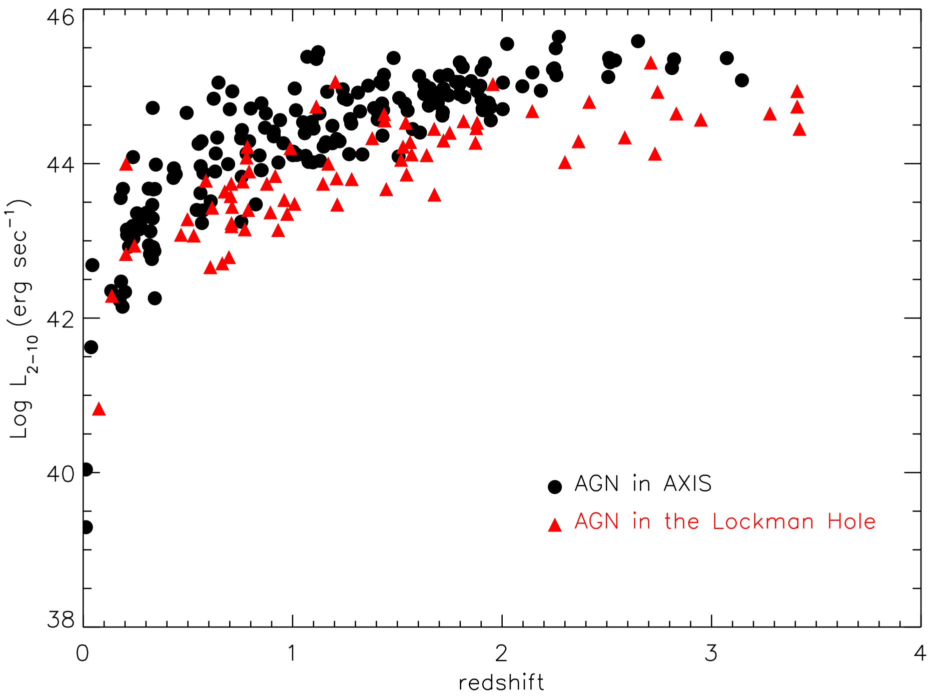

Figure 2.9: *Hard (2-10 keV) X-ray luminosity (corrected for absorption) as a function of redshift for type-1 and type-2 AGN in AXIS and and Lockman Hole surveys.*

redshift distributions because the number of objects in the *Lockman Hole* survey is rather small.

There might still be significant biases in the redshift distribution of identified sources, as optically fainter ones are still being targeted for optical spectroscopy. This might affect more strongly type-2 AGN which, being obscured, are fainter.

The redshift-luminosity diagram for the combined sample of AXIS-*Lockman Hole* AGN is shown in Fig. 2.9. X-ray luminosities were corrected for Galactic and intrinsic absorption. The plot clearly illustrates how both surveys are complementary, in the sense that, although they cover similar redshift intervals, the *Lockman Hole* survey is more efficient for detecting of lower luminosity sources at all redshifts, while AXIS has higher overall number of sources.

Throughout this thesis we have adopted the *WMAP* consensus cosmology: $H_0 = 70\,\mathrm{km\,s^{-1}\,Mpc^{-1}}$, $\Omega_M = 0.3$ and $\Omega_\Lambda = 0.7$ [223].

Chapter 3

X-ray spectroscopy of AXIS sources

In this chapter we describe the results of a statistical study of the X-ray spectral properties of a large sample of sources at intermediate X-ray fluxes detected serendipitously with the *XMM-Newton* observatory. The aim of this study is to learn about the X-ray emission properties of AGN within the medium flux range where it is known that ∼50% of the 0.5-2 keV and ∼40% of the 2-8 keV [18] accretion power in the Universe is produced.

As we explained in Chapter 2, thanks to an ongoing optical follow-up identification programme of the sources detected in the selected fields, at the time of this analysis we had representative samples of different classes of identified objects, most of them being identified as type-1 and type-2 AGN. We carried out a detailed spectral study of these sources in order to find the dependence of the X-ray emission properties of AGN on X-ray flux and luminosity. The understanding of the X-ray emission properties of AGN and their dependence on different X-ray spectral parameters is an essential ingredient of the synthesis models of the XRB aiming at explaining the origin of this emission as the superposition of faint AGN. We finally analyse the dependence of the emission properties on redshift in order to better understand the history of accretion in the Universe.

3.1 The AXIS X-ray catalogue

In order to carry out this study we selected 25 target fields from the public *XMM-Newton* data archive. The observations cover a total solid angle of ∼3.5 deg^2. To obtain a clean extragalactic sample of objects and to maximise the efficiency of the survey, the X-ray observations were selected according to the following criteria:

1. Sky positions at high galactic latitudes ($|b| > 20\,\mathrm{deg}$) to reduce the contamination of the X-ray images by Galactic stars.

2. Observations for which there is data available from the EPIC-pn detector (that in general provides the deepest observation of the field) and in FULL-FRAME MODE, to guarantee that the observation has covered the full FOV of the EPIC-pn detector[1].

---

[1] See the *XMM-Newton* users' handbook at `http://xmm.vilspa.esa.es/`.

Table 3.1: *Breakdown of sources with optical spectroscopic identifications (type-1 AGN: broad line AGN; type-2 AGN: narrow emitting line galaxy).*

Object class	N^{a}	N^{b}_{good}
type − 1 AGN	149	141
type − 2 AGN	32	29
stars	40	32
BL Lac	1	1
Total	222	203

[a] Number of sources identified

[b] Number of sources identified that fulfil the quality thresholds applied to the X-ray spectra (see Sec. 3.1)

3. Fields containing bright point or extended targets were avoided because targets can raise significantly the background over a substantial fraction of the FOV, reducing substantially the sky area where detection of serendipitous sources not affected by target emission is possible.

A detailed description of the AXIS survey was given in previous chapter (see Sec. 2.7) while the list of *XMM-Newton* selected observations for this survey together with the details of each observation is shown in Table 2.4

The source lists of each observation were screened as explained in Sec. 2.4. The screening process removed ∼10% of objects resulting in a list with 2145 sources. For each source X-ray spectral products were extracted following the procedure explained in Sec. 2.5. In order for the χ^2 minimisation technique in the fitting process to be valid, the raw spectra were binned such that each bin contained ≥ 10 counts (source plus background). We have checked that a grouping of at least 10 counts per bin is enough for the χ^2 technique to be correct. The details of this test are presented in Appendix A.1.

As some of the sources in our list are very faint, the signal-to-noise ratio of their X-ray spectra might be not high enough as to avoid "overfitting" when using spectral models such as `model B` or `model C` (for model definitions see Sec. 2.6.1). An "overfitting" using these models will result in a spurious correlation between Γ and $\mathrm{N_H}$. In order to avoid this effect we imposed two quality thresholds on the grouped spectra: total number of bins (MOS+pn) $\geq$5, and total number of background subtracted counts (MOS+pn) $\geq$50. This spectral quality filtering resulted in a final sample of 1137 sources having X-ray spectra of sufficient quality for the analysis. In Fig. 3.1 we show, as an example, the X-ray spectra of some of the objects that we have analysed. Table 3.1 lists the number of identified sources of each class along with those which have good quality X-ray spectra.

3.1.1 Source detection sensitivity

In order to interpret the results of our analysis, for example the dependence of the broad band continuum shape with different source parameters, it is important to know whether

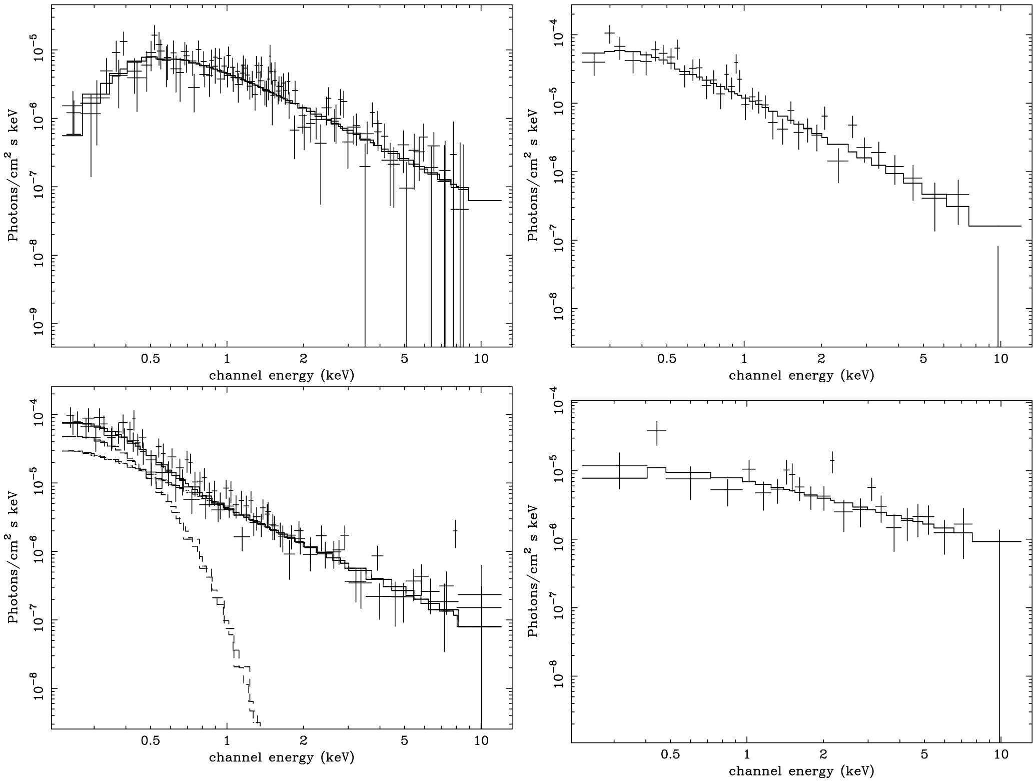

Figure 3.1: *Unfolded EPIC X-ray spectra of* **XMMU J221454.9-173949** *an absorbed type-1 AGN (top left);* **XMMU J084132.3+704757** *an unabsorbed type-2 AGN with* $L_{2-10\,\mathrm{keV}} \sim 6 \times 10^{42}\,\mathrm{erg\,s^{-1}}$ *(top right);* **XMMU J133106.2+241326** *a type-1 AGN with detected soft excess emission (bottom left; see Sec. 3.3.3 for details);* **XMMU J021908.3-044731** *a flat spectrum (*$\Gamma = 0.94^{+0.23}_{-0.25}$*) unabsorbed object, still not identified (bottom right).*

the results are affected by detection biases in the sample. The variety of data that we have used in our study, e.g. observations with a very broad range of exposure times and wide range in the spectral quality of the sources, make it difficult to calculate the source detection sensitivity as a function of the X-ray flux, because in principle it depends on the exposure times of the fields and their Galactic absorbing columns, N_H^{Gal} [254].

The *XMM-Newton* EPIC-pn detector is sensitive to X-ray photons of energies ranging from ∼0.2 to ∼12 keV. The sensitivity is maximum between 0.5 and 4.5 keV, where it depends only mildly on energy, i.e., objects with different spectral shapes are detected with similar efficiency. However, outside this energy interval, the sensitivity is a much stronger function of energy.

Because the energy band where we carried out the detection of sources is wide, we do not expect the use of fields with different N_H^{Gal} (ranging from $\sim 10^{20}$ to $9 \times 10^{20}\,\mathrm{cm^{-2}}$) to introduce any significant bias (e.g. detections in fields with the higher values of Galaxy absorption biased towards hardspectrum sources) in the broad band spectral properties of our objects.

However, as we see in Table 2.4, the exposure times of the observations vary significantly. At 0.5-10 keV fluxes below $\sim 10^{-14}\,\mathrm{erg\,cm^{-1}\,s^{-1}}$, where only a small number of fields contribute to the source list, we expect our survey to be biased against objects with spectra peaking outside the 0.5-4.5 keV energy range (where most X-ray photons are collected), for example highly obscured AGN.

To build our source lists, the *XMM-Newton* source detection algorithm was ran simultaneously in five energy bands as explained in Sec. 2.3. This makes the situation more complicated, as we have analysed sources that might have been detected in different energy bands. It is important to take this into account when interpreting the observed results, because different source populations may contribute at different flux levels in different energy bands.

In order to calculate the source detection efficiency function for different spectral continua and as a function of the X-ray flux, we carried out simulations. A detailed description on how we obtained this selection function is given in Appendix B. Our work shows that there is indeed a mild dependence of the selection function on the continuum spectral slope at any given flux (see Fig. B.1) and therefore we need to correct our observed results for this effect.

3.2 Overall results of spectral fits

For the selected acceptance level (an spectral model is rejected if the null hypothesis probability P(χ^2) is less than 5%; see Sec. 2.6), 139 (12%) objects had statistically unacceptable fits with `model A` (power law; see Sec. 2.6.1), the expected number of spurious bad fits for the selected confidence level being 57. `Model A` could not be accepted for 10 (7%) type-1 AGN and 9 (31%) type-2 AGN.

The top panel in Fig. 3.2 compares the P(χ^2) distributions obtained with `model A` with the results from `model B` (observer's frame absorbed power law; see Sec. 2.6.1) for the whole sample of sources. We see that the number of unacceptable fits ($P(\chi^2) \leq 5\%$) has been reduced by a factor of ~2 (from ~140 to ~70), implying the presence of intrinsically absorbed objects among the sources in our sample.

Fig. 3.2 compares the quality of the fits obtained with `model A` and `model C` (rest-frame absorbed power law; see Sec. 2.6.1), for type-1 (middle panel) and type-2 (bottom panel) AGN. In the case of the type-1 AGN, we did not find a substantial improvement in the overall quality of the fits, suggesting that the majority of type-1 AGN do not require intrinsic absorption in excess of the Galactic value. Therefore, for the statistically unacceptable fits, more complicated models might be needed to reproduce the emission properties of these sources. On the contrary, the observed significant improvement in the quality of the spectral fits obtained with `model C` for type-2 AGN suggests that a large fraction of type-2 AGN are intrinsically absorbed.

The soft excess has been shown to be a common feature of the X-ray spectra of Seyfert 1 galaxies [234]. The physical origin of this emission is still unclear, since its determination depends on a knowledge of the shape of the power law and the quantity of absorption. As

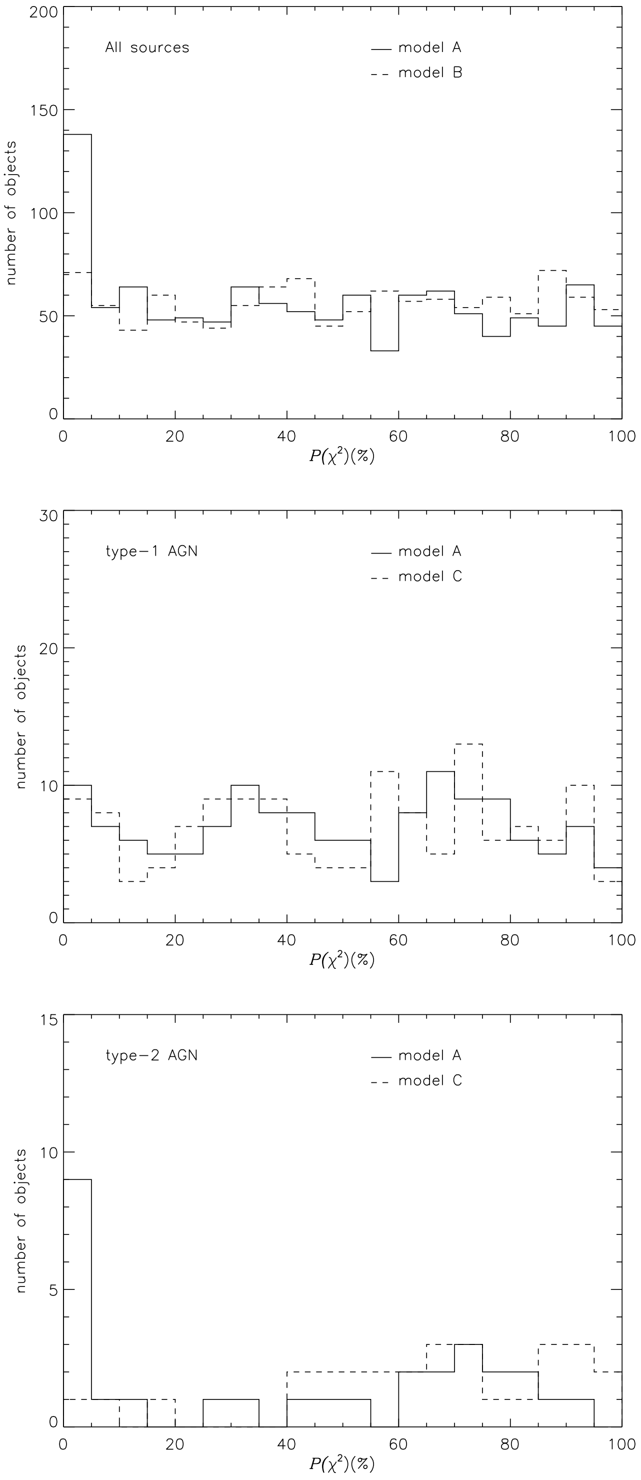

Figure 3.2: *Comparison of the null hypothesis probability distributions, $P(\chi^2)$, obtained from* `model A` *(simple power law, solid lines) and* `model B` *and* `model C` *(observer frame absorbed power law and rest frame absorbed power law models, dashed lines). From top to bottom: whole sample of sources, type-1 AGN and type-2 AGN.*

we have seen in Sec. 1.4.2, soft excess emission has been frequently interpreted as primary emission from the accretion disc, gravitational energy released by viscosity in the disc, or as secondary radiation from the reprocessing of hard X-rays in the surface layers of the disc.

We have searched for soft excess emission among our samples of type-1 AGN and type-2 AGN. We first fitted the X-ray spectra of our AGN with `model D` (power law with black body component (at the sources' rest-frame), both emission components absorbed by the Galaxy; see Sec. 2.6.1). The soft excess, parameterised as a black body, adds to the spectral model two parameters, the temperature of the black body and its normalisation.

We then have compared the χ^2 of the fits with the values obtained with `model A`, searching for cases where the significance of a χ^2 improvement was above 95%. From the 170 sources analysed (141 type-1 AGN and 29 type-2 AGN) we found evidence of soft excess emission with a significance of more than 95% in 12 objects (~7%), 10 being type-1 AGN and 2 type-2 AGN. All of them improved with `model B`/`model C` with respect to `model A`.

As explained before, if soft excess is present in the spectra of the objects, it must be modelled properly to prevent the continuum slope Γ and/or the intrinsic absorption $\mathrm{N_H^{intr}}$ being incorrectly determined. Therefore we have analysed the X-ray spectra of these 12 sources in more detail. All the spectra have large enough number of bins, 35<bins<317, to use `model D` (power law and low energy black body components, both absorbed by the Galaxy ($\mathrm{N_H^{Gal}}$; fixed) and `model E` (the power law component absorbed by absorption at the redshift of the sources, $\mathrm{N_H^{intr}}$; free). Results from this specific exercise are presented in Sec. 3.3.3.

3.3 Analysis of the X-ray spectra

3.3.1 The continuum shape

Although we have evidence that a significant fraction of sources in our list are absorbed, we have studied the results obtained when using `model A`. This allows comparison with existing spectral analyses of data with similar signal-to-noise ratio for which a proper modelling of excess absorption or soft excess emission was not conducted.

To calculate the mean photon index of the objects as measured with `model A`, $\langle\Gamma\rangle$, we have used the standard formula for the weighted mean (see Appendix A.2),

$$\langle\Gamma\rangle = \sum P_i \times \Gamma_i \qquad (3.1)$$

where the weight, P_i, of each individual best fit value, Γ_i, is a function of the statistical error obtained from the fit, σ_i,

$$P_i = \frac{1/\sigma_i^2}{\sum(1/\sigma_i^2)} \qquad (3.2)$$

To calculate the corresponding uncertainty in $\langle\Gamma\rangle$ we have used the error on the mean [22]

$$\sigma^2 = \frac{1}{(\mathrm{N}-1)} \sum P_i \times (\Gamma_i - \langle\Gamma\rangle)^2 \qquad (3.3)$$

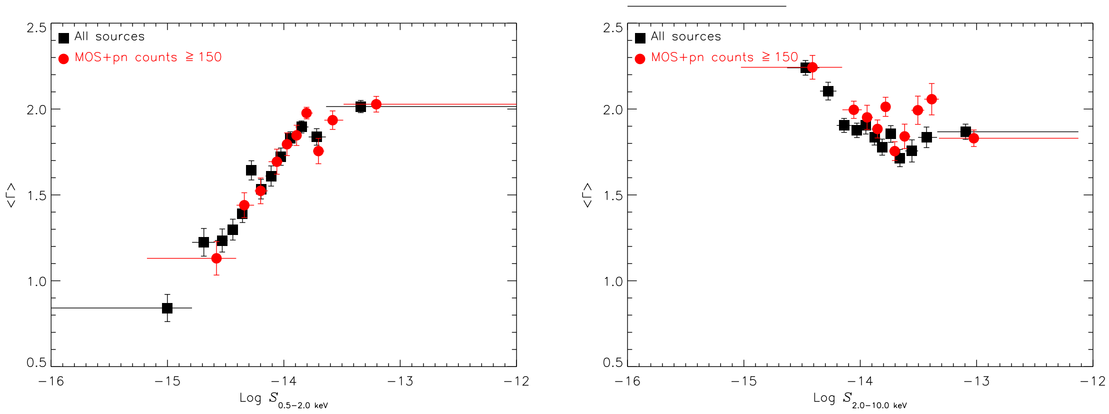

Figure 3.3: *Weighted photon index versus $S_{0.5-2\,\mathrm{keV}}$ (left) and $S_{2-10\,\mathrm{keV}}$ (right) from* `model A` *(simple power law) in squares. The results obtained for the objects with X-ray spectra with more than 150 counts (background subtracted) are included for comparison (circles). Errors correspond to the 1σ confidence interval.*

that includes both the measurement errors, σ_i, and the dispersion of each Γ_i from the estimated mean value $\langle\Gamma\rangle$.

Following these definitions, we found our sources to have a continuum emission with an average slope in the observed energy interval from 0.2 to 12 keV of $\langle\Gamma\rangle = 1.86 \pm 0.02$ (the arithmetic mean being 1.70 ± 0.02). To study the dependence of the objects' average spectrum on the X-ray flux, we calculated $\langle\Gamma\rangle$ in bins of 0.5-2 and 2-10 keV flux (each bin containing the same number of objects and therefore they may not have the same size). Fig. 3.3 shows the results that we obtained. We see that the average spectrum of our sources becomes harder with decreasing 0.5-2 keV flux, with $\langle\Gamma\rangle$ going from 2.01 ± 0.03 at fluxes $\sim 4.4 \times 10^{-14}\,\mathrm{erg\,cm^{-2}s^{-1}}$ to 0.95 ± 0.12 at fluxes $\sim 10^{-15}\,\mathrm{erg\,cm^{-2}\,s^{-1}}$. The same dependence, i.e., hardening of $\langle\Gamma\rangle$ at fainter 0.5-2 keV fluxes, was observed using the arithmetic mean to calculate $\langle\Gamma\rangle$, therefore the result is not an artifact of the weighted mean. This trend (harder sources at fainter 0.5-2 keV fluxes) has been found in previous X-ray spectral analyses (see e.g. [140] [161] [228] [241]). Its origin is still not clear, although it could be explained as a rapid increase in the intrinsic absorption of the objects with decreasing flux, as it is predicted by some AGN synthesis models [84].

Such effect is not seen using 2-10 keV fluxes instead (see Fig. 3.3 right plot). Indeed in this case the mean spectral slope of the sources becomes softer at fainter fluxes. It is important to note that this softening of $\langle\Gamma\rangle$ is not a real property of our objects. It is due to the fact that we are using different energy bands simultaneously for source detection (see Sec. 2.3). As we go to fainter 2-10 keV fluxes, it is more difficult to detect sources with flat spectral slopes (hard objects), because their spectra do not have enough counts at energies below $\sim$2, keV where we know the sensitivity of the EPIC detectors is maximum. Hence, the number of objects only detected in the soft band becomes more important at fainter 2-10 keV fluxes, specially below $\sim 2 \times 10^{-14}\,\mathrm{erg\,cm^{-2}\,s^{-1}}$, where the mean spectral slope starts to become softer. Note that the last bin at the faintest fluxes is located at a

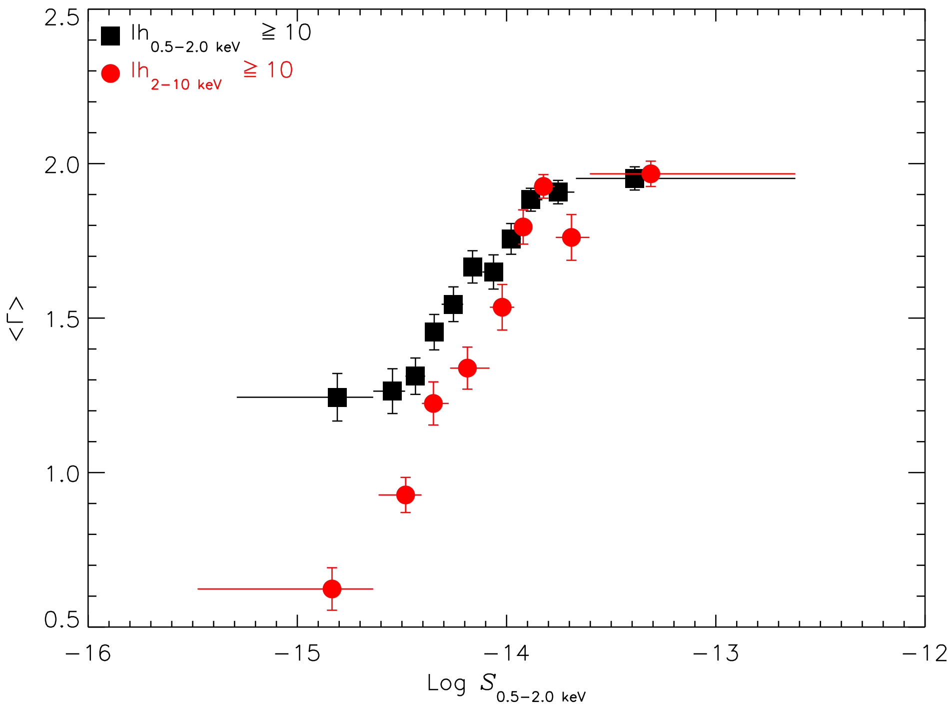

Figure 3.4: *Weighted photon index versus* $S_{0.5-2\,\mathrm{keV}}$ *from* `model A` *(simple power law) for sources with detection likelihood ≥10 in the 0.5-2 keV band (squares) and for sources with detection likelihood ≥10 in the 2-10 keV band (circles). Errors correspond to the 1σ confidence interval.*

value of $\langle\Gamma\rangle$ of more than 2.5. We have checked that the objects that contribute to this bin have spectra with very few counts and therefore most values of Γ that contribute to this bin are poorly constrained.

We have studied in more detail whether the observed hardening of $\langle\Gamma\rangle$ with decreasing soft flux could be affected by any bias introduced during our analysis. One effect is the poor quality of the spectra of some sources, a problem that will become more important at fainter fluxes. In order to check this, we obtained the distribution of $\langle\Gamma\rangle$ using only sources with more than 150 background subtracted counts (circles in Fig. 3.3). We see that the same dependence is still observed, and therefore we conclude that sources with poor spectral quality are not introducing any bias in our observed results.

We expect the majority of the observations that we have used to be too shallow to detect sources with a 0.5-2 keV flux of $\sim 10^{-15}\,\mathrm{erg\,cm^{-2}\,s^{-1}}$ in the soft band. Hence, it could be possible that $\langle\Gamma\rangle$ becomes harder with decreasing flux partly due to the contribution to each bin from bright hard sources not detected in the soft band. This can be checked by repeating the plot of Fig. 3.3 using only those sources detected on each band. We used a detection likelihood threshold of 10 to select sources. The results, plotted in Fig. 3.4,

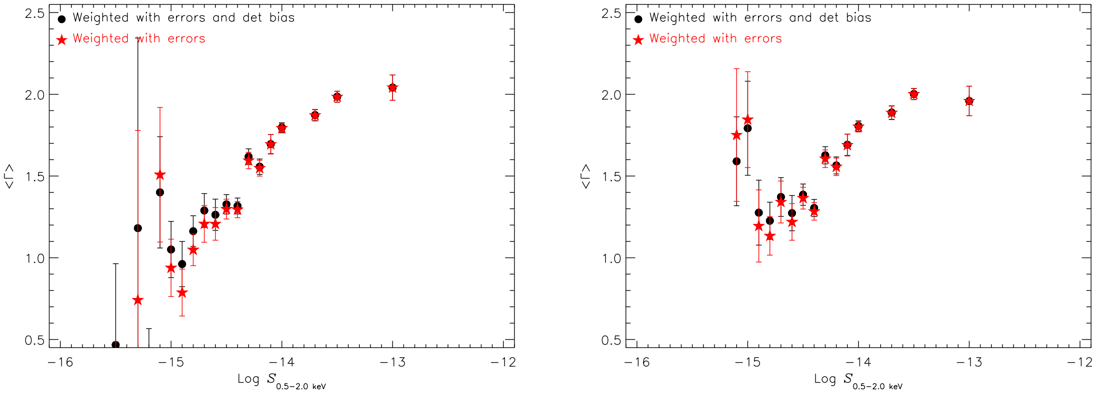

Figure 3.5: *Comparison of the weighted photon index versus* $S_{0.5-2\,\mathrm{keV}}$ *from* `model A` *(simple power law) with the values obtained after correcting for biases associated with the spectral shape of the objects. Left for the whole sample of objects and right for the sub-sample of sources with detection likelihood* $\geq$*10 in the 0.5-2 keV band. Errors correspond to the* 1σ *confidence interval.*

show a very similar dependence of $\langle\Gamma\rangle$ with flux for objects detected in both the 0.5-2 keV and 2-10 keV energy bands. Only the value of $\langle\Gamma\rangle$ in the bin at the faintest soft fluxes in Fig. 3.3, could be affected or even dominated by bright hard sources not detected in the soft band. It is interesting to note that the hardening of $\langle\Gamma\rangle$ is more important for objects detected in the 2-10 keV band (see Fig. 3.4; circles). If absorption is producing the hardening of Γ, this result suggests that we are seeing the same population of objects in both the soft and hard bands, the only difference being that the objects detected in the 2-10 keV band are more absorbed on average.

Finally, we have calculated the source detection efficiency function, $\mathrm{W}(\Gamma, S)$, that gives us the dependence of the efficiency of detection of sources on the sources' X-ray flux and on the slope of their broad band continuum, Γ. We have used this function to correct our results for biases associated to the spectral shape of the objects. For a detailed explanation on how we obtained $\mathrm{W}(\Gamma, S)$ see Appendix B. The de-biased average values of $\langle\Gamma\rangle$ at each bin of flux were obtained weighting each individual value, Γ_i, with the function

$$P_i = \frac{1/(\sigma_i^2 \times W(\Gamma_i, S_i))}{\sum_i 1/(\sigma_i^2 \times W(\Gamma_i, S_i))} \tag{3.4}$$

where the sum is calculated over all sources falling in the specified bin in the Γ, S plane. The results are shown in Fig. 3.5 (circles), the left plot for the whole sample of sources, and the right plot for the sources detected in the soft band with a detection likelihood $\geq$10. For comparison we have calculated $\langle\Gamma\rangle$ values weighted only with the fitting errors in the same flux bins (stars). We still see the hardening of $\langle\Gamma\rangle$ with the 0.5-2 keV flux after correction for selection effects. Therefore we conclude that this dependence is indeed a real property of the population of sources analysed.

Table 3.2: *Summary of the results of detection of X-ray absorption (*`model B` *and* `model C` *with respect to* `model A` *and F-test significance ≥95%) for different samples of AXIS sources.*

Sample (1)	N_{tot} (2)	N_{abs} (3)	f_{-}^{+} (4)	F (5)
All	1137	245	$0.17^{+0.02}_{-0.02}$	0.1335
type − 1 AGN	141	16	$0.06^{+0.05}_{-0.04}$	0.0089
type − 2 AGN	29	13	$0.40^{+0.15}_{-0.14}$	0.1740

Columns are as follows: (1) classification of sources from optical spectroscopy; (2) total number of objects in group; (3) number of objects in group with detected X-ray absorption (F-test significance ≥ 95%); (4) fraction of sources in group with detected X-ray absorption. The fractions, *f*, are defined as the mode of the function *P(f)* while the errors correspond to the 1σ confidence interval (see Appendix A.4 for details); (5) value of the fraction for which $P(f \geq \mathrm{F})$=0.9973 (3σ)

3.3.2 Excess absorption

We saw in Sec. 3.2 that the fit to the X-ray spectra with a single power law leaves a large number of sources (12%) with statistically unacceptable fits. However, when using `model B` and `model C`, the number of unacceptable fits was reduced significantly (see also Fig. 3.2), suggesting that a substantial fraction of our sources have excess absorption above the Galactic value.

To search for absorption in our objects we used the F-test, measuring the improvement in the χ^2 of the fits after adding absorption to the model. We adopted a confidence threshold of 95% to accept the detection of additional spectral components. In Table 3.2, we show the total number of objects of different types, the number of objects with detected absorption of that type for the selected confidence level, and the fraction of absorbed objects of each type corrected for spurious detections, f, following the method described in Appendix A.4.

The last column gives the value of the fractions, F, for which $P(f \geq F) = 0.9973$, where $P(f)$ is the probability distribution function of f, i.e., the fractions of absorbed objects that we have detected within each class of sources with a significance of more than 3σ. For example, we know with a confidence of more than 3σ that at least ~1% of type-1 AGN and ~17% of type-2 AGN are absorbed.

It appears that the fraction of absorbed objects varies substantially among different classes of objects, type-2 AGN having the highest fraction. We have used the method described in [224] and in Appendix A.4 to study whether our samples of type-1 and type-2 AGN have different fractions of absorbed objects. We found that the fraction of absorbed type-2 AGN is higher than that of absorbed type-1 AGN with a significance of more than 3σ.

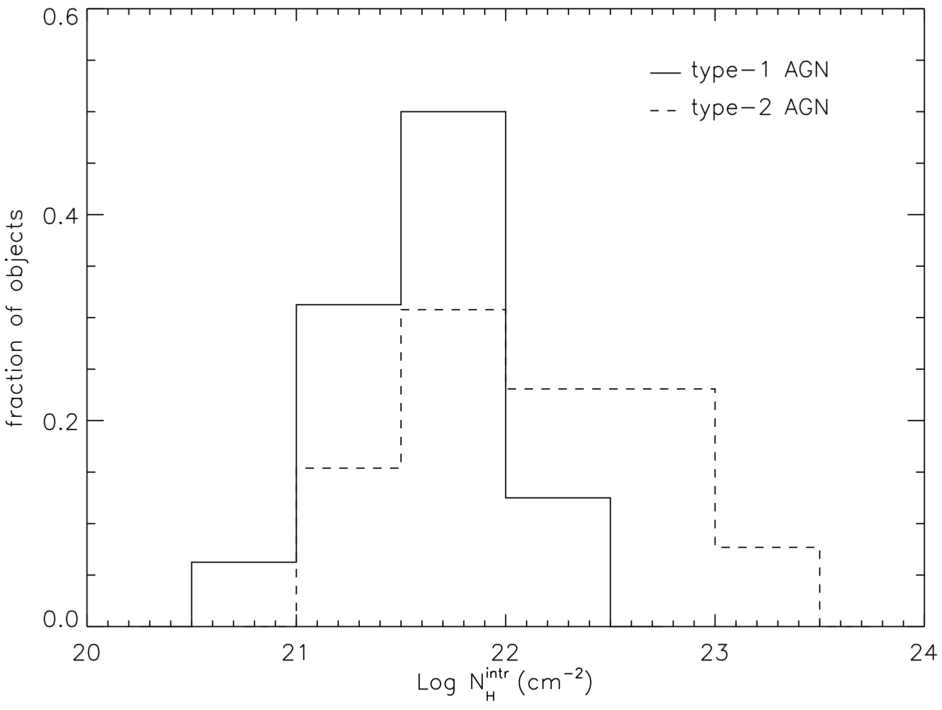

Figure 3.6: *Distributions of intrinsic (rest-frame) absorption for absorbed (F-test≥95%) type-1 AGN (solid histogram) and type-2 AGN (dashed histogram).*

Fig. 3.6 shows the distributions of rest-frame excess absorption, N_H^{intr}, measured with `model C` for absorbed type-1 and type-2 AGN. Type-1 AGN show column densities in the range $4.5 \times 10^{20} < N_H^{intr} < 2.3 \times 10^{22}\,\mathrm{cm}^{-2}$ while type-2 AGN cover a much wider range of absorption values, with $1.1 \times 10^{21} < N_H^{intr} < 1.7 \times 10^{23}\,\mathrm{cm}^{-2}$. The small number of objects with detected absorption does not allow us to find a significantly different (in terms of the Kolmogorov-Smirnov test) distribution of absorbing columns between absorbed type-1 and type-2 AGN.

To be confident that the detected intrinsic absorptions in our AGN were not affected by the quality of the spectra, we have plotted Γ versus N_H^{obs} (Fig. 3.7; left) and Γ versus N_H^{intr} (Fig. 3.7; right) to search for any correlation between these two spectral parameters. Such a correlation would be expected if the detections of absorption were spurious and due to data with low signal-to-noise ratio. The plot shows no apparent correlation between Γ and excess absorption.

A Kolmogorov-Smirnov comparison between the redshift distributions of unabsorbed and absorbed type-1 AGN does not indicate a significant difference between the two samples. The same result is obtained when comparing 2-10 keV luminosity distributions of absorbed and unabsorbed type-1 AGN and type-2 AGN (we used the 2-10 keV energy band because it is less affected by absorption). We conclude that X-ray absorption does

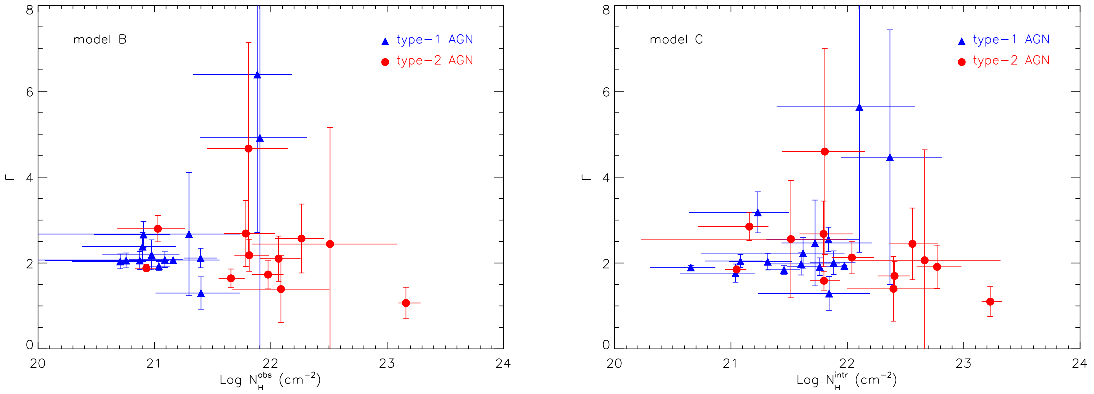

Figure 3.7: *Photon index versus observed excess absorption ($\mathrm{N_H^{obs}}$; left) and versus rest-frame excess absorption ($\mathrm{N_H^{intr}}$; right) for type-1 (triangles) and type-2 (diamonds) AGN with detected X-ray absorption (F-test significance $\geq 95\%$). Errors correspond to the 90% confidence interval.*

not occur preferentially at any particular redshift or X-ray luminosity for both type-1 and type-2 AGN populations.

Finally, we have used our data to test whether the lack of optical broad emission lines in unabsorbed type-2 AGN can be explained as being due to an AGN/host galaxy contrast effect, i.e., the AGN in these objects are faint and therefore the emission at optical wavelengths is dominated by the emission from their host galaxy [136] [166] [180] [218]. To this end, we have compared the 2-10 keV luminosity distributions of two sub-samples of unabsorbed type-1 and type-2 AGN detected with redshifts ranging from 0.17 to 0.7, where the redshift distributions of type-1 and type-2 AGN overlap (see Fig. 2.8). The Kolmogorov-Smirnov significance of the two distributions being different is ∼99%. Furthermore, the average luminosities of the selected type-1 and type-2 unabsorbed AGN were found to be 43.7±0.16 and 43.2±0.11 (in log cgs. units). Therefore, our unabsorbed type-2 AGN are on average significantly less luminous than our unabsorbed type-1 AGN at similar redshifts, and hence, the non detection of broad optical lines in unabsorbed type-2 AGN is consistent with being due to an AGN/host-galaxy contrast effect.

3.3.3 Soft excess

We have shown in Sec. 3.2 that ∼7% of the sources identified as type-1 or type-2 AGN exhibit significant soft excess emission. To measure the broad band spectral parameters of these sources, and in particular the underlying power law spectral index, Γ, we have used `model E`, which fits the signatures of soft excess emission with a black body component, and allows for excess absorption above the Galactic value (see Sec. 2.6).

Table 3.3: *Spectral parameters of sources with soft excess detected in their X-ray spectra.*

Name (1)	Class (2)	redshift (3)	Γ^{+}_{-} (4)	N_H^{intr} (5)	kT^{+}_{-} (6)	L_{BB} (7)	L_{PO} (8)	S_{fracc} (9)	L_{fracc} (10)	`model` C (11)	`model` E (12)
XMMU J133106.2 + 241326	type − 1	0.174	$1.83^{+0.45}_{-0.26}$	$< 10^{20}$	85^{+116}_{-64}	41.52	42.11	14.7	25.2	Nabs	Nabs
XMMU J061728.6 + 710600	type − 1	0.219	$1.68^{+0.56}_{-0.37}$	$< 10^{20}$	214^{+253}_{-111}	42.38	42.75	39.5	44.6	Nabs	Nabs
XMMU J074311.9 + 742935	type − 1	0.332	$2.05^{+0.03}_{-0.05}$	$< 10^{20}$	119^{+130}_{-106}	43.96	44.54	12.2	22.1	Nabs	Nabs
XMMU J212904.5 − 154448	type − 1	0.431	$1.29^{+0.27}_{-0.36}$	$14.21^{+32.59}_{-5.81}$	205^{+251}_{-142}	43.53	43.64	54.6	72.7	Nabs	abs
XMMU J001831.7 + 162924	type − 1	0.551	$2.35^{+0.17}_{-0.18}$	$4.15^{+11.25}_{-2.37}$	186^{+259}_{-126}	43.67	44.02	22.5	35.4	Nabs	abs
XMMU J021808.2 − 045844	type − 1	0.712	$2.08^{+0.04}_{-0.05}$	$< 10^{20}$	142^{+164}_{-111}	44.09	44.71	6.6	19.5	Nabs	Nabs
XMMU J222823.6 − 051306	type − 1	0.758	$1.52^{+0.14}_{-0.15}$	$15.61^{+12.39}_{-7.20}$	262^{+379}_{-171}	43.87	44.18	35.8	54.6	Nabs	abs
XMMU J221523.6 − 174321	type − 1	0.956	$2.15^{+0.17}_{-0.23}$	$< 10^{20}$	112^{+234}_{-21}	43.43	44.02	1.9	19.2	Nabs	Nabs
XMMU J221515.1 − 173224	type − 1	1.165	$2.06^{+0.37}_{-0.35}$	$< 10^{20}$	212^{+233}_{-192}	44.66	44.70	24.8	49.7	Nabs	Nabs
XMMU J021830.5 − 045622	type − 1	1.430	$2.28^{+0.10}_{-0.18}$	$< 10^{20}$	129^{+223}_{-82}	44.48	44.73	1.9	30.1	Nabs	Nabs
XMMU J061730.9 + 705955	type − 2	0.200	$2.02^{+1.13}_{-1.00}$	$< 10^{20}$	207^{+272}_{-142}	42.14	42.21	44.1	49.3	abs	Nabs
XMMU J122206.1 + 752616	type − 2	0.238	$1.82^{+0.14}_{-0.10}$	$11.17^{+2.43}_{-2.30}$	146^{+208}_{-112}	43.12	43.84	6.1	9.1	abs	abs

Columns are as follows: (1) *XMM-Newton* source name; (2) class from optical spectroscopy; (3) spectroscopic redshift; (4) broad band continuum slope; (5) intrinsic X-ray absorption in units of $10^{20}\,\mathrm{cm}^{-2}$; (6) temperature of the soft excess emission in units of eV; (7) logarithm of the 0.5-2 keV luminosity of the black body, obtained setting absorption and powerlaw components to zero; (8) logarithm of the 2-10 keV luminosity of the powerlaw component obtained setting absorption and black body components to zero; (9) contribution to the soft (0.5-2 keV) flux from the soft excess component, measured as the ratio of the soft excess to power law 0.5-2 keV fluxes; (10) contribution to the soft (0.5-2 keV) luminosity from the soft excess component, measured as the ratio of the soft excess to power law 0.5-2 keV luminosities; (11) detection of intrinsic absorption with `model C` (F-test comparison of the χ^2 from `model A` and `model C`); (12) detection of intrinsic absorption with `model E` (F-test comparison of the χ^2 from `model A` and `model E`). Errors correspond to the 90% confidence interval.

The results of the fits of the 9 AGN with detected soft excess emission are summarised in Table 3.3. For each source we list its IAU-style *XMM-Newton* source name, the optical classification, redshift, and the spectral parameters measured with `model E`. We have also included the 0.5-2 keV luminosity of the black body component and the 2-10 keV luminosity of the power law component and the contribution of the soft excess component to the 0.5-2 keV flux and 0.5-2 keV luminosity. Finally the F-test results obtained from the comparison of the χ^2 values obtained from `model A` to χ^2 from `model C` and `model E` are shown.

Using a thermal component to model the soft excess emission in our AGN yields temperatures with a narrow range (0.1-0.3 keV) and independent of the luminosity of the AGN in agreement with previous analyses. In most AGN the luminosities of this spectral component are too large to correspond to starburst emission. No obvious dependence of the contribution of the soft excess to the 0.5-2 keV flux/luminosity with the luminosity of the objects is seen.

We now discuss some particular sources in detail.

XMMU J001831.7+162924, XMMU J222823.6-051306, XMMU J212904.5-154448. We obtained an improvement in the spectral fits with `model C`, but the F-test significance was in all cases below our threshold of 95%, therefore the sources were classified as unabsorbed. A proper modelling of the soft excess emission with `model E` allowed us to detect significant absorption above the Galactic value in all these sources.

XMMU J221515.1-173224. We obtained an unusually steep spectral slope with `model A`, $\Gamma = 2.67^{+0.05}_{-0.06}$ suggesting the presence of soft excess emission. The quality of the fit did not improve significantly with `model C`. However with `model E` we obtained a significant improvement in the fit ($> 99.99\%$) although this model did not require absorption in excess of the Galactic value. The measured temperature of the soft excess emission is kT=$0.05^{+0.03}_{-0.01}$ keV, below the typical values found for the rest of our sources. The fitted continuum is still significantly steep, $\Gamma = 2.60^{+0.04}_{-0.11}$. We tried to find a more typical value of Γ fitting the continuum slope at high energies (>2 keV) with `model A`. This yields Γ=$2.06^{+0.37}_{-0.35}$ in line with the average spectral slope of unabsorbed AGN. With Γ fixed to the above value the fit did not improve with `model C`, but with `model E` we still obtain an F-test significance >99.99%. The model did not require absorption in excess of the Galactic value, therefore we believe the improvement in the fit when using `model E` is due entirely to the soft excess component. We adopted this model as the best fit model for the source although the χ^2 of the fit was slightly worse than the value obtained with Γ fully variable.

XMMU J061730.9+705955. We found a significant column density with `model C`, hence the source was classified as absorbed. However we obtained a very steep spectral slope, $\Gamma = 2.87^{+0.35}_{-0.31}$. With `model E` we obtained a better fit of the data and more typical values for the spectral parameters, although `model E` did not require intrinsic absorption. We have chosen `model E` in preference to `model C` for this source.

It is interesting to note that for some of the sources that we have analysed in this section, we found flat spectral slopes with `model A`, but they all required significant quantities of soft excess emission. This is the case for **XMMU J122206.1+752616** with measured

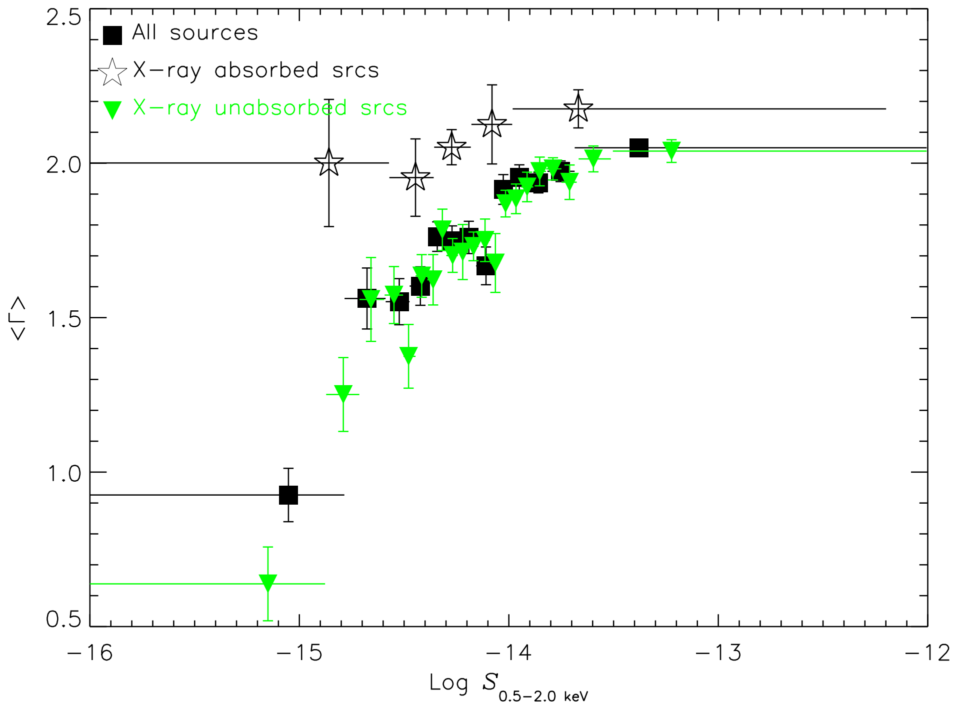

Figure 3.8: *$\langle\Gamma\rangle$ versus $S_{0.5-2\,\mathrm{keV}}$ obtained from the best fit model of each object. Squares denote the whole sample; stars absorbed sources (F-test$\geq$ 95%) and triangles unabsorbed sources (F-test$<$ 95%). Errors correspond to the 1σ confidence interval.*

`model A` spectral slope of $\Gamma = 1.52^{+0.04}_{-0.04}$. It is evident from the results of this analysis that, if soft excess emission is not properly modelled, it can affect significantly the results of the spectral fits, including the measured values of the continuum shape and the detection of other features.

3.3.4 Results from best fit model

To test whether the spectral hardening observed using `model A` is due to an increase in intrinsic absorption at the faintest fluxes, we have studied the dependence of Γ (from the best fit model of each source in terms of the F-test results) on the soft X-ray flux. The best fit model can be `model A` or `model B` for unidentified sources, `model A` or `model C` for identified sources and `model D` or `model E` for objects with detected soft excess emission. Using the best fit model for each object we obtained a mean value of the spectral slope of $\langle\Gamma\rangle = 1.96 \pm 0.01$ (the unweighted value being 2.08 ± 0.04). The dependence of $\langle\Gamma\rangle$ with the soft flux is plotted in Fig. 3.8 for all sources (squares), objects with detected absorption (stars) and objects without detected absorption (triangles). We see that:

1. The average continuum of absorbed sources is significantly softer than that of unab-

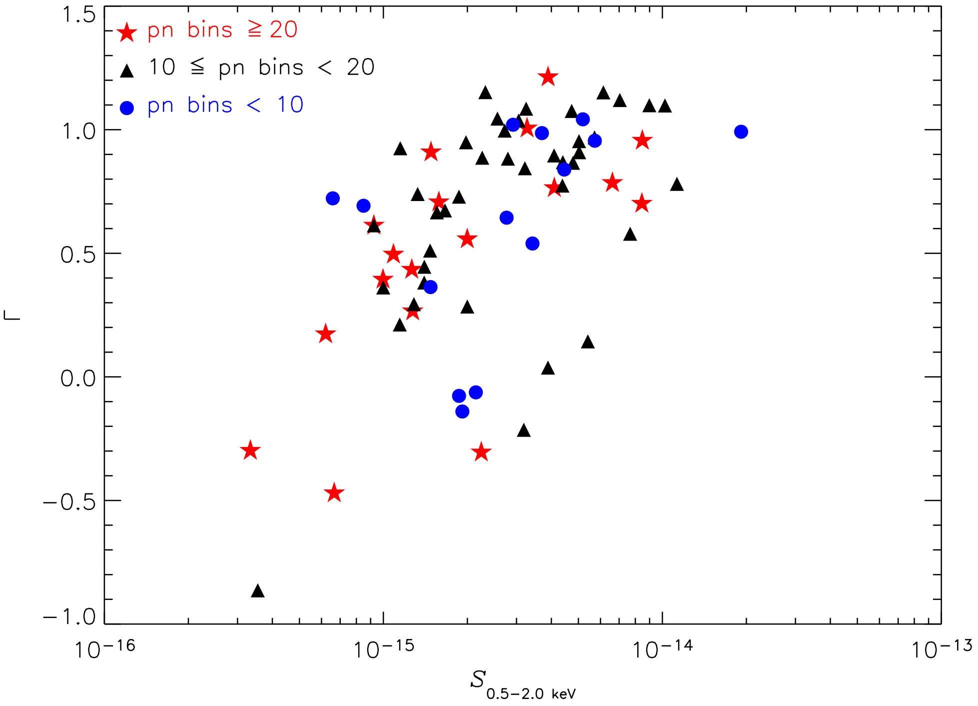

Figure 3.9: *Γ versus $S_{0.5-2\,\mathrm{keV}}$ for objects with flat spectrum (selected as those sources having Γ positive error bar <1.5). Objects were grouped in terms of the number of bins in their pn spectrum.*

sorbed sources, specially at the faintest fluxes, with $\langle\Gamma\rangle = 2.15 \pm 0.04$ (the unweighted value being 3.12 ± 0.12[2]) for the absorbed sources and $\langle\Gamma\rangle = 1.94 \pm 0.01$ (the unweighted value being 1.79 ± 0.02) for the unabsorbed sources.

2. We do not see hardening of the average spectral slope for sources with detected absorption. Therefore the hardening of ⟨Γ⟩ seen in these objects when using Γ from `model A` is likely to be an effect of absorption only.

3. For the sources where absorption was not detected in terms of the F-test, we still observe a significant hardening of the average spectral slope with the X-ray flux.

The sources where absorption is detected do not exhibit any significant variation of the underlying spectral index with flux, does this hold true for the remaining sources? We first have checked whether any effect could lead to an apparent flattening of the spectral shape towards fainter fluxes, when absorption is included in the fitting model. To this goal, we

---

[2] The unweighted mean in this case is significantly higher than the typical value found for type-1 AGN, and different from the value obtained using the weighted mean. This is due to the fact that we have a number of absorbed objects (176 with best-fit continuum slopes ≥ 2.5) which best fit Γ values higher than 2.5 but with large errors bars.

have generated a number of fake spectra with an underlying power law $\Gamma = 2$ at various fluxes spanning those of our sample, and different amounts of absorption at $z = 0$.

We have then first fitted these spectra with `model A` and `model B`, and then we have compared the χ^2 of the fits with the F-test. We found a range of low values of N_H^{obs} where absorption was not significantly detected when `model A` was replaced by `model B` (F-test significance <95%). In these cases, the best fit value of Γ (i.e., the value obtained with `model A`) was indeed lower than the input one, and it can indeed reach measured values in the range $\Gamma \sim$1-2.

A second result of this exercise is that, if we hold the absorption in the simulated spectra but vary the flux, at fainter fluxes the typical values of Γ fitted are marginally harder than at higher fluxes (and then fitted values of absorption tend to be lower than the input ones). We believe this effect to be due to a degradation of the spectral resolution of the X-ray spectrum, produced by the necessary grouping in very wide bands to achieve the desired statistics (10 counts/bin). This leads, in particular, to a smoothing of the model count rate function (which is the effective area times the input spectrum, convolved with the redistribution matrix) in the whole spectral range, but in particular in the vicinity of its peak at soft energies where most of the counts are detected. This produces an undesired slight hardening of the spectrum.

However, this effect is unlikely to produce the hardening of the unabsorbed sources that we see. The reason is that in this case we should see the lowest quality spectra (i.e., those with the smaller number of bins) being more prone to this effect, but as we showed in Sec. 3.3.1 this is not the case. Fig. 3.9 shows the sources that we detected in the real sample with flat spectra (best fit Γ error bar upper limit below 1.5), grouped in terms of the number of bins in their EPIC-pn spectra. We clearly see that the hardening is not correlated with the quality of the spectra, and therefore the above effect does not dominate.

We conclude that the hardening towards fainter fluxes is real. However, this still leaves two options for its origin: intrinsic flattening of the power law or undetected low level absorption. Although the current data do not allow us to distinguish between them, there is nothing inconsistent with the simplest hypothesis that these sources are absorbed at a level which is undetectable in the current data. This is also supported by the results of Fig. 3.3 (right) where we do not see hardening of $\langle\Gamma\rangle$ with the 2-10 keV flux down to $\sim 2\times10^{-14}\mathrm{erg\,cm^{-2}\,s^{-1}}$. If absorption is producing the hardening effect that we see in our objects, we do not expect to see the same effect using 2-10 keV fluxes, because they are less affected by absorption. Deeper observations are needed to assess this point for sources at fluxes similar to those of the sources in our sample. We will come back to this in the following chapter, with the analysis of the *Lockman Hole* spectra, of better quality than those presented in this chapter. Those results confirm that absorption is at the heart of the spectral hardening towards faint soft fluxes.

The average spectral indices for the best fit model in the samples of type-1 and type-2 AGN are 1.99 ± 0.02 and 2.35 ± 0.09 respectively. The value for type-1 AGN is in agreement with the canonical value measured for nearby unabsorbed type-1 AGN [174], while the value found for type-2 AGN seems to be slightly higher. We will address this point in more detail in Sec. 3.3.5. Both sub-samples of sources exhibit the same dependence of $\langle\Gamma\rangle$ with the soft X-ray flux as shown in Fig. 3.10. We still detect a clear correlation

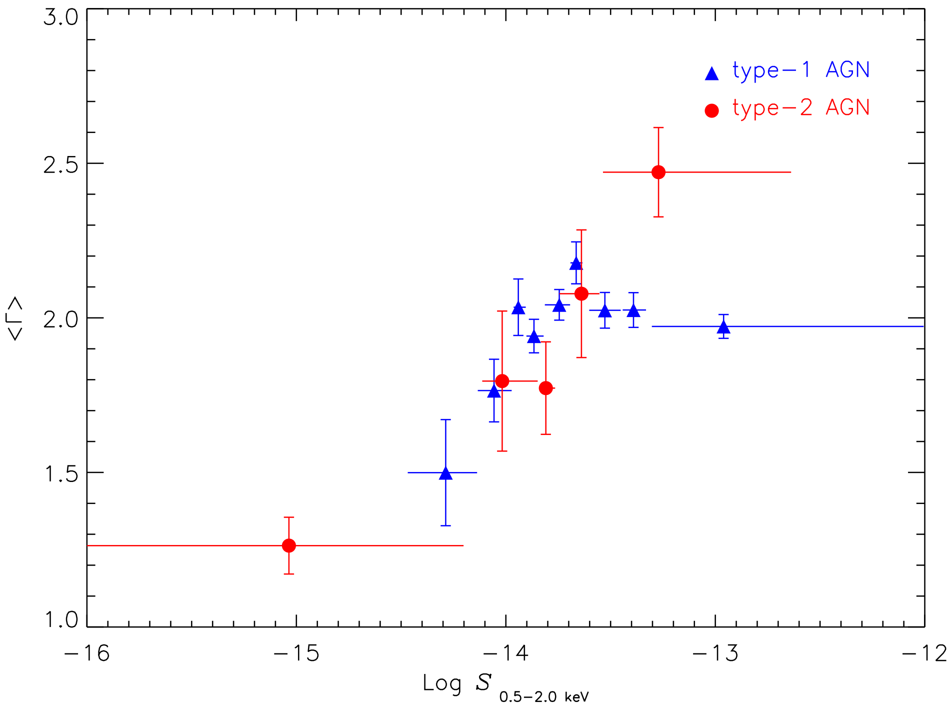

Figure 3.10: *$\langle\Gamma\rangle$ from the best fit model of each object versus $S_{0.5-2\,\mathrm{keV}}$ for type-1 AGN (triangles) and type-2 AGN (circles). A hardening of the mean spectral slope at the faintest fluxes covered by our survey is evident in both sub-samples of sources. Errors correspond to the 1σ confidence interval.*

between the mean spectral slope and the soft X-ray flux for both samples of AGN.

3.3.5 Photon index intrinsic dispersion

In all the above analysis, we have seen that a clear dispersion in the measured spectral slopes of our objects exist, even within the sub-samples of type-1 and type-2 AGN, with the largest scatter in Γ being observed for type-2 AGN. To test whether the observed scatter is intrinsic to the sources we have followed the maximum likelihood technique (ML) described in Appendix A.3 ([138] [174]), where the distribution of source spectral indices is assumed to be well reproduced by a Gaussian distribution of mean $\langle\Gamma\rangle$ and dispersion $\sigma_{\langle\Gamma\rangle}$. The distribution of best fit Γ values for all sources is shown in Fig. 3.11. We see that the assumption that this distribution can be well reproduced with a Gaussian function holds for our sample of sources except for the long tail towards steeper slopes. The same result applies to the distribution of best fit Γ values for type-1 AGN which is shown in Fig. 3.12 (left). On the other hand, for type-2 AGN the distribution of Γ has a much larger dispersion of values with a less well defined peak. Note that there is a number of outliers (sources with spectral slopes significantly higher than 2) in all the distributions of best fit spectral

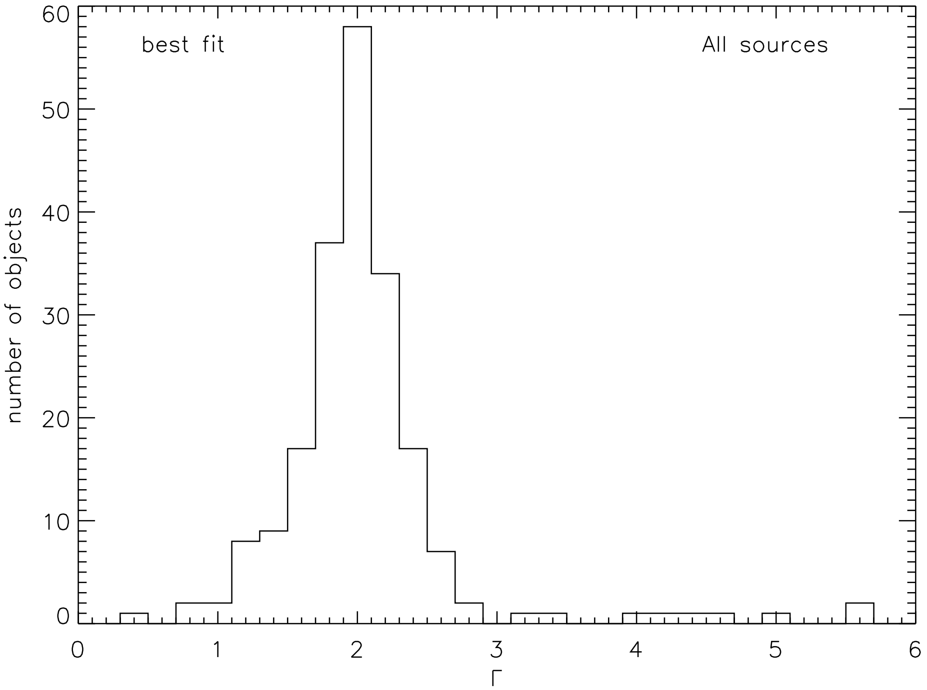

Figure 3.11: *Distribution of best fit spectral slopes for the whole sample of sources.*

slopes. The spectra of these objects have poor quality and therefore these Γ values are poorly constrained and have large error bars. This can be seen in Fig. 3.7 (right) for the outliers in the distributions of Γ for AGN. The best estimates of $\langle\Gamma\rangle$ and $\sigma_{\langle\Gamma\rangle}$ obtained with the ML technique are shown in Table 3.4. In all cases we measured a significant dispersion in spectral slopes. The large error in Γ obtained for type-2 AGN did not allow us to check whether, once we account for intrinsic dispersion in Γ, the average spectral index of type-2 AGN is still significantly different from that of type-1 AGN. We see that the mean values of Γ computed with the ML method and the weighted mean are substantially different, in particular for the type-2 AGN. The reason is that with the ML method, objects with untypical values of Γ (i.e. outliers) and not very large errors, will increase the dispersion of the fitted Gaussian distribution rather than significantly affecting the mean as we saw in Sec. 3.3.4, where the weighted mean was used.

Fig. 3.13 shows the 1σ, 2σ and 3σ contour diagrams of $\langle\Gamma\rangle$ versus $\sigma_{\langle\Gamma\rangle}$ for the subsamples of type-1 AGN (solid lines) and type-2 AGN (dashed lines), clearly showing the existence of an intrinsic dispersion in Γ with a confidence of more than 3σ in both classes of objects.

Our results do not show any trend in the underlying power law of type-2 AGN to be harder than that of type-1 AGN even at the faintest fluxes. Previous results based on *ROSAT* data (see e.g. [4] [209]) found a flatter average spectral slope for type-2 AGN

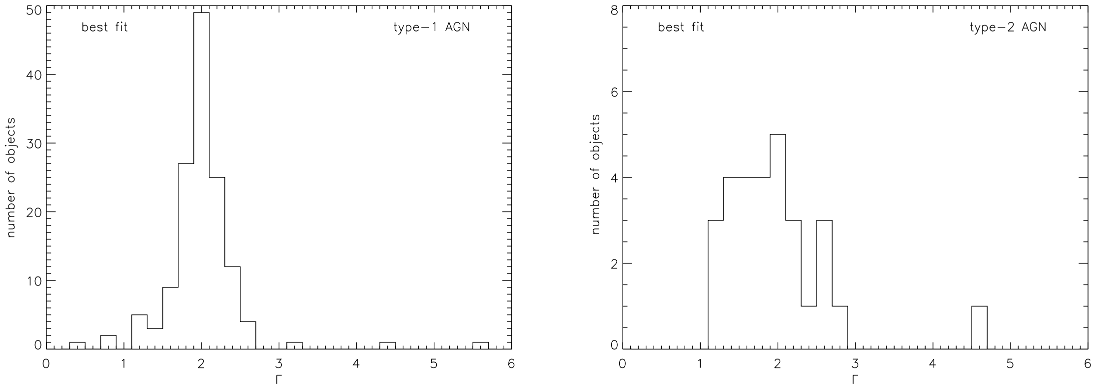

Figure 3.12: *Distribution of type-1 (left) and type-2 (right) AGN spectral slopes obtained from the best fit model of the X-ray spectrum of each source.*

(∼1.5) than for type-1 AGN (∼2). Our data shows that spectral differences between these two classes of sources are due mostly (if not totally) to different amounts of absorption, rather than to differences in the shape of the underlying power law. Therefore many objects classified as type-2 AGN have X-ray spectral properties consistent with those of type-1 AGN, but often with higher absorption.

3.3.6 Spectral cosmic evolution

No correlation was found between Γ and the rest-frame 2-10 keV luminosities (corrected for absorption), as shown in Fig. 3.14. For the sub-sample of type-1 AGN we studied the measured Γ that we obtained from each best fit model as a function of redshift. Although there have been claims of a flattening of the average spectral slope with redshift [24] [240]

Table 3.4: *Comparison of the weighted mean spectral photon index obtained for different types of sources with the values from the Maximum Likelihood analysis. Best fit spectral slopes for each object were used in the calculations. Errors correspond to the 1σ confidence interval.*

	Maximum Likelihood		Weighted Mean
Sample	$\langle\Gamma\rangle$	σ	$\langle\Gamma\rangle$
Whole sample	$1.86^{+0.02}_{-0.03}$	$0.36^{+0.01}_{-0.04}$	1.96 ± 0.01
$\mathrm{type-1\,AGN}$	$1.98^{+0.04}_{-0.04}$	$0.21^{+0.05}_{-0.04}$	1.99 ± 0.02
$\mathrm{type-2\,AGN}$	$1.85^{+0.16}_{-0.17}$	$0.36^{+0.14}_{-0.10}$	2.35 ± 0.09

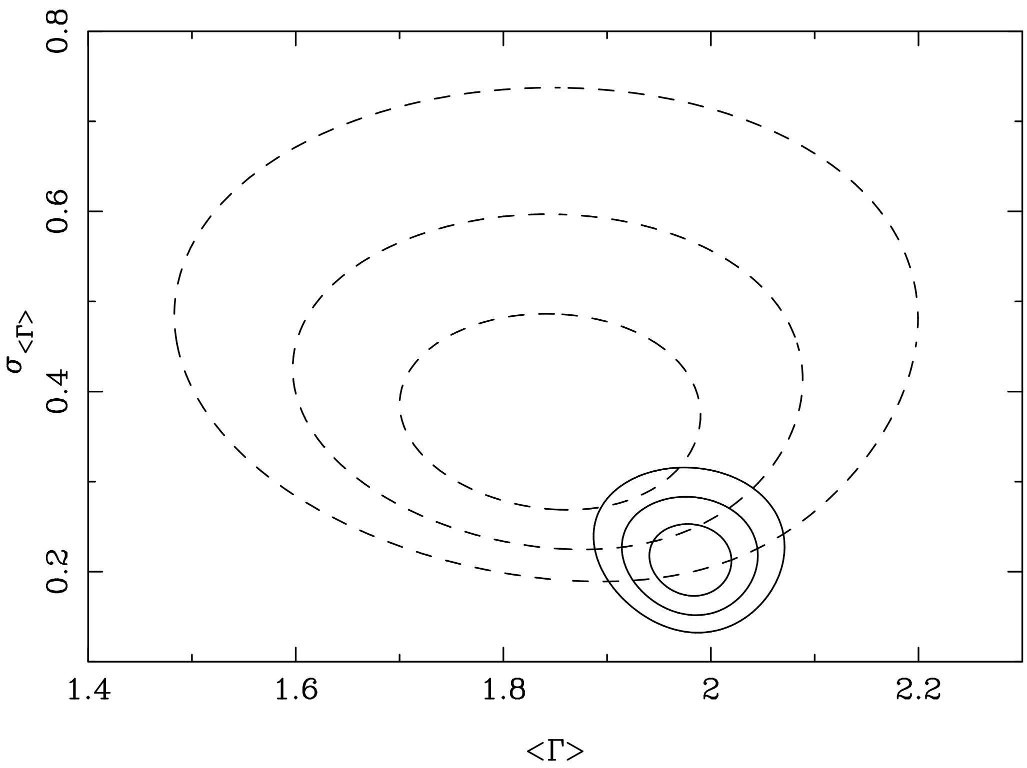

Figure 3.13: *Contour diagrams for the average spectral slope and intrinsic dispersion of our objects obtained from the Maximum Likelihood analysis (see Sec. 3.3.5). The spectral slopes obtained from the best fit model were used in the calculations. Solid line for type-1 AGN and dashed line for type-2 AGN. The contours are defined as* $\Delta\chi^2$*=2.3, 6.17 and 11.8 corresponding to standard 1,2 and* 3σ *confidence regions for two parameters.*

we did not find any clear correlation between these two parameters in our sample of type-1 AGN as we show in Fig. 3.15.

We have studied the redshift distribution of the measured rest frame absorbing column densities for the absorbed sub-samples of type-1 and type-2 AGN. The results, shown in Fig. 3.16, show no evidence for evolution of $\mathrm{N_H^{intr}}$ with redshift. However, the ranges of the 2-D parameter space that we fully sample with our source list are difficult to quantify.

We expect the minimum detected absorption to increase with redshift. This can be easily explained in terms of absorption being redshifted towards lower energies and further decreased by a factor $(1+z)^{2.7}$ (see Sec. 2.6.1) as we move upwards in z.

To study whether there exists a maximum detected column (only the brightest sources being actually detectable when heavy absorption is present), and whether this limit depends on redshift, we have carried out simulations as follows.

A 3-D parameter space was defined with the axes being redshift, luminosity and intrinsic (rest-frame) absorption. For each parameter we defined a grid of values covering the observational limits established by our sources. For each point in the $\mathrm{N_H^{intr}}$-z plane and for

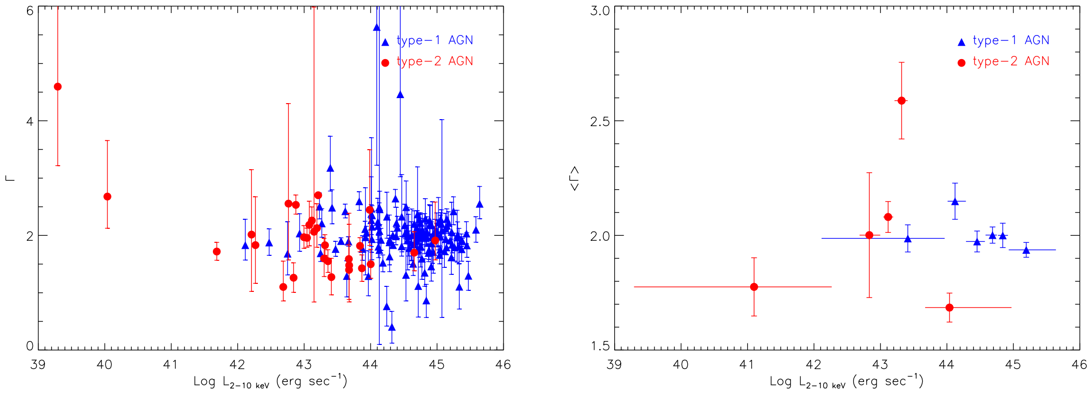

Figure 3.14: *Left: best fit* Γ *values versus* $\mathrm{L}_{2-10\,\mathrm{keV}}$ *for type-1 AGN (triangles) and type-2 AGN (circles). Errors correspond to the 90% confidence interval. Right: weighted* $\langle\Gamma\rangle$ *versus* $\mathrm{L}_{2-10\,\mathrm{keV}}$ *for type-1 AGN (triangles) and type-2 AGN (circles). Errors correspond to the 1*σ *confidence interval.*

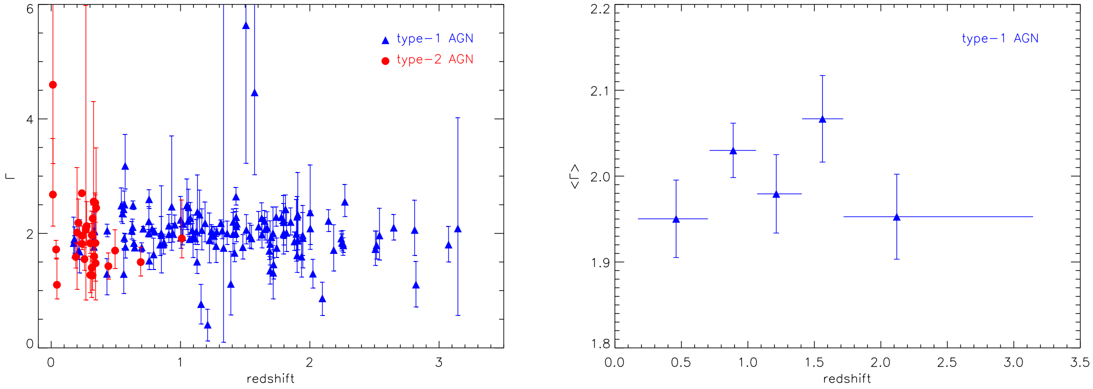

Figure 3.15: *Left:* Γ *values versus redshift for type-1 AGN (triangles) and type-2 AGN (circles). Errors correspond to the 90% confidence interval. Right: weighted* $\langle\Gamma\rangle$ *in bins of redshift for type-1 AGN. Errors correspond to the 1*σ *confidence interval. To make these plots we have used the values of* Γ *from the best fit model for each object (i.e. with absorption and soft excess if required).*

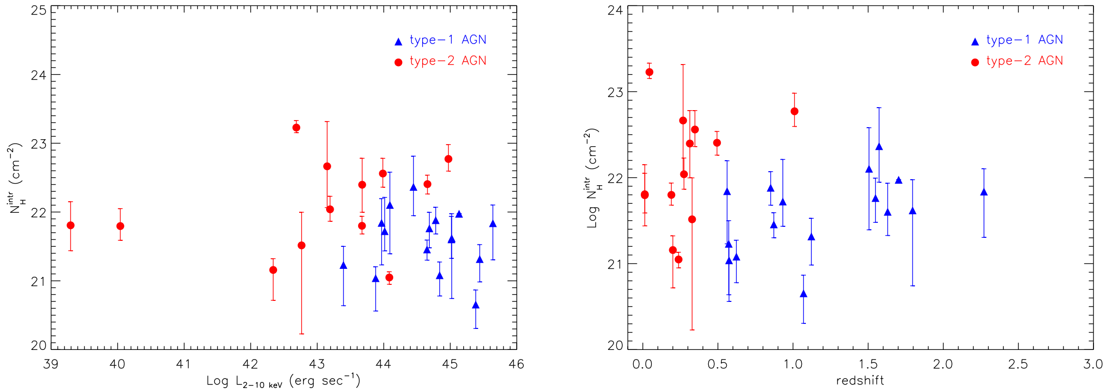

Figure 3.16: *Left: intrinsic (rest-frame) absorption as a function of* $\mathrm{L}_{2-10\,\mathrm{keV}}$ *for absorbed (F-test significance ≥95%) type-1 AGN (triangles) and type-2 AGN (circles). Right: intrinsic (rest-frame) absorption as a function of redshift for absorbed (F-test significance ≥95%) type-1 AGN (triangles) and type-2 AGN (circles). Errors correspond to the 90% confidence interval.*

each type-1 AGN and type-2 AGN we simulated a spectrum using the response matrices and exposure times of the corresponding real sources and assuming Γ=2 for all sources. As explained in Sec. 3.1 we have analysed only those spectra with more than 50 counts (background subtracted). We use this limit to calculate the required minimum luminosity for each source in order to fulfil this constraint. Luminosities lower than this value would produce a spectrum outside our quality bounds.

Second, for a number of luminosities above this limit (and for each value of absorption and redshift) we simulated a spectrum for every source. These spectra were analysed following the same procedure as for real sources giving a full coverage of the above 3-D parameter space.

We then examined the fitted values of $\mathrm{N}_\mathrm{H}^\mathrm{intr}$ as a function of redshift for a range of luminosities. The simulations confirm that the minimum detected column density depends strongly on z because the absorption is redshifted out of the observed band, as explained before. We also found two limits to the maximum amount of absorption detected as a function z. The first one is the source detection itself: heavy absorption reduces significantly the flux of the source, and makes its detection more difficult, specially for higher redshift (fainter) sources. The second limit is the detection of absorption: even if the source is detected, if its luminosity is not high enough, we will measure a column density of absorption smaller than the real one, and below the detection limit just explained.

This strong dependence on luminosity and redshift makes it very difficult to derive the real absorbing column distribution in terms of the fitted values. The best way we found to tackle this problem is to compare our results with predictions of specific models for the distribution of absorbing columns, folding the input values through the same effects as the real data. This is discussed in Sec. 3.4 in the framework of unified AGN models for the XRB.

3.4 Testing population synthesis models

Standard population synthesis models of the XRB, based on unification schemes of AGN, can reproduce successfully the XRB with an appropriate mixture of unobscured and obscured AGN, as well as a number of observational constraints. One of the input parameters of these models is the X-ray spectrum of type-1 and type-2 AGN and its cosmological evolution. In general the models assume the intrinsic unabsorbed spectrum to be identical in both classes of sources. The X-ray luminosity function of absorbed objects is still unknown, but it is assumed to be the same as for unabsorbed objects which is well known since *ROSAT* [164]. The ratio of absorbed to unabsorbed AGN predicted by these models comes out to be rather large. A key descriptor of these models is the distribution of absorbing column densities among sources. The $\mathrm{N_H^{intr}}$ distribution is now observationally known for local Seyfert galaxies [207], and in general these models assume it to be independent of redshift and luminosity (with the exception of the Ueda et al.(2003) model [235]).

The analysis that we have conducted has allowed us to measure the distribution of absorption in one of the largest samples of type-1 and type-2 AGN studied up to now, and its cosmic evolution over a wide range of redshifts. In Sec. 3.3.4 we reported that the measured absorption is slightly lower than the real one, depending on the luminosity and redshift of the source. Hence, in order to compare the predictions of XRB models to our data, we assumed an input distribution for $\mathrm{N_H^{intr}}$ (independent of luminosity and redshift), and then fold it through the same detection effects as in our data.

We have used the $\mathrm{N_H^{intr}}$ distributions adopted by Comastri et al.(1995) [44], Gilli et al.(2001) [84] and Pompilio, La Franca & Matt (2000) [193], as input parameters to their analytical models of the XRB. We have simulated spectra for each type-1 and type-2 AGN included in our list, by fixing their redshifts, exposure times, position and luminosities. The slope of the continuum was assumed to be Γ=2 for all sources as in the simulations work of previous section. For each source we extracted $\mathrm{N_H^{intr}}$ values from the specific model distribution, until the simulated spectrum fulfilled the quality filters that we used for the real spectra (binned spectra with at least 5 bins and source net counts above 50). Indeed, heavily obscured sources do not pass our quality filters, just as happens for real sources. We fitted the simulated spectra with `model A` and `model C` using the same calibration matrices, and computed F-test significances for detection of absorption.

Fig 3.17 (left) compares the distribution of values of $\mathrm{N_H^{intr}}$ measured in the real data and in the simulations for the XRB model of Gilli et al.(2001) [84]. Obviously, the adopted distribution is not able to reproduce our observational results. Very similar graphs are obtained for the models of Comastri et al.(1995) [44] and Pompilio et al.(2000) [193]. For all three models we found a clear excess of sources with intrinsic absorptions $\mathrm{N_H^{intr}} \geq 10^{22}\,\mathrm{cm^{-2}}$, which are not present in our real data. For an F-test confidence level of $\geq$ 95% we detect, in our real sample, absorption in 29 sources out of 179. The number of absorbed sources detected in the simulated data sets were 79, 67 and 71 for the Comastri et al.(1995) [44], Gilli et al.(2001) [84] and Pompilio et al.(2000) [193] distributions, in all cases a factor of more than 2.5 over the observed value. This result is also evident from Fig 3.17 (right), where the predicted distribution of absorbing columns with the Gilli et al.(2001) [84] model is plotted against redshift. We find an excess of absorbed objects all

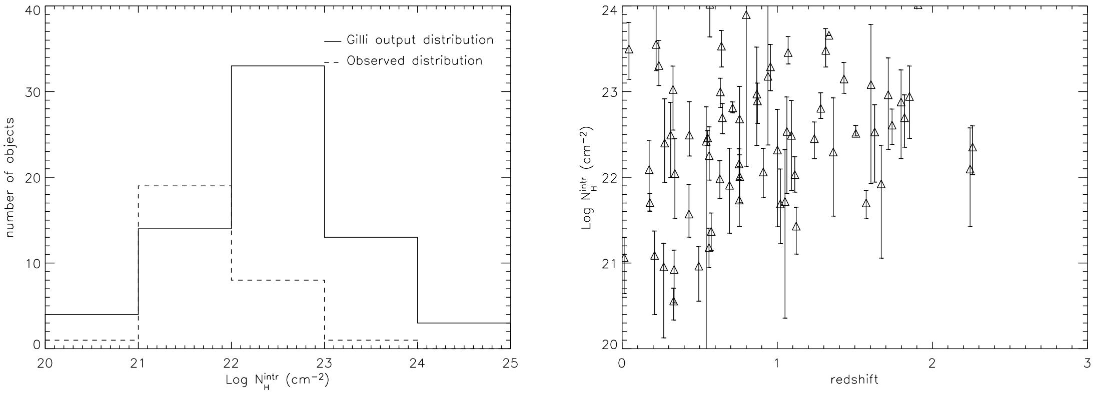

Figure 3.17: *Left: Histograms of column density distributions in absorbed objects obtained from a simulated input distribution of* $\mathrm{N_H^{intr}}$ *according to the model of Gilli et al.(2001) [84]. The dashed histogram represents the observed distribution for our sources. Right:* $\mathrm{N_H^{intr}}$ *as a function of sources' redshifts from simulations. Errors correspond to the 90% confidence interval.*

over the redshift interval covered by our data up to redshifts of ~2. Discrepancies between the predictions from synthesis models and what it is obtained from observations have been observed previously [30] [72] [187] [190].

In the recent "modified unified scheme" of Ueda et al.(2003) [235] the AGN absorbing column density distribution depends on luminosity (not redshift dependence), with the fraction of absorbed AGN ($\mathrm{N_H} > 10^{22}\,\mathrm{cm^{-2}}$) decreasing significantly with luminosity. This model will reduce the observed discrepancies with our data fundamentally at high luminosities, and therefore at high redshifts. However, the XRB model of Ueda et al.(2003) predicts a significant fraction of objects with $\mathrm{N_H} > 10^{22}\,\mathrm{cm^{-2}}$ at the typical luminosities of our sample, that we do not detect. The Ueda et al.(2003) [235] model, although more in line with our results, still overpredicts the number of absorbed objects ($\mathrm{N_H} > 10^{22}\,\mathrm{cm^{-2}}$) especially at low redshifts.

One possible caveat is that some of these absorbed sources, that we do not detect in the real spectra, might be hiding within the unidentified sources. Our simulations indicate that ~40% should have detectable absorption. However, even for the full sample of 1137 objects we only detect absorption in 10-20% of them. Assuming that the redshift distribution of the identified sources does not strongly deviate from the true one (and there is evidence that this is the case by comparing our distribution with others from more complete surveys [91]), then 40% of absorbed sources predicted by the simulations should also be found in the whole sample, while only ~20% are seen. This confirms that XRB synthesis models predict twice as many absorbed sources at our flux levels than we actually observe.

3.5 Summary

We have conducted a detailed analysis of the broad band spectral properties of a large sample of sources detected serendipitously with the *XMM-Newton* observatory. Various spectral fitting models have been tested in order to reproduce the 0.2-12 keV emission of our sources.

Fitting the spectra of all sources with a single power law, `model A`, we obtained a weighted mean of $\langle\Gamma\rangle = 1.86 \pm 0.02$, in good agreement with previous surveys. However we found that for a significant number of sources, the quality of their fits was very poor, with 7-12% of the sources having statistically unacceptable fits (null hypothesis probability <5%).

In addition, using `model A` we found a strong dependence of the continuum average spectral slope with soft (0.5-2 keV) flux, the observed effect being a hardening of the mean spectra of our sources with decreasing flux. We saw the same results using only sources with best spectral quality, and hence we concluded that this effect is not produced by the sources with lowest spectral quality. We performed simulations to calculate the efficiency function of detection of sources as a function of the spectral slope and X-ray flux. After correcting our data with the calculated selection function for all the biases that could be affecting our results, we still saw the same dependence, therefore we concluded that the hardening of the mean spectral slope with decreasing soft flux is real.

Many objects in our sample exhibit absorption in excess of the Galactic value. In terms of the F-test (95% confidence level), we found the fraction of objects in our sample with detected excess absorption to be 17%. Objects with detected X-ray absorption were found both among type-1 AGN (~6%) and type-2 AGN (~40%), i.e. **excess absorption was detected in a fraction of type-1 AGN, while not all type-2 AGN were found to be X-ray absorbed**. For these absorbed type-1 AGN and unabsorbed type-2 AGN there seems to be an apparent mismatch between their optical and X-ray spectral properties, the apparent mismatch **suggesting that AGN unification schemes might need some revision.**

The distributions of absorbing column densities detected in type-1 and type-2 AGN do not appear significantly different within the limitations of our sample, except for the overall factor that **type-2 AGN are 4 times more frequently absorbed than type-1 AGN.**

The typical absorption columns derived for type-1 AGN ($N_H < 10^{22}\,\mathrm{cm}^{-2}$) indicate that perhaps the host galaxy, or some sort of weak distant absorber, might provide the absorbing gas, without blocking too much the line of sight to the BLR. However this point deserves further exploration.

Using the best fit model for each object, i.e., including absorption and soft excess when required by the data, we still detected a substantial hardening of the average spectral index towards fainter soft fluxes. The same effect was also observed for the sub-samples of type-1 and type-2 AGN. With the current data quality, we cannot distinguish between these sources having the same underlying power law ($\Gamma\sim2$) with moderate absorption, and that there is a population with genuinely flatter spectral index. However, when hard fluxes are used to study this effect, there is no evidence for a change of average spectral slope. This supports the hypothesis that **absorption is producing the hardening of the average spectra of our sources**, because hard band fluxes are less affected by absorption. In addition, this is consistent with the results of the X-ray spectral analysis of a sample of objects at the same fluxes detected in the *Lockman Hole* field that will be presented in Chapter 4, and for which the data have much higher signal-to-noise ratio, allowing a better detection of signatures of X-ray absorption.

Using a maximum likelihood fit, where the distribution of continuum slopes is assumed to be well reproduced with a Gaussian function, we detected significant intrinsic dispersion of the measured spectral slopes of our sources, and also in both sub-samples of type-1 and type-2 AGN. The largest scatter was observed for the distribution of spectral slopes of type-2 AGN. **Once we account for the intrinsic dispersion of the mean continuum, our results do not show any trend in the underlying power law of type-2 AGN to be harder than that of type-1 AGN, i.e. the observed spectral differences among both samples of objects are due mostly to different amounts of absorption, rather than to differences in the shape of the underlying power law.**

We did not find a tendency for absorbed type-1 AGN to occur preferentially at any particular redshift. The same result is obtained when comparing the 2-10 keV luminosity distributions of absorbed and unabsorbed type-1 AGN and type-2 AGN. Therefore, **no evidence was found for unabsorbed type-1 and type-2 AGN having different X-ray luminosities to the absorbed objects.**

The standard unified model of AGN predicts that all type-2 AGN should exhibit photoelectric absorption that is obscuring their nuclear emission and their BLR. However we have detected a significant fraction of unabsorbed type-2 AGN in our sample. This result can be explained if these sources have a weak or lack a BLR so they do not need to be absorbed to show only narrow lines, as we see from the X-ray spectral analysis. This is more likely for low luminosity AGN where the low luminosity of the nuclear region may be unable to ionise the BLR. Another possibility is that they are absorbed, but the absorber has non-standard properties, for example a low gas-to-dust ratio. This hypothesis seems to work in some sources [142]. We have seen that our unabsorbed type-2 AGN are on average less luminous than the unabsorbed type-1 AGN, and hence **our data are consistent with the explanation of the lack of observed broad lines in the optical spectra of unabsorbed type-2 AGN as an AGN/ host-galaxy contrast effect.** Another hypothesis is that, since our unabsorbed type-2 AGN are less luminous, the nuclear emission in these sources is not high enough as to ionise the BLR clouds. From this second hypothesis we would expect a dependence of the fraction of unabsorbed type-2 sources with luminosity, with the fraction being higher for the lowest luminosity sources. However the number of type-2 objects in our study is not high enough to test this hypothesis.

A soft excess component was detected with a high significance in $\sim$7% of type-1 and type-2 AGN. **Using a thermal component to model the soft excess emission in our AGN its temperature is kT$\sim$0.1-0.3 keV, and independent of the luminosity of the AGN, in agreement with previous analyses. In most AGN, the luminosities of this spectral component are too large to come from starburst emission.**

For XRB synthesis models based on the AGN unified schemes, simulations were conducted to test the distribution of absorbing columns from these models on the population of type-1 AGN and type-2 AGN. In general, the number of sources where absorption was detected in the simulated spectra (in about ~40% of them) was a factor of ~2.5 above the measured values for all models. **Regardless of the incompleteness of the identifications, the XRB synthesis model prediction of detectable absorption in 40% of the sources is at odds with the overall observed rate of absorbed sources in our sample of objects (~20%).**

The distributions of absorbing column densities predicted by synthesis models and the ones measured through our simulations are significantly skewed towards high column densities $\mathrm{N_H^{intr}} \sim 10^{22} - 10^{24}\,\mathrm{cm}^{-2}$. These highly absorbed sources, predicted by XRB models at our flux levels, were not detected in our sample.

Chapter 4

X-ray spectroscopy of *Lockman Hole* sources

In order to understand better the X-ray emission properties and cosmic evolution of AGN, X-ray spectral analyses of large samples of objects detected in medium and deep X-ray surveys (in order to reach the fluxes that match the dominant population of the XRB) are being carried out (see e.g. [30] [49] [72] [140] [152] [187] [190] [189]). However, only a small number of these studies have conducted a proper spectral analysis of each individual source, and in most cases some assumptions had to be made prior to the spectral analysis (frequently on the spectral slope). Therefore most of the existing studies provide observational information with large uncertainties.

To gain insight into the overall emission properties and their dependence with redshift and luminosity for AGN, at the fluxes where the bulk of the XRB is emitted, we have conducted a detailed X-ray spectral analysis of a sample of 123 X-ray sources detected with *XMM-Newton* in the deepest observation carried out with *XMM-Newton* so far in the direction of the *Lockman Hole* field. The sources analysed have similar X-ray fluxes (flux limit $\sim 4\times10^{-15}\,\mathrm{erg\,cm^{-2}\,sec^{-1}}$) to the sources typically detected in medium X-ray surveys such as the AXIS survey (see Sec. 2.9). However, because the *Lockman Hole* survey is a deep observation, the signal-to-noise ratio of the data is much higher (more than 500 MOS+pn background subtracted counts in the 0.2-12 keV band spectra of all objects) and a more detailed study of their X-ray spectra is possible.

4.0.1 X-ray data

We report the summary of the observations used in this analysis in Table 4.1. The *Lockman Hole* was also observed during revolutions 071 (~61 ksec) and 344 (~80 ksec duration). However at the time of this analysis there was no Observation Data File (ODF) available for the observation in revolution 071, and hence, we could not reprocess the data, which was necessary in order to use the existing analysis tools. On the other hand, we could not use the data from revolution 344 because most of the observation was affected by high and flaring background. The first column in Table 4.1 shows the revolution number and observation identifier. The second column shows the name of the phase of observation (i.e. PV for observations during the Payload Verification Phase, and AO1 and AO2 for observations during the first and second Announcement of Opportunity). The third and fourth columns list the pointing coordinates of the observation. Column five lists the observation dates, while the last three columns show the filters that were used during each observation for each EPIC X-ray detector, together with the exposure times after removal of periods of high background. The 17 *XMM-Newton* observations gave a total exposure time (after removal of periods of high background) of ~850 ksec for M1 and M2 detectors and ~650 ksec for pn.

4.1 X-ray source list

The final (after visual screening) number of objects that we detected in the total *XMM-Newton* observation of the *Lockman Hole* following the procedure described in Sec. 2.3 is 268. From this sample of objects we selected the 123 brightest sources, i.e., the sources with best quality spectra. In addition, because we were mainly interested in studying the X-ray spectral properties of AGN, we did not include in the sample objects identified as clusters of galaxies or stars. In the following we will refer to the sample of 123 brightest sources as the list of *Lockman Hole* objects. A full catalogue of X-ray sources found in this observation taking full advantage of the *XMM-Newton* sensitivity is in preparation [28]. The differences between that work and ours do not affect, however, to the 123 bright sources used here.

In order to allow comparison with previous surveys conducted in the soft (0.5-2 keV) and hard (2-10 keV) X-ray bands, we checked whether our objects were detected in these bands. We have likelihoods of detection for the soft band, because this band was used for source detection. We calculated the likelihoods in the hard (2-10 keV) band combining the likelihoods of bands 2-4.5 keV, 4.5-7.5 keV and 7.5-12 keV following the recipe described in Sec. 2.3. This will give us the detection likelihood for the objects in the 2-12 keV energy band. However, because the effective area of the X-ray telescopes decreases rapidly at hard energies, we do not expect the detection likelihoods in band 2-12 keV to differ substantially from those values in the 2-10 keV band. Note however that these detection likelihoods are not exactly the same as the ones we would obtain by running the source detection algorithm in the 2-10 keV band. By selecting a threshold in likelihood of 10 we obtained that the number of objects that were detected in both the soft and hard bands was 117 (out of 123). Three objects were only detected in the hard band, while three were only detected in the soft band. These numbers indicate that the source population that we are studying is detected in the two bands, and therefore our list of sources is also representative of a hard or soft band survey at similar fluxes.

Table 4.1: *Summary of XMM-Newton observations in the Lockman Hole.*

Rev/ObsId (1)	obs phase (2)	R.A. (3)	Dec (4)	obs. date (5)	Filter/GTI (6) pn	MOS1	MOS2
070 / 0123700101	PV	10 52 43.0	+57 28 48	2000-04-27	Th/34	Th/34	Tck/33
073 / 0123700401	PV	10 52 43.0	+57 28 48	2000-05-02	Th/14	Th/14	Tck/14
074 / 0123700901	PV	10 52 41.8	+57 28 59	2000-05-05	Th/5	Th/8	Tck/5
081 / 0123701001	PV	10 52 41.8	+57 28 59	2000-05-19	Th/27	Th/36	Tck/28
345 / 0022740201	AO1	10 52 43.0	+57 28 48	2001-10-27	M/40	M/37	M/24
349 / 0022740301	AO1	10 52 43.0	+57 28 48	2001-11-04	M/35	M/34	M/31
522 / 0147510101	AO2	10 51 03.4	+57 27 50	2002-10-15	M/79	M/81	M/55
523 / 0147510801	AO2	10 51 27.7	+57 28 07	2002-10-17	M/55	M/56	M/46
524 / 0147510901	AO2	10 52 43.0	+57 28 48	2002-10-19	M/55	M/57	M/50
525 / 0147511001	AO2	10 52 08.1	+57 28 29	2002-10-21	M/78	M/79	M/61
526 / 0147511101	AO2	10 53 17.9	+57 29 07	2002-10-23	M/45	M/52	M/27
527 / 0147511201	AO2	10 53 58.3	+57 29 29	2002-10-25	M/30	M/34	M/23
528 / 0147511301	AO2	10 54 29.5	+57 29 46	2002-10-27	M/28	M/33	M/14
544 / 0147511601	AO2	10 52 43.0	+57 28 48	2002-11-27	M/104	M/103	M/68
547 / 0147511701	AO2	10 52 40.6	+57 28 29	2002-12-04	M/98	M/98	M/89
548 / 0147511801	AO2	10 52 45.3	+57 29 07	2002-12-06	M/86	M/86	M/72

Columns are as follows: (1) *XMM-Newton* revolution and observation identifier; (2) Observation phase: Verification Phase (PV), first and second announcements of opportunity (AO1 and AO2); (2) and (3) pointing coordinates right ascension and declination (J2000); (4) Observation date; (5) For each EPIC camera blocking filter[a] used during the observation and good time interval after subtracting periods of the observation affected by high background flares.

[a] Blocking filters: Th: Thin at 40nm A1; M: Medium at 80nm A1; Tck: Thick at 200nm A1

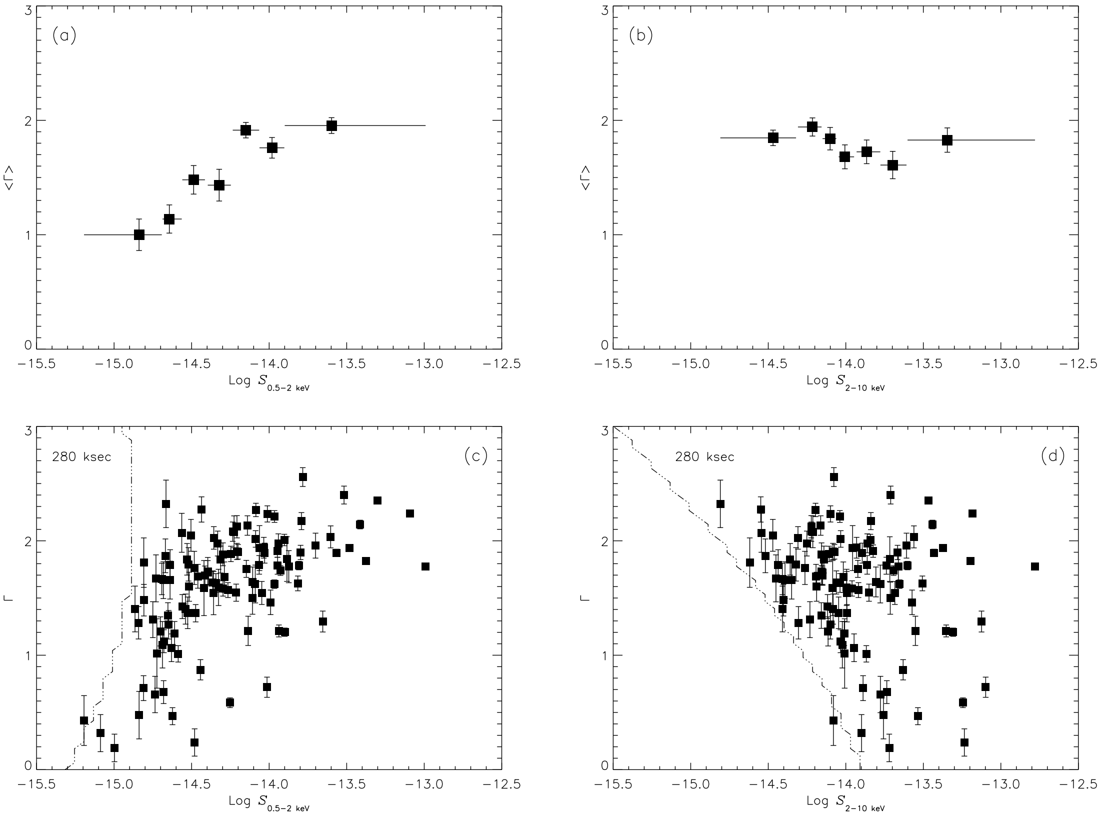

Figure 4.1: *Dependence of* Γ *with soft (0.5-2 keV) and hard (2-10 keV) flux when all spectra are fitted with a single power law model. In plots (a) and (b) we show the dependence of the weighted mean (with the error of each individual value). The bins in flux were defined in order to have the same number of sources per bin. Errors correspond to the* 1σ *confidence interval. In plots (c) and (d) we show the values of* Γ *for each individual source. Errors correspond to the 90% confidence interval. The dash-dot lines in these plots show for an exposure time of 280 ksec the limit in flux for detection of an object as a function of* Γ *(see Sec. 4.3 for details).*

Spectra for each source, EPIC camera and observation were extracted in the energy range from 0.2 to 12 keV (where the EPIC detectors are best calibrated) following the method described in Sec. 2.5. In order to increase the signal-to-noise ratio of the data M1 and M2 spectra were combined. MOS and pn co-added spectra were obtained for each object following the recipe of Appendix D.1. In order to use the χ^2 minimisation during the spectral fitting, we grouped the spectra with a minimum of 30 counts per bin. At the time of this analysis, 74 (~60%) of the sources had optical spectroscopic identifications. Of these, 46 were classified as type-1 AGN and 28 as type-2 AGN.

4.2 Spectral analysis

We have used the `Xspec11.3.0` software package to fit the X-ray spectra of our objects. MOS and pn co-added spectra were fitted simultaneously and with the same spectral model, including the normalisation. At the time of our analysis it was found that there was an offset of ~1 arcmin between the optical axis of the three EPIC instruments and the values in the calibration (CCF)[1]. This could be introducing discrepancies between MOS and pn effective areas due to an incorrect vignetting correction. These flux discrepancies could be as high as ±14% at the largest offaxis angles. However, we did not find a significant improvement in the quality of our fits when different normalisations were used to fit MOS and pn spectra. There were objects where we found large offset between the normalisations, but it had indeed a different origin. In fact we interpreted this effect as changes in flux of the sources during the observations (notice that the co-added spectra of MOS and pn in the majority of the cases were not necessarily built with the same set of observations, because the FOV and the positions of the gaps are different for MOS and pn, and in different observations). Significant changes in flux between observations, with typical variability amplitudes ~20%, were detected in the great majority of the objects, as we will see in more detail in the next chapter.

The X-ray spectral fitting has been carried out in two steps. First, we have fitted the spectra of all sources with a single power law model (`model A`). This enabled us to compare our results with previous spectral analyses of data with lower signal-to-noise ratio such as the analysis presented in the previous chapter. `Model A` includes the effect of photoelectric absorption by our Galaxy, N_H^{Gal}, which we fixed to the 21cm value ($5.7 \times 10^{19}\,\mathrm{cm}^{-2}$) for all sources [53]. Thanks to the good quality of the data, we can study in more detail the origin of the hardening of the average spectral slope of AGN with soft X-ray flux found in AXIS sources, and see whether the same effect is also present if 2-10 keV fluxes are used instead. In order to quantify the contribution of X-ray absorption to the hardening of the average spectra of the sources with flux, we fitted the spectra of our sources with an absorbed power law (`model B`).

Finally, we studied the spectra of each object individually in order to obtain the best fit model for each source. This analysis will allow us to quantify the occurrence of additional spectral components, such as soft excess emission, in the spectra of faint AGN. The signal-to-noise ratio of the spectra of our objects allowed us to search for soft excess emission and Fe Kα emission line complex signatures in most of the objects.

We used the F-test to measure the significance of detection of spectral signatures in the sources emission. We have chosen a confidence level threshold of 95% (the same threshold as we used for the spectral analysis of AXIS sources) to accept an additional spectral component as being real.

---

[1] `http://xmm.vilspa.esa.es/docs/documents/CAL-SRN-0156-1-3.ps.gz`.

4.3 Broad band continuum shape

The results of the fits using `model A` have been used to help understanding the observed dependence of the mean continuum shape of our sources with soft (0.5-2 keV) X-ray flux. The results for *Lockman Hole* sources are plotted in Fig. 4.1. In plots (a) and (b) we show the dependence of $\langle\Gamma\rangle$ with 0.5-2 keV and 2-10 keV fluxes. Bin sizes were defined in order to have the same number of objects per bin and therefore they may not have the same size. When a single power law model is used, we see that the average continuum shape becomes harder with 0.5-2 keV decreasing flux as we observed for AXIS sources. However, it is interesting to note that we do not see any dependence of $\langle\Gamma\rangle$ with the 2-10 keV flux down to $\sim 3\times10^{-15}\,\mathrm{erg\,cm^{-2}\,s^{-1}}$. This also confirms that the softening of the mean spectral slope for faint AXIS sources, when calculated as a function of the hard X-ray flux, was indeed a selection effect of AXIS objects. The values of $\langle\Gamma\rangle$ and corresponding 1σ errors were obtained using the expressions of Appendix A.2. Using these expressions we found the weighted mean for our objects to be $\langle\Gamma\rangle$=1.79 ± 0.03 when their spectra is fitted with `model A` (the value is 1.60±0.05 if we use the unweighted mean).

In order to understand better the origin of the hardening of $\langle\Gamma\rangle$ with the 0.5-2 keV flux, and the reason why we do not see the same effect using 2-10 keV fluxes, we have plotted in Fig. 4.1 the mean continuum slope as a function of the flux (plots (a) and (b)) and also the values of Γ that we obtained for each individual object (plots (c) and (d)) . Thanks to the good quality of our data it is possible to see that $\langle\Gamma\rangle$ becomes harder with the 0.5-2 keV flux because at faint fluxes a population of faint sources with very hard ($\leq$1) spectral slopes arises. We also see that the number of faint hard objects becomes more important as we go to fainter soft fluxes. On the other hand, we do not see hardening of $\langle\Gamma\rangle$ with 2-10 keV flux because these hard objects are detected at all 2-10 keV fluxes and their number does not seem to vary with flux, apart from a cutoff at $\sim10^{-14}\,\mathrm{erg\,cm^{-2}\,s^{-1}}$ (see below).

We have studied whether our criteria for selection of objects (i.e. MOS+pn background subtracted counts above 500) could be introducing any bias in our results, in particular whether, for a given flux, we are favouring objects with a given spectral slope. To study this, we have carried out simulations. We first have defined a grid of points in Γ and flux, S (first using 0.5-2 keV flux and later 2-10 keV flux), covering the same range of Γ-S values as our sources. Using on-axis response matrices, ARF and RMF, and typical background spectra selected from one of our objects, we simulated a spectrum on each grid cell, and then we calculated the minimum exposure time that is needed to reach the threshold in number of counts that we have used to select our sources. With these simulations we were not interested in quantifying the detection limits as a function of X-ray flux and spectral slope, but to study the biases in our sample, and whether they affect our results. Therefore we only need to do one simulation on each grid cell and then we just have to search for the points in the Γ-S grid with constant exposure time.

For a constant exposure time of 280 ksec the dot-dash lines in plots (c) and (d) on Fig. 4.1 represent the values of Γ and S that are required to obtain 500 counts in the simulated spectra. We see that in the soft band, for a given flux, we have the same efficiency of detection for different values of Γ down to 1.5. At fluxes above $\sim10^{-15}\,\mathrm{erg\,cm^{-2}\,s^{-1}}$ we did not find any detection bias that could contribute to the observed hardening of $\langle\Gamma\rangle$.

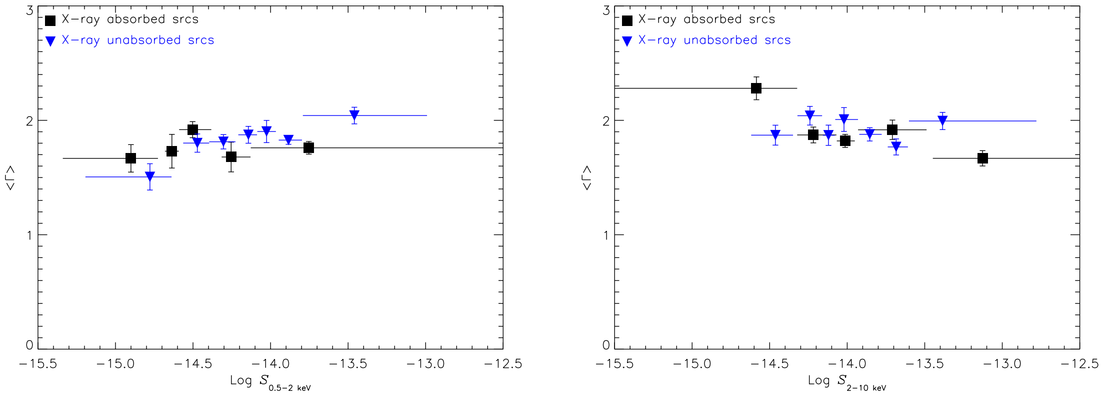

Figure 4.2: *Dependence of $\langle\Gamma\rangle$ with 0.5-2 and 2-10 keV flux for absorbed (F-test $\geq 95\%$) and unabsorbed (F-test $< 95\%$) sources. For each source we used Γ and S from its best fit model (*`model A`* or *`model B`*). Errors correspond to the 1σ confidence interval.*

Only the bin at the faintest 0.5-2 keV fluxes (panel a) could be affected by a detection bias. Therefore our simulations showed that the hardening in $\langle\Gamma\rangle$ is an intrinsic property of our objects. The objects responsible for the hardening of $\langle\Gamma\rangle$ can be sources with larger absorption or with intrinsically harder spectra.

In the 2-10 keV band we obtained different results from the simulations. At the faintest fluxes objects with soft spectra are better detected. This is an expected result because the effective area decreases rapidly at hard energies and therefore it is more difficult to detect faint objects with flat spectral slopes. However, down to the flux level where we start to loose faint hard objects, $\sim 6 \times 10^{-15}\,\mathrm{erg\,cm^{-2}\,s^{-1}}$, we see that there is no dependence of Γ with hard flux because, as we said before, hard objects are detected at all fluxes.

We conclude that none of the detected dependences of $\langle\Gamma\rangle$ on the soft or hard X-ray flux are associated with selection effects in our sample of objects.

4.4 Excess absorption

In order to study the nature of the population of faint hard sources responsible for the hardening of $\langle\Gamma\rangle$ with the 0.5-2 keV flux we have fitted the spectra of all objects with an absorbed power law model, `model B`. Using this spectral model when needed we obtained a value for the weighted mean of $\langle\Gamma\rangle = 1.87 \pm 0.04$ (the value being $\langle\Gamma\rangle = 1.95 \pm 0.08$ when using the arithmetic mean) for the objects where absorption was detected (51 out of 123 objects) with an F-test significance $\geq 95\%$, and $\langle\Gamma\rangle = 1.95 \pm 0.03$ (the value being $\langle\Gamma\rangle = 1.82 \pm 0.04$ when using the arithmetic mean) for the objects where we did not detect absorption (72 out of 123 objects; F-test $< 95\%$).

The dependence of $\langle\Gamma\rangle$ on 0.5-2 keV and 2-10 keV fluxes that we found fitting the spectra of our objects with `model B` is shown in Fig. 4.2. For objects where absorption

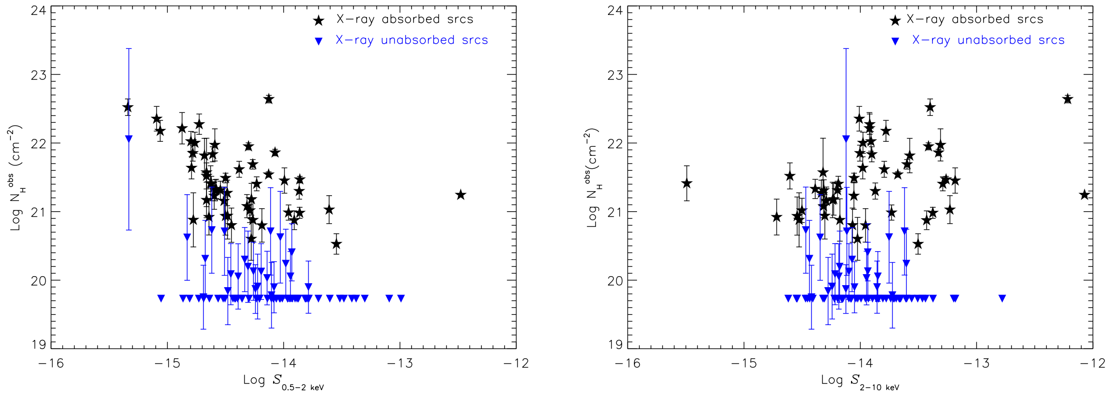

Figure 4.3: *Distribution of* N_H^{obs} *for absorbed (F-test* $\geq$ *95%; quares) and unabsorbed (F-test* $<$ *95%; triangles) objects. Errors correspond to the 90% confidence interval.*

was detected (squares) we used the spectral parameters (Γ and observed S) obtained with `model B`, while for unabsorbed sources (triangles) we used the parameters from `model A`. It is evident from the plots that absorption can account for virtually all the hardening of $\langle\Gamma\rangle$ with soft X-ray flux. We also see in Fig. 4.2 that the same dependence of $\langle\Gamma\rangle$ with X-ray flux is found for both absorbed and unabsorbed objects. We did rule out the existence of a significant population of faint sources with intrinsically harder spectral slopes down to fluxes $\sim 3 \times 10^{-15}\,\mathrm{erg\,cm^{-2}\,s^{-1}}$.

The results using hard fluxes did not vary significantly. This is exactly what we would expect if absorption produces the hardening of Γ, because 2-10 keV fluxes are less affected by absorption.

4.4.1 Dependence of excess absorption with X-ray flux

In Fig. 4.3 we plot the values of excess absorption (observer's frame) that we obtained with `model B` for both absorbed (F-test$\geq$95%; stars) and unabsorbed (F-test$<$95%; triangles) as a function of 0.5-2 keV and 2-10 keV fluxes. We see that while an anti-correlation between absorption and the observed soft flux exists, the distribution of absorbing column densities does not appear to vary with the hard flux.

We have studied whether the fraction of X-ray absorbed objects depends on the flux after correcting for the effect of absorption (the N_H^{obs} columns measured in our sample of sources will not affect the measured 2-10 keV fluxes and hence the correction of 2-10 keV fluxes is not significant). The results are plotted in Fig. 4.4 (triangles). For comparison we have plotted the results that we obtained using absorbed fluxes (circles). As expected, we do not see significant differences using absorbed or de-absorbed 2-10 keV fluxes. However important differences are seen when 0.5-2 keV fluxes are used. If we do not correct for the effect of absorption in the measured 0.5-2 keV fluxes, we find an increase in the fraction of absorbed objects at fainter fluxes. However, if de-absorbed fluxes are used instead, the

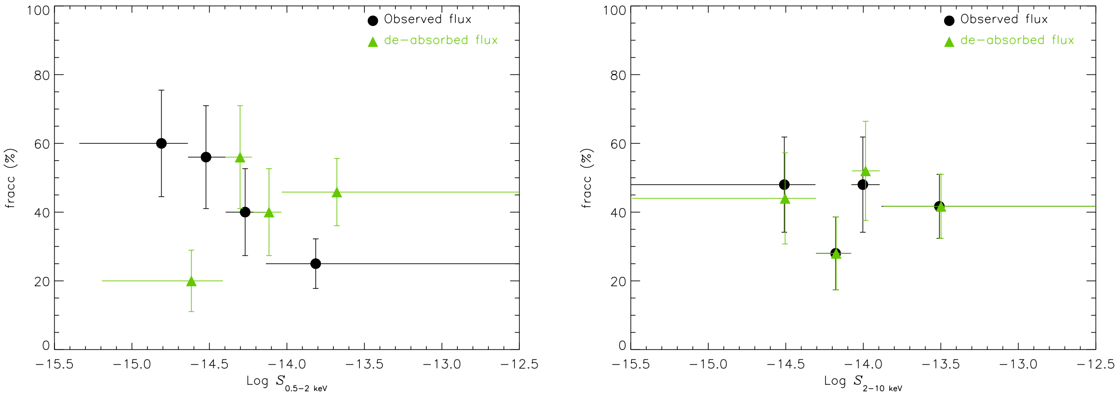

Figure 4.4: *Fraction of absorbed (F-test≥95%) objects vs 0.5-2 (left) and 2-10 (right) keV flux. For each source we used the fluxes from its best fit model (single power law or absorbed power law). Circles show the results that we obtained using observed fluxes, while the triangles show the results using fluxes corrected for the effect of absorption (see Sec. 4.4.1 for details). Errors correspond to the 1σ confidence interval.*

fraction of absorbed objects stays constant with the X-ray flux, in agreement with the 2-10 keV band results.

Note that the fraction of absorbed sources at the very faintest de-absorbed 0.5-2 keV fluxes (∼20%) is significantly lower than the values found at brighter fluxes (∼40%). The absorbed sources that should contribute to the bin at the faintest fluxes have an observed flux below the quality threshold applied to our objects, and therefore are not included in our sample (remember that to select our sources we used 0.2-12 keV counts, i.e. ∼fluxes without correction for absorption). Another effect that could also contribute to this effect is that at the faintest fluxes mild absorption might pass unadverted, but this is unlikely to be important as the mean spectral slope for unabsorbed sources does not become harder at the faintest 0.5-2 keV fluxes (see Fig. 4.2).

4.5 Overall spectral properties of *Lockman Hole* sources

Up to now we have shown the results from spectral fits where only the X-ray continuum and the intrinsic absorption were modelled. However, there are other spectral components that can also contribute significantly to the emission in the 0.2-12 keV energy band. There is evidence for them in the results that we have shown previously. For example we have seen in Fig. 4.2 that $\langle\Gamma\rangle$ does not appear to vary with X-ray flux when absorption is included in the fitting model. However we still see a scatter in the points which cannot be explained if Γ does not vary significantly with flux for the objects in our sample as our results appear to show. Such scatter is to be expected if other spectral components are present in the data (e.g. soft excess emission) and they are not properly modelled, as we saw during the

Table 4.2: *Results from the X-ray spectral analysis.*

Model (1)	N_{tot} (2)	type-1 AGN (3)	type-2 AGN (4)	Not id.[b] (5)
`SPL`	65	35	5	25
SPL + SE	4	4	0	0
APL	39	6	16	17
APL + SE	5	0	4	1
CAPL	9	1	3	5
CR	1	0	0	1
Total	123	46	28	49

Columns are as follows: (1) Best fit model: SPL: single power law (`model A`); APL: absorbed power law (`model B` for unidentified objects, `model C` for identified objects); SPL+SE: `model D` for identified objects; APL+SE: `model E` for identified objects, for unidentified objects `model E` but with black body at redshift=0; CAPL: partial covering (`model F` for identified objects; CR: Compton reflection (see Sec.4.5 for details). (2), (3), (4), (5) number of objects on each class with that best fit spectral model. [b]Objects without optical identifications.

spectral analysis of AXIS sources (see Sec. 3.3.3). Besides the soft excess, other spectral components that can contribute to the 0.2-12 keV emission are ionised absorption, the Fe Kα emission complex and the Compton reflection hump (see Sec. 1.4.2).

In order to search for these spectral components we have studied in detail the MOS and pn co-added spectra of each individual object. To model soft excess emission we used a thermal black-body model. For the objects for which we could not obtain a good fit with this, a good fit was obtained using a partial covering model (i.e., only part of the X-ray emission from the inner most region of the AGN is absorbed). The only emission line that we expect to detect with the quality of our spectra is the Fe Kα complex at 6.4-6.7 keV (rest frame energy). To search for this component we have used a Gaussian line profile, and compute the centroid (in most cases we fixed the centroid at 6.4 keV), width and normalisation of the line. Absorption signatures were found in the spectrum of one object and were modelled as an absorption edge. The most prominent spectral signature from reflection in AGN is a change in the slope of the X-ray continuum at energies above 10 keV (rest frame). This component is known as the Compton reflection hump. Unless the signatures of reflection are strong, we do not expect most of our objects to be bright enough as to detect with high significance a change in the shape of the continuum at high energies given the limited bandpass of *XMM-Newton* at these energies. To search for reflection we have added a second power law to the fit (see Sec. 2.6 for a detailed description of the different fitting models used for our spectral analysis).

A summary of the results of our spectral analysis is presented in Table 4.2 while best fit spectral parameters for each source are shown in Table 4.8. We have only included in the table information on the observed X-ray spectral properties of the objects, which is the aim of our analysis, so we have not included in the table any information on the properties of these objects at other wavelengths. In the present work we identified our objects with the same numbers that will be used in a forthcoming catalogue paper of the *XMM-Newton* deep survey in the *Lockman Hole* field [28]. Best fit parameters were obtained fitting MOS and pn spectra simultaneously. Unless otherwise required by the data, we used the same MOS and pn model normalisations. For the sources for which the spectral fit required different normalisations for the MOS and pn spectra, we list the fluxes and luminosities obtained with the spectrum with best quality.

For 65 objects (∼53%) the best fit model was a single power law (`model A`). Among these objects there were 35 type-1 AGN and 5 type-2 AGN. We detected absorption in 53 objects out of 123 (43%), including 7 type-1 AGN and 23 type-2 AGN. Table 4.3 lists the fraction of objects with detected absorption in our sample and in the samples of type-1 and type-2 AGN. These values were corrected for spurious detections[2] following the method described in Appendix A.4. We used the method described in Mateos et al.(2005a) [152] and Stevens et al.(2005) [224] and in Appendix A.4, to compare the fractions of absorbed objects in type-1 and type-2 AGN. We found the fractions to be different (the fraction of absorbed objects in type-2 AGN being larger than in type-1 AGN) with a significance of more than 99.99%. Note that the fractions of objects with detected absorption are significantly larger than those found for AXIS sources, supporting the result that significant fraction of AXIS sources have undetected absorption due to the much lower signal-to-noise ratio of their spectra.

Table 4.3: *Results of detection of X-ray absorption.*

Sample (1)	N_{tot} (2)	N_{abs} (3)	f_{-}^{+} (4)	$1-F$ (5)
All sources	123	53	$0.38^{+0.07}_{-0.07}$	$\geq$0.27
type-1 AGN	46	7	0.10	$\leq$0.29
type-2 AGN	28	23	0.77	$\geq$0.51

Columns are as follows: (1) sample of objects; (2) number of objects on each sample; (3) number of objects with detected absorption on each sample; (4) fraction of absorbed objects corrected for the expected fraction of spurious detections (see Appendix A.4). Errors correspond to the 1σ confidence interval. For type-1 and type-2 AGN we do not give error bars because in the former the lower error bar reaches the zero value and in the later it reaches 1; (5) value of the fraction of absorbed objects for which $P(f \geq F)=0.9973$ for all sources and type-2 AGN and $P(f \leq F)=0.9973$ for type-1 AGN.

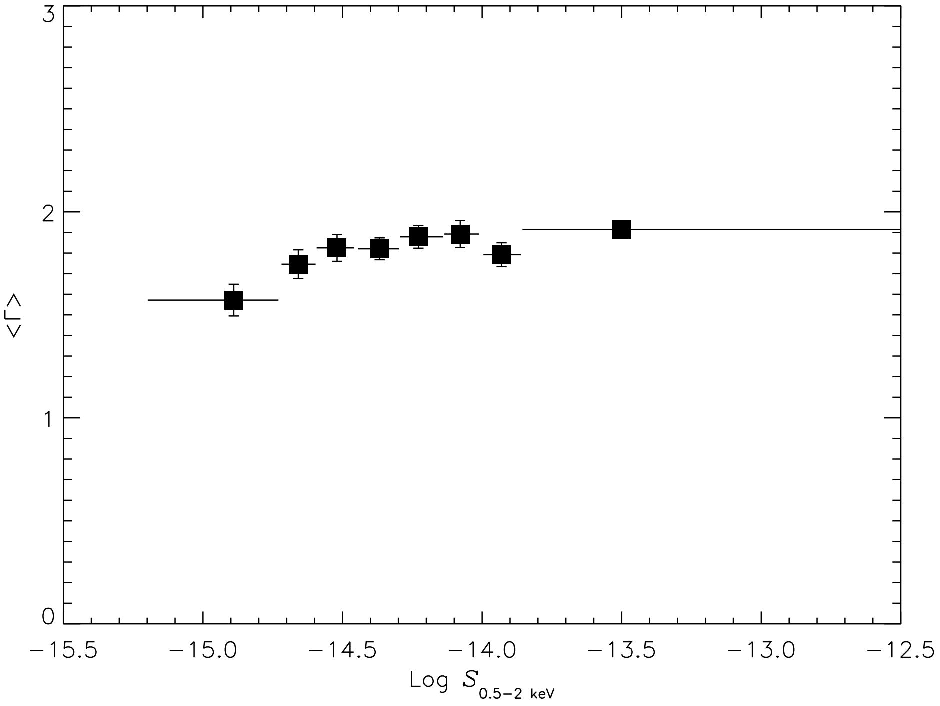

Figure 4.5: *Dependence of weighted ⟨Γ⟩ with 0.5-2 keV flux. For each source we used the spectral parameters obtained from its best fit model (see Sec. 4.5 for details). Errors correspond to the 1σ confidence interval.*

4.5.1 Broad band continuum

Using the best fit spectral slopes we obtained a weighted ⟨Γ⟩ of 1.87 ± 0.02 (1.86 ± 0.02 if the arithmetic mean is used). In Fig. 4.5 we show the dependence of ⟨Γ⟩ with 0.5-2 keV flux using the best fit parameters (Γ and S) for each object. We see that when all detected spectral components are taken into account during the fitting, the scatter in measured ⟨Γ⟩ (see Fig. 4.2) is reduced significantly, and most of the points are consistent with the obtained mean value for the whole sample of objects.

The mean best fit spectral slope was found to be 1.89 ± 0.03 (1.88 ± 0.03 with the arithmetic mean) for type-1 AGN and 1.71 ± 0.03 (1.82 ± 0.06 with the arithmetic mean) for type-2 AGN. In Fig. 4.6 we compare ⟨Γ⟩ for type-1 AGN and type-2 AGN as a function of 0.5-2 and 2-10 keV fluxes. For type-1 AGN, for which 7 out of 46 are X-ray absorbed, we obtained the same results using 0.5-2 and 2-10 keV fluxes, i.e., no dependence of ⟨Γ⟩ with the X-ray flux. However, X-ray absorption is important in type-2 AGN (~77% of type-2 AGN being X-ray absorbed and with larger absorbing column densities than type-1 AGN). We found that the ratio of type-2 AGN/type-1 AGN increases at fainter 0.5-2 keV fluxes

---

[2] We accepted the spectral signatures as being real if the significance of detection from the F-test was ≥95%. Hence 5% of detections are expected to be spurious.

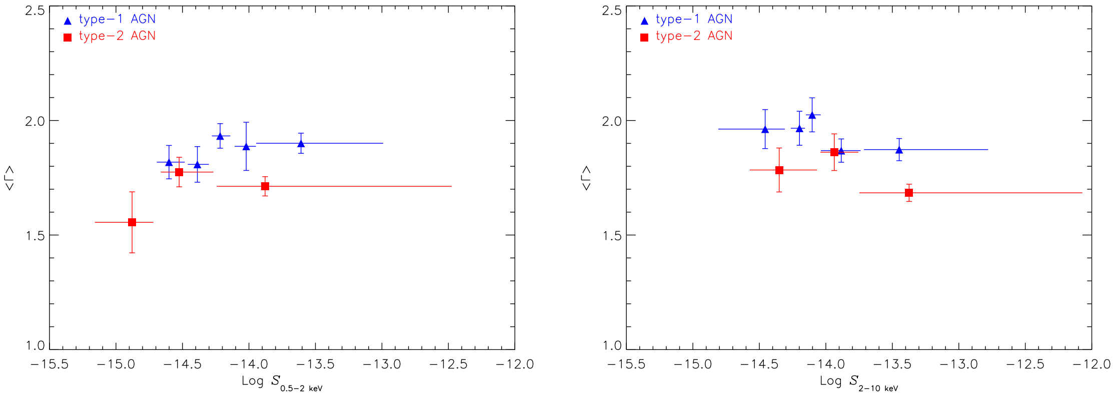

Figure 4.6: *Dependence of $\langle\Gamma\rangle$ with 0.5-2 and 2-10 keV flux for type-1 and type-2 AGN. For each source we used Γ and S from its best fit model (single power law or absorbed power law; see Sec. 4.5.1 for details). Errors correspond to the 1σ confidence interval.*

(not corrected for absorption), while it remains constant with 2-10 keV flux. We explained this effect in Sec. 4.3 as being due to the existing anti-correlation between absorption and soft absorbed flux, i.e., the most absorbed objects have the faintest fluxes in the 0.5-2 keV band. We also see in Fig. 4.6 that

1. Type-2 AGN tend to have $\langle\Gamma\rangle$ slightly lower than type-1 AGN at all fluxes
2. A clear dispersion in Γ is still present in both samples of type-1 and type-2 AGN

We have followed the procedure described in Nandra & Pounds [174] and Maccacaro et al.(1988) [138] to quantify the intrinsic dispersion in the distribution of photon indices for type-1 and type-2 AGN as we did for AXIS sources, and to see whether, after allowing for intrinsic dispersion in Γ, we still find type-2 AGN to be flatter on average than type-1 AGN. We assumed that the dispersion in Γ values can be well described with a Gaussian function of mean $\langle\Gamma\rangle$ and dispersion $\sigma_{\langle\Gamma\rangle}$. In Fig. 4.7 we show the distributions of Γ values for all sources, type-1 AGN and type-2 AGN.

The results of this analysis are listed in Table 4.4, where we have included the values obtained using the weighted mean for comparison. This quantitative analysis confirms the qualitative information obtained from Fig. 4.6: there is a significant dispersion in both type-1 and type-2 AGN and that type-2 AGN are slightly harder than type-1 AGN.

In Fig. 4.8 we show the contours in $\langle\Gamma\rangle$-$\sigma_{\langle\Gamma\rangle}$ space for $\Delta\chi^2$ of 2.3, 6.17 and 11.8 that correspond to 1, 2 and 3σ for two parameters. The significance of type-2 AGN being on average flatter than type-1 AGN is only of 1.62σ (using the values of Γ obtained with the ML method[3]), and therefore with the current data we cannot conclude that the average continuum of type-2 AGN is significantly flatter than that of type-1 AGN.

---

[3] Note that the significance of Γ being different for type-1 AGN and type-2 AGN is $\sim4\sigma$ if the values obtained with the weighted mean are used and no intrinsic dispersion in Γ is considered.

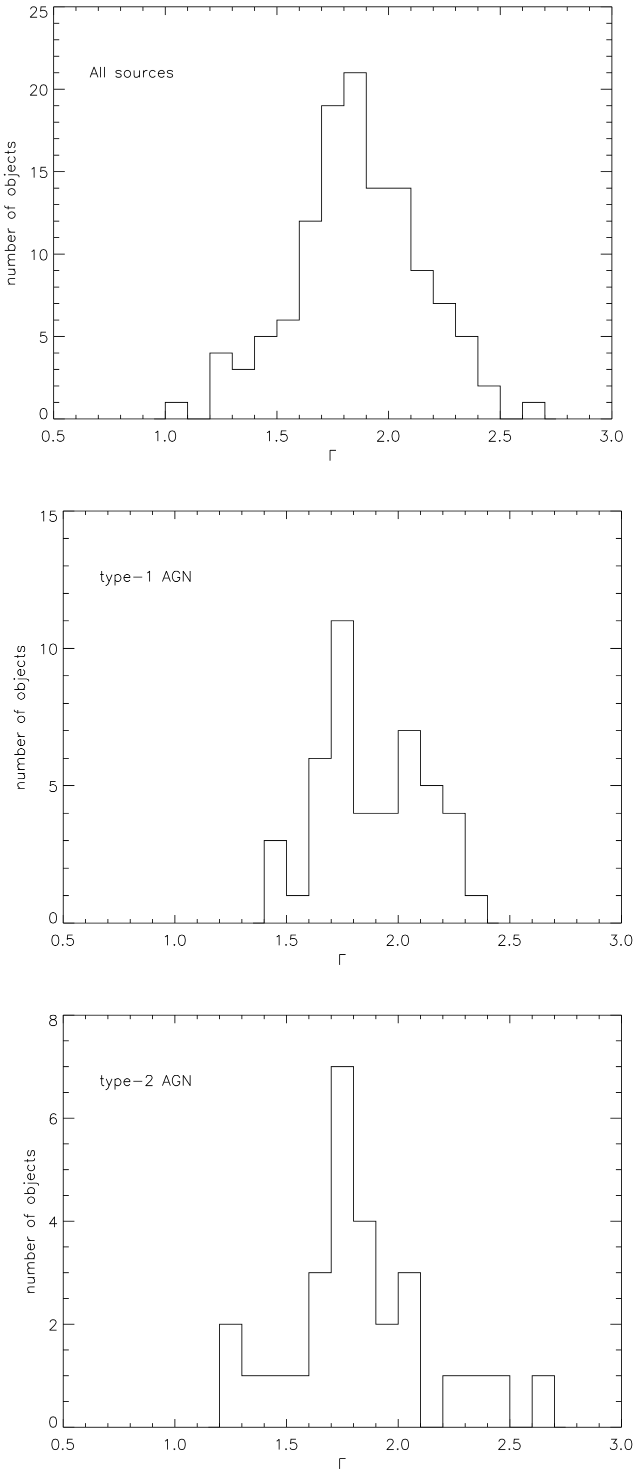

Figure 4.7: *Distributions of Γ values obtained from the best fit model of each object. Top: all sources; middle: type-1 AGN and bottom: type-2 AGN.*

Table 4.4: *Comparison of the weighted mean spectral photon index obtained for different types of sources with the values from the Maximum Likelihood analysis. Best fit spectral slopes for each object were used in the calculations. Errors correspond to the 1σ confidence interval.*

Sample	Maximum Likelihood $\langle\Gamma\rangle$	σ	Weighted Mean $\langle\Gamma\rangle$
Whole sample	$1.92^{+0.03}_{-0.18}$	$0.28^{+0.04}_{-0.13}$	1.87 ± 0.02
$\mathrm{type-1\,AGN}$	$1.89^{+0.06}_{-0.05}$	$0.20^{+0.04}_{-0.04}$	1.89 ± 0.03
$\mathrm{type-2\,AGN}$	$1.72^{+0.10}_{-0.08}$	$0.20^{+0.10}_{-0.07}$	1.71 ± 0.03

4.5.2 X-ray absorption

We have detected excess X-ray absorption in ~37% of the sources in our sample. Absorption was found in ~10% of type-1 AGN and ~77% of type-2 AGN. A correlation between Γ and N_H is expected if we have "overfitting", i.e., if the signal-to-noise ratio of the spectra is not high enough to use some of our spectral models. The results are plotted in Fig. 4.9 for sources with known redshifts. We do not see any evident correlation between these two spectral parameters. For sources with large Γ, the values including the error bars are in all cases consistent with a $\Gamma \sim 2$.

We see in Fig. 4.9, that the N_H^{intr} distributions of type-1 and type-2 AGN are different. The measured column densities in absorbed type-1 AGN were found to be between $10^{21} - 10^{22}\,\mathrm{cm}^{-2}$, while type-2 AGN have a much wider distribution of values, many objects having $N_H^{intr} \geq 10^{23}\,\mathrm{cm}^{-2}$. We show the distributions for N_H^{intr} in type-1 AGN and type-2 AGN in Fig. 4.10. In the left plot we included all sources for which we did not detect absorption, most of them being type-1 AGN. We assigned all these objects the same value of the column density, $N_H^{intr} = 10^{20}\,\mathrm{cm}^{-2}$. The distributions appear to be different, with type-2 AGN being in general more absorbed than type-1 AGN. Using the KS test to compare the two distributions we obtained a probability of them of being different of $> 92\%$.

In terms of the unified model of AGN, X-ray absorption and optical obscuration should be correlated, i.e., type-1 AGN are expected to be unabsorbed in X-rays, while type-2 AGN are expected to be X-ray absorbed (see Sec. 1.5). There are observational evidences that this assumption does not hold for all AGN, although there are only a few examples where the results are based on a proper spectral analysis such as our spectral analysis of AXIS sources (see Sec. 3.3.2) where we found that these discrepancies exist in a significant fraction of AGN. This result is confirmed now with our analysis of *Lockman Hole* sources. We saw in the previous chapter some indications that an AGN/host galaxy contrast effect[4]

---

[4] In a redshift interval where the distributions of type-1 AGN and type-2 AGN overlapped, we found

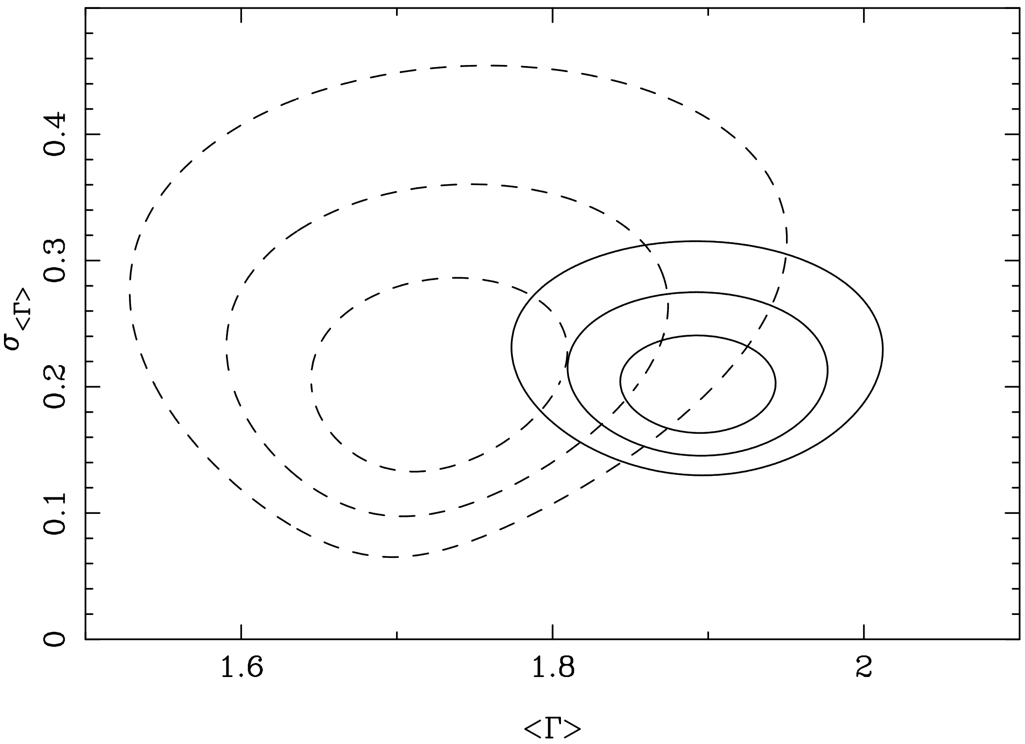

Figure 4.8: *Contour diagrams for the value of the average spectral slope and intrinsic dispersion of our samples of type-1 AGN (solid lines) and type-2 AGN (dashed lines) obtained from the Maximum Likelihood analysis (see Sec. 4.5). The contours are defined as $\Delta\chi^2$=2.3, 6.17 and 11.8 corresponding to standard 1, 2 and 3σ confidence regions for two parameters.*

might explain why broad optical lines are not observed in unabsorbed type-2 AGN. In Fig. 4.11 we show the redshift distribution of the AGN in our sample. Because our sample of absorbed AGN is much smaller than the AXIS sample, the number of absorbed type-1 and type-2 AGN within the redshift interval where both samples overlap (necessary in order to compare their luminosities) is not high enough as to perform a test similar to that carried out for the unabsorbed type-2 AGN in AXIS.

4.5.3 Soft excess

We detected soft excess emission ($\geq$95% confidence limit from an F-test) in 18 (15%) objects. The number of MOS+pn counts in the soft excess component varied from 100 to 1000 except for one source for which the soft excess component has ~3000 counts. Within AGN we found soft excess in 5 (11%) type-1 AGN and 7 (25%) type-2 AGN. The significance of the fractions of type-1 AGN and type-2 AGN with detected soft excess emission being different is 97% (87% using only objects in the redshift range where we

---

that the unabsorbed type-2 AGN were less luminous than the type-1 AGN.

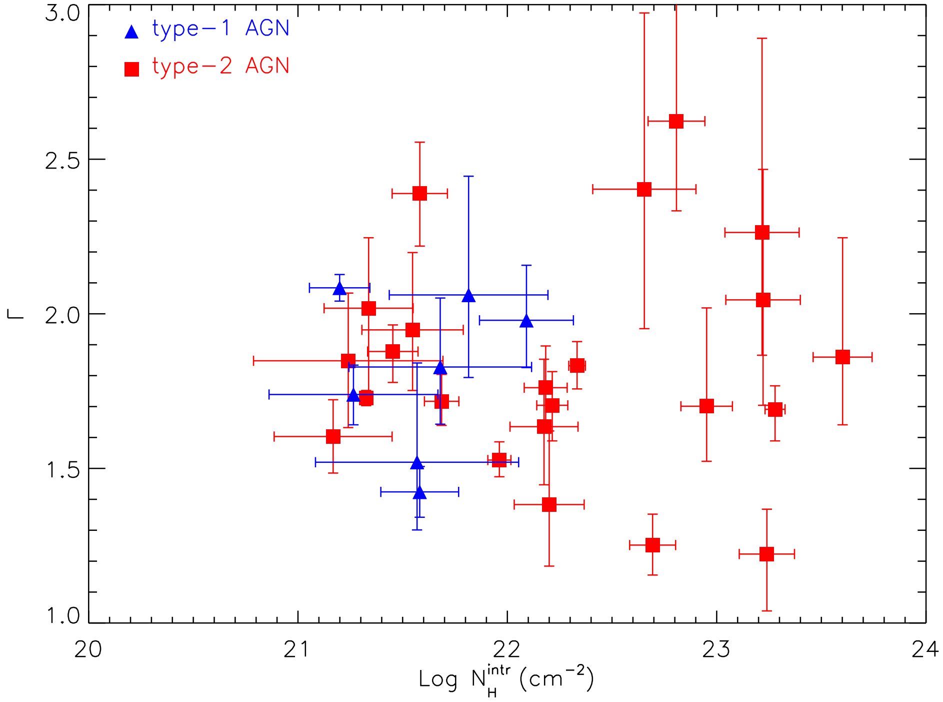

Figure 4.9: *Γ vs.* N_H^{intr} *(rest-frame) for type-1 and type-2 AGN where absorption was detected. Note that all type-1 AGN have column densities between* $10^{21} - 10^{22}\,\mathrm{cm}^{-2}$ *while type-2 AGN have a much wider distribution of* N_H^{intr}*. Errors correspond to the 90% confidence interval.*

detected soft excess, i.e. z<1.568). Therefore our data do not show any strong tendency of soft excess to be more common in type-2 AGN than type-1 AGN.

In 9 sources (4 type-1 AGN, 4 type-2 AGN and 1 unidentified object) we fitted the soft excess emission with a black body model (a Raymond-Smith thermal plasma model gave an equally good fit). The properties of the soft excess component in our AGN, i.e. temperature, 0.5-2 keV luminosity and strength, are listed in Table 4.5. The measured properties do not correlate with the 2-10 keV X-ray luminosity of the objects, as we found for AGN in AXIS with detected soft excess emission. For the unidentified object with detected soft excess for which a black body model gave an acceptable fit, we found a black body temperature of $0.164^{-0.046}_{+0.033}$ keV in the observer's frame. The average temperatures of the black bodies were 0.09±0.01 keV for type-1 AGN and 0.26±0.08 keV for type-2 AGN. The average 0.5-2 keV luminosities of these black bodies (in log units) were $43.42 \pm 0.43\,\mathrm{erg\,s^{-1}}$ for type-1 AGN and $44.11 \pm 0.44\,\mathrm{erg\,s^{-1}}$ for type-2 AGN. The 0.5-2 keV luminosities of the soft excess component in type-1 AGN and type-2 AGN were not significantly different (a KS test of the luminosity distributions gave a significance of them of being different of just 90%). However the measured temperatures of the soft excess are higher in type-2 AGN

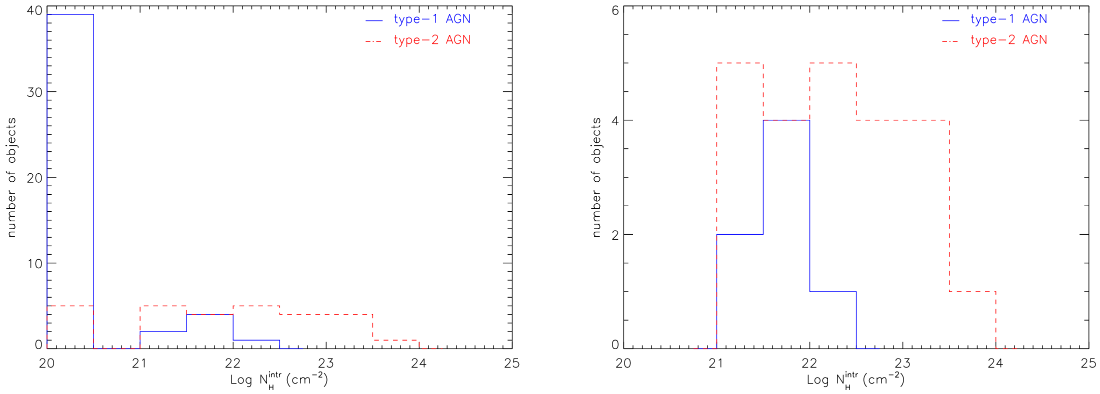

Figure 4.10: *Distributions of intrinsic (rest frame) absorption in type-1 AGN and type-2 AGN obtained from the sources best fit model. In the left plot we included all AGN for which we did not detect excess absorption in their co-added spectra. Right: Same distributions but for AGN with detected excess absorption.*

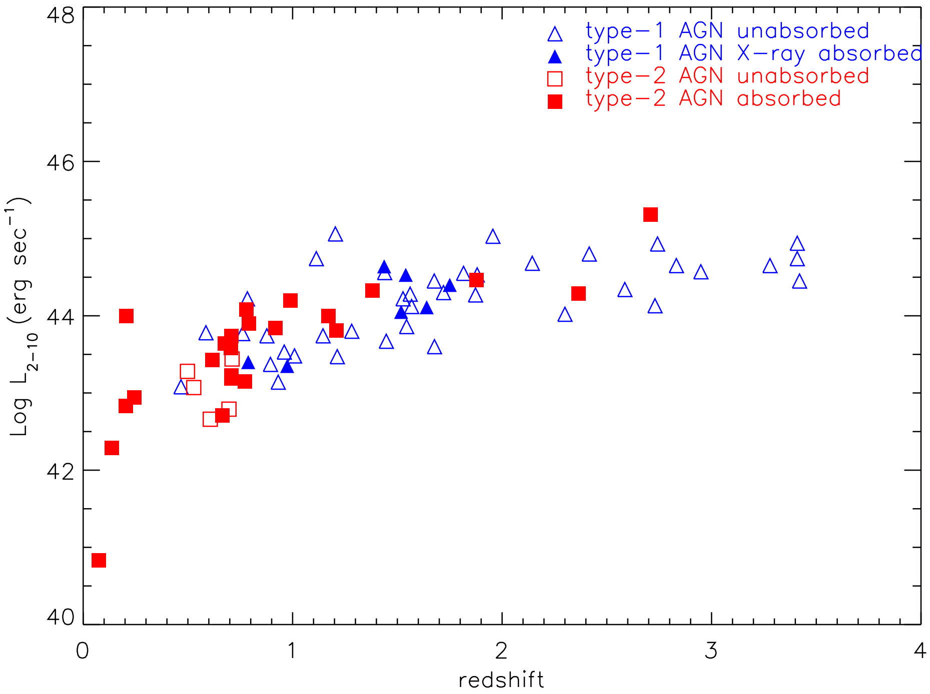

Figure 4.11: *2-10 keV luminosity (corrected for absorption) vs. redshift for type-1 and type-2 AGN. We do not see that absorbed sources have systematically different luminosities (higher) than unabsorbed sources.*

Table 4.5: *Properties of the soft excess emission in type-1 AGN and type-2 AGN that was modelled with a black body.*

ID (1)	Class (2)	redshift (3)	kT^{+}_{-} (4)	L_{BB} (5)	L_{PO} (6)	$S_{\rm fracc}$ (7)	$L_{\rm fracc}$ (8)
90	type − 1	0.467	105^{+17}_{-20}	42.64	43.08	9.6	33.2
342	type − 1	0.586	67^{+3}_{-7}	42.79	43.78	12.0	13.9
148	type − 1	1.113	78^{+6}_{-8}	44.44	44.74	3.0	43.8
270	type − 1	1.568	109^{+10}_{-15}	43.80	44.12	0.8	76.0
290	type − 2	0.204	188^{+17}_{-15}	41.32	42.83	4.0	5.0
511	type − 2	0.704	83^{+87}_{-38}	42.12	43.58	1.8	1.9
424	type − 2	0.707	474^{+26}_{-153}	42.25	43.74	7.6	6.9

Columns are as follows: (1) *XMM-Newton* source name; (2) class from optical spectroscopy; (3) spectroscopic redshift; (4) temperature of the soft excess emission in units of eV. Errors correspond to the 90% confidence interval; (6) logarithm of the 0.5-2 keV luminosity of the black body obtained setting absorption and powerlaw components to zero; (7) logarithm of the 2-10 keV luminosity of the black body obtained setting absorption and black body components to zero; (8) contribution to the soft (0.5-2 keV) flux from the soft excess component, measured as the ratio of the soft excess to power law 0.5-2 keV fluxes; (9) contribution to the soft (0.5-2 keV) luminosity from the soft excess component, measured as the ratio of the soft excess to power law 0.5-2 keV luminosities.

than in type-1 AGN. This could be because the soft excess in type-2 AGN might contain a fraction of scattered radiation. The origin of the soft excess emission in AGN is still uncertain. In a significant number of sources the temperatures of the black body are well above 60 eV[5], and hence it is difficult to explain the origin of their soft excess as thermal emission from the accretion disc only. An alternative explanation could be reflection of hard X-rays by the accretion disk or an additional comptonizing medium. A superposition of a scattering component and a black body can reproduce equally well the spectral signatures of soft excess emission in our objects, however the signal-to-noise ratio of the data is not high enough to separate the contribution from each component. Gierlinski & Done [82] have proposed that a single power law can reproduce both the soft and hard X-ray emission, and soft excess signatures are due to strong absorption of the primary power law in a "velocity-smeared", high column ionised gas.

In 9 objects in our sample (1 type-1 AGN, 3 type-2 AGN and 5 unidentified objects) the black body could not fit the signatures of the soft excess. An alternative method that has been frequently used to fit the curvature at soft energies is a scattering or partial covering

---

[5] The hottest thermal emission expected from an accretion disk surrounding a $10^6 M_\odot$ black hole.

Table 4.6: *Parameters of the Gaussian line in the six identified sources where signatures of line emission where detected with an F-test significance* $\geq 95\%$.

ID (1)	Class (2)	redshift (3)	L_{2-10} $\mathrm{erg\,s^{-1}}$ (4)	Line energy (keV) (5)	σ (keV) (6)	Equivalent width (eV) (7)	$\mathrm{F-test}$ prob. (%) (8)
270	$\mathrm{type-1\,AGN}$	1.568	44.12	$6.24^{+0.48}_{-0.08}$	$0.00^{+0.82}_{-0.00}$	176	99
21	$\mathrm{type-2\,AGN}$	0.498	43.28	$5.90^{+0.92}_{-1.64}$	$0.56^{+2.19}_{-0.45}$	976	95
172	$\mathrm{type-2\,AGN}$	1.170	44.00	$6.40^{+1.87}_{-0.41}$	$0.09^{+2.93}_{-0.00}$	166	99
290	$\mathrm{type-2\,AGN}$	0.204	42.83	$6.32^{+0.07}_{-0.61}$	$0.00^{+0.14}_{-0.00}$	235	96
326	$\mathrm{type-2\,AGN}$	0.780	44.08	$6.59^{+0.06}_{-0.09}$	$0.02^{+2.12}_{-0.00}$	126	99
407	$\mathrm{type-2\,AGN}$	0.990	44.20	$6.40^{+0.10}_{-0.43}$	$0.40^{+0.10}_{-0.18}$	328	> 99.99

Columns are as follows: (1) source X-ray identification number; (2) optical class; (3) redshift; (4) logarithm of the 2-10 keV luminosity (corrected for absorption); (5) energy of the centroid of the line; (6) width of the line in keV; (7) line equivalent width in eV; (8) F-test probability of detection of the line. Errors are 90% confidence. Errors correspond to the 90% confidence interval.

model (`pcfabs` in `Xspec`). The model consists of the sum of two power law components having the same spectral index, but affected by different absorption (quantified with the covering fraction parameter). This model improved significantly the quality of our fits for these objects. The average covering fraction that we obtained for these 9 objects was 0.82 ± 0.06 (the maximum and minimum values being 0.98 and 0.50). This value implies that the scattering fraction in these sources is rather large ($18 \pm 6\%$) compared to the values observed in nearby Seyfert 2 galaxies [232].

4.5.4 Reprocessed components

The presence of a rest-frame 6.4 keV Fe emission line and the so-called Compton reflection hump in the X-ray spectra of AGN indicates the existence of cold, optically thick material that reprocesses and reflects a fraction of X-rays. Detailed X-ray spectral analyses have found a variety of profiles for Fe Kα lines. In some cases the lines are found to be broad, redshifted and ionised supporting an origin for the emission in the inner most regions of the accretion disk. However most lines observed by *XMM-Newton* [202] and *Chandra* [250] are found to be narrow, more consistent with an origin for the line further away from the accretion disk, probably in the putative molecular torus.

We have searched for this component in our sources using a Gaussian model to fit the line emission. We detected signatures of line emission with an F-test significance $\geq 95\%$ in the MOS and pn spectra of 8 objects (1 type-1 AGN, 5 type-2 AGN and 2 unidentified sources). In Fig 4.12 we show the MOS+pn unfolded co-added spectra of all these sources while the parameters of the measured Gaussian lines are listed in Table 4.6.

Sources 21 and 407: In these sources we found a significant width in the line profile (as we see in Table 4.6 the significance of detection of width in the line is >90% but probably not greater than 2σ), which might be indicating that the line was formed in the inner parts of the accretion disc, and hence it should have a relativistic profile (with a red wing component due to gravitational redshift). When fitted with a Gaussian model, we would expect the line centroid to be found at an energy slightly below 6.4 keV. While in source 407 the line centroid is consistent with being neutral iron, in source 21 it was ∼5.9 keV (although consistent with being neutral iron within the error bars).

Sources 270 and 290: In these sources we detected a narrow Gaussian line and line centroids lower (but consistent within the error bars) than the value for neutral iron.

Sources 172 and 326: In these sources the fit also returned a non-zero line width, although in both cases it was consistent with zero at 90% confidence. In source 172 the line centroid was consistent with being neutral iron, but in source 326 it was significantly higher (even within the error bars). In this source the line might be originating in an ionised accretion disc. In the X-ray spectrum of source 172 we also found (F-test significance of 99%) an absorption edge at a rest-frame energy of $\sim 7.56^{-0.54}_{+0.76}$ keV and $\tau = 1.4^{-0.8}_{+0.6}$. An emission line at a rest-frame energy of 6.4 keV together with an absorption edge at a rest-frame energy slightly higher than 7.1 keV are expected[6]. The lack of detection of this spectral feature in most sources with detected Fe line emission might be due to the strong decrease of the effective area of the *XMM-Newton* mirrors at these energies which makes the detection of this spectral component very difficult.

In all the spectra where we detected the line, we did not have enough signal-to-noise ratio in the data in order to use a more physical model to fit the profile of the line (`Xspec` models `laor` for a maximally-rotating Kerr black hole or `diskline` for a Schwarzchild -non-rotating- black hole). The equivalent width of the line in the type-1 AGN where we detected this component was found to be ∼176 eV. In most type-2 AGN the measured values were between 126 and 328 eV. However there is one source, 21 for which we found an EW of 976 eV, substantially higher than in the other type-2 AGN. It is important to note that in this source the F-test significance of detection of line was the lowest among all sources (95%) and hence the measured properties of the line have the highest uncertainties.

Our results differ significantly from the results presented in Streblyanska et al.(2005) [225] where the same sample of AGN was used. However, it is important to note that in order to constrain the properties of line emission, they used the stacked (de-redshifted) spectra of type-1 AGN and type-2 AGN, and hence, their accumulated data had much better signal-to-noise ratio. If the objects in our sample have broad Fe lines, the contribution of the broad component is difficult to detect on the individual spectra, since its contribution is less than 10% above the continuum over most of the spectrum.

We have searched for a flattening of the continuum at high energies (i.e. Compton reflection hump) adding a second power law to the spectral models. We found signatures

---

[6] When iron absorbs a photon with the energy required to excite an inner-shell(K) electron (7.1 for neutral iron) another electron from the n=2 shell drops to fill the hole and a photon with an energy equal to the difference between the energy of the two shells (6.4 keV) is emitted.

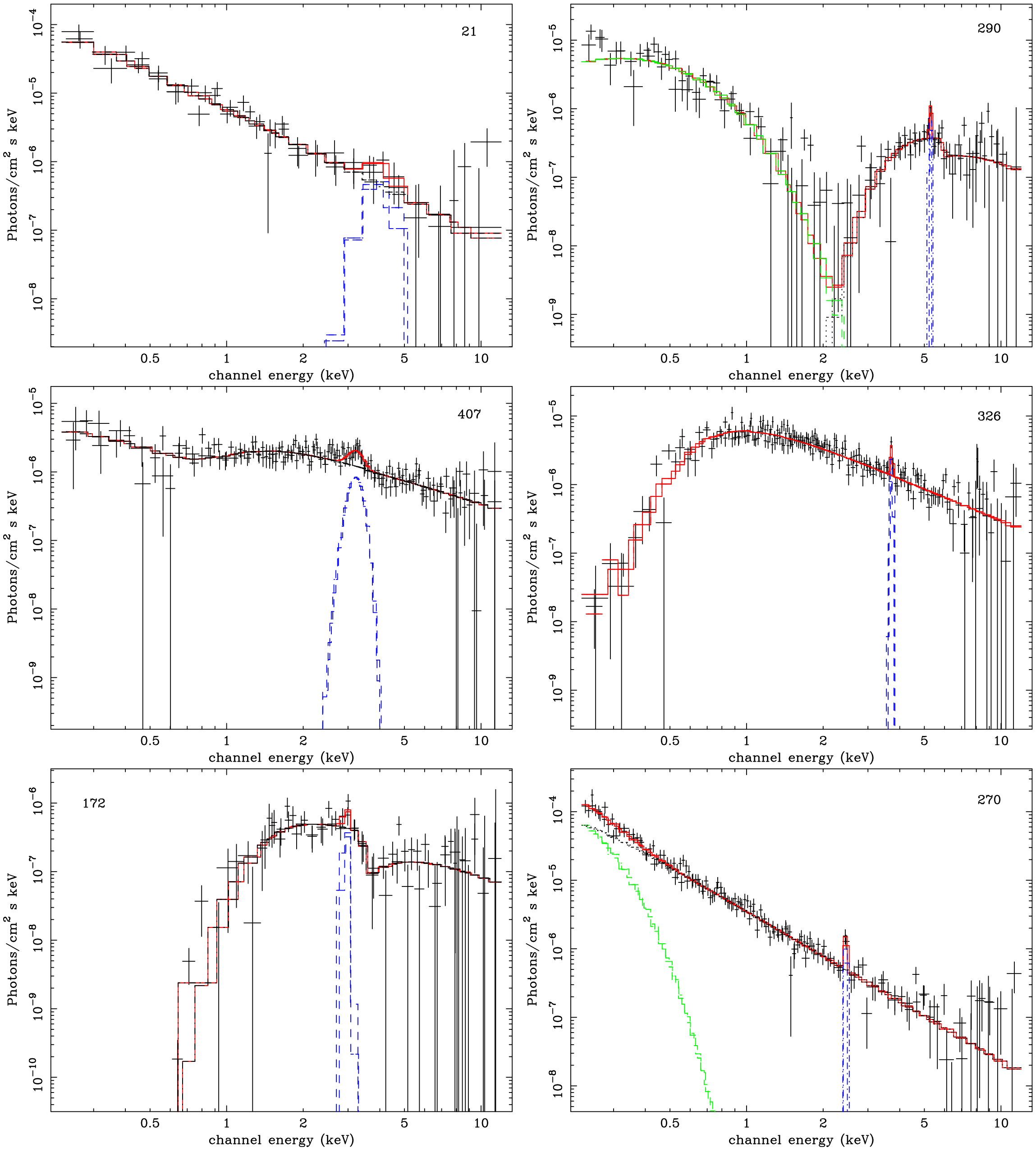

Figure 4.12: *Unfolded MOS and pn co-added spectra of the 6 AGN where we detected signatures of emission line at high energies (F-test significance ≥95%). In the X-ray spectrum of source 172 (type-2 AGN) we also found an absorption edge at a rest-frame energy of* $\sim 7.56^{-0.54}_{+0.76}$ *keV and* $\tau = 1.4^{-0.8}_{+0.6}$ *(F-test significance of 99%).*

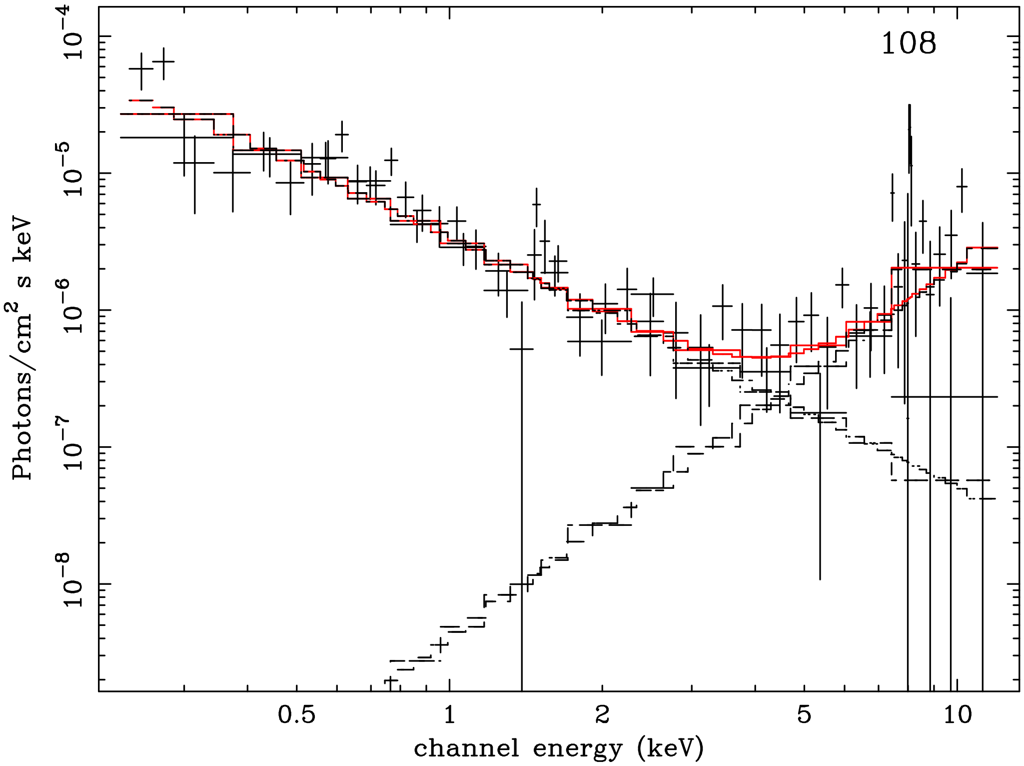

Figure 4.13: *Unfolded MOS and pn spectrum of the only source in the sample (number 108) where we detected a hardening in the X-ray continuum emission at high energies (Compton reflection hump). Because this object is still unidentified we fitted the hard spectral component with a second power law. The F-test significance of this component was found to be 99.98%. The co-added spectra seems to show line emission at an observed energy of ∼1.6 keV, however the significance of the detection of this spectral signature (using a Gaussian model) was found to be very low.*

of spectral hardening at high energies in only one object, source 108, which is still not identified. The unfolded MOS and pn spectra of this object are show in Fig. 4.13. We first fitted its X-ray spectrum with a single power law. We found $\Gamma \sim 1.5$. The fit was not good, with a χ^2 of 127 for 67 degrees of freedom, the main reason for this result being an excess emission at high energies. We then fitted the spectrum with two power laws. With this model χ^2 significantly decreased to 98 for 65 degrees of freedom. The F-test significance of improvement of the fit with the new component was 99.98%. In this case we obtained a value of $\Gamma=1.83\pm0.17$ for the continuum emission flattening out of $\Gamma = -2.56^{+0.61}_{-0.19}$ at high energies. We did not find evidence for X-ray absorption or emission lines in the spectrum of this source. We will have to wait until we have the optical identification of this source before saying more about its nature.

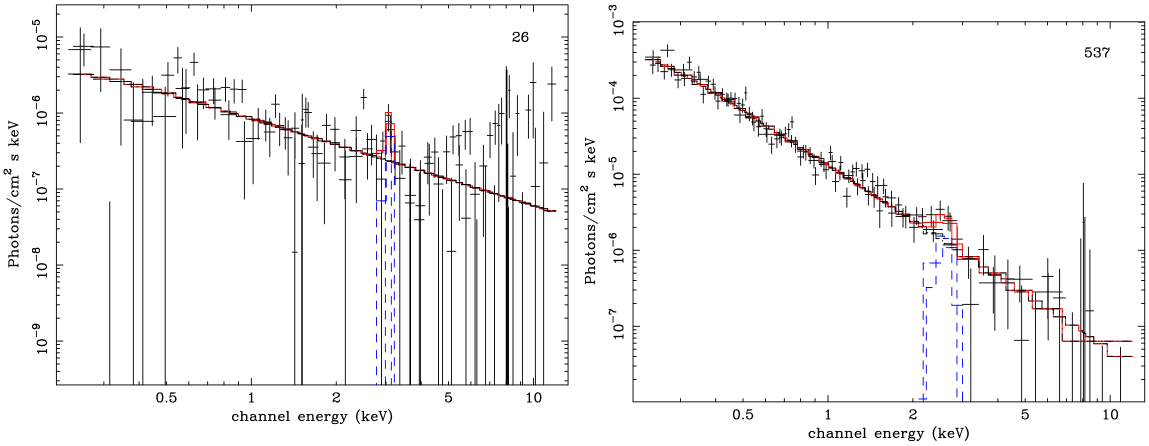

Figure 4.14: *Unfolded MOS and pn co-added spectra of two still unidentified sources (26 and 537) where we detected signatures of emission line at high energies (F-test significance ≥95%).*

4.6 Dependence of sources spectra with luminosity and redshift

We show Γ and N_H^{intr} vs. redshift for type-1 AGN and type-2 AGN in Fig. 4.15. In these plots we can see the different redshift distributions between the type-1 and type-2 AGN in our sample. Most detected type-2 AGN have redshifts below 1, while we find type-1 AGN up to a redshift of ∼3.5. We do not see evidence for evolution of Γ or N_H^{intr} with redshift. We have applied a Spearman test to search for any correlation between Γ and redshift for type-1 AGN. We found a correlation of -0.22 and a significance of Γ being flatter at higher redshifts of 86%. Although the continuum shape of type-1 AGN does not appear to evolve

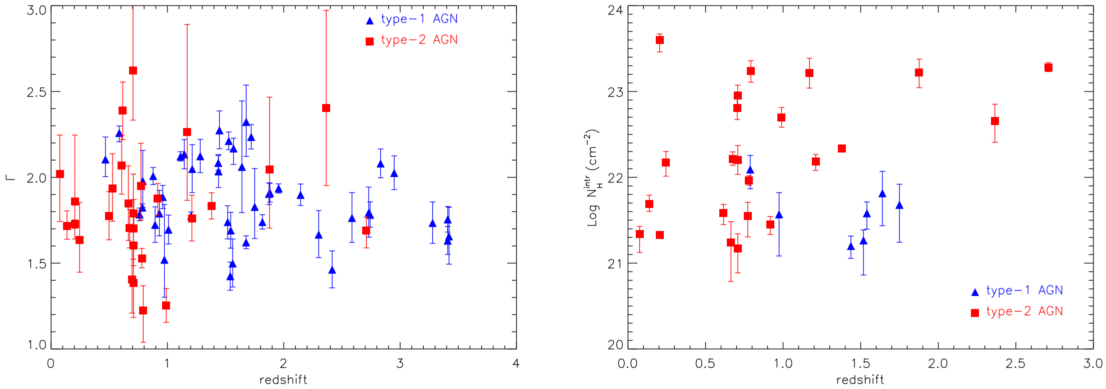

Figure 4.15: *Evolution with redshift of Γ and N_H^{intr} (rest-frame) for type-1 and type-2 AGN. Errors correspond to the 90% confidence interval.*

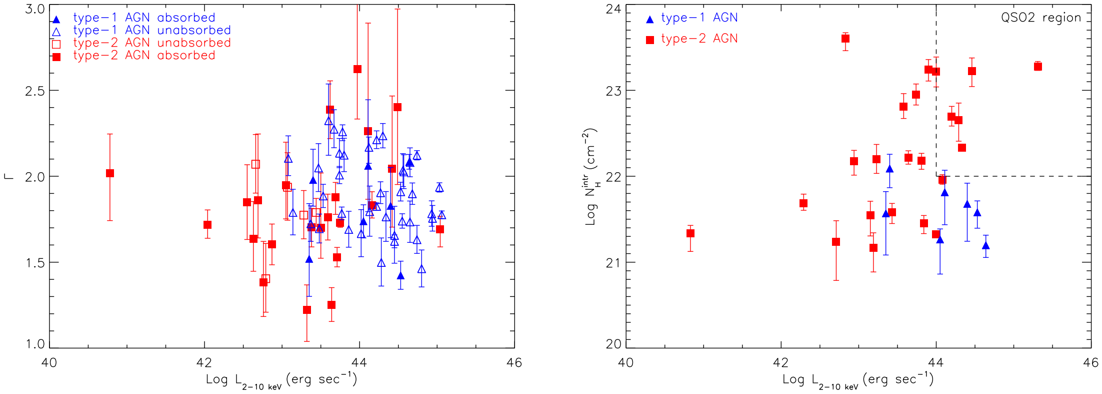

Figure 4.16: *Left* Γ *vs. 2-10 keV luminosity and right* $\mathrm{N_H^{intr}}$ *vs. 2-10 keV luminosity for type-1 and type-2 AGN. In the* $\mathrm{N_H^{intr}}$ *vs. 2-10 keV plot we show the QSO2 region (defined as* $\mathrm{L_{2-10}} \geq 10^{44}\mathrm{erg\,s^{-1}}$ *and* $\mathrm{N_H^{intr}} \geq 10^{22}\,\mathrm{cm^{-2}}$*) where we have 6 QSO2 candidates. Errors correspond to the 90% confidence interval.*

with redshift, our sample of type-1 AGN at high redshift is too small to reach any strong conclusion.

We obtained the same results for $\mathrm{N_H^{intr}}$, i.e., type-1 and type-2 AGN at high redshift are not more absorbed that the local ones. The apparent scarcity of high redshift low $\mathrm{N_H^{intr}}$ sources seen in Fig. 4.15 is probably a selection effect. The signature of absorption is easier to detect in highly absorbed sources at high redshifts because these signatures will be redshifted outside the observed energy band, making more difficult the detection of low absorbing column densities.

We have studied the dependence of Γ and $\mathrm{N_H^{intr}}$ with 2-10 keV X-ray luminosity (we use the 2-10 keV luminosity because the values are less affected by X-ray absorption). The results are plotted in Fig 4.16. We did not see correlation between the X-ray luminosity and the spectral slope or the column density values of our AGN. Note in Fig. 4.16 that our sample contains 6 objects (all optically identified as type-2 AGN) that fall within the "standard" QSO2 region, i.e., $\mathrm{L_X} \geq 10^{44}\,\mathrm{erg\,s^{-1}}$ and $\mathrm{N_H^{intr}} \geq 10^{22}\,\mathrm{cm^{-2}}$.

4.7 Unabsorbed type-2 AGN

We have found 5 objects identified as type-2 AGN but with no clear evidence of X-ray absorption in their X-ray spectrum (∼23% of the sample of type-2 AGN, see Table 4.3). In Fig. 4.17 we show the unfolded MOS and pn spectra of these sources obtained with their best fit model (in all cases the best fit model was a single power law). Several authors have found AGN with weak or no broad emission lines in their optical spectrum, and with unabsorbed X-ray spectra [10] [34] [45] [152] [181] [183].

One possible explanation for this apparent mismatch between observed optical/X-ray properties could be that the signal-to-noise ratio of the spectra of these sources is not high enough as to detect signatures of X-ray absorption [152]. As we see in Fig. 4.17 this is not the case for these sources if the column densities are within the range of values found for our absorbed type-2 AGN. We have calculated upper limits (at 90% confidence) to the X-ray absorption in these sources. These are listed in Table 4.7. The values that we obtained are significantly lower than the typical column densities found in our absorbed type-2 AGN. These upper limits are consistent as arising in absorption from their host galaxy at most.

Another possibility that might explain the lack of X-ray absorption in these sources is X-ray spectral variability. The optical and X-ray observations of these sources have not been obtained simultaneously, and therefore the absorbing/obscuring material in these sources might have changed with time. Corral et al.(2005) [45] studied the hypothesis of spectral variability using simultaneous X-ray and optical observations of the Seyfert galaxy Mrk993. They found the source to be X-ray unabsorbed but in a type 1.9 optical 'state'. Moreover, as we will see in Chapter 5, where the X-ray variability properties of the *Lockman Hole* sources are presented, variability is unlikely to explain the lack of X-ray absorption in our unabsorbed type-2 AGN.

Nicastro et al.(2000) [176] developed a model where the existence of the broad line region in AGN is related to the accretion mechanism. For very low accretion rates the BLR might be unable to develop. This model could explain the absence of broad emission lines in low luminosity sources. As we see in Figure. 4.11 our type-2 unabsorbed AGN do not have particularly low X-ray luminosities, hence this model is unlikely to explain the lack of X-ray absorption in our sources.

We have checked whether our sources could be Compton-thick type-2 AGN. If the torus is Compton-thick, even 2-10 keV photons will not be directly seen, and hence the direct radiation in these sources would be completely blocked. In some cases scattered radiation (with no or little apparent absorption) could be the only radiation seen below 10 keV. In Compton-thick sources, because the primary radiation is fainter, the equivalent width (EW) of the Kα line increases. Bassani et al.(1999) [17] constructed a diagnostic diagram of the EW of the Fe line as a function of the transmission parameter $T = S_{\rm X}/S_{\rm [OIII]}$[7]. This diagram can be used to identify Compton-thick sources. We do not know the value of $S_{\rm [OIII]}$ for our sources, but we have measured the EW of the Fe line, so we can constrain the region of the diagram where our sources fall. We measured EW fitting Gaussian lines to the spectra of our sources. Only in source 21, there might be emission from iron Kα line (F-test significance ~95%). The upper limits to the EW that we have found are listed in column (6) of Table 4.7. In all the cases we obtained a value of the EW below 1000 eV, which means that our sources fall outside the region of Compton-thick sources in the Bassani et al.(1999) diagram. However, to reach a stronger conclusion about the nature of these sources, and specially for sources 21 and 476, with EW values close to 1000 eV, we would need a reliable measurement of the [OIII] flux to see whether our sources fall outside the region of Compton-thick sources. These measurements are, unfortunately, unavailable at the moment.

---

[7] $S_{\rm X}$ is the 2-10 keV X-ray flux and $S_{\rm [OIII]}$ the optical flux of the [OIII] λ5007 emission line. [OIII] λ5007 has been frequently used as an isotropic indicator of the intrinsic brightness of the sources.

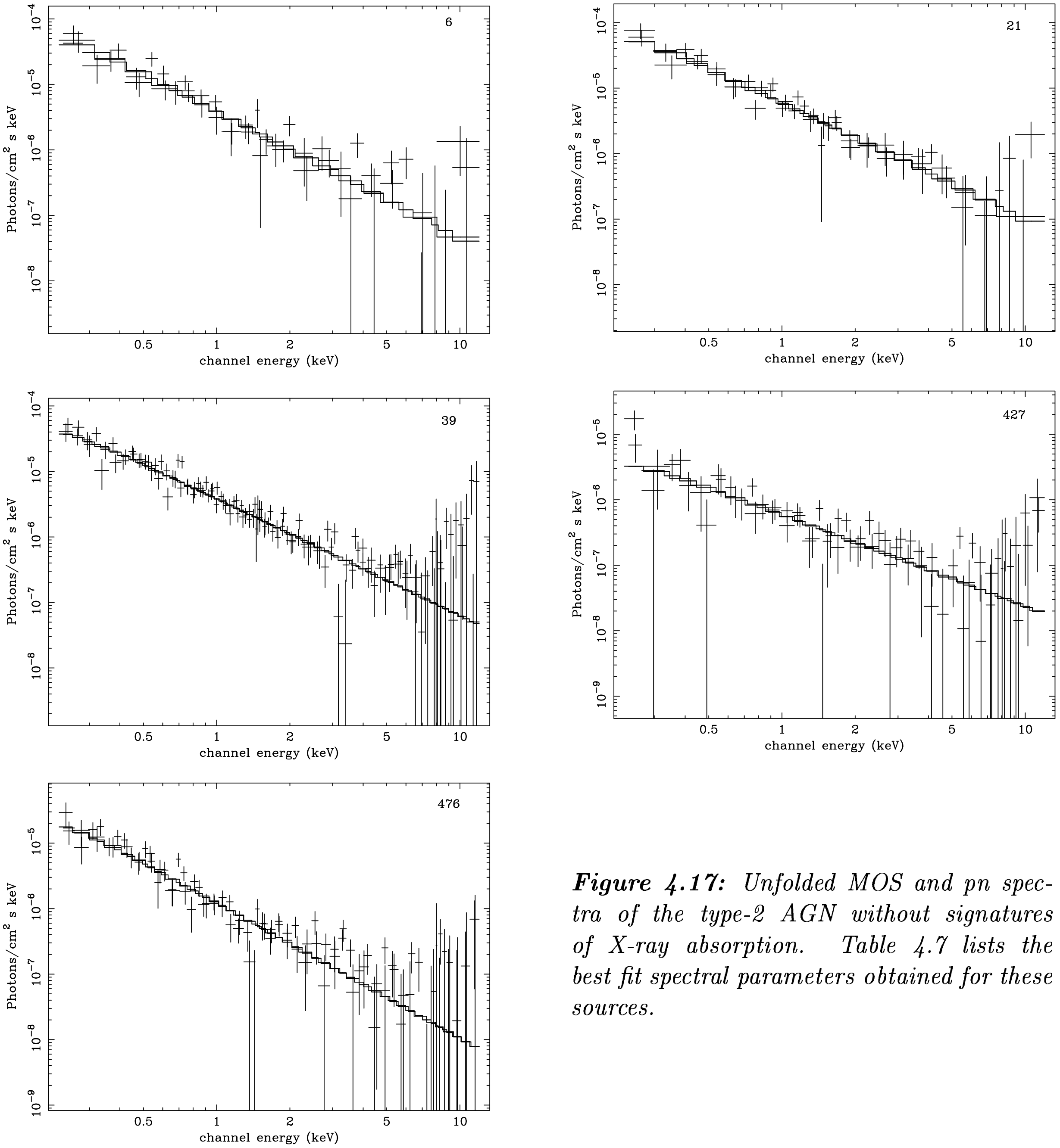

Figure 4.17: *Unfolded MOS and pn spectra of the type-2 AGN without signatures of X-ray absorption. Table 4.7 lists the best fit spectral parameters obtained for these sources.*

Table 4.7: *X-ray properties of the type-2 AGN for which we did not find absorption in their X-ray spectrum.*

ID (1)	redshift (2)	Γ (3)	N_H^{intr} (4)	L_{2-10} (5)	Equivalent width (eV) (6)
6	0.528	1.94 ± 0.20	≤ 20.91	43.07	377
21	0.498	1.77 ± 0.14	≤ 20.62	43.28	976
39	0.711	1.79 ± 0.08	≤ 20.66	43.44	171
427	0.696	1.40 ± 0.20	≤ 21.08	42.79	147
476	0.607	2.07 ± 0.17	≤ 20.22	42.66	867

Columns are as follows: (1) source X-ray identification number; (2) redshift; (3) Γ from best fit model (note that for all sources the best fit model was a single power law). Errors correspond to the 90% confidence interval; (4) upper limit in intrinsic (rest-frame) X-ray absorption (90% confidence); (5) logarithm of the 2-10 keV luminosity of the sources (in units of $\mathrm{erg\,s^{-1}}$); (6) equivalent width of an emission line centred at 6.4 keV and σ=0 (the value of the EW was obtained using a Gaussian to model the emission line.)

4.8 Extragalactic X-ray background

We have carried out a stacking of the co-added MOS/pn spectra of the sources that we have analysed. The goal of this analysis is to compare the integrated emission from our sources, with an average spectral shape of ~1.92 (see Sec. 4.5.1), with the spectrum of the XRB. Therefore this is a different analysis than the one presented in Streblyanska et al.(2005) [225], where they obtained the stacked average rest-frame spectra of type-1 and type-2 AGN, while in our analysis we want to stack the observed X-ray spectra of AGN, as we are interested in calculating the contribution of our AGN to the intensity of the XRB. We kept MOS and pn data separately because of the different instrumental responses. In addition, as explained in Sec. 4.2, MOS and pn co-added spectra were not necessary built using the same set of observations, hence the normalisations of the XRB spectrum obtained with MOS and pn might be slightly different.

At the time of this study there were calibration uncertainties between MOS and pn data at energies below ~1 keV (pn gives higher fluxes below 0.7 keV by 10-15% with respect to MOS, see Kirsh et al.(2004) [119]). We also found our data to be rather uncertain at energies ≥ 7 keV. Because of the rapid decrease in the effective area of the X-ray detectors at energies ≥ 5 keV the signal-to-noise ratio of the data becomes very low. In addition we know that particle background is very important at high energies. Therefore we restricted our analysis to the 2-7 keV (observer's frame) energy interval where we know that our results will not be affected by calibration problems or inaccurate background subtraction.

MOS and pn stacked spectra were obtained following the procedure described in Appendix D.

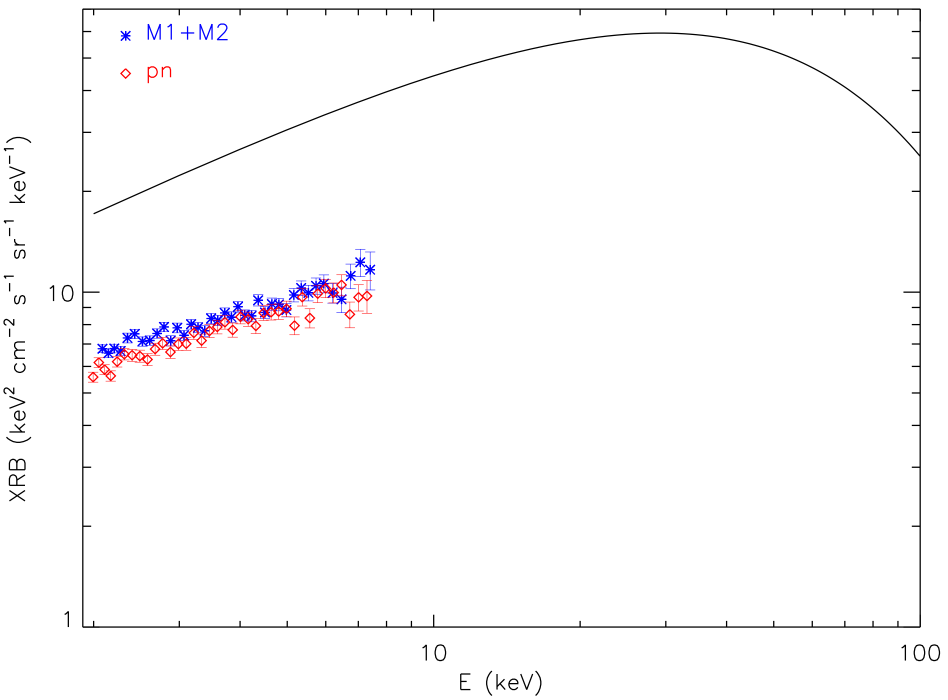

Figure 4.18: *Spectrum of the extragalactic X-ray background as measured by the HEAO-1 experiment but renormalised to the 2-8 keV intensity observed by De Luca & Mondeli [48] (solid line). The points show MOS1+MOS2 (diamonds) and pn (stars) 2-10 keV stacked spectra of the sources that we have analysed. Errors correspond to the 90% confidence interval.*

We fitted MOS and pn stacked spectra with `Xspec` using a single power law model. Then we divided the measured XRB intensities (in units of keV^2 keV^{-1} cm^{-2} s^{-1} at 1 keV) by the total solid angle covered by the *XMM-Newton* observations (0.4 deg^2 or 1.2185×10^{-4} sr) to obtain the resolved fraction of XRB in the area surveyed.

Fig. 4.18 shows the total extragalactic XRB spectrum as measured by the *HEAO-1* experiment (solid line), but renormalised to the 2-8 keV intensity put forward by De Luca & Molendi [48]. The points show the 2-7 keV XRB spectrum seen by MOS (diamonds) and pn (stars). Using a power law to fit the data we obtained a $\Gamma = 1.59 \pm 0.03$ and N=4.78 ± 0.15 keV^2 keV^{-1} cm^{-2} s^{-1} sr^{-1} (at 1 keV) for MOS data and $\Gamma = 1.54 \pm 0.04$ and N=4.38 ± 0.14 keV^2 keV^{-1} cm^{-2} s^{-1} sr^{-1} (at 1 keV) for pn. MOS and pn spectral slopes are consistent within the error bars. We see that the shape of the integrated emission of our sources is significantly harder than the average spectrum of the individual objects. However, our value is still softer than the shape of the XRB spectrum at these energies (see Sec. 1.3). Note that we have selected our sources in terms of the number of 0.2-12 keV counts, and therefore we favoured sources with spectrum peaking in this energy band. Because the effective area of the *XMM-Newton* EPIC detectors decreases rapidly at energies above ~5 keV, this selection implies a bias towards less absorbed sources. We expect the measured shape of the XRB in the *Lockman Hole* to become harder when the fainter sources detected in the field are included. However, with our analysis we cannot confirm whether, after including the fainter sources detected in the field, the resulting XRB spectrum will have a spectral slope consistent with the value of ~1.4 observed for the XRB. There might be still a missing component coming from heavily absorbed sources as concluded by Worsley et al.(2004) [248].

We also note that the 2-10 keV normalisation of the XRB that we obtain is significantly smaller than the value reported in Worsley et al.(2004) [248]. We expected this result because we selected our sources in terms of the 0.2-12 keV number of counts, and hence, our list of objects does not include all sources with 2-10 keV flux $\geq 10^{-15}\,\mathrm{erg\,cm^{-2}\,s^{-1}}$. Worsley et al.(2004) [248] did include fainter sources than the present study, and hence they reached a significantly higher integrated emission at 1 keV of $11 \pm 0.5\,\mathrm{keV^2\,keV^{-1}\,cm^{-2}\,s^{-1}\,sr^{-1}}$.

4.9 Summary

We have carried out a detailed study of the X-ray spectra of a sample of 123 objects detected with *XMM-Newton* in a deep observation of the *Lockman Hole* field. The EPIC spectra of these sources have all more than 500 background subtracted counts (MOS+pn) in the energy interval form 0.2-12 keV. Thanks to the good signal-to-noise ratio of the data we could study in detail the different spectral components that contribute to the X-ray emission of AGN in the above energy interval.

The 0.2-12 keV spectra of many AGN cannot be well reproduced with a single power law model. We found that this model is the best fit model for only ~53% of the sample. **The average continuum shape of our sources appears to harden at fainter 0.5-2 keV fluxes** [80] [140] [152] but there are some hints that **the same effect is seen for objects detected in the 2-10 keV band** [225] [228]. Two hypotheses have been suggested to explain it: X-ray absorption is more important at fainter fluxes or there exists a population of faint sources with intrinsically flatter continuum.

We have found that this apparent effect is due to absorption only. Both because we do not seen it in the 2-10 keV band, and because it disappears when absorption is taken into account. **We do not see any evidence for a population of intrinsically harder sources at faint fluxes.** However, if sources with larger column densities were found, then we should see the hardening of $\langle\Gamma\rangle$ in the 2-10 keV band [228]. Using a single power law model for the overall 0.2-12 keV band, most of our absorbed sources had the faintest 0.5-2 keV fluxes, but they had the same distribution of 2-10 keV fluxes as unabsorbed sources. Because of this, the average Γ obtained using a single power law model as a function of the 2-10 keV flux was measured to be harder (Γ ~1.7) than the typical value of ~1.9 found in unabsorbed AGN.

In the hard band we found no dependence of X-ray absorption or fraction of absorbed sources with flux. If observed (not corrected for absorption) 0.5-2 keV fluxes are used, then the column density and the fraction of absorbed sources increase significantly at fainter fluxes. However, **using de-absorbed 0.5-2 keV fluxes** (i.e. fluxes corrected for the effect of absorption) the correlations are not observed and **we obtained the same results as in the 2-10 keV band.** Therefore to study the dependence of Γ with the X-ray flux it is important to first correct the fluxes for the effect of X-ray absorption, or select hard X-ray fluxes, where this effect is smaller.

Another interesting result that we found in our analysis is that allowing the objects to be X-ray absorbed $\langle\Gamma\rangle$ ~1.9 at all 0.5-2 keV and 2-10 keV fluxes, but there is a significant scatter in the points. We have carried out a detailed study of the X-ray spectra of each individual object. We have searched for soft excess emission and for signatures of reflection at high energies (Compton reflection). We also studied the presence of Fe Kα emission. Using for each source the value of Γ obtained after including all these components to the fitting model we found that the scatter in $\langle\Gamma\rangle$ is much smaller.

However we still expect some intrinsic scatter in Γ. To calculate the intrinsic dispersion in the continuum shape of our objects, **we assumed that the distribution of Γ could be well represented by a Gaussian. Under this hypothesis, we found our sources to have an average spectral slope of ~1.92 with an intrinsic dispersion of ~0.28.**

Soft excess was detected in the co-added spectra of 18 sources. However only in 9 objects (4 type-1 AGN, 4 type-2 AGN and 1 unidentified source) could we fit the spectral signatures with a black body model (a Raymond Smith gave an equally good fit). We found the average temperature of the black body to be 0.09 ± 0.01 keV for type-1 AGN and 0.26 ± 0.08 keV for type-2 AGN. **The average 0.5-2 keV luminosities of the black body were found to be** (in log units) $43.42 \pm 0.43\,\mathrm{erg\,s^{-1}}$ in type-1 AGN and $44.11 \pm 0.44\,\mathrm{erg\,s^{-1}}$ in type-2 AGN. These luminosities are **too high to be attributable to thermal radiation from the host galaxy**. The 0.5-2 keV luminosities of the soft excess component do not differ significantly between type-1 AGN and type-2 AGN, but **our results seem to indicate that the black body temperatures are slightly higher in type-2 AGN than in type-1 AGN. This might be due to a higher contribution from scattering in type-2 AGN.** However due to the small number of AGN with soft excess analysed we cannot confirm this hypothesis. **The temperatures of the black body are in most cases ≥60 eV, and therefore the origin of the soft excess component in these sources cannot be explained as thermal emission from the accretion disc only.** Comptonization of cool disc photons by hot electrons surrounding the accretion disc might be an alternative additional explanation.

In 9 sources (including 1 type-1 AGN, 3 type-2 AGN and 5 sources unidentified) the black body model could not fit the soft excess emission. For these sources **we obtained a good fit with a scattering or partial covering model** (two power laws with the same spectral index but different absorptions). **The average covering fraction of the absorber was** 0.82 ± 0.06**, which means that the scattering fraction in them is rather large** (18±6%)**.** A combination of blackbody and scattered radiation could provide an equally good fit, with physically meaningful parameters, but we do not have means to disentangle the contribution between both components when none of them dominates.

We found only one object in our sample with a hardening at high energies. The source is still not identified so we used a model with two power laws to fit its X-ray emission.

Signatures of an emission line at high energies were found (F-test significance ≥95%)

in 8 sources (1 type-1 AGN, 5 type-2 AGN and 2 not identified sources). Although in some sources the profiles of the lines did not appear to be symmetrical, the signal-to-noise ratio of the spectra was not high enough to use more physical models. Therefore we fitted the lines in all the sources with a Gaussian model. For most AGN we found the centroids of the lines to be consistent (within the error bars) with being Fe Kα at an energy of $\sim$6.4 keV (rest frame). Only in one object we found the line centroid to be slightly higher than the expected value for neutral iron. In this source the line might arise as reflection in an ionised accretion disc.

In two objects we found significant intrinsic widths for the lines. In another two sources the centroids of the lines were found at energies lower than 6.4 keV. In all these sources the emission lines might have relativistic line profiles, and therefore they might have been emitted in the inner regions of the black hole accretion disc.

Once all additional spectral components have been modelled out, we found the best fit spectral slope to be 1.89 ± 0.03 in type-1 AGN and 1.71 ± 0.03 in type-2 AGN. These values are suggesting that type-2 AGN have harder spectral slopes than type-1 AGN. However assuming that the values of Γ that we have obtained follow a Gaussian distribution, and **allowing the distribution of spectral slopes to have intrinsic dispersion, the significance of type-2 AGN being harder than type-1 AGN is of 1.62σ only. We found an intrinsic dispersion in Γ of $\sim$0.20 in both type-1 AGN and type-2 AGN.**

X-ray absorbed objects were found among type-1 AGN ($\sim$10%) and type-2 AGN ($\sim$77%). We found the fraction of absorbed objects in type-1 AGN and type-2 AGN to be different with a significance of $>$ 99.99%. The distribution of absorbing column densities also suggest that **absorbed type-1 AGN are less strongly absorbed than absorbed type-2 AGN.** A comparison with a KS test gave a significance of type-2 AGN being absorbed by larger columns than type-1 AGN of 92%.

There have been claims of a flattening of the average spectral slope with redshift from *ROSAT* [24] ($0.1\leq z\leq3.2$) and *ASCA* [240] ($z>2$) spectral studies of AGN. However recent X-ray spectral analyses of high redshift ($z>4$) AGN detected with *Chandra* and *XMM-Newton* have reached different conclusions on the cosmic evolution of the broad band continuum shape of AGN: Bechtold et al.(2003) [20] reported a hardening of the continuum of high redshift ($3.70\leq z\leq6.28$) AGN ($\Gamma=1.5\pm0.5$) while Grupe et al.(2006) [97] reported a steepening ($\Gamma=2.21\pm0.52$). Vignali et al.(2005) [239] from a joint X-ray spectral fitting of a sample of 48 $z>4$ AGN observed with *Chandra* in the redshift range 3.99-6.28, concluded that the X-ray spectral properties of AGN do not show any significant evolution or luminosity dependence. We have not seen a dependence of the continuum shape or the column density of the AGN in our *Lockman Hole* sample with the X-ray luminosity or redshift.

We studied in more detail the X-ray emission of the 5 type-2 AGN with unabsorbed MOS and pn X-ray spectra. All these sources have spectra with enough signal-to-noise ratio, hence we should have been able to detect signatures of X-ray absorption if they were present. We have calculated 90% upper limits of the column density for these objects. The values were found to be lower than those found in our sample of absorbed type-2 AGN. Such low values of the column density could be explained as arising in the host galaxy. We argue that spectral variability is unlikely to be at the heart of this apparent X-ray/optical mismatch (see Chapter 5).

Finally we do not find compelling evidence that these sources are Compton-thick, based on the lack of obvious Fe lines, although the [OIII] flux needs to be measured to reach a firm conclusion.

To calculate the contribution to the XRB from our sources, MOS and pn spectra have been stacked. **We found that the 2-7 keV XRB resolved by our sources** has a spectral shape best fitted with a power law of slope $\Gamma = 1.59 \pm 0.03$ and normalisation $N{=}4.78 \pm 0.15\,\mathrm{keV^2\,keV^{-1}\,cm^{-2}\,s^{-1}\,sr^{-1}}$ (at 1 keV) for MOS data and $\Gamma = 1.54 \pm 0.04$ and $N{=}4.38 \pm 0.14\,\mathrm{keV^2\,keV^{-1}\,cm^{-2}\,s^{-1}\,sr^{-1}}$ (at 1 keV) for pn data. The contribution is indeed **harder than the spectrum of the brightest AGN, but still softer than the XRB.** Since our sources have been selected in the 0.2-12 keV band, we probably missed faint heavily absorbed sources in our sample. This is why we only get ~1/2 of the intensity that Worsley et al.(2004) [248], obtained by stacking hard X-ray selected sources on the same data. **A further component not detectable by *XMM-Newton* arising above 5 keV might also be present, as argued by Worsley et al.(2004) [248].**

Table 4.8: X-ray emission properties of *Lockman Hole* sources.

XMM (1)	*ROSAT* (2)	R.A. (3)	Dec (4)	Class (5)	redshift (6)	Model (7)	Γ (8)	N_H (9)	$S_{0.5-2}$ (10)	S_{2-10} (11)	$L_{0.5-2}$ (12)	L_{2-10} (13)
607	-	10 53 01.86	+57 15 00.69	–	-	SPL	$1.21^{0.13}_{0.13}$		0.73	2.81		
599	54A	10 53 07.46	+57 15 05.84	type-1	2.416	SPL	$1.46^{0.11}_{0.11}$		1.02	2.68	44.36	44.80
400	13A	10 52 13.29	+57 32 25.58	type-1	1.873	SPL	$1.90^{0.06}_{0.06}$		0.63	0.84	44.14	44.27
63	-	10 52 36.49	+57 16 04.07	–	-	APL	$2.13^{0.32}_{0.23}$	$20.88^{0.24}_{0.38}$	0.54	0.66		
5	52A	10 52 43.30	+57 15 45.95	type-1	2.144	SPL	$1.90^{0.06}_{0.06}$		1.60	2.16	44.68	44.68
6	504(51D)	10 51 14.30	+57 16 16.88	type-2	0.528	SPL	$1.94^{0.20}_{0.19}$		0.87	1.11	42.97	43.07
16	-	10 51 46.64	+57 17 16.02	–	-	APL	$2.27^{2.08}_{0.98}$	$21.59^{0.40}_{0.24}$	0.22	0.44		
21	48B	10 50 45.67	+57 17 32.60	type-2	0.498	SPL	$1.77^{0.14}_{0.14}$		1.34	2.18	43.07	43.28
26	-	10 52 32.99	+57 17 50.96	–	-	SPL	$1.09^{0.20}_{0.20}$		0.21	0.95		
31	-	10 52 00.34	+57 18 08.24	–	-	CAPL	$2.34^{0.30}_{0.63}$	$22.29^{0.12}_{0.16}$	0.15	0.99		
41	46A	10 51 19.14	+57 18 34.09	type-1	1.640	APL	$2.06^{0.38}_{0.27}$	$21.82^{0.25}_{0.38}$	0.53	0.68	44.09	44.11
39	45Z	10 53 19.09	+57 18 53.58	type-2	0.711	SPL	$1.79^{0.08}_{0.08}$		0.86	1.37	43.24	43.44
53	43A	10 51 04.39	+57 19 23.90	type-1	1.750	APL	$1.83^{0.22}_{0.18}$	$21.68^{0.24}_{0.44}$	0.84	1.43	44.22	44.40
65	-	10 52 55.46	+57 19 52.80	–	-	APL	$1.57^{0.27}_{0.22}$	$21.24^{0.15}_{0.26}$	0.25	0.86		
74	905A	10 52 51.13	+57 20 15.70	–	-	SPL	$1.67^{0.21}_{0.20}$		0.19	0.35		
72	84Z	10 52 16.94	+57 20 19.71	type-2	2.710*	APL	$1.69^{0.08}_{0.10}$	$23.28^{0.06}_{0.05}$	0.85	4.67	45.04	45.31
85	38A	10 53 29.50	+57 21 06.22	type-1	1.145	SPL	$2.13^{0.09}_{0.08}$		0.72	0.69	43.77	43.74
86	-	10 53 09.68	+57 20 59.58	type-1	3.420	SPL	$1.66^{0.17}_{0.16}$		0.23	0.45	44.16	44.45
88	39B	10 52 09.37	+57 21 05.43	type-1	3.279	SPL	$1.73^{0.12}_{0.12}$		0.40	0.70	44.41	44.65
90	37A	10 52 48.09	+57 21 17.43	type-1	0.467	SPL+SE	$2.10^{0.13}_{0.10}$		1.56	1.40	43.21	43.08
96	814(37G)	10 52 44.87	+57 21 24.84	type-1	2.832	SPL	$2.08^{0.09}_{0.08}$		0.58	0.60	44.64	44.65
107	-	10 52 19.49	+57 22 15.26	type-2	0.075	APL	$2.02^{0.23}_{0.28}$	$21.34^{0.09}_{0.21}$	0.26	0.48	40.78	40.83
120	-	10 52 25.17	+57 23 07.02	–	-	SPL	$1.91^{0.07}_{0.07}$		0.62	0.83		
108	-	10 50 50.91	+57 22 15.65	–	-	2SPL	$1.56^{0.18}_{0.18}$		0.78	8.48		
900	-	10 54 59.43	+57 22 18.84	–	-	APL	$1.72^{0.15}_{0.16}$	$21.03^{0.14}_{0.27}$	2.46	5.83		
121	434B	10 52 58.08	+57 22 51.95	type-2	0.772	APL	$1.95^{0.25}_{0.20}$	$21.55^{0.16}_{0.24}$	0.31	0.52	43.05	43.15

Table 4.8: Continued.

XMM (1)	*ROSAT* (2)	R.A. (3)	Dec (4)	Class (5)	redshift (6)	Model (7)	Γ (8)	$\mathrm{N_H}$ (9)	$S_{0.5-2}$ (10)	S_{2-10} (11)	$L_{0.5-2}$ (12)	L_{2-10} (13)
135	513(34O)	10 52 54.39	+57 23 43.89	type-1	0.761	SPL	$1.78^{0.04}_{0.04}$		1.56	2.50	43.56	43.77
124	634A	10 53 11.72	+57 23 09.07	type-1	1.544	SPL	$1.69^{0.11}_{0.10}$		0.35	0.64	43.60	43.86
125	607(36Z)	10 52 19.90	+57 23 07.92	–	-	SPL	$1.66^{0.16}_{0.16}$		0.21	0.41		
142	-	10 52 03.74	+57 23 39.62	–	-	SPL	$1.81^{0.22}_{0.21}$		0.16	0.24		
133	35A	10 50 38.77	+57 23 39.67	type-1	1.439	SPL	$2.04^{0.10}_{0.10}$		2.49	2.75	44.52	44.56
148	32A	10 52 39.66	+57 24 32.83	type-1	1.113	SPL+SE	$2.12^{0.03}_{0.03}$		7.72	7.45	44.93	44.74
166	-	10 52 31.98	+57 24 30.82	–	-	APL	$1.44^{0.19}_{0.24}$	$22.19^{0.14}_{0.16}$	0.09	1.48		
156	-	10 51 54.59	+57 24 09.28	type-2**	2.365	APL	$2.40^{0.57}_{0.45}$	$22.65^{0.20}_{0.25}$	0.22	0.27	44.49	44.29
163	33A	10 51 59.88	+57 24 26.31	type-1	0.974	APL	$1.52^{0.32}_{0.22}$	$21.57^{0.25}_{0.49}$	0.22	0.63	42.97	43.35
168	31A	10 53 31.72	+57 24 56.19	type-1	1.956	SPL	$1.93^{0.03}_{0.03}$		3.30	4.22	44.92	45.03
172	-	10 53 15.71	+57 24 50.84	type-2	1.17	APL	$2.26^{0.63}_{0.40}$	$23.22^{0.17}_{0.18}$	0.08	0.83	44.11	44.00
183	82A	10 53 12.27	+57 25 08.28	type-1	0.96	SPL	$1.88^{0.07}_{0.07}$		0.57	0.78	43.39	43.53
176	30A	10 52 57.25	+57 25 08.77	type-1	1.527	SPL	$2.21^{0.05}_{0.05}$		1.08	0.92	44.29	44.22
179	-	10 52 31.64	+57 25 03.93	–	-	CAPL	$2.07^{0.26}_{0.52}$	$22.42^{0.14}_{0.22}$	0.06	0.56		
174	-	10 51 20.63	+57 24 58.24	–	-	SPL	$1.37^{0.14}_{0.14}$		0.30	0.90		
186	-	10 51 49.93	+57 25 25.13	type-2	0.676	APL	$1.70^{0.11}_{0.12}$	$22.21^{0.08}_{0.07}$	0.54	2.44	43.38	43.64
171	28B	10 54 21.22	+57 25 45.40	type-2	0.205	APL	$1.73^{0.02}_{0.03}$	$21.33^{0.02}_{0.02}$	33.50	84.89	43.75	44.00
200	-	10 53 46.81	+57 26 07.77	–	-	APL	$2.37^{0.36}_{0.26}$	$20.93^{0.24}_{0.32}$	0.32	0.28		
187	-	10 50 47.96	+57 25 22.71	–	-	SPL	$1.98^{0.08}_{0.08}$		1.15	1.38		
191	29A	10 53 35.03	+57 25 44.13	type-1	0.784	SPL	$1.82^{0.02}_{0.02}$		4.20	6.35	44.04	44.22
199	-	10 52 25.28	+57 25 51.27	–	-	APL	$1.80^{0.28}_{0.21}$	$21.99^{0.14}_{0.14}$	0.16	1.14		
217	-	10 51 11.60	+57 26 36.67	–	-	APL	$1.87^{0.11}_{0.12}$	$20.80^{0.17}_{0.31}$	0.65	1.10		
214	-	10 53 15.09	+57 26 30.65	–	-	APL	$1.88^{0.18}_{0.19}$	$21.41^{0.09}_{0.13}$	0.24	0.63		
222	-	10 53 51.67	+57 27 03.64	type-2	0.917	APL	$1.88^{0.09}_{0.10}$	$21.45^{0.09}_{0.12}$	1.04	1.76	43.69	43.84
2020	27A	10 53 50.19	+57 27 11.61	type-1	1.720	SPL	$2.23^{0.07}_{0.07}$		0.97	0.80	44.39	44.30
226	-	10 51 20.49	+57 27 03.47	–	-	SPL	$1.88^{0.10}_{0.10}$		0.50	0.70		
243	-	10 51 28.14	+57 27 41.55	–	-	CAPL	$1.82^{0.19}_{0.17}$	$22.02^{0.08}_{0.08}$	0.51	3.49		

Table 4.8: Continued.

XMM (1)	*ROSAT* (2)	R.A. (3)	Dec (4)	Class (5)	redshift (6)	Model (7)	Γ (8)	$\mathrm{N_H}$ (9)	$S_{0.5-2}$ (10)	S_{2-10} (11)	$L_{0.5-2}$ (12)	L_{2-10} (13)
254	486A	10 52 43.37	+57 28 01.49	type-2	1.210	APL	$1.76^{0.13}_{0.13}$	$22.18^{0.08}_{0.10}$	0.32	0.91	43.59	43.81
261	80A	10 51 44.63	+57 28 08.89	type-1	3.409	SPL	$1.63^{0.08}_{0.08}$		0.45	0.92	44.44	44.74
259	-	10 53 05.60	+57 28 12.50	type-2	0.792	APL+SE	$1.22^{0.14}_{0.18}$	$23.24^{0.12}_{0.13}$	0.07	3.39	43.32	43.90
270	120A	10 53 09.28	+57 28 22.65	type-1	1.568	SPL+SE	$2.17^{0.06}_{0.09}$		0.80	0.72	44.32	44.12
267	428E	10 53 24.54	+57 28 20.65	type-1	1.518	APL	$1.74^{0.10}_{0.10}$	$21.27^{0.12}_{0.40}$	0.53	0.97	43.81	44.05
287	821A	10 53 22.04	+57 28 52.76	type-1	2.300	SPL	$1.67^{0.14}_{0.13}$		0.20	0.39	43.74	44.02
268	-	10 53 48.09	+57 28 17.75	–	-	APL	$1.83^{0.19}_{0.20}$	$21.81^{0.13}_{0.11}$	0.24	1.21		
277	25A	10 53 44.85	+57 28 42.24	type-1	1.816	SPL	$1.74^{0.04}_{0.04}$		1.18	2.03	44.31	44.55
272	26A	10 50 19.40	+57 28 13.99	type-2	0.616	APL	$2.39^{0.17}_{0.17}$	$21.58^{0.10}_{0.13}$	1.39	1.38	43.62	43.43
290	901A	10 52 52.74	+57 29 00.81	type-2	0.204	APL+SE	$1.86^{0.39}_{0.22}$	$23.60^{0.07}_{0.14}$	0.14	1.79	42.69	42.83
369	-	10 51 06.50	+57 15 31.92	–	-	SPL	$1.96^{0.11}_{0.11}$		1.99	2.46		
300	426A	10 53 03.64	+57 29 25.56	type-1	0.788	CAPL	$1.98^{0.18}_{0.15}$	$22.09^{0.16}_{0.22}$	0.50	0.87	43.32	43.40
306	-	10 52 06.84	+57 29 25.43	type-2	0.708	APL	$1.38^{0.24}_{0.20}$	$22.20^{0.17}_{0.17}$	0.16	1.03	42.76	43.23
321	23A	10 52 24.74	+57 30 11.40	type-1	1.009	SPL	$1.70^{0.08}_{0.08}$		0.39	0.71	43.22	43.48
326	117Q	10 53 48.80	+57 30 36.09	type-2	0.78	APL	$1.53^{0.06}_{0.05}$	$21.96^{0.06}_{0.06}$	1.38	5.49	43.71	44.08
350	-	10 52 41.65	+57 30 39.97	–	-	SPL	$1.28^{0.14}_{0.14}$		0.14	0.50		
332	77A	10 52 59.16	+57 30 31.81	type-1	1.676	SPL	$1.62^{0.04}_{0.04}$		1.08	2.22	44.14	44.45
411	53A	10 52 06.02	+57 15 26.41	type-2	0.245	CAPL	$1.63^{0.22}_{0.19}$	$22.18^{0.13}_{0.16}$	0.85	4.84	42.63	42.94
2024	-	10 54 10.68	+57 30 56.73	–	-	SPL	$2.02^{0.07}_{0.07}$		0.82	0.93		
343	-	10 50 41.22	+57 30 23.31	–	-	SPL	$1.54^{0.19}_{0.18}$		0.44	1.01		
342	16A	10 53 39.62	+57 31 04.89	type-1	0.586	SPL+SE	$2.26^{0.04}_{0.05}$		4.84	3.81	43.92	43.78
351	-	10 51 46.39	+57 30 38.14	–	-	SPL	$1.87^{0.15}_{0.14}$		0.21	0.30		
353	19B	10 51 37.27	+57 30 44.43	type-1	0.894	SPL	$1.72^{0.10}_{0.10}$		0.40	0.71	43.12	43.37
354	75A	10 51 25.25	+57 30 52.33	type-1	3.409	SPL	$1.75^{0.08}_{0.07}$		0.71	1.20	44.71	44.94
358	17A	10 51 03.86	+57 30 56.65	type-1	2.742	SPL	$1.78^{0.08}_{0.07}$		1.13	1.83	44.72	44.93
355	-	10 52 37.33	+57 31 06.67	type-2	0.708	APL	$1.60^{0.12}_{0.12}$	$21.17^{0.17}_{0.28}$	0.36	0.86	42.87	43.19
385	14Z	10 52 42.37	+57 32 00.64	type-2	1.380	APL	$1.83^{0.08}_{0.08}$	$22.33^{0.04}_{0.04}$	0.76	2.10	44.16	44.33

Table 4.8: Continued.

XMM (1)	*ROSAT* (2)	R.A. (3)	Dec (4)	Class (5)	redshift (6)	Model (7)	Γ (8)	N_H (9)	$S_{0.5-2}$ (10)	S_{2-10} (11)	$L_{0.5-2}$ (12)	L_{2-10} (13)
364	18Z	10 52 28.36	+57 31 06.57	type-1	0.931	SPL	$1.79^{0.13}_{0.13}$		0.23	0.37	42.94	43.14
901	-	10 50 05.55	+57 31 09.01	–	-	SPL	$1.64^{0.14}_{0.12}$		0.79	1.58		
902	73C	10 50 09.12	+57 31 46.29	type-1	1.561	SPL	$1.50^{0.14}_{0.14}$		0.78	1.94	43.88	44.28
377	-	10 52 52.11	+57 31 38.02	–	-	APL	$1.81^{0.21}_{0.21}$	$21.87^{0.11}_{0.12}$	0.17	0.92		
384	-	10 53 21.63	+57 31 49.44	–	-	APL	$2.22^{0.19}_{0.26}$	$21.33^{0.11}_{0.17}$	0.26	0.40		
387	15A	10 52 59.78	+57 31 56.69	type-1	1.447	SPL	$2.27^{0.11}_{0.11}$		0.37	0.28	43.78	43.67
394	-	10 52 51.40	+57 32 02.03	type-2	0.664	APL	$1.85^{0.22}_{0.22}$	$21.24^{0.24}_{0.45}$	0.17	0.29	42.55	42.71
406	828A	10 53 57.16	+57 32 44.00	type-1	1.282	SPL	$2.12^{0.10}_{0.10}$		0.62	0.60	43.82	43.80
419	-	10 54 00.46	+57 33 22.19	–	-	APL	$1.81^{0.23}_{0.17}$	$21.62^{0.12}_{0.11}$	0.41	1.54		
407	12A	10 51 48.69	+57 32 50.07	type-2	0.990	CAPL	$1.25^{0.10}_{0.10}$	$22.69^{0.12}_{0.11}$	0.57	4.89	43.64	44.20
424	-	10 52 37.93	+57 33 22.65	type-2	0.707	APL+SE	$1.70^{0.32}_{0.18}$	$22.95^{0.12}_{0.12}$	0.22	2.36	43.50	43.74
427	-	10 52 27.88	+57 33 30.65	type-2	0.696	SPL	$1.40^{0.20}_{0.20}$		0.14	0.39	42.33	42.79
430	11A	10 51 08.19	+57 33 47.06	type-1	1.540	APL	$1.42^{0.08}_{0.08}$	$21.58^{0.13}_{0.19}$	1.24	3.83	44.09	44.53
458	-	10 51 06.22	+57 34 36.67	–	-	CAPL	$1.34^{0.39}_{0.16}$	$22.31^{0.16}_{0.20}$	0.28	4.43		
442	805A	10 53 47.28	+57 33 50.41	type-1	2.586	SPL	$1.76^{0.15}_{0.14}$		0.33	0.55	44.12	44.34
443	-	10 52 36.89	+57 33 59.80	type-2	1.877	APL	$2.05^{0.42}_{0.34}$	$23.22^{0.16}_{0.18}$	0.17	0.97	44.42	44.46
474	-	10 51 28.13	+57 35 04.20	–	–	SPL	$1.98^{0.11}_{0.11}$		0.47	0.56		
451	-	10 52 07.87	+57 34 17.48	–	-	APL	$1.94^{0.18}_{0.21}$	$21.31^{0.11}_{0.15}$	0.29	0.62		
450	477A	10 53 05.98	+57 34 26.70	type-1	2.949	SPL	$2.03^{0.10}_{0.10}$		0.44	0.49	44.53	44.57
453	804A	10 53 12.24	+57 34 27.39	type-1	1.213	SPL	$2.05^{0.14}_{0.14}$		0.31	0.34	43.44	43.47
456	9A	10 51 54.30	+57 34 38.66	type-1	0.877	SPL	$2.01^{0.05}_{0.05}$		1.25	1.44	43.68	43.74
491	-	10 51 41.91	+57 35 56.00	–	-	APL	$2.18^{0.23}_{0.25}$	$21.24^{0.15}_{0.25}$	0.33	0.48		
469	-	10 54 07.21	+57 35 24.89	–	-	SPL	$2.14^{0.04}_{0.04}$		3.86	3.62		
475	6A	10 53 16.51	+57 35 52.23	type-1	1.204	SPL	$1.78^{0.02}_{0.02}$		10.21	16.61	44.85	45.06
476	827A	10 53 03.43	+57 35 30.80	type-2	0.607	SPL	$2.07^{0.17}_{0.17}$		0.27	0.29	42.64	42.66
505	104A	10 52 41.54	+57 36 52.85	type-2	0.137	CAPL	$1.72^{0.09}_{0.08}$	$21.69^{0.11}_{0.08}$	1.36	3.96	42.04	42.29
504	-	10 54 26.22	+57 36 49.05	–	-	APL+SE	$1.98^{0.19}_{0.10}$	$22.66^{0.06}_{0.06}$	1.01	42.52		

Table 4.8: Continued.

XMM (1)	*ROSAT* (2)	R.A. (3)	Dec (4)	Class (5)	redshift (6)	Model (7)	Γ (8)	$\mathrm{N_H}$ (9)	$S_{0.5-2}$ (10)	S_{2-10} (11)	$L_{0.5-2}$ (12)	L_{2-10} (13)
511	-	10 53 38.50	+57 36 55.47	type-2	0.704	APL+SE	$2.62^{0.73}_{0.29}$	$22.81^{0.15}_{0.14}$	0.19	0.96	43.97	43.58
518	-	10 53 36.33	+57 37 32.14	–	–	APL	$2.38^{0.52}_{0.19}$	$21.09^{0.14}_{0.20}$	0.48	0.47		
523	-	10 51 29.98	+57 37 40.71	–	-	SPL	$1.94^{0.09}_{0.09}$		0.92	1.17		
529	-	10 51 37.30	+57 37 59.11	–	-	CAPL	$1.98^{0.20}_{0.21}$	$21.93^{0.23}_{0.20}$	1.51	2.88		
532	801A	10 52 45.36	+57 37 48.69	type-1	1.677	SPL	$2.32^{0.21}_{0.20}$		0.22	0.16	43.74	43.60
527	5A	10 53 02.34	+57 37 58.62	type-1	1.881	SPL	$1.91^{0.06}_{0.05}$		1.13	1.50	44.40	44.53
537	-	10 50 50.04	+57 38 21.79	–	-	SPL	$2.40^{0.08}_{0.08}$		3.04	1.95		
548	832A	10 52 07.53	+57 38 41.40	type-1	2.730	SPL	$1.79^{0.15}_{0.14}$		0.30	0.48	44.15	44.13
557	-	10 52 07.75	+57 39 07.49	–	-	APL	$2.01^{0.36}_{0.17}$	$20.94^{0.22}_{0.45}$	0.33	0.49		
553	2A	10 52 30.06	+57 39 16.81	type-1	1.437	APL	$2.08^{0.04}_{0.04}$	$21.20^{0.12}_{0.14}$	2.87	3.14	44.62	44.64
555	-	10 51 52.07	+57 39 09.41	–	-	SPL	$1.84^{0.12}_{0.12}$		0.49	0.72		
594	-	10 52 48.40	+57 41 29.14	–	-	SPL	$1.59^{0.24}_{0.24}$		0.38	0.82		
2045	-	10 52 04.47	+57 41 15.65	–	-	SPL	$1.89^{0.09}_{0.09}$		0.94	1.28		
584	-	10 52 06.28	+57 41 25.53	–	-	SPL	$2.17^{0.07}_{0.08}$		1.61	1.45		
591	-	10 52 23.17	+57 41 24.62	–	–	SPL	$2.08^{0.14}_{0.14}$		0.59	0.61		
601	-	10 51 15.91	+57 42 08.59	–	-	SPL	$1.84^{0.20}_{0.19}$		1.30	1.92		

Columns are as follows: (1) XMM-Newton identification number; (2) *ROSAT* identification number; (3) right ascension (J2000); (4) declination (J2000) (5) optical class from optical spectroscopy; (6) Source redshift (7) best fit model of the X-ray spectrum of each object: SPL: single power law, APL: absorbed power law, SE: Soft-excess emission, CAPL: absorption with partial covering absorber, 2SPL: two power laws; (8) slope of the broad band continuum emission; (9) Logarithm of the hydrogen column density of the X-ray absorber (observed $\mathrm{N_H}$ if the source was not identified or rest-frame absorption if the source was identified; (10)(11) 0.5-2 and 2-10 keV flux in units of $10^{-14}\,\mathrm{erg\,cm^{-2}\,s^{-1}}$ obtained from the best fit model; (12)(13) logarithm of the 0.5-2 and 2-10 keV luminosities (corrected for absorption) for the identified sources obtained from the best fit model. Errors correspond to the 90% confidence interval.

[*] Source photometric redshift.

[**] BALQSO

Chapter 5

Variability properties of X-ray sources in the *Lockman Hole*

Active Galactic Nuclei (AGN) are strongly variable sources in all wave bands [54] [172] on different time scales, showing their largest amplitude and fastest variability in X-rays. The later is usually taken as evidence for X-ray emission in AGN originating in a small region close to the central source, which is thought to be a supermassive ($10^6 - 10^9 \mathrm{M}_\odot$) black hole. Current instrumentation cannot spatially resolve the innermost regions of AGN and, although the origin of X-ray variability in AGN is poorly understood, it is considered a powerful method to obtain information on the scale and the structure of X-ray emitting regions in AGN.

In this chapter we present the results of a study of the flux and spectral variability properties of the 123 brightest objects detected with *XMM-Newton* in the *Lockman Hole* field, for which their time-averaged X-ray spectral properties are known, and were presented in the previous chapter. The aim of this study is to provide further insight into the origin of the X-ray emission in AGN, by analysing the time dependence of the emission properties of the detected components in the co-added X-ray spectra of the objects.

5.1 X-ray data

The *XMM-Newton* deep survey in the *Lockman Hole* is composed of 17 observations (see Table 4.1 for information on the observational details) carried out from 2000 to 2002, which allow us to study the X-ray variability properties of our sources on long time scales, from months to years. Our variability analysis does not allow us to study fluctuations in the accretion disc, as the dynamical time scales (light-crossing time) are much shorter than the ones sampled in our analysis. Intra-orbit variability studies (i.e. on time scales <2 days) cannot be performed on the *Lockman Hole* sources, as these are too faint. The time scales sampled here will allow us to detect changes in the global accretion rate or in the environment of the AGN, e.g. fluctuations in the accretion flow outside the X-ray emitting region and/or changes in the absorbing material.

As explained in Sec. 2.8, in order to extract the spectral products of our objects, source detection was carried out on the data from each individual observation, and therefore we have all the relevant parameters for the sources in our sample from all observations where they were detected. We have used measured 0.2-12 keV count rates[1] from each individual observation where sources were detected, to build light curves that we used to study X-ray flux and spectral variability.

Source parameters become very uncertain for objects detected close to CCD gaps. To avoid this problem affecting our results, we did not use data from observations where the objects were detected near CCD gaps, bad columns, or near the edge of the Field of View (FOV) in the terms explained in Sec. 2.4.

The three *XMM-Newton* EPIC cameras (M1, M2 and pn) have different geometries, therefore for a given observation, it is common to find that a significant number of serendipitously detected objects fall near or inside CCD gaps in at least one of the cameras. This means that, for the same object, we will have light curves from different data sets (i.e. data from different revolutions) for each camera and therefore the sampling of data is different. In addition, because of their different instrumental responses we cannot combine the count rates from the three EPIC cameras. The fact that light curves from each EPIC camera are sampled differently in most sources, makes comparing the results of our variability analysis between detectors very difficult. Due to the geometry of the pn detector, the number of sources falling in the pn CCD gaps will be larger than in MOS detectors; however the former provides the deepest observation of the field for each exposure, which allows to detect lower variability amplitudes, and to measure better the amplitude of detected variability. Therefore, we have used only pn data in the analysis presented in this chapter.

5.2 Flux variability

In order to search for flux variability, we created a light curve for each source using the count rates in the observed 0.2-12 keV energy band in each revolution. We used this energy band because it was used to study the X-ray properties of the co-added spectra of the sources, and therefore we can compare directly the detected variability properties with the average spectral properties of the sources. In addition, using 0.2-12 keV count rates we have more than 10 counts (background subtracted) on each point of the light curves, and therefore we can assume Gaussian statistics during the analysis. Using EPIC-pn 0.2-12 keV count rates we obtained light curves with at least two data points for 120 out of the 123 sources in our sample, including 45 type-1 AGN and 27 type-2 AGN.

Not all EPIC-pn observations were carried out with the same blocking filter (see Table 4.1). During the PV phase, the Thin filter was used, but for all AO1 and AO2 observations the Medium filter was used instead. We cannot directly compare the observed count rates, because blocking filters affect in a different way the low energy photons that arrive in the detectors, and hence measured 0.2-12 keV count rates will be different even for a non varying source. Moreover, changes in background modelling/calibration during the lifetime of the mission can introduce systematic differences between measured count

---

[1] The SAS source detection task `emldetect` (see Sec. 2.3) provides count rates corrected for vignetting and Point Spread Function (PSF) losses on each energy band.

rates. The observations we are using were carried out in a time interval spanning two years, and therefore we need to study whether any instrumental drift is present in our data, and whether it is affecting the measured variability properties of our sources. In order to do that, we have calculated the mean (averaged over all sources) deviation of the count rates measured on each observation from the mean count rates of the light curves. We then corrected the count rates from these mean deviations. This is explained in detail in Appendix D, where it is shown that any instrumental drifts are in all cases very small. All count rates used for the study presented in this chapter are corrected for this small effect.

To search for deviations from the null hypothesis, consisting in that the 0.2-12 keV mean count rates of the objects have remained constant during all observations, we used the χ^2

$$\chi^2 = \sum_{i=1}^{N} \frac{(x_i - \langle x \rangle)^2}{\sigma_i^2} \tag{5.1}$$

where x_i are 0.2-12 keV count rates on each observation and σ_i the corresponding 1σ statistical errors, N is the number of points on each light curve and $\langle x \rangle$ is the unweighted mean count rate for that source. We accepted a source as variable if the significance of χ^2 of being higher than the obtained value just by random effects is lower than 2.7×10^{-3} i.e. 3σ.

The results of detection of flux variability are summarised in columns 3 and 4 of Table 5.1. We have corrected the fractions of sources with detected flux variability for spurious detections for the given confidence level (3σ) using the method described in Appendix A.4. We have detected flux variability in ~50% of the sources with a significance of more than 3σ. Flux variability was detected in 31 out of 45 (68±11%) type-1 AGN and 13 out of 27 (48±15%) type-2 AGN. The fraction of AGN with detected flux variability was not found to vary with redshift, i.e., the different sampling of rest-frame energies for sources at different redshifts does not seem to affect the detection of flux variability. We compared the obtained fractions of varying sources for different samples of objects using the method described in Appendix A.4. We found that the probability of obtaining more than 13 type-1 AGN with detected flux variability in a sample of 45 objects is ~75%. Therefore there is no evidence that the fraction of sources showing flux variability in the 0.2-12 keV band on long time scales is different for type-1 and type-2 AGN. We see that the fraction of variable sources among unidentified objects is lower than the fractions obtained for type-1 and type-2 AGN and for the whole sample of objects. This could be due to the fact that most unidentified objects are among the faintest sources in the sample, and therefore they will tend to have light curves with lower signal-to-noise ratio. In addition, some of these unidentified sources might not be variable. For example, unidentified heavily obscured AGN (i.e. much more obscured than the identified type-2 AGN) may show only reprocessed emission which will also have lower variability amplitude, as multiple scatterings smear out the variability.

Our sources exhibit different flux variability patterns. Some objects became fainter with time, while others became brighter. However for a significant fraction of sources, we find irregular flux variations with respect to their mean flux level. Some examples of the typical

Table 5.1: *Fractions of sources with detected 0.2-12 keV flux and spectral variability.*

Group (1)	N$_{\rm tot}$ (2)	n$_{\rm flux}$ (3)	fracc$_{\rm flux}$(%) (4)	n$_{\rm sp}$ (5)	fracc$_{\rm sp}$(%) (6)
All	120	62	51±7	24	20±6
type-1 AGN	45	31	68±11	6	14±8
type-2 AGN	27	13	48±15	9	34±14
Unidentified	48	18	37±11	9	19±9

Columns are as follows: (1) group of sources; (2) total number of objects in the group; (3) number of sources with detected flux variability (confidence $\geq 3\sigma$); (4) fraction (corrected for spurious detections; see Appendix A.4) of sources in group with detected flux variability; (5) number of sources with detected spectral variability (confidence $\geq 3\sigma$); (6) fraction (corrected for spurious detections) of sources in group with detected spectral variability. Errors correspond to the 1σ confidence interval.

light curves used in our analysis are shown in Fig. 5.7. It is important to note that our variability analysis does not allow us to measure variability time scales in the light curves of our sources, because the detected variability might have occur at some point during the time intervals not covered by our data. On the other hand, each point in the light curves represents the measured count rate of the objects during the whole observation, and therefore we do not have information in our light curves on when the variability occurred even for the cases where the variability occurred during the observations.

5.2.1 Amplitude of variability

The method we have used to calculate the amplitude of flux variability (noise-subtracted) in our light curves is fully described in Almaini et al.(2000) [3]. This method is the most appropriate in the regime of Gaussian statistics, an assumption that, as we saw before, is satisfied by our data. In addition, this method can be used for light curves with points having significantly different measurement errors.

The method assumes that the measured dispersion in light curves has two different contributions:

$$\sigma^2_{\rm total} = \sigma^2_{\rm noise} + \sigma^2_Q \tag{5.2}$$

the first contribution, σ_{noise}, being the intrinsic fluctuation of the points due to the noise in the data and the second, σ_Q, the intrinsic fluctuation due to variations in the source flux. We are interested in the second quantity, σ_Q, as it measures the variability in flux of the objects. In order to calculate σ_Q, a maximum likelihood method is used by defining the function $L(\sigma_Q|x_i,\sigma_i)$ that represents, for a set of points (x_i,σ_i), the likelihood function

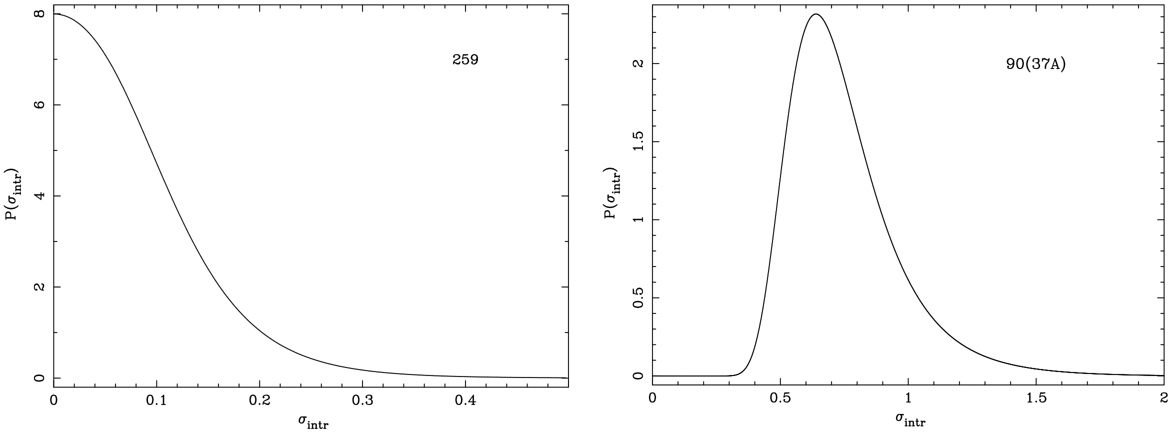

Figure 5.1: *Typical probability distributions of the excess variance, $\sigma_{\rm intr}$, for sources without detected variability (left) and detected variability (right).*

of σ_Q,

$$L(\sigma_Q|x_i,\sigma_i) = \prod_{i=1}^{N} \frac{\exp[-\frac{1}{2}(x_i - \langle x\rangle)^2/(\sigma_i^2+\sigma_Q^2)]}{(2\pi)^{1/2}(\sigma_i^2+\sigma_Q^2)^{1/2}} = P(\sigma_Q) \tag{5.3}$$

To compute the most likely variability amplitude (the mode of $P(\sigma_Q)$) we have to solve the equation

$$\sum_{i=1}^{N} \frac{[(x_i - \langle x\rangle)^2 - (\sigma_i^2+\sigma_Q^2)]}{(\sigma_i^2+\sigma_Q^2)} = 0 \tag{5.4}$$

In general, Eq. 5.4 can only be solved numerically. The maximum of the function gives the most probable value of σ_Q for the given set of data points. The errors in σ_Q were calculated by integrating the function from the maximum value to both sides until the desired probability is encompassed. We have calculated 1σ errors that correspond to a probability of 68%. In the cases where the lower error bound of the integrals reached zero we calculated 1σ upper limits for σ_Q.

To allow comparison of variability amplitudes for sources with different mean count rates we have calculated the value of the normalised excess variance, $\sigma_{\rm intr}$, for each source,

$$\sigma_{\rm intr} = \frac{\sigma_Q}{\langle \mathtt{CR}\rangle} \tag{5.5}$$

where $\langle \mathtt{CR}\rangle$ is the mean 0.2-12 keV count rate of that source. This parameter gives the fraction of the total flux that is variable, and therefore can be used to compare amplitudes of flux variability for sources with different fluxes. Fig. 5.1 shows typical probability distributions of $\sigma_{\rm intr}$ of sources without detected (left) and detected (right) variability.

The distributions of $\sigma_{\rm intr}$ values measured in the light curves of our sources are shown in Fig. 5.2 for the whole sample of objects (solid line) and for objects where flux variability was detected in terms of the χ^2 test (filled histogram).

We see that our variable sources have a broad range of values of excess variance from ~10% to ~65%, with the maximum of the distribution (for objects with detected

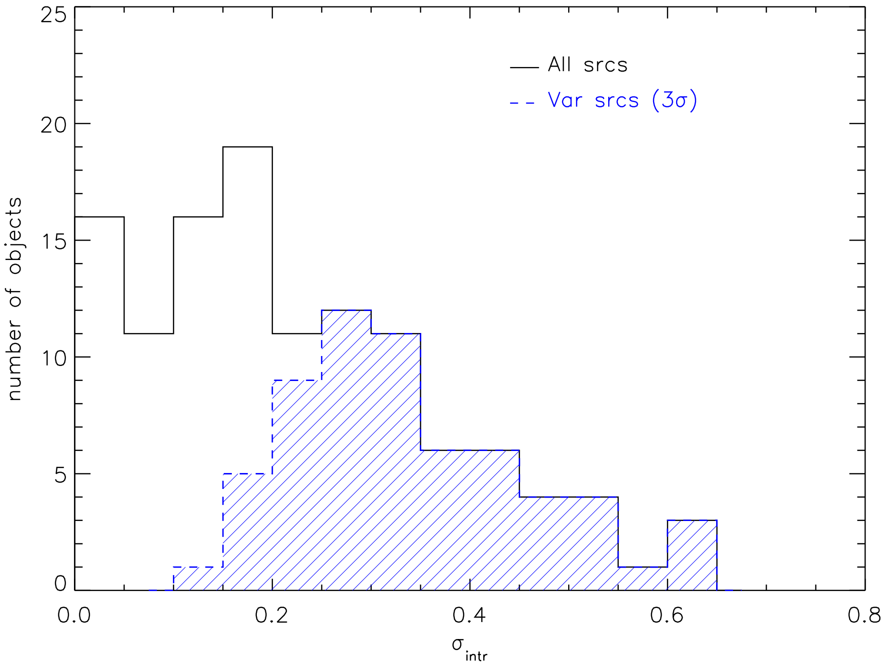

Figure 5.2: *Distribution of measured amplitude of variability for all objects (solid line) and for the sources where flux variability was detected with a confidence level $\geq 3\sigma$ (filled histogram).*

variability[2]) being at a value of ~30%. Values of the excess variance above ~50-60% do not seem to be very common.

We expect the efficiency of detection of variability to be a strong function of the signal-to-noise ratio of the data, but also of the amplitude of variability. Therefore the fraction of sources with detected variability from the χ^2 test should decrease for lower variability amplitudes. This effect is evident from Fig. 5.2, where we see that, for variability amplitudes lower than 20%, we do not detect flux variability in a large fraction of sources. Therefore our distribution of observed flux variability amplitudes for variable objects should not be interpreted as a true distribution of variability amplitudes for the overall sample of sources. Indeed we might be missing sources with low variability amplitudes or faint sources with strong variability due to the large statistical errors in our data. We will return to this point in Sec. 5.5.1.

5.2.2 Mean variability amplitude

Mean values of $\sigma_{\rm intr}$ for the whole sample of sources and for type-1 and type-2 AGN and unidentified sources are listed in Table 5.2. We show values obtained using the both

---

[2] Note that the values outside the filled area correspond to sources with undetected variability ($<3\sigma$) and therefore they cannot be considered significant detections.

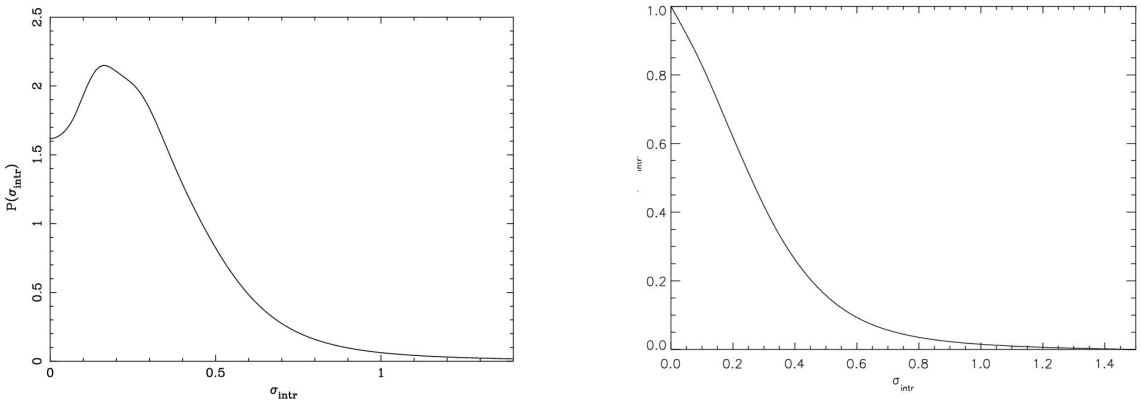

Figure 5.3: *Left: Mean probability distribution of the excess variance, $P(\sigma_{\mathrm{intr}})$, in our sample of objects. The distribution was obtained from the mean of the individual probability distributions of σ_{intr}. Right: Cumulative distribution of $P(\sigma_{\mathrm{intr}})$ that gives, for each σ_{intr}, the probability of obtaining a value of the excess variance equal to or larger than σ_{intr}.*

the arithmetic and weighted mean for comparison. We see that average values from the weighted mean are significantly lower that the ones obtained with the arithmetic mean in all cases. This is because we have a number of sources with measured σ_{intr} values of zero but with errors of the same order as the ones for $\sigma_{\mathrm{intr}}>0$. These values shift the weighted mean to lower values. The obtained mean values for the amplitude of flux variability for type-1 and type-2 AGN do not seem to differ significantly.

We have calculated the mean probability distribution of the excess variance, $P(\sigma_{\mathrm{intr}})$, for our sample of sources as the average of the probability distributions of σ_{intr} obtained from each light curve. As we want to describe the variability properties for the whole sample of sources, we have included in the calculation data for variable and non variable sources. The obtained distributions are shown in Fig. 5.3 for the whole sample of sources and in Fig. 5.4 for type-1 and type-2 AGN. We show both the mean probability distributions, and the corresponding cumulative distributions that give the probability of detection of a value of the excess variance equal to or larger than σ_{intr}. The most probable values (modes) and errors (68% integrals) obtained from the distributions of $P(\sigma_{\mathrm{intr}})$ are listed in column 6 of Table 5.2. The mode for the whole sample of sources was found to be σ_{intr} $\sim$0.15 (68% upper limit =0.36), consistent with the value obtained from the arithmetic mean of the values for each source, as expected because we did not use weights when averaging individual probability distributions.

We see that the average probability distributions of σ_{intr} for type-1 and type-2 AGN do not differ significantly, although the most probable value of σ_{intr} is marginally lower for type-2 AGN than for type-1 AGN.

The flux variability properties for all our sources (probability of detection and amplitude of variability) are listed in Table 5.4.

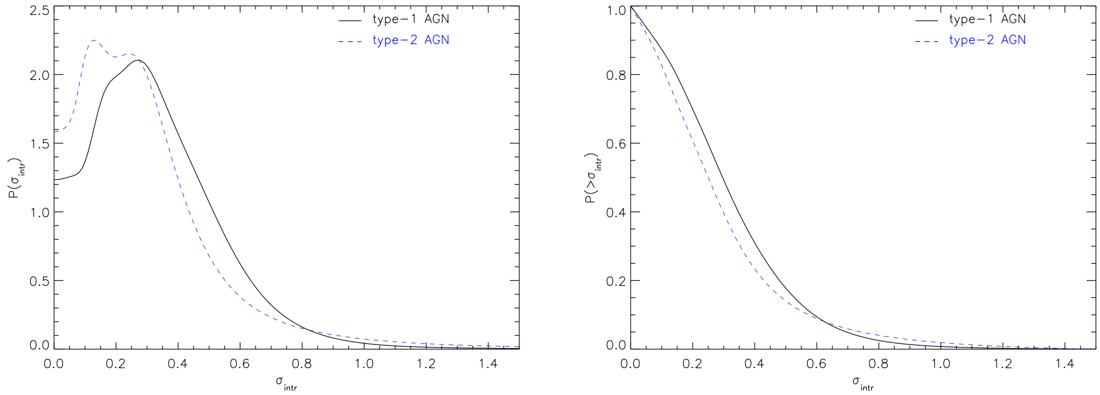

Figure 5.4: *Left: Mean probability distributions of the excess variance, $P(\sigma_{\rm intr})$, for type-1 (solid line) and type-2 (dashed line) AGN. The distributions were obtained from the mean of the individual probability distributions of $\sigma_{\rm intr}$. Right: Cumulative distributions of $P(\sigma_{\rm intr})$, that gives for each $\sigma_{\rm intr}$ the probability of obtaining a value of the excess variance equal to or larger than $\sigma_{\rm intr}$.*

Table 5.2: *Measured values of 0.2-12 keV flux variability amplitudes in Lockman Hole sources.*

Sample (1)	$\langle\sigma_{\rm intr}\rangle_{\rm all}$ (2)	$\langle\sigma_{\rm intr}\rangle^{\rm w}_{\rm all}$ (3)	$\langle\sigma_{\rm intr}\rangle_{\rm var}$ (4)	$\langle\sigma_{\rm intr}\rangle^{\rm w}_{\rm var}$ (5)	$\sigma_{\rm intr}$ (6)
All	0.22 ± 0.01	0.15 ± 0.01	0.34 ± 0.01	0.28 ± 0.01	≤0.36
type-1 AGN	0.27 ± 0.02	0.18 ± 0.02	0.34 ± 0.02	0.27 ± 0.02	$0.27^{+0.47}_{-0.08}$
type-2 AGN	0.21 ± 0.03	0.15 ± 0.02	0.34 ± 0.04	0.28 ± 0.02	≤0.35
Unidentified	0.19 ± 0.02	0.11 ± 0.02	0.35 ± 0.03	0.30 ± 0.02	≤0.33

Columns are as follows: (1) group of sources; (2) arithmetic means and corresponding 1σ errors of the measured variability amplitudes for different types of sources; (3) weighted means and corresponding 1σ errors of the measured variability amplitudes for different types of sources; (4) and (5) arithmetic and weighted means of the measured variability amplitudes considering only objects with detected variability from the χ^2 test; (6) mode and 1σ confidence intervals from the average $\mathrm{P}(\sigma_{\rm intr})$ distributions. For the cases where the integral of the $\mathrm{P}(\sigma_{\rm intr})$ distribution to the left reached zero 68% confidence upper limits are given.

5.3 Spectral variability

We are now interested in studying which fraction of sources in our sample show spectral variability and whether flux and spectral variability are correlated. As we have seen in Sec. 1.4.3, Comptonization models are most popular in explaining the X-ray emission in

AGN [102]. In these models the X-ray emission is thought to be produced by Compton up-scattering of optical/UV photons in a hot electron corona above the accretion disc. One of the predictions of these models is that, if the nuclear emission increases, the Compton cooling in the corona should increase too, and therefore the corona will become colder. If the temperature of the corona decreases, the observed X-ray spectrum should become steeper.

This flux-spectral behaviour is similar to the one observed in different states of Galactic Black Hole Candidates (GBHCs) [159]. In the *low/hard state*[3], most commonly observed in these objects, their X-ray fluxes are low and their 2-10 keV X-ray spectra are dominated by non thermal emission, best reproduced by a hard (Γ ~1.5-2.1) power law component along with a weak or undetected thermal component (multi-temperature accretion disk component). In the *high/soft state* their fluxes are high and their 2-10 keV spectra are soft, dominated by the thermal component with a temperature of about ~1 keV. Finally in the *very high state* the same two spectral components are observed, however with a very steep power law dominating the emission.

The accretion disk-hot corona model of Haardt et al.(1997) [102] predicts that, if the corona is pair dominated, an intensity variability of a factor of 10 will correspond to a change in the spectral slope of ~0.2 over the rest-frame band pass 2-10 keV, while the relation between spectral shape and intensity is less clear for a low pair density corona.

Because our sources are typically faint, we cannot use their spectra from each revolution, as the uncertainties in the measured spectral parameters will be in most cases too large to detect the spectral variability predicted by Comptonization models. Therefore instead of using the X-ray spectra we have used a broad band X-ray colour or hardness ratio ($\mathtt{HR}$), that allows us to search for changes in the broad band spectral shape of the sources. We calculated for each source a "colour" curve were the points are the X-ray colours from each observation which is obtained as

$$\mathtt{HR}^{\mathtt{r}} = (\mathtt{CR}^{\mathtt{r}}_{\mathtt{h}} - \mathtt{CR}^{\mathtt{r}}_{\mathtt{s}})/(\mathtt{CR}^{\mathtt{r}}_{\mathtt{h}} + \mathtt{CR}^{\mathtt{r}}_{\mathtt{s}}) \tag{5.6}$$

where $\mathtt{CR}^{\mathtt{r}}_{\mathtt{s}}$ and $\mathtt{CR}^{\mathtt{r}}_{\mathtt{h}}$ are corrected count rates (see Appendix C.1) in the 0.5-2 keV (soft) and 2-12 keV (hard) energy bands for revolution r respectively. We used these two energy band definitions to separate better the most important emission components found in the co-added spectra of our objects. Changes in the intrinsic absorbing column density or in the properties of the soft excess emission component will affect mostly the soft count rate, while changes in the shape of the broadband continuum will affect both soft and hard band count rates.

In order to search for objects with spectral variability, we used the χ^2 test (see Sec. 5.2) and a threshold in the significance of detection of 3σ. The results of detection of spectral variability are summarised in columns 5 and 6 of Table 5.1. The fractions of sources with detected spectral variability have been corrected for the expected fraction of spurious detections at the selected confidence level as shown in Appendix A.4. We have detected spectral variability above a confidence level of 3σ in 24 out of the 120 objects with light

---

[3] The *soft state* is usually seen at a higher luminosity than the *hard state* motivating the names *high/soft* and *low/hard* states for GBHCs. However it now appears that all states may occur at any given luminosity.

curves with at least 2 points. Spectral variability was detected in 6 out of 45 type-1 AGN and 9 out of 27 type-2 AGN. Among sources still not identified we detected spectral variability in 9 out of 48 (but note again the possible identification bias). These results indicate that spectral variability is much less common than flux variability for our sources, and the same result holds for both samples of type-1 and type-2 AGN. This is not an unexpected result, as we know that with a limited number of counts, spectral variability is more difficult to detect than flux variability. A change in spectral slope of $\Delta\Gamma\sim0.2$-0.3 corresponds to a change in the observed X-ray colour of $\Delta\mathtt{HR}\sim0.1$ while $\Delta\mathtt{HR}\sim0.2$ requires $\Delta\Gamma\sim0.4$-0.6. The typical dispersion in `HR` values observed in our sources with detected spectral variability is $\sim$0.1-0.2 while most of the errors in the `HR` in a single observation are $\sim$0.1-0.2. Therefore detection of changes in the continuum shape $\leq$0.3 will be only detectable in a small number of objects in our sample.

On the other hand, our results might be also suggesting that spectral variability is truly less common that flux variability, and even that in a number of sources in our sample spectral and flux variability are not correlated. We will come back to this point in more detail in Sec. 5.5.

Finally, the fraction of objects with detected spectral variability was not found to vary with redshift, indicating that the effect of sampling harder rest-frame energy bands at higher redshifts does not reduce the detection of spectral variability in our high redshift sources.

We have compared the fractions of type-1 and type-2 AGN with detected spectral variability using the method described in Appendix A.4. We found that the significance of these fractions being different is 99%. Our results hint that spectral variability might be more common in type-2 AGN, although the samples of sources analysed are still too small to reach a strong conclusion. However, if true, this is not a surprising result, as the contribution to the X-ray emission from scattered nuclear radiation (probably in the torus) is expected to be higher in type-2 AGN. This scattered component will not be variable, as it will be related to much slower time variability of the very distant reflector. Therefore changes in the intensity of the hard X-ray component alone would result in larger changes in the observed `HR`.

As we have said before, most of the objects in our sample are too faint to search for spectral variability comparing the emission properties measured on the X-ray spectrum from each revolution. Therefore, we grouped the *XMM-Newton* observations in four different periods of time corresponding to the *XMM-Newton* phases PV, AO1 and AO2a and AO2b (see second column in Table 4.1). A significant fraction of the exposure time was achieved during the AO2 phase, so we separated the AO2 data into two contiguous groups and still obtain data with enough signal-to-noise ratio for this analysis. We built for each object a co-added spectrum using the data from each observational phase. This approach allowed us to study spectral variability directly on the X-ray spectra of the sources on time scales of months and years. We were able to carry out this study in 109 out of 123 objects for which we had more than one spectrum available. In order to search for spectral variability, we fitted the spectra of each observation phase with the best fit model and best fit parameters obtained from the total spectrum of each source (Chapter 4). We left free the normalisation of the continuum emission since we are only interested here in searching for spectral variability, and we have seen that flux variability is common. For sources with detected soft excess emission, we kept fixed the ratio of the soft excess/power law normalisations that we found in the best fit of the co-added spectra. We then repeated the fits using the same spectral models, but allowing all fitting parameters to vary. We compared the χ^2 of the two fits and searched for all cases where $\Delta\chi^2$=9 for one parameter and 11.8 for two parameters, i.e. where we found a significant improvement in the quality of the fits varying the best fit spectral form. From this analysis we detected spectral variability in 8 (7%) sources, including 6 type-1 and 1 type-2 AGN. The fraction of objects with detected spectral variability increased to ∼17% if we used instead a confidence level of 2σ. We show the observed spectral variability properties of the sources with detected spectral variability from this analysis in Fig. 5.5 for the 4 objects (3 type-1 AGN and one source still not identified) best fitted with a power law (`model A`, see Sec. 2.6.1). Fig. 5.6 shows the 1σ, 2σ and 3σ contour diagrams for the variable sources where absorption or soft excess were detected (3 type-1 AGN and 1 type-2 AGN). We found that in all objects with detected spectral variability (including all AGN), this was associated mainly with changes in the shape of the broad band continuum ($\Delta\Gamma$ ∼0.2-0.3 for all objects except source 90, where the observed maximum change in Γ ∼1 although with very large uncertainties). We did not see important changes in the properties of other spectral components such as soft excess or intrinsic absorption. This is the case also for the one type-2 AGN in our sample with detected spectral variability.

These results support the argument that the low fraction of objects with detected spectral variability could be due to the fact that typical changes in the continuum shape are of the order of ∼0.2-0.3, which corresponds to changes in `HR`∼`0.1`, undetectable in most of the sources in our sample.

The results shown in this section support the idea that the main driver for spectral variability on month-years scales in AGN is the change in the mass accretion rate, resulting in changes in the underlying power law Γ. This result can be used as a handle to interpret the `HR` variability study that we presented before.

5.3.1 Variability properties of unabsorbed type-2 AGN

We showed in the previous chapter that, among the spectroscopically identified type-2 AGN in our sample, five did not show signatures of X-ray absorption in their co-added X-ray spectra (objects with identification number 6, 21, 39, 427 and 476). We have studied the flux and spectral variability properties of all these sources except source 21, for which only one data point was available. One of the hypotheses that could explain the disagreement between observed optical-X-ray properties in these sources is spectral variability: because the optical and X-ray observations of these sources were not obtained simultaneously, there might have been changes in their absorption properties during the time interval between the observations. Table 5.4 lists the flux and spectral variability properties of these sources, while their flux and X-ray colour curves are shown in Fig 5.7 and Fig. 5.8 respectively. We detected flux variability in 3 of the sources (39, 427 and 476); however spectral variability was only detected in one of the objects, source 427. Fig. 5.9 shows the flux vs spectral variability properties for source 427. We see that in four of the available observations flux variability was not seen, however changes in the `HR` are evident.

We have made a simple calculation to estimate the expected magnitudes of flux and spectral variability that we would observe if the absorption has varied while the shape and normalisation of the broad band continuum have remained constant. We want to use this study to see whether changes in the X-ray absorption of the sources can explain the observed variability properties of our unabsorbed type-2 AGN. Our sources were detected in a narrow redshift interval, from 0.5-0.7, therefore the results will not change significantly with the redshift, and hence we only show the calculations for the mean redshift, z=0.6. We have assumed a continuum shape of Γ=2 and then we have calculated `HR` for different values of $\mathrm{N_H}$. Our study shows that small changes in the column density, $\mathrm{N_H} \sim 10^{21}\,\mathrm{cm^{-2}}$, affect the observed flux by $\geq$20%. However the corresponding change in the X-ray colour is only Δ`HR`$\sim$0.05, and therefore is impossible to detect in our data. If the changes in absorption were to be of the same magnitude as the typical absorption detected in our absorbed type-2 AGN ($\sim 10^{22}\,\mathrm{cm^{-2}}$; see Fig. 4.10 in Chapter 4), then changes in flux and in the X-ray colour will be significant (Δ`CR`$\geq$ 30% and Δ`HR`$\geq$ 0.3) and therefore we should have been able to detected them. Therefore, the lack of correlation of flux and spectral variability in our objects indicates that, for our unabsorbed type-2 AGN, variations in absorption of $\mathrm{N_H} \geq 10^{22}\,\mathrm{cm^{-2}}$ cannot explain the non detection of X-ray absorption in the co-added spectra of these sources. Moreover, the lack of detection of significant spectral variability in most of the sources makes unlikely that spectral variability alone can explain the observed mismatch of their optical-X-ray spectral properties.

Finally, the non detection of X-ray absorption in these objects cannot be explained by these sources being Compton-thick, because in this case, the X-ray emission should be dominated by scattered radiation (the varying nuclear component is undetected), and therefore we would not expect to detect flux or spectral variability in the sources on a time scale of $\leq$2 years.

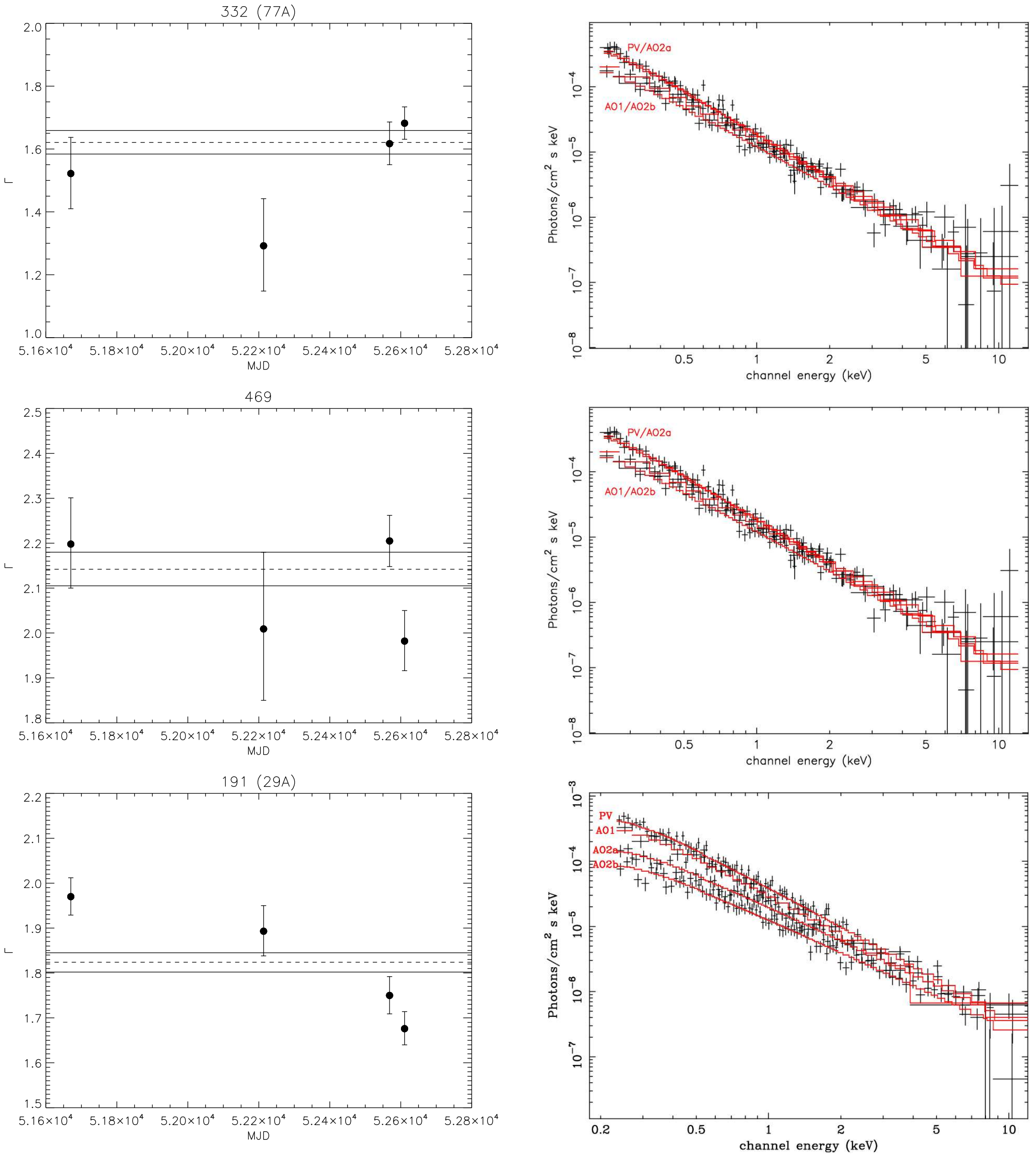

Figure 5.5: Observed spectral variability of the three type-1 AGN in our sample for which their co-added spectra were best fitted with a simple power law. Left: Variation of the continuum shape (Γ) with time (errors correspond to the 90% confidence interval). Horizontal lines indicate the best fit continuum shape (dashed lines) and the corresponding 90% confidence intervals (solid lines) measured in the co-added spectra. Right: Co-added spectra in different observational phases and the corresponding bet fits (solid lines). In all these cases we found the detected spectral variability to be associated with changes in the shape of the broad band continuum.

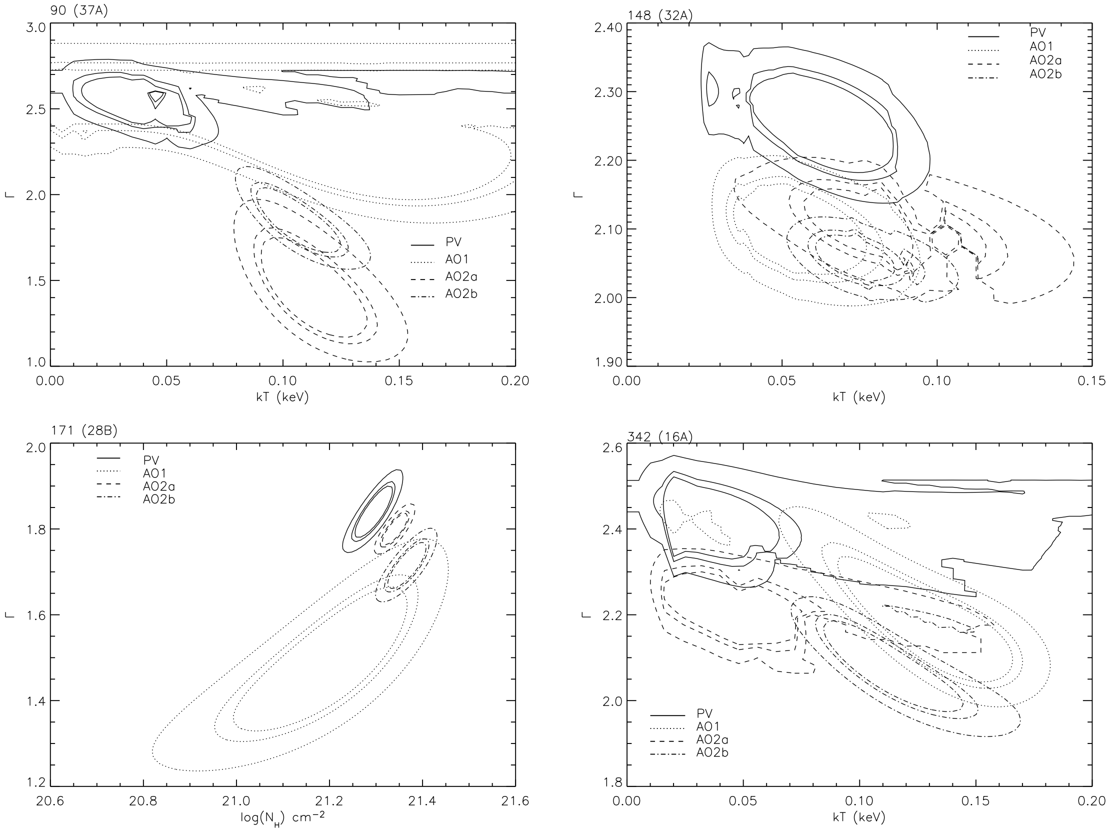

Figure 5.6: *Contour diagrams showing the observed spectral variability in the three type-1 AGN (objects 90, 148 and 342) and the one type-2 AGN (object 171) with detected soft excess emission or absorption (spectral variability was not detected in any of the sources in our sample with both soft excess emission and absorption signatures detected) in their co-added spectra. Note that in all of them we found spectral variability to be associated mainly with changes in the broad band continuum shape but not so much in the other detected spectral components. Contours correspond to 1*σ*, 2*σ *and 3*σ *confidence*

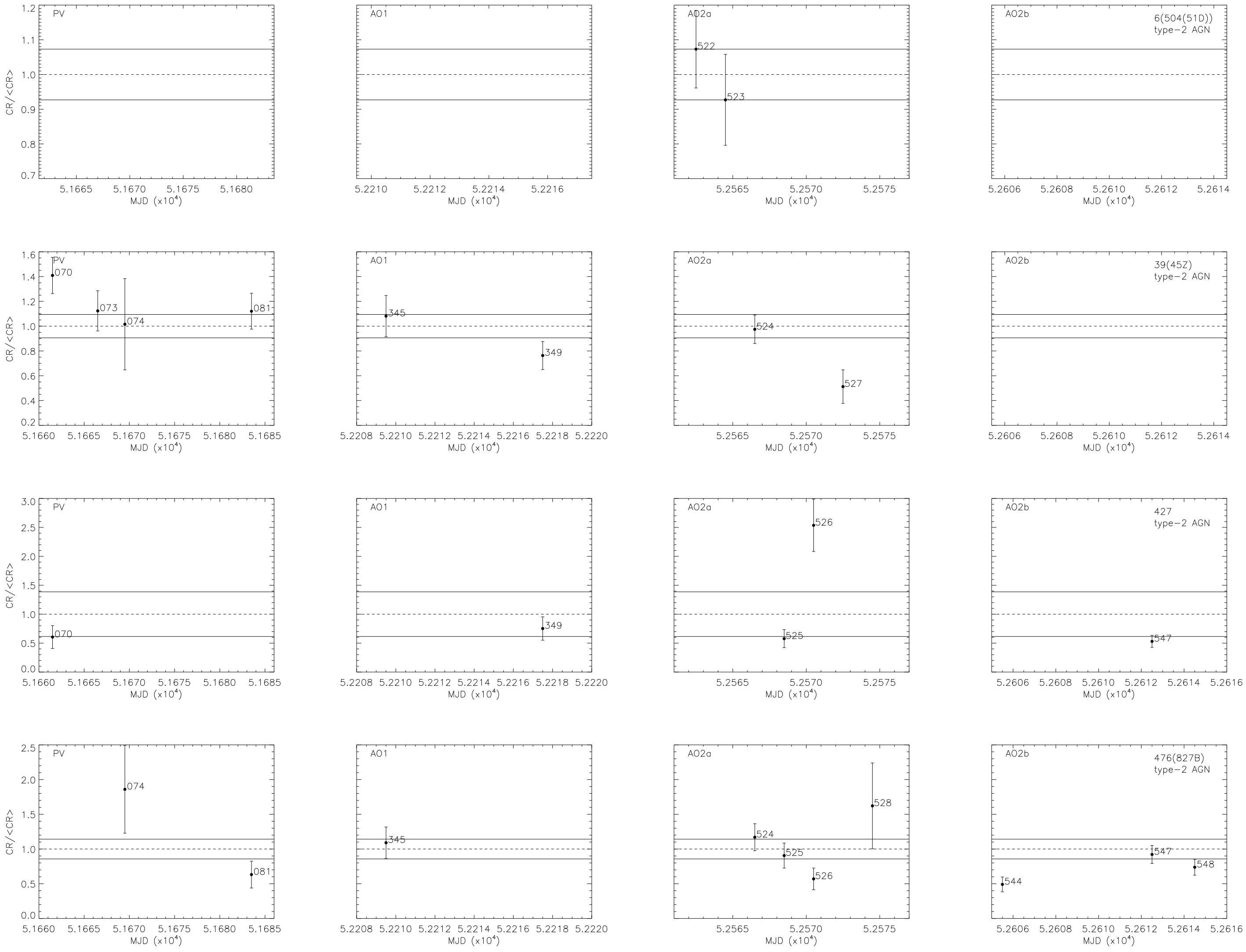

Figure 5.7: *Flux variability properties for 4 of the sources in our sample spectroscopically classified as type-2 AGN but for which no absorption signatures were found in their co-added spectra. Errors correspond to the 1σ confidence interval. Horizontal lines indicate the mean* `CR` *over all revolutions (dashed lines) and the corresponding 1σ confidence interval (solid lines).*

Figure 5.8: *Spectral variability properties for the sources in our sample spectroscopically classified as type-2 AGN but for which no absorption signatures were found in their co-added X-ray spectra. Errors correspond to the 1σ confidence interval. Horizontal lines indicate the mean* `HR` *over all revolutions (dashed lines) and the corresponding 1σ confidence interval (solid lines).*

5.4 Flux variability vs spectral variability

The results of our analysis suggest that flux and spectral variability are not correlated for a significant fraction of the objects in our sample. Indeed 38 sources in our sample show flux variability but not spectral variability, while 9 show spectral but not flux variability. Fig. 5.9 shows the distribution of `HR` values as a function of `CR` for these sources. In addition, no correlation between flux-spectral variability was found for the 15 objects in our sample for which both flux and spectral variability were detected. The `HR`-`CR` plots for these objects are shown in Fig. 5.10.

For a spectrum best described by a power law of slope Γ=2 (absorbed by the column density of the Galaxy) the amplitude of flux variability associated with changes in `HR` of up to $\sim$0.2 due to variations in the continuum shape alone is less than 20%. Therefore in order to explain the typical detected amplitudes of flux variability a change in the X-ray colour of magnitude $\Delta\mathtt{HR} \geq 0.3$ is required (which corresponds to $\Delta\Gamma\sim$0.6-1.2). However these flux-spectral changes are not observed in our sources. Hence we conclude that

1. the lack of correlation between the observed flux and spectral variability properties of our objects indicates that the observed spectral variability is not triggered by changes in the X-ray luminosity of the sources.

2. the amplitude of the observed flux variability cannot be explained due to changes in the X-ray continuum shape alone.

Note that even in the objects with both spectral and flux variability detected, significant changes in `HR` are seen for almost constant values of the `CR`.

Because of the apparent lack of correlation between flux and spectral variability, it is very unlikely that variations in X-ray absorption alone can explain the variability properties of our sources. Changes in absorption can be produced, for example, due to variations in the ionisation state of the absorber following changes in the ionising radiation, making the absorber more transparent. In this case variations in the absorber should be correlated with intrinsic flux variations, i.e, spectral and flux variability should be correlated. On the other hand, if the absorber is not homogeneous but clumpy (for example if it is made of clouds of gas moving around the central source), then variations on the column density along the line of sight will be expected due to clouds passing through the line of sight. In this case both spectral and flux variability should be detected, but again, this is not the case for many objects in our sample.

Due to the apparent lack of correlation of flux and spectral variability, the *two-component spectral model* and the *spectral pivoting model* (see Sec. 1.4.4 for a description of the models), which have been frequently used to describe the variability properties in local Seyfert 1 galaxies, are inappropriate for our sources.

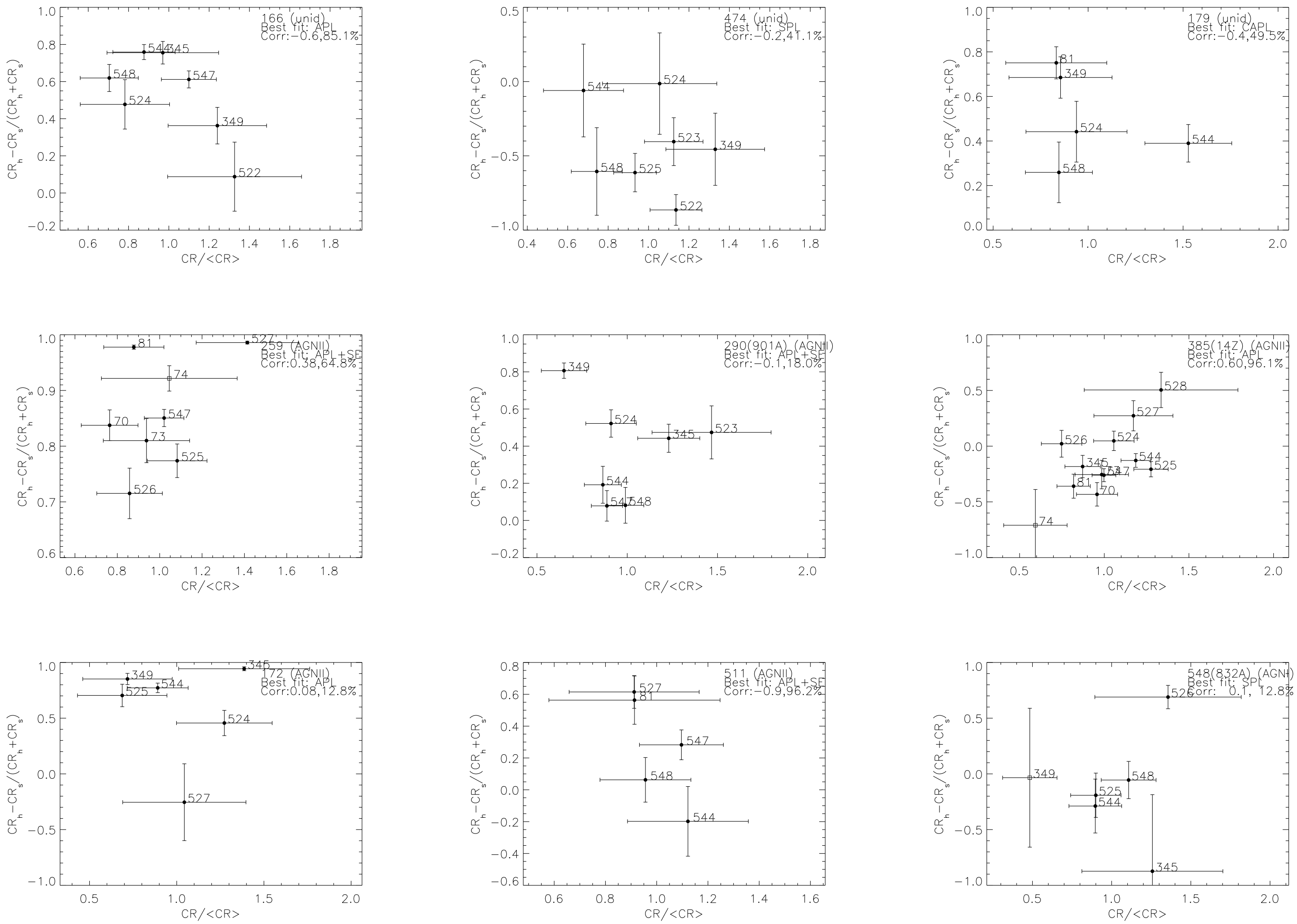

Figure 5.9: *Correlation of flux and spectral variability properties for the 9 objects in our sample for which we did not detect flux variability but we detected spectral variability with a confidence of more than 3σ. Errors correspond to the 1σ confidence interval.*

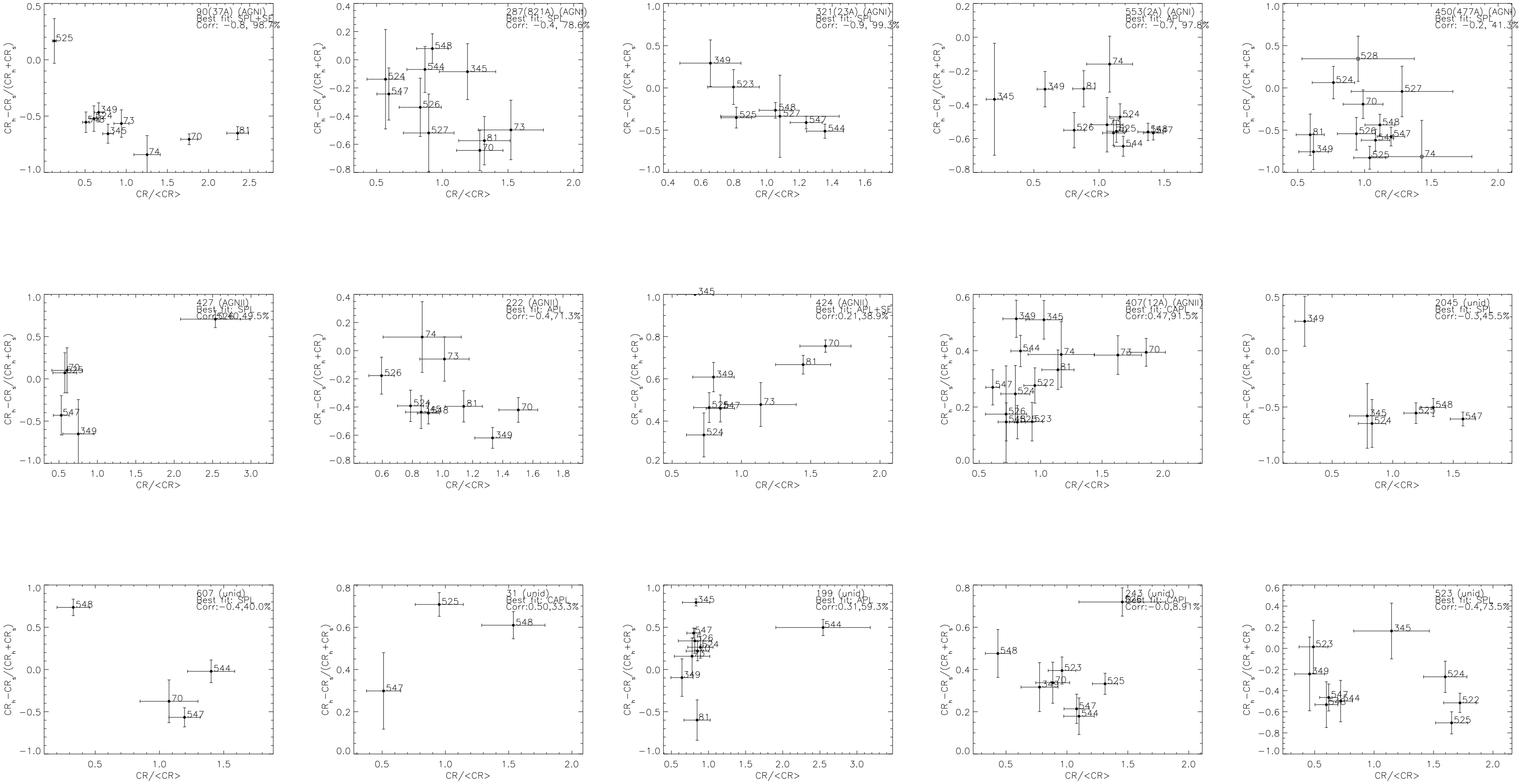

Figure 5.10: Correlation of flux and spectral variability properties for the 15 objects in our sample with detected flux and spectral variability with a confidence of more than 3σ. Errors correspond to the 1σ confidence interval.

5.5 Fraction of sources with detected X-ray variability

In Fig. 5.11 (top) we show the fraction of objects in our sample with detected flux variability as a function of the mean 0.2-12 keV count rate. We see that the fraction of sources with detected flux variability is a strong function of the mean count rate, and hence the number we obtained for the whole sample of objects (∼50%) has to be taken as a lower limit. Indeed the plot suggests that the fraction of sources with flux variability might be even higher than 80% (the maximum fraction). The result that the majority of our sources are variable in flux is in agreement with previous variability analyses, that found long time scale variability in AGN to be more common than short time scale variability (see e.g. [39] [89]). However we do not expect that all sources in our sample have flux variability, as some of the objects still not identified might either not be AGN, or be heavily obscured AGN.

The middle panel of Fig. 5.11 shows the fraction of objects in our sample with detected spectral variability as a function of the error in the mean 0.2-12 keV hardness ratio in the light curves. We see that the detection of spectral variability varies with the quality of our data, although in this case a clear dependence is only evident for the first bin, which suggests that the fraction of sources in our sample with spectral variability could be higher than ∼40%.

Even if the fraction of sources with spectral variability is as high as ∼40%, this fraction will still be significantly lower than the fraction of sources with flux variability. If spectral variability is less common than flux variability in our sample, then for many sources flux variability will not be correlated with spectral variability as we saw in the previous section. Our results could be explained if one single spectral component dominates the emission in the energy band used for our variability study.

Finally the bottom panel in Fig. 5.11 shows the fraction of objects in our sample with detected flux (circles) and spectral (triangles) variability as a function of the number of points in the light curves (top). We see that the detection of flux variability strongly depends on the number of points in the light curves: having more points increases the probability of picking up changes in the X-ray properties. However, we do not see the same effect for detection of spectral variability.

5.5.1 Probability distribution of excess variance

There are a number of factors that could be affecting the observed values and distributions of the excess variance that we used to model the flux variability, like for example low signal-to-noise ratio in our data. In the previous section we saw that the number of points in the light curves can also affect the detection of variability. We have made simulations in order to obtain the true probability distribution of excess variance for our sources, after accounting for all the selection effects in our sample of objects. The details on how the simulations were carried out are given in Appendix C.2.

Our simulations have shown that the observed amplitude of variability depends strongly on the number of points in the light curves, in the sense that systematically lower amplitudes of variability are measured for objects with lower number of bins in the light curves.

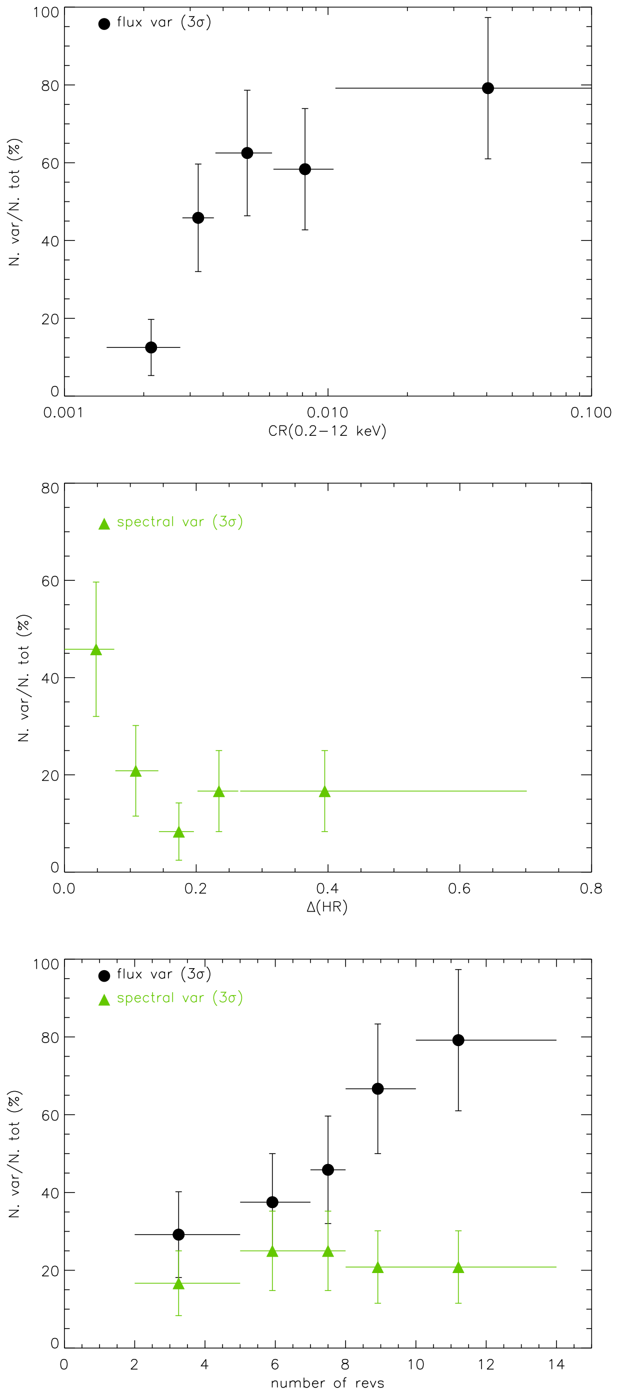

Figure 5.11: *Fraction of variable sources (flux and spectral variability) as a function of the mean 0.2-12 keV count rate (top), error in the mean hardness ratio (middle), and the number of points in the light curves (bottom). Errors correspond to the 1σ confidence interval.*

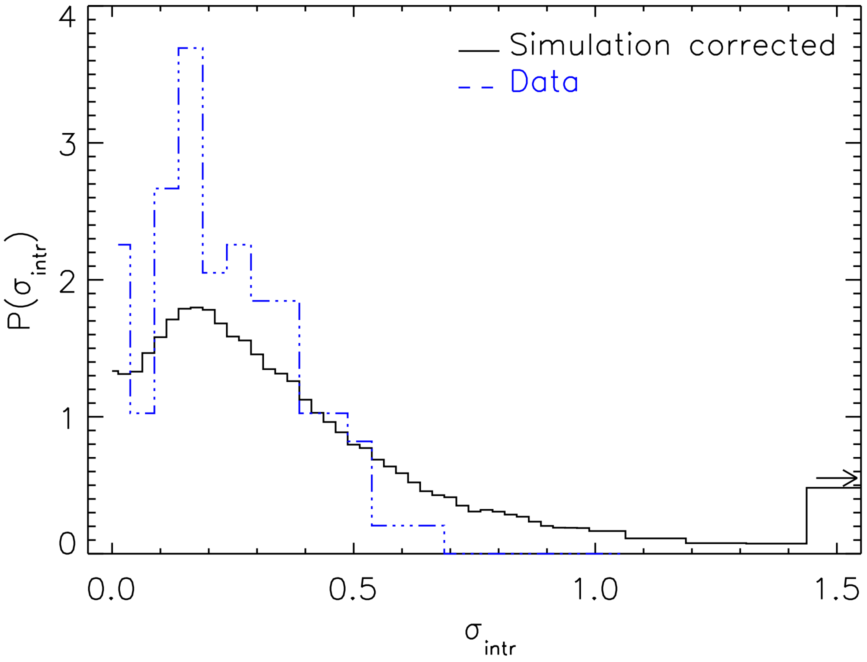

Figure 5.12: *Distribution of intrinsic amplitude of flux variability,* $P(\sigma_{\rm intr})$*, obtained from our simulations (solid line). Note that in our simulations (see Appendix C.2) we referred to the measured amplitude of flux variability as* σ_{obs} *or* S_o *instead of* σ_{intr}*. The distribution of values obtained for our sample of sources (excluding objects with less than 5 points in their light curves, see Sec. 5.5.1) is shown for comparison (dashed line).*

Therefore in this section we use only sources with light curves with at least 5 points. The "corrected" probability distribution of $P(\sigma_{\rm intr})$ obtained from our simulations work is shown in Fig. 5.12 (solid line). To witness the effects that go into this exercise, we also have included the observed probability distribution of $\sigma_{\rm intr}$ values (dashed-line) for our sources (excluding objects with less than 5 points in their light curves; see Fig. 5.2).

We see that both distributions peak at similar values of $\sigma_{\rm intr} \sim 0.2$ and therefore possible selection effects, as the ones listed before, are not affecting significantly the observed bulk of amplitudes of flux variability. However the distribution of intrinsic excess variances shows a long tail towards high values of $\sigma_{\rm intr}$ ($\geq$0.6), which is not seen in the observed excess variance distribution. At values of $\sigma_{\rm intr}$ below ~0.5 the measured distribution of the excess variance shows an excess of sources with respect to the intrinsic distribution, which suggests that our measured values of $\sigma_{\rm intr}$ could be significantly lower than the intrinsic values.

Table 5.3: *Amplitudes of variability obtained from the mean probability distributions of $\sigma_{\rm intr}$ for type-1 AGN at different luminosities and redshifts.*

Group (1)	$\sigma_{\rm intr}$ (2)
type-1 AGN z<1.5	$0.32^{+0.17}_{-0.23}$
type-1 AGN z>1.5	$0.18^{+0.17}_{-0.17}$
type-1 AGN $L_{(2-12\,{\rm keV})} > 10^{44}$	$\leq$0.38
type-1 AGN $L_{(2-12\,{\rm keV})} < 10^{44}$	$0.29^{+0.20}_{-0.20}$

Columns are as follows: (1) type-1 AGN group; (2) variability amplitude, $\sigma_{\rm intr}$, obtained from the mode of the mean probability distributions, $P(\sigma_{\rm intr})$, of each group of sources. Errors correspond to the 1σ confidence interval. In the cases where the lower error bound of the integrals reached zero we calculated 90% upper limits for σ_{intr}.

5.6 Dependence of variability properties with luminosity and redshift

It has been suggested that flux variability amplitude, when measured on a fixed temporal frequency, correlates inversely with X-ray luminosity (this has been confirmed on short time scales, ~1 day) for nearby Seyfert 1 galaxies [16] [128] [173], i.e., more luminous sources show lower variability amplitudes than less luminous sources. However there is significant scatter in this correlation on both short and long time scales, which has been attributed for example, to a dependence of the amplitude of variability on the spectral properties (spectral shape) of the objects [67] [90]. Furthermore, there are also indications that the strength of the correlation decreases towards longer time scales [148].

Fig. 5.13 (top left) shows the measured variability amplitudes for our AGN as a function of the 2-10 keV luminosity. We have used the 2-10 keV luminosities (corrected for absorption) obtained from the best fit of the co-added spectrum of each object. The values we used are listed in Table 4.8. Comparing the values obtained for each object we do not see a clear correlation between these parameters, as expected given the large error bars of our measurements. To enhance any correlation between the two quantities we calculated weighted mean values of $\sigma_{\rm intr}$ in luminosity bins (all bins containing the same number of points and therefore they not necessarily having the same size). The results (see Fig. 5.13 bottom left) seem to suggest, on the contrary, that there is an increase in $\sigma_{\rm intr}$ with luminosity; however this is due to the fact that we have several points with zero excess variance, and errors of the same magnitude as for points with non-vanishing excess variance values. These points are mostly found at low luminosities, probably because for high luminosity sources the signal-to-noise ratio of their light curves is higher (and therefore it becomes easier to detect the variability which is why this apparent cross-correlation is also seen for variable AGN). We do not find any evidence for the anticorrelation between excess

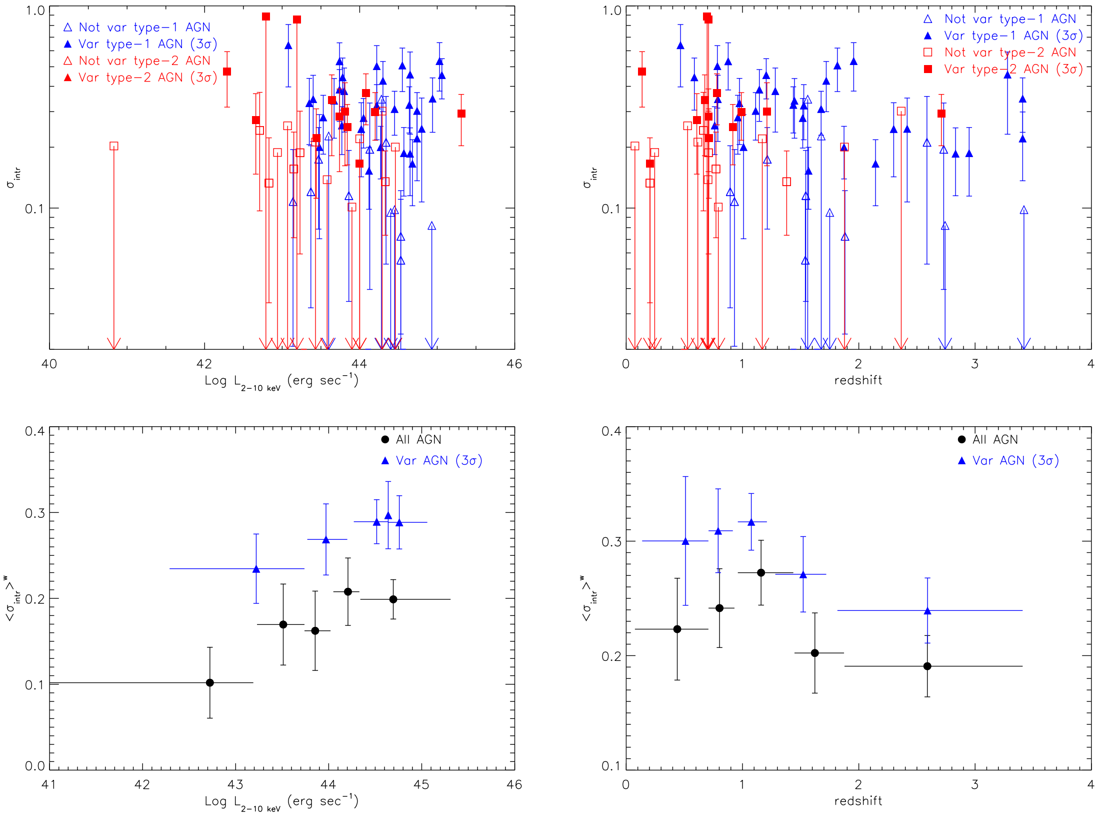

Figure 5.13: *Top: Dependence of the excess variance, $\sigma_{\rm intr}$, on the absorption corrected 2-10 keV luminosity (obtained from the best fit model of each object, left) and redshift (right) for our sample of AGN. Errors correspond to the 90% confidence interval. Arrows indicate 90% confidence upper limits. Bottom: Dependence of the weighted mean excess variance, $\langle\sigma_{\rm intr}\rangle$, on the absorption corrected 2-10 keV luminosity (obtained from the best fit model of each object, left) and redshift (right) for our sample of AGN. Errors correspond to the 1σ confidence interval.*

variance and luminosity. However it is important to note that the known anticorrelation was found when using the same rest-frame frequency interval for all sources, while the light curves of our sources are not uniformly distributed in time and cover much longer time scales than the ones used in those works. Note that there are evidences that the strength of the correlation decreases towards longer variability time scales [148]. In addition, the anticorrelation is weaker for sources at higher redshifts [3] [146].

We have used the same observed energy band to study the variability properties of our sources, but because our sources span a broad range in redshifts we are sampling different rest-frame energies at different redshifts (harder energies for higher redshift sources). This could be a problem when comparing observed variability properties between sources, if

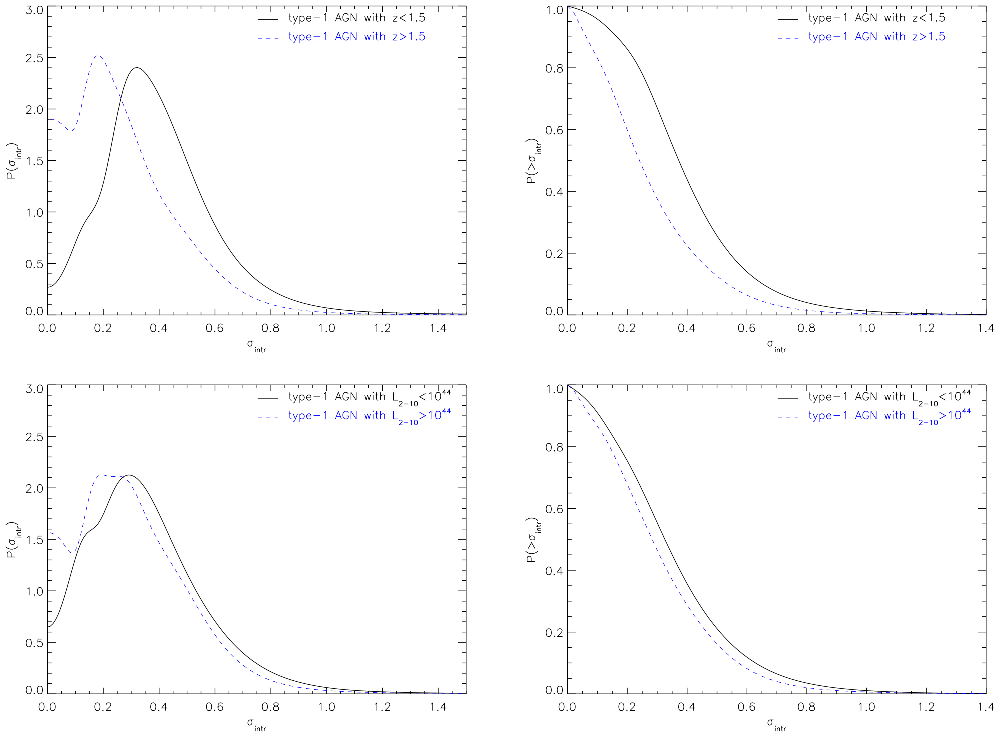

Figure 5.14: *Top: Average probability distributions of* $\sigma_{\rm intr}$ *and the corresponding cumulative distributions for sources with redshifts below 1.5 and above 1.5. Bottom: The same for sources at 2-10 keV luminosities above and below* $10^{44}\,{\rm erg\,s^{-1}}$. *The probability distributions were obtained using all AGN, variable and non variable in terms of the* χ^2 *test.*

there exists a dependence of variability properties with energy (stronger variability in the soft band compared to the hard band, has been observed in a number of Seyfert 1 galaxies). By plotting the excess variance versus redshift we should be able to see whether this effect is present in our data. This dependence of $\sigma_{\rm intr}$ with redshift is shown in the right plots of Fig. 5.13. The right top plot shows the individual values of $\sigma_{\rm intr}$ for each source and the right bottom plot the weighted average values on different redshift bins. The large error bars in the measured individual values do not allow us to see whether the amplitude of variability correlates with redshift, but no clear dependence of the mean $\sigma_{\rm intr}$ with redshift is seen.

To enhance any underlying correlation between the amplitude of variability and the X-ray luminosity or redshift, we have obtained average probability distributions for our sample of type-1 AGN (we cannot repeat the experiment for type-2 AGN as the sample size is too small) in bins of redshift and luminosity. In order to have enough number of objects per bin and enough data points we have used only two bins in redshift and luminosity (all bins having the same number of objects). The results are shown in Fig. 5.14 while the values of $\sigma_{\rm intr}$ obtained from these distributions are shown in Table 5.3. The variability amplitude appears to be independent of the 2-10 keV luminosity, confirming the above results from the weighted mean. The same result seems to hold for the dependence of variability amplitude with redshift. Note that although there is some indication that the amplitude of flux variability is lower for higher redshift sources, the effect is not significant.

In addition, we have not seen that the detection of flux variability varies with redshift, indicating that the effect of sampling harder rest-frame energy bands at higher redshifts does not seem to affect the flux variability properties of our sources (detection of variability and the observed amplitudes of flux variability).

5.7 Summary

We have carried out a detailed study of the X-ray spectral and flux variability properties of a sample of 123 sources detected with *XMM-Newton* in a deep observation in the *Lockman Hole* field. To study variability in flux, we built for each object a light curve using the EPIC-pn 0.2-12 keV count rates of each individual observation. We obtained light curves for 120 out of 123 sources (the other three sources only had one bin in their light curves). We have searched for variability using the χ^2 test. We detected flux variability with a confidence level of at least 3σ in 62 sources (~52%). However the efficiency of detection of variability depends on the amplitude of the variability. The observed strong decrease in the detection of variability in our sources at amplitudes $\geq$0.20 indicates that amplitudes of variability lower than this value cannot be detected in the majority of our sources, because higher signal-to-noise ratio is required. However we found that the fraction of sources with detected flux variability depends substantially on the quality of the data. The observed dependence suggests that the fraction of flux-variable sources in our sample could be 80% or higher, and therefore that **the great majority of the X-ray source population (which at these fluxes is dominated by AGN) vary in flux on time scales of months to years, perhaps responding to changes in the accretion rate.** Our results are consistent with the variability studies of Bauer et al.(2003) [19] in the Chandra Deep Field-North and Paiolino et al.(2004) [182] in the Chandra Deep Field-South which found that the fraction of variable sources could be higher than ~90%.

To measure the magnitude of detected flux variability on each light curve above the statistical fluctuations of the data (excess variance), we used the method described in Almaini et al.(2000) [3] which can be used if Gaussian statistics applies.We found **the mean value of the excess variance to be ~0.15 (68% upper limit being $\leq$0.36)** for the whole sample of objects ($\sim 0.34 \pm 0.01$ considering only sources with detected flux variability), **although with a large dispersion in observed values (from ~0.1 to ~0.65)**. Values of excess variance larger than ~50-60% were found not to be very common in our sources.

Similar values of the mean flux variability amplitude were found for the sub-samples of sources identified as type-1 and type-2 AGN. In addition we did not find strong evidence that flux variability is more common in any of the two AGN types, the fraction of sources with detected flux variability being

68±11% for type-1 AGN and 48±15% for type-2 AGN.

We carried out extensive simulations in order to quantify the intrinsic true distribution of excess variance for our sources corrected for any selection biases. The most probable value of the true intrinsic amplitude of flux variability for our sample of objects is ~0.2, as before correcting for selection biases. In addition, the simulations work showed that the probability of detection of large variability amplitudes in our sample of sources is low. We show that the scarcity of sources with large variability amplitudes (≥0.5-0.6) is at least in part a selection effect, due to low signal-to-noise ratio in a sizeable fraction of our sample.

Short time scale X-ray variability studies of Seyfert 1 galaxies have shown that the majority of these objects soften as they brighten. Our data does not support this. This should not be too surprising as this effect is observed on light curves that sample an uniform time interval, and on time scales much smaller than the ones we sampled in our study, for which the strength of the anticorrelation seems to be higher.

Because of the low signal-to-noise ratio of some of our data we could not study spectral variability using the X-ray spectra of the sources from each observation, as the uncertainties on the fitted parameters would be too large. Hence, we used a broad band hardness ratio to quantify the spectral shape of the emission of the objects on each observation. A χ^2 shows spectral ("colour") variability with a confidence of more than 3σ in 24 objects (~20±6% of the sample). However, we found the fraction of sources with detected spectral variability to vary with the quality of the data, **hence the fraction of sources with spectral variability in our sample of objects could be as high as ~40% although still significantly lower than the fraction of sources in our sample with detected flux variability** (which is the fraction for our highest quality data). However, spectral variability is more difficult to detect than flux variability. We have shown that a change in spectral slope of $\Delta\Gamma$~0.2-0.3 corresponds to a change in the observed X-ray colour of just Δ`HR`~0.1. The typical dispersion in `HR` values in our sources with detected spectral variability is ~0.1-0.2, i.e. of the same magnitude as most errors in the `HR` in a single observation. Therefore changes in the continuum shape ≤0.3 will be only detectable in a small number of objects in our sample.

The fractions of AGN with detected spectral variability were found to be ~14±8% for type-1 AGN and ~34±14% for type-2 AGN with a significance of the fractions being different of ~99%, i.e. **0.2-12 keV spectral variability on long time scales might be more common in type-2 AGN than in type-1 AGN**. This result could be explained if part of the emission in type-2 AGN comes from scattered radiation, i.e. nuclear light scattered, for example, by the material responsible for the X-ray absorption in these objects (molecular torus). This component is expected to be much less variable and therefore changes in the intensity of the hard X-ray component alone would result in larger changes in the observed `HR`. Therefore we will detect spectral variability in the cases where only changes in the relative normalisations of the different spectral components have occurred.

Our samples of type-1 and type-2 AGN cover a broad range in redshifts, specially the former. Therefore we have studied variability properties on significantly different rest-frame energy bands. However we did not find a dependence on redshift of the observed variability properties of our sources, the fraction of sources with detected spectral and flux variability, or the detected amplitudes of flux variability, and therefore we conclude that

the overall flux and spectral X-ray variability properties of our AGN are very similar over the rest frame energy band from ∼0.2keV to ∼54 keV.

We also grouped the spectra of our objects in four different observational phases, and compared the spectral fits to the grouped spectra. With this study we detected spectral variability in 8 objects, including 6 type-1 AGN and 1 type-2 AGN. A detailed analysis of their emission properties showed that the origin of the detected spectral variability is due to a change in the shape of their broad band continuum alone. In none of the sources we detected strong or significant changes in the properties of other spectral components, such as soft excess emission and/or X-ray absorption.

This result is confirmed by the spectral variability analysis of the 4 out of the 5 spectroscopically identified type-2 AGN for which we did not detect absorption in their co-added spectra in Chapter 4. Flux variability was detected in 3 of the objects while only for one of them we detected spectral variability. The lack of detection of significant spectral variability in 3 out of 4 of the sources makes unlikely that spectral variability alone can explain the observed mismatch of their optical-X-ray spectral properties. In addition, we have shown that, if the change in absorption is of the same magnitude as the typical absorption detected in absorbed type-2 AGN, $N_H \sim 10^{22}\,\mathrm{cm}^{-2}$, then, changes in flux and in the X-ray colour will be significant ($\Delta\mathtt{CR} \geq 30\%$ and $\Delta\mathtt{HR} \geq 0.3$) and therefore we should have detected them in the light curves of our sources. Therefore, the lack of correlation between flux and spectral variability in our objects indicates that, for our unabsorbed type-2 AGN, variations in absorption cannot explain the non detection of X-ray absorption in the time-averaged spectra of these sources. Finally, a Compton-thick origin for these sources is also very unlikely, as they are seen (3 out of 4) to vary.

We cannot exclude from the results of our study that X-ray spectral variability in AGN on long time scales is less common than flux variability. The same result seems to hold for both samples of type-1 and type-2 AGN. This could be explained if a single emission component dominates the emission in the energy band where we carried out our variability analysis. Therefore, flux and spectral variability might not be correlated in a significant fraction of our sources. Indeed in 38 objects we detected flux variability but not spectral variability, while spectral variability but not flux variability was detected in 9 objects. A correlation analysis of the flux-spectral variability properties on the 15 objects were both spectral and flux variability were detected only showed no correlation. We have seen that in order to explain the detected amplitudes of flux variability a $\Delta\mathtt{HR} \geq 0.3$ is required (which corresponds to $\Delta\Gamma \sim 0.6 - 1.2$). However they are not observed in our sources. Therefore, **the lack of correlation between the observed flux and spectral variability properties of our objects indicates that the observed spectral variability is not triggered by changes in the X-ray luminosity of the sources**. Furthermore, **the amplitude of the observed flux variability cannot be explained due to changes in the X-ray continuum shape alone.** This is confirmed by the fact that even in the objects with both spectral and flux variability detected, significant changes in `HR` are seen for almost constant values of the `CR`. Because of the apparent lack of correlation between flux and spectral variability, it is very unlikely that variations in X-ray absorption alone can explain the variability properties of our sources. Changes in absorption can be produced, for example, due to variations in the ionisation state of the absorber produced by variations in the ionising radiation, making the absorber more transparent. In this case variations in the absorber should be correlated with intrinsic flux variations, i.e, spectral and flux variability should be correlated. On the other hand, if the absorber is not homogeneous but clumpy (for example if it is made of gas clouds moving around the central source) then, variations on the column density along the line of sight will be expected due to clouds passing through the line of sight. In this case both spectral and flux variability should be detected, but as we explained before, this is not the case for many objects in our sample.

Due to the apparent lack of correlation of flux and spectral variability, the *two-component spectral model* and the *spectral pivoting model* frequently used to explain the X-ray variability properties in local Seyfert 1 galaxies, are unlikely to be able to explain the variability properties of our sources, as both require flux-spectral variability to be correlated.

Our variability study supports the idea that the main driver for spectral variability on month-years scales in our AGN cannot be a change in the mass accretion rate alone. However trying to unveil the origin of the observed spectral and flux variability properties of our objects is out of the scope of this thesis.

Table 5.4: Summary of detection of X-ray variability in *Lockman Hole* sources

XMM (1)	*ROSAT* (2)	R.A. (3)	Dec (4)	Class (5)	redshift (6)	Model (7)	Flux var (8)	Spec var (9)	$\sigma_{\rm intr}$ (10)
607	-	10 53 01.86	+57 15 00.69	–	-	SPL	>99.99	>99.99	≤ 0.65
599	54A	10 53 07.46	+57 15 05.84	type-1	2.416	SPL	>99.99	45.9	$0.25^{0.35}_{0.11}$
400	13A	10 52 13.29	+57 32 25.58	type-1	1.873	SPL	>99.99	81.5	$0.20^{0.25}_{0.14}$
63	-	10 52 36.49	+57 16 04.07	–	-	APL	5.5	93.4	≤ 0.11
5	52A	10 52 43.30	+57 15 45.95	type-1	2.144	SPL	>99.99	25.1	$0.17^{0.22}_{0.10}$
6	504(51D)	10 51 14.30	+57 16 16.88	type-2	0.528	SPL	60.9	66.7	≤ 0.26
16	-	10 51 46.64	+57 17 16.02	–	-	APL	44.0	45.9	≤ 0.31
21	48B	10 50 45.67	+57 17 32.60	type-2	0.498	SPL	-1.0	-1.0	$-^{-}_{-}$
26	-	10 52 32.99	+57 17 50.96	–	-	SPL	12.1	1.3	≤ 0.20
31	-	10 52 00.34	+57 18 08.24	–	-	CAPL	>99.99	99.8	≤ 0.77
41	46A	10 51 19.14	+57 18 34.09	type-1	1.640	APL	-	-	$-^{-}_{-}$
39	45Z	10 53 19.09	+57 18 53.58	type-2	0.711	SPL	>99.99	51.9	$0.22^{0.31}_{0.11}$
53	43A	10 51 04.39	+57 19 23.90	type-1	1.750	APL	19.3	61.6	≤ 0.10
65	-	10 52 55.46	+57 19 52.80	–	-	APL	87.6	85.3	$0.18^{0.32}_{0.03}$
74	905A	10 52 51.13	+57 20 15.70	–	-	SPL	83.9	69.5	≤ 0.28
72	84Z	10 52 16.94	+57 20 19.71	type-2	2.710	APL	>99.99	55.0	$0.29^{0.36}_{0.20}$
85	38A	10 53 29.50	+57 21 06.22	type-1	1.145	SPL	>99.99	70.7	$0.39^{0.48}_{0.27}$
86	-	10 53 09.68	+57 20 59.58	type-1	3.420	SPL	8.3	54.1	≤ 0.10
88	39B	10 52 09.37	+57 21 05.43	type-1	3.279	SPL	>99.99	74.4	$0.46^{0.59}_{0.23}$
90	37A	10 52 48.09	+57 21 17.43	type-1	0.467	SPL+SE	>99.99	>99.99	$0.64^{0.81}_{0.40}$
96	814(37G)	10 52 44.87	+57 21 24.84	type-1	2.832	SPL	>99.99	43.3	$0.19^{0.25}_{0.12}$
107	-	10 52 19.49	+57 22 15.26	type-2	0.075	APL	89.6	84.9	≤ 0.20
120	-	10 52 25.17	+57 23 07.02	–	-	SPL	>99.99	69.9	≤ 0.41
108	-	10 50 50.91	+57 22 15.65	–	-	2SPL	88.7	49.0	≤ 0.16
900	-	10 54 59.43	+57 22 18.84	–	-	APL	35.3	34.6	≤ 0.17

Table 5.4: Continued

XMM (1)	*ROSAT* (2)	R.A. (3)	Dec (4)	Class (5)	redshift (6)	Model (7)	Flux var (8)	Spec var (9)	$\sigma_{\rm intr}$ (10)
121	434B	10 52 58.08	+57 22 51.95	type-2	0.772	APL	98.2	29.4	$0.16^{0.24}_{0.07}$
135	513(34O)	10 52 54.39	+57 23 43.89	type-1	0.761	SPL	>99.99	63.2	$0.26^{0.32}_{0.18}$
124	634A	10 53 11.72	+57 23 09.07	type-1	1.544	SPL	90.0	64.0	$0.12^{0.19}_{0.03}$
125	607(36Z)	10 52 19.90	+57 23 07.92	–	-	SPL	>99.99	28.1	≤ 0.47
142	-	10 52 03.74	+57 23 39.62	–	-	SPL	88.5	97.7	$0.16^{0.27}_{0.05}$
133	35A	10 50 38.77	+57 23 39.67	type-1	1.439	SPL	-1.0	-1.0	$-^{-}_{-}$
148	32A	10 52 39.66	+57 24 32.83	type-1	1.113	SPL+SE	>99.99	65.7	$0.30^{0.37}_{0.22}$
166	-	10 52 31.98	+57 24 30.82	–	-	APL	78.2	>99.99	$0.10^{0.20}_{0.01}$
156	-	10 51 54.59	+57 24 09.28	type-2	2.365	APL	99.2	95.6	≤ 0.30
163	33A	10 51 59.88	+57 24 26.31	type-1	0.974	APL	>99.99	89.7	$0.33^{0.44}_{0.21}$
168	31A	10 53 31.72	+57 24 56.19	type-1	1.956	SPL	>99.99	68.6	$0.53^{0.66}_{0.38}$
172	-	10 53 15.71	+57 24 50.84	type-2	1.17	APL	60.2	>99.99	≤ 0.22
183	82A	10 53 12.27	+57 25 08.28	type-1	0.96	SPL	>99.99	74.4	$0.28^{0.36}_{0.18}$
176	30A	10 52 57.25	+57 25 08.77	type-1	1.527	SPL	>99.99	59.1	$0.32^{0.41}_{0.22}$
179	-	10 52 31.64	+57 25 03.93	–	-	CAPL	85.5	>99.99	$0.15^{0.31}_{0.01}$
174	-	10 51 20.63	+57 24 58.24	–	-	SPL	>99.99	53.3	≤ 0.64
186	-	10 51 49.93	+57 25 25.13	type-2	0.676	APL	>99.99	41.0	$0.34^{0.46}_{0.18}$
171	28B	10 54 21.22	+57 25 45.40	type-2	0.205	APL	>99.99	62.0	≤ 0.17
200	-	10 53 46.81	+57 26 07.77	–	-	APL	90.6	45.8	$0.14^{0.25}_{0.03}$
187	-	10 50 47.96	+57 25 22.71	–	-	SPL	>99.99	81.6	≤ 0.49
191	29A	10 53 35.03	+57 25 44.13	type-1	0.784	SPL	>99.99	90.6	$0.50^{0.64}_{0.31}$
199	-	10 52 25.28	+57 25 51.27	–	-	APL	99.9	>99.99	$0.16^{0.25}_{0.06}$
217	-	10 51 11.60	+57 26 36.67	–	-	APL	99.3	60.0	$0.14^{0.23}_{0.06}$
214	-	10 53 15.09	+57 26 30.65	–	-	APL	98.8	97.9	$0.18^{0.30}_{0.06}$
222	-	10 53 51.67	+57 27 03.64	type-2	0.917	APL	>99.99	>99.99	$0.25^{0.33}_{0.16}$
2020	27A	10 53 50.19	+57 27 11.61	type-1	1.720	SPL	>99.99	53.6	$0.43^{0.53}_{0.30}$
226	-	10 51 20.49	+57 27 03.47	–	-	SPL	99.9	98.8	$0.21^{0.30}_{0.09}$

Table 5.4: Continued

XMM (1)	*ROSAT* (2)	R.A. (3)	Dec (4)	Class (5)	redshift (6)	Model (7)	Flux var (8)	Spec var (9)	$\sigma_{\rm intr}$ (10)
243	-	10 51 28.14	+57 27 41.55	–	-	CAPL	>99.99	>99.99	$0.25^{0.33}_{0.14}$
254	486A	10 52 43.37	+57 28 01.49	type-2	1.210	APL	>99.99	13.6	$0.30^{0.42}_{0.16}$
261	80A	10 51 44.63	+57 28 08.89	type-1	3.409	SPL	>99.99	95.9	$0.22^{0.30}_{0.14}$
259	-	10 53 05.60	+57 28 12.50	type-2	0.792	APL+SE	71.2	>99.99	≤ 0.10
270	120A	10 53 09.28	+57 28 22.65	type-1	1.568	SPL+SE	>99.99	97.7	$0.15^{0.20}_{0.10}$
267	428E	10 53 24.54	+57 28 20.65	type-1	1.518	APL	>99.99	32.1	$0.28^{0.35}_{0.20}$
287	821A	10 53 22.04	+57 28 52.76	type-1	2.300	SPL	>99.99	99.8	$0.25^{0.33}_{0.14}$
268	-	10 53 48.09	+57 28 17.75	–	-	APL	96.0	99.1	$0.17^{0.27}_{0.06}$
277	25A	10 53 44.85	+57 28 42.24	type-1	1.816	SPL	>99.99	77.1	$0.51^{0.62}_{0.38}$
272	26A	10 50 19.40	+57 28 13.99	type-2	0.616	APL	80.9	33.0	≤ 0.21
290	901A	10 52 52.74	+57 29 00.81	type-2	0.204	APL+SE	98.3	>99.99	$0.13^{0.22}_{0.03}$
369	-	10 51 06.50	+57 15 31.92	–	-	SPL	96.9	15.7	≤ 0.31
300	426A	10 53 03.64	+57 29 25.56	type-1	0.788	CAPL	>99.99	99.0	$0.35^{0.45}_{0.21}$
306	-	10 52 06.84	+57 29 25.43	type-2	0.708	APL	98.3	77.0	$0.19^{0.30}_{0.06}$
321	23A	10 52 24.74	+57 30 11.40	type-1	1.009	SPL	>99.99	>99.99	$0.20^{0.29}_{0.07}$
326	117Q	10 53 48.80	+57 30 36.09	type-2	0.78	APL	>99.99	96.7	$0.37^{0.46}_{0.26}$
350	-	10 52 41.65	+57 30 39.97	–	-	SPL	43.1	94.1	≤ 0.12
332	77A	10 52 59.16	+57 30 31.81	type-1	1.676	SPL	>99.99	98.4	$0.31^{0.38}_{0.23}$
411	53A	10 52 06.02	+57 15 26.41	type-2	0.245	CAPL	95.4	4.8	≤ 0.19
2024	-	10 54 10.68	+57 30 56.73	–	-	SPL	98.9	99.6	$0.15^{0.23}_{0.07}$
343	-	10 50 41.22	+57 30 23.31	–	-	SPL	70.5	96.3	≤ 0.32
342	16A	10 53 39.62	+57 31 04.89	type-1	0.586	SPL+SE	>99.99	34.7	$0.44^{0.55}_{0.31}$
351	-	10 51 46.39	+57 30 38.14	–	-	SPL	99.1	37.4	$0.19^{0.29}_{0.08}$
353	19B	10 51 37.27	+57 30 44.43	type-1	0.894	SPL	94.7	77.0	$0.12^{0.20}_{0.03}$
354	75A	10 51 25.25	+57 30 52.33	type-1	3.409	SPL	>99.99	80.9	$0.35^{0.44}_{0.24}$
358	17A	10 51 03.86	+57 30 56.65	type-1	2.742	SPL	49.8	99.3	≤ 0.08
355	-	10 52 37.33	+57 31 06.67	type-2	0.708	APL	>99.99	18.4	≤ 0.86

Table 5.4: Continued

XMM (1)	*ROSAT* (2)	R.A. (3)	Dec (4)	Class (5)	redshift (6)	Model (7)	Flux var (8)	Spec var (9)	$\sigma_{\rm intr}$ (10)
385	14Z	10 52 42.37	+57 32 00.64	type-2	1.380	APL	99.6	>99.99	$0.14^{0.19}_{0.07}$
364	18Z	10 52 28.36	+57 31 06.57	type-1	0.931	SPL	93.2	99.7	$0.11^{0.19}_{0.02}$
901	-	10 50 05.55	+57 31 09.01	–	-	SPL	86.3	35.1	≤ 0.21
902	73C	10 50 09.12	+57 31 46.29	type-1	1.561	SPL	92.4	99.5	≤ 0.35
377	-	10 52 52.11	+57 31 38.02	–	-	APL	>99.99	62.0	$0.43^{0.62}_{0.16}$
384	-	10 53 21.63	+57 31 49.44	–	-	APL	64.0	71.6	≤ 0.15
387	15A	10 52 59.78	+57 31 56.69	type-1	1.447	SPL	>99.99	86.2	$0.34^{0.44}_{0.22}$
394	-	10 52 51.40	+57 32 02.03	type-2	0.664	APL	98.8	21.0	$0.24^{0.37}_{0.10}$
406	828A	10 53 57.16	+57 32 44.00	type-1	1.282	SPL	>99.99	28.9	$0.38^{0.49}_{0.24}$
419	-	10 54 00.46	+57 33 22.19	–	-	APL	97.3	54.2	$0.16^{0.27}_{0.06}$
407	12A	10 51 48.69	+57 32 50.07	type-2	0.990	CAPL	>99.99	>99.99	$0.30^{0.37}_{0.22}$
424	-	10 52 37.93	+57 33 22.65	type-2	0.707	APL+SE	>99.99	>99.99	$0.28^{0.39}_{0.15}$
427	-	10 52 27.88	+57 33 30.65	type-2	0.696	SPL	>99.99	>99.99	≤ 0.89
430	11A	10 51 08.19	+57 33 47.06	type-1	1.540	APL	91.0	95.3	≤ 0.11
458	-	10 51 06.22	+57 34 36.67	–	-	CAPL	>99.99	94.7	≤ 0.34
442	805A	10 53 47.28	+57 33 50.41	type-1	2.586	SPL	95.7	52.1	$0.21^{0.36}_{0.05}$
443	-	10 52 36.89	+57 33 59.80	type-2	1.877	APL	69.7	99.1	≤ 0.20
474	-	10 51 28.13	+57 35 04.20	–	–	SPL	90.8	99.9	$0.11^{0.20}_{0.02}$
451	-	10 52 07.87	+57 34 17.48	–	-	APL	67.4	97.0	≤ 0.19
450	477A	10 53 05.98	+57 34 26.70	type-1	2.949	SPL	>99.99	>99.99	$0.19^{0.25}_{0.11}$
453	804A	10 53 12.24	+57 34 27.39	type-1	1.213	SPL	99.6	45.2	$0.17^{0.25}_{0.08}$
456	9A	10 51 54.30	+57 34 38.66	type-1	0.877	SPL	>99.99	90.0	$0.53^{0.66}_{0.38}$
491	-	10 51 41.91	+57 35 56.00	–	-	APL	91.3	87.9	$0.14^{0.26}_{0.02}$
469	-	10 54 07.21	+57 35 24.89	–	-	SPL	>99.99	38.8	$0.43^{0.53}_{0.29}$
475	6A	10 53 16.51	+57 35 52.23	type-1	1.204	SPL	>99.99	5.4	$0.45^{0.55}_{0.35}$
476	827B	10 53 03.43	+57 35 30.80	type-2	0.607	SPL	>99.99	67.9	$0.27^{0.37}_{0.15}$
505	104A	10 52 41.54	+57 36 52.85	type-2	0.137	CAPL	>99.99	99.6	$0.47^{0.59}_{0.32}$

Table 5.4: Continued

XMM (1)	*ROSAT* (2)	R.A. (3)	Dec (4)	Class (5)	redshift (6)	Model (7)	Flux var (8)	Spec var (9)	$\sigma_{\rm intr}$ (10)
504	-	10 54 26.22	+57 36 49.05	–	-	APL+SE	>99.99	66.0	≤ 0.54
511	-	10 53 38.50	+57 36 55.47	type-2	0.704	APL+SE	7.0	>99.99	≤ 0.14
518	-	10 53 36.33	+57 37 32.14	–	–	APL	67.4	60.8	≤ 0.20
523	-	10 51 29.98	+57 37 40.71	–	-	SPL	>99.99	99.8	$0.49^{0.62}_{0.30}$
529	-	10 51 37.30	+57 37 59.11	–	-	CAPL	99.0	71.2	$0.13^{0.21}_{0.04}$
532	801A	10 52 45.36	+57 37 48.69	type-1	1.677	SPL	76.9	38.7	≤ 0.23
527	5A	10 53 02.34	+57 37 58.62	type-1	1.881	SPL	92.6	4.3	$0.07^{0.12}_{0.02}$
537	-	10 50 50.04	+57 38 21.79	–	-	SPL	>99.99	84.2	≤ 1.26
548	832A	10 52 07.53	+57 38 41.40	type-1	2.730	SPL	95.1	>99.99	$0.20^{0.33}_{0.04}$
557	-	10 52 07.75	+57 39 07.49	–	-	APL	1.1	4.5	≤ 0.12
553	2A	10 52 30.06	+57 39 16.81	type-1	1.437	APL	>99.99	99.9	$0.32^{0.40}_{0.24}$
555	-	10 51 52.07	+57 39 09.41	–	-	SPL	98.8	17.9	$0.18^{0.29}_{0.02}$
594	-	10 52 48.40	+57 41 29.14	–	-	SPL	99.9	80.0	≤ 0.58
2045	-	10 52 04.47	+57 41 15.65	–	-	SPL	>99.99	99.9	≤ 0.59
584	-	10 52 06.28	+57 41 25.53	–	-	SPL	>99.99	97.7	$0.28^{0.39}_{0.13}$
591	-	10 52 23.17	+57 41 24.62	–	–	SPL	88.6	89.5	$0.11^{0.20}_{0.02}$
601	-	10 51 15.91	+57 42 08.59	–	-	SPL	76.9	81.3	≤ 0.21

Columns are as follows: (1) Source X-ray identification number; (2) *ROSAT* identification number; (3) Right ascension (J2000); (4) Declination (J2000); (5) object class based on optical spectroscopy; (6) redshift; (7) Best fit model of the co-added spectrum of each individual source (from Mateos et al.(2005b) [153]); (8) Significance of 0.2-12 keV flux variability (in %); (9) Significance of spectral variability (in %); (10) Variability amplitude. Errors correspond to the 1σ confidence interval. For the objects where the lower error bar reached zero 68% upper limits are given.

Chapter 6

Discussion of the results

The aim of the work presented in this thesis was to exploit the large collecting area and wide field of view (FOV) of *XMM-Newton* to learn about the physical properties and cosmological evolution of the X-ray population of Active Galactic Nuclei (AGN) at the fluxes where the bulk of the XRB emission resides. As the main source of energy in these objects is accretion of matter onto a supermassive black hole ($10^6 - 10^8\,\mathrm{M}^{\odot}$) our studies have allowed us to make progress in the studies of accretion in the Universe. In order to do that we have conducted X-ray spectroscopy and variability analyses of objects detected with the *XMM-Newton* observatory (most of them AGN) in two different X-ray surveys:

1. AXIS (An *XMM-Newton* International Survey): AXIS is a programme of follow-up and identification of *XMM-Newton* serendipitously discovered sources. The survey is a wide field (Ω_{total} ~3.5 deg^2) medium to deep survey (0.5-10 keV fluxes between $\sim 10^{-15} - 10^{-12}\,\mathrm{erg\,cm^{-2}\,s^{-1}}$). We selected 25 *XMM-Newton* observations from the AXIS project all with available follow-up information in the optical. This guarantees that we can build large enough samples of spectroscopically identified type-1 and type-2 AGN to carry out population studies of these objects. The sample of X-ray selected sources that we analysed was 1137 objects of which ~11% had optical spectroscopic identifications at the time of our analisis. The majority of the objects identified were found to be BLAGN (or type-1 AGN; ~64%) while the rest of the objects were identified as NELG (or type-2 AGN; ~14%) and stars (~17%). All NELG were found to have X-ray luminosities $\geq 10^{43}\,\mathrm{erg\,cm^{-2}\,s^{-1}}$, consistent with all of them hosting an AGN.
2. The *Lockman Hole* deep survey: The *Lockman Hole* (R.A.:10:52:43 and Dec:+57:28:48) is one of the regions in the sky best studied at different wavelengths including X-rays, and therefore optical spectroscopic identifications are available for a large number of objects in the field. *XMM-Newton* has carried out its deepest observation up to date in the direction of the *Lockman Hole*. It consists of 17 observations carried out from 2000-2002, covering a total solid angle of ~0.4 deg^2 and that give a total exposure time of more than ~ 600 ksec with each EPIC camera. From the list of objects detected in the total *XMM-Newton* observation, we selected the 123 brightest

objects (excluding from the sample sources already identified as clusters of galaxies and stars). All selected objects had enough signal in their X-ray spectra to allow a detailed analysis of the emission properties of each source individually. At the time of our analysis 74 ($\sim$60%) of the selected sources had optical spectroscopic identifications. Of these, 46 were classified as type-1 AGN and 28 as type-2 AGN.

The spectral analysis of AXIS sources is one of the most detailed X-ray spectral analyses and over one of the largest samples of X-ray selected objects carried out so far. Thanks to this analysis we have been able to study the X-ray emission properties of AGN over a broad range of source parameters, with special emphasis in investigating whether the emission properties of the population of AGN have some dependence with the intrinsic X-ray luminosity or the redshift of the objects.

On the other hand, the spectral analysis of *Lockman Hole* sources has been an excellent complement, because although the sample of objects in this case is significantly smaller than the AXIS one, thanks to the much better signal of the data we have been able to refine the majority of the results that came out from the analysis of objects from AXIS. In addition we have been able to study the emission properties of spectral components, such as soft excess, for which better signal in the data is required.

Finally in order to provide further insight into the nature of our selected objects we complemented the two spectral studies with a variability analysis of the *Lockman Hole* sources.

Some of the most important results that came out of our **spectral analyses** were:

1. The mean continuum shape of the sources depends strongly on the soft (0.5-2 keV) X-ray flux, in the sense that it becomes harder at the faintest fluxes. The dependence was found to be much less significant if hard (2-10 keV) X-ray fluxes are used instead. However, we have been able to explain this effect (seen in both samples of objects) as being due to an increase in X-ray absorption at the faintest fluxes. Therefore it is easy to understand the lack of a dependence of the mean continuum shape of our sources with hard X-ray fluxes, as hard X-ray fluxes are less affected by X-ray absorption. Once absorption is properly modelled, the mean continuum shape of the objects does not vary with X-ray flux. Our results do not show any evidence of the existence of a population of faint, intrinsically harder sources, as it had been suggested by previous spectral analyses.

2. Both the fraction of X-ray absorbed sources and the amount of absorption, do not appear to depend strongly on the 0.5-2 or 2-10 keV flux of the objects, once fluxes are corrected for the effect of absorption.

3. The mean X-ray continuum power-law photon index at energies from $\sim$0.2 to 12 keV was found to be $\Gamma\sim$1.9-2, consistent with previous spectral analyses. Although some of these analyses have claimed that type-2 AGN might be intrinsically harder than type-1 AGN, we do not see such effect in our data, once X-ray absorption is properly modelled. Both the spectral analysis of AXIS and *Lockman Hole* sources have confirmed that, there exists an intrinsic dispersion in the mean continuum shape

of the AGN population. However it is difficult to quantify the magnitude of such dispersion, as other spectral components contributing to the X-ray emission, such as soft excess and undetected X-ray absorption, can increase significantly the measured magnitude of the dispersion, if they are undetected or not properly modelled. This effect will be more important for type-2 AGN as they are more affected by X-ray absorption. For the AXIS sources, we found a value for the intrinsic dispersion of $0.36\,^{+0.01}_{-0.04}$ while the corresponding values for the samples of AGN were $0.21\,^{+0.05}_{-0.04}$ for type-1 AGN and $0.36\,^{+0.14}_{-0.10}$ for type-2 AGN. We explained the higher measured value obtained for the type-2 AGN as being due to undetected or not properly modelled absorption. This was confirmed by the results of the spectral analysis of the *Lockman Hole* sources, where we found the intrinsic dispersion in the distribution of spectral slopes to be ∼0.20 for both type-1 and type-2 AGN respectively. Our analyses show that type-1 and type-2 AGN exhibit the same intrinsic emission properties, and that the observed differences in the shape of their broad band continuum are primarily due to X-ray absorption, that affects more type-2 AGN.

4. X-ray absorption was detected in both type-1 and type-2 AGN. The fractions of absorbed type-1 AGN were found to be ∼6% for AXIS objects and ∼10% for *Lockman Hole* objects. The corresponding fractions for type-2 AGN were found to be ∼40% for AXIS objects and 77% for *Lockman Hole* objects. We found the fractions of absorbed objects among type-1 and type-2 AGN to be different (∼ a factor of 4) with a significance of more than 99.99% (using the *Lockman Hole* AGN). In addition, type-2 AGN seem to be in general more strongly absorbed than absorbed type-1 AGN. However, in both samples of objects analysed, we found a significant number of AGN where the existing correlation between their observed optical/UV and X-ray properties are not clearly met, questioning the validity of the unification model of AGN for these objects.

5. X-ray absorption in type-1 AGN: The measured distribution of absorbing column densities in type-1 AGN was found to be concentrated to low values. This could be suggesting that the material responsible for the X-ray absorption in type-1 and type-2 AGN is different. One of the possibilities is that the X-ray absorber in type-1 AGN is the host galaxy. However the lack of any evident correlation between optical obscuration and X-ray absorption could be also explained if the absorber is clumpy and it is located closer to the central source, for example inside the BLR [206], or if the properties of the absorber (such as the gas to dust ratio) differ significantly from those of our Galaxy [142]. Finally, it is important to note that the optical/UV and X-ray observations of these objects are not simultaneous. AGN are strongly variable sources in X-rays, hence we cannot exclude the possibility that spectral variability (e.g. in the column density or in the ionisation state of the absorber) could explain the observed discrepancies. Changes in the column density of the order of $10^{21}\,\mathrm{cm}^{-2}$ on long time scales, months-years, are common in both type-1 and type-2 objects [144].

6. Unabsorbed type-2 AGN: X-ray absorption was only detected in ∼40% of the type-2 AGN in the AXIS sample and in ∼77% of the *Lockman Hole* type-2 AGN. The results

of our spectral analyses have allowed us to study some of the existing hypotheses that try to explain the optical/UV and X-ray properties in unabsorbed type-2 AGN. Using the results from the analysis of AXIS sources we could study whether the AGN/host galaxy contrast effect can explain the lack of detection of X-ray absorption in some type-2 AGN. If these objects are intrinsically faint, then their optical emission can be dominated by the emission of their host galaxy, and in these cases we should not be able to detect broad emission lines in their optical spectra. In order to test this hypothesis we compared the distribution of intrinsic (corrected for absorption) luminosities of unabsorbed type-2 AGN with that of type-1 AGN at the same redshifts. Using the Kolmogorov-Smirnov test we found that the significance of the distributions being different is ~99%, i.e., the mean intrinsic luminosity of unabsorbed type-2 AGN is smaller than that of type-1 AGN at the same redshifts. Therefore our results suggest that the lack of detection of broad optical lines in some type-2 AGN could be explained as an AGN/host galaxy contrast effect. We could not confirm whether the same result applies to unabsorbed type-2 AGN in the *Lockman Hole* as the sample of objects in this case is too small to allow any comparison. Another hypothesis that could explain the lack of broad optical/UV emission lines in these objects is that the luminosity of these objects might not be high enough to ionise the BLR where the broad lines originate. However in this case we would expect a dependence of the fraction of unabsorbed type-2 AGN with the X-ray luminosity, the fraction being higher at the lowest luminosities. We do not see evidence for such effect in the results of our analysis: unabsorbed type-2 AGN have a similar distribution of X-ray luminosities as absorbed type-2 AGN. Therefore it is unlikely that this second hypothesis can explain the results of our spectral analyses. Finally, our unabsorbed type-2 AGN could be Compton-thick objects. In this case all direct X-ray photons with energies below ~10 keV are absorbed, the only emission observed being photons with higher energies ≥10 keV scattered to the observed energies. However in Compton-thick sources, as the nuclear radiation is completely blocked by the absorber, the Fe Kα line emission should be strong and easier to detect. This is not the case in any of our unabsorbed type-2 AGN so it is unlikely that our sources are Compton-thick.

7. Soft excess is a common emission component of the X-ray spectra of AGN. We detected soft excess emission in ~7% of the AGN of AXIS, and in ~11% of the type-1 AGN and 25% of the type-2 AGN in the *Lockman Hole*. We did not find evidence that soft excess emission is more common in type-1 or type-2 AGN. On the other hand, the detected temperatures of this component, when fitted with a thermal model, were found to be rather constant, all within the range 0.1-0.3 keV in both AXIS and *Lockman Hole* AGN. The temperatures of the soft excess are in most cases ≥60 eV, and therefore the origin of this emission component cannot be explained as thermal emission from the accretion disc only. Comptonization of cool disc photons by hot electrons surrounding the accretion disc might be an alternative explanation. We also did not see any clear dependence of the emission properties of the soft excess, temperature and intrinsic luminosity with the X-ray luminosity or redshift of our AGN. We found the majority of our AGN to have soft excess components with

0.5-2 keV intrinsic luminosities $> 10^{43}\,\mathrm{erg\,s^{-1}}$. These luminosities are to high as to being due to starbursts (the typical X-ray luminosities in a starburst galaxy is of the order of $\sim 10^{41} - 10^{42}\,\mathrm{erg\,s^{-1}}$). However, we cannot exclude the possibility that part (but not all) of the emission comes from thermal radiation from the host galaxy while another fraction comes from the AGN. Unfortunately the signal of the X-ray spectra of our sources is not high enough as to try to separate both components. The distributions of X-ray luminosities of the soft excess component were found to be similar for both type-1 and type-2 AGN; the temperature of the soft excess tends to be higher in type-2 AGN than in type-1 AGN. This might be due to a higher contribution from scattering in type-2 AGN. For a number of *Lockman Hole* objects a thermal model did not provide a good fit of the spectral signatures of the soft excess emission. For these sources we obtained a good fit with a scattering or partial covering model. We found the average covering fraction of the absorber $\sim$0.82±0.06, which means that the scattering fraction in them is rather large (18±6%). A combination of blackbody and scattered radiation could provide an equally good fit, with physically meaningful parameters, but we do not have means to disentangle the contribution of both components.

8. We do not detect any dependence of the emission properties of AGN with the X-ray luminosity of the objects. Some studies suggest that the fraction of X-ray absorbed AGN decreases with the X-ray luminosity, but we do not confirm this. In addition, the distributions of X-ray luminosities for absorbed and unabsorbed sources were found to be consistent. On the other hand we do not see any significant dependence of the shape of the broad band continuum with the X-ray luminosity.

9. X-ray spectral analyses of objects detected with *ROSAT* [24] and *ASCA* [240] have found evidences that the mean continuum shape of AGN becomes harder at higher redshifts [20]. However, more recent spectral studies based on sources detected with *XMM-Newton* and *Chandra* find contradictories results: some studies have found the mean spectrum to become harder [20] while other studies suggest that it becomes softer [97]. Finally, some studies suggest that there is no significant evolution [239]. We did not find in any of our spectral analyses evolution of the mean continuum shape of our AGN. Neither, have found that absorption occurs at any preferred redshift in type-1 AGN. No clear dependence of the amount of absorption with redshift was seen in any sample of absorbed type-1 and type-2 AGN.

10. We used the results of the absorption properties of the AGN in the AXIS sample (number of absorbed objects and the measured distributions of X-ray absorption) to test some of the predictions of the most popular XRB synthesis models. Our analysis showed that all models predict an excess of absorbed objects (by more than a factor of 2) compared to the results of our analysis. Even the Ueda et al.(2003) [235] model, that assumes a dependence of the fraction of absorbed objects with the luminosity (less absorbed sources at higher luminosities) still overpredicts the number of absorbed objects, specially at low redshifts.

Some of the most important results from our **variability analysis** of *Lockman Hole* sources were:

1. The great majority of X-ray selected AGN (our variability analysis suggest that more than 80%) have varied their flux between observations on time scales of months-years. The amplitudes of flux variability detected in the light curves of our objects were found to be within the range 10-65%. Higher amplitudes of flux variability were found to be not very common in our objects, at least on the time scales covered sampled with our light curves. We found that both, type-1 and type-2 AGN show similar amplitudes of flux variability. In addition flux variability does not seem to be more common in any of the two types of AGN. We did not find any dependence of flux variability on the luminosity or redshift of the objects. The lack of a clear evolution of the flux variability properties of our objects over a broad range of redshifts is suggesting that the variability properties of our sources do not depend strongly on the observation band, as harder rest-frame energies are sampled for sources at higher redshifts. So, X-ray flux variability appears ubiquitous in all AGN, regardless of any parameters.

2. X-ray spectral variability was detected in 20% of the objects in the sample using X-ray colours. However our results suggest that for a fraction of objects we are not detecting the variability due to the low signal of the data, and that the fraction of objects that have spectral variability on long time scales is of the order of 40%. Keeping in mind that spectral variability is more difficult to detect than flux variability, our results seem to suggest that flux and spectral variability are not correlated for a large fraction of objects in our sample. This result could be explained if the flux variability is produced by changes in just one spectral component, such as the broad band continuum. Although flux variability does not seem to be more common in any of the samples of AGN, our results suggest that spectral variability is more common in type-2 AGN than in type-1 AGN.

3. Most of the objects in our sample showed only flux or spectral variability while the number of objects with both flux and spectral variability was rather small (15 out of 121). This result suggests that the flux and spectral variability detected in our objects on long time scales seem not to be correlated. This is confirmed by the results of the cross-correlation analysis of objects with detected flux and spectral variability. In none of the objects we found the variability properties to be correlated. Therefore it is unlikely that the detected spectral variability is triggered by changes in the intrinsic X-ray luminosity of the objects. Comptonization models predict typical changes in Γ of the order of $\Delta\Gamma \sim 0.2$. We found that the amplitude of flux variability associated with changes in Γ of 0.2 is $\sim$20%, below the detected amplitude of flux variability found in many of our objects. In order to explain the magnitudes of flux variability detected in our sources, changes in $\Delta\mathtt{HR} \geq 0.3$ are required, which correspond to $\Delta\Gamma \sim 0.6$-1.2, well above the expected values from Comptonization models. Hence it is unlikely that the observed flux variability is produced by changes in the broad band continuum shape alone.

4. To give more insight into the origin of the detected spectral variability we defined four different periods of time and co-added the X-ray spectra of the objects from each period. In this way we were able to study spectral variability on similar time scales than those covered by the X-ray colours. From this analysis we detected spectral variability in 8 objects, 6 being type-1 AGN and 1 type-2 AGN. We found that in all cases the origin of the detected spectral variability was associated with changes in the shape of the broad band continuum emission, while changes in the properties of other spectral components such as soft excess emission and X-ray absorption were not detected.

5. Spectral variability was detected in one out of the 4 unabsorbed type-2 AGN found in the *Lockman Hole* sample. We have shown that changes in N_H of magnitude $\sim 10^{22}\,cm^{-2}$ (the typical column density detected in our sample of absorbed type-2 AGN) produce changes in `HR` of the order of $\Delta HR \geq 0.3$ which we should have been able to detect. Therefore it is unlikely that spectral variability, for example associated with changes in the column density, can explain the lack of correlation between the observed optical/UV and X-ray properties in these objects. This is also consistent with the fact that flux and spectral variability do not appear correlated for our objects, as changes in absorption associated for example with changes in the ionisation state of the material, should be correlated with changes in flux. In addition, if the absorber is clumpy, then variations of the column density produced by clouds passing through the line of sight, would produce significant changes in both the flux and X-ray colour of the objects (unless changes are $\Delta N_H \sim 10^{21}\,cm^{-2}$) and both flux and spectral variability should have been detected, which is not the case for many of the objects in our sample. On the other hand significant flux variability was detected in 3 out of the four objects, which makes very difficult to explain the non detection of X-ray absorption in these objects as being due to the fact that they are Compton-thick. In Compton-thick objects X-ray emission should be dominated by scattered radiation and therefore we would not expect to detect flux or spectral variability in these objects on time scales of ≤ 2 years. Due to the apparent lack of correlation of flux and spectral variability the *two component spectral model* and the *spectral pivoting model*, frequently used to explain the variability properties in local Seyfert 1 galaxies, are unable to explain the variability properties of our objects.

Appendix A

Statistical techniques

A.1 Fitting statistics

In the first of the studies presented in Chapter 3 we carried out a spectral analysis using the χ^2 statistic on spectra that were binned with a minimum of 10 counts (source plus background) per bin. In the spectral studies conducted in Chapter 4, and thanks to the higher signal, we binned the spectra in channels with $\geq$30 counts where Gaussian statistics can be safely applied. The χ^2 statistics assumes that all the spectral bins are Gaussian distributed. To check whether the Gaussian assumption is correct for our data, we have compared the obtained χ^2 distributions with the expected distributions. Anomalously small values of χ^2 could be due only to the Gaussianity hypothesis not being valid, so it is important to compare χ^2 histograms with the expected distribution.

The expected global χ^2 probability density distribution for a set of χ^2 variables, each one of them with ν_i d.o.f. is

$$P(\chi^2) = \frac{\sum\limits_i N_{\mathrm{i}} p_{\nu_{\mathrm{i}}}(\chi^2)}{\sum\limits_i N_{\mathrm{i}}} \tag{A.1}$$

where

$$p_\nu(\chi^2) = \frac{2^{-\frac{\nu}{2}}}{\Gamma(\frac{\nu}{2})} \chi^{\nu-2} e^{-\frac{\chi^2}{2}} \tag{A.2}$$

is the χ^2 probability distribution for ν degrees of freedom, and N_{i} are the number of sources in our catalogue with a fit with ν_{i} degrees of freedom. From Eq. A.1 we can define the expected number of fits with a χ^2 value as $N(\chi^2) = P(\chi^2)\sum_i N_i$ and the χ^2 expected distribution for our sample of sources as $P(\chi^2)\sum_i N_{\mathrm{i}}$.

Fig. A.1 shows the results obtained when using `model A` and `model B` and for all sources. We do not find any excess of fits with low values of χ^2 and therefore we have no argument to believe that the assumption of Gaussian statistics during the fitting process is correct. However, we observed that the expected and obtained χ^2 distributions are substantially different, specially for `model A`, while a marginal improvement is obtained using `model B`. We quantified this difference with the Kolmogorov-Smirnov test, that gave a significance

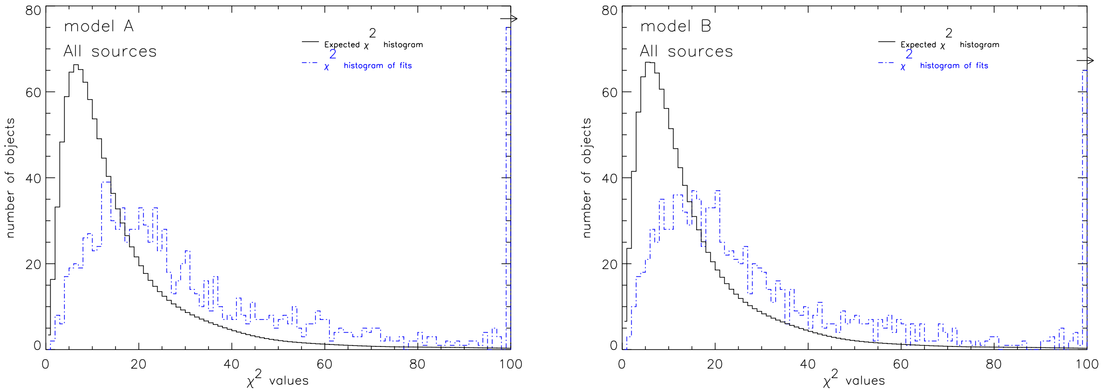

Figure A.1: *Comparison of expected (solid histograms) and obtained (dashed-dot histograms) χ^2 distributions for all sources using spectral models A and B. For clarity we grouped all χ^2 values above 100 in one bin.*

of the two distributions (observed and expected) being different of more than 99.99% for both models. Similar results are obtained when using `model A` and only sources identified as type-1 or type-2 AGN.Although `model B` seems to give better results for the sample of type-2 AGN, the Kolmogorov-Smirnov test gives a significance of the two distributions being different still higher than 99.99% for both type-1 and type-2 AGN and `model C`. These results are in agreement with the results obtained in terms of the P(χ^2) statistic for individual sources (see Sec. 3.2), and therefore confirm that more complicated spectral models are required (for example including a soft excess component) to reproduce the emission properties of a substantial fraction of the objects in our sample.

A.2 Averaging of the spectral parameters of the sources

During the X-ray spectral analyses presented in Chapter 3 and Chapter 4 we have calculated average values of the spectral parameters of the sources (e.g. see Sec. 3.3.1 and Sec. 3.3.4 in Chapter 3 and Sec. 4.5 in Chapter 4). However, it is necessary to be careful when calculating average values, to avoid any bias induced by "outliers", or when large errors are present, etc. Average values weighted with the errors of the individual measurements are frequently used. The standard expressions for the weighted mean and its corresponding statistical error are

$$\hat{\mu} = \frac{\sum_i \dfrac{x_i}{\sigma_i^2}}{\sum_i \dfrac{1}{\sigma_i^2}} \tag{A.3}$$

$$\sigma^2(\hat{\mu}) = \frac{1}{\sum\limits_i \frac{1}{\sigma_i^2}} \tag{A.4}$$

In the standard weighted mean the values that contribute more to the mean are the ones that are best measured, i.e., with lower errors, which it is in general what it is desired. However, the above expression of the error in the weighted mean does not include any information about the dispersion of the individual values around the mean. In order to take into account the intrinsic dispersion in the distribution of values we have modified the expression for the error in the weighted mean using the standard expression for the dispersion of the mean,

$$\sigma^2(\hat{\mu}) = \frac{1}{N-1} \sum_i P(x_i)\,(x_i - \hat{\mu})^2 \tag{A.5}$$

where $P(x_i)$ are the weights of each individual value x_i,

$$P(x_i) = \frac{1}{\sigma_i^2 \sum\limits_j \frac{1}{\sigma_j^2}} \tag{A.6}$$

If we include the definition of $P(x_i)$ in the above expression we obtain

$$\sigma^2(\hat{\mu}) = \frac{1}{N-1} \left[\frac{\sum\limits_i (x_i^2/\sigma_i^2)}{\sum\limits_j 1/\sigma_j^2} - \hat{\mu}^2 \right] \tag{A.7}$$

We have not used in our analysis the standard expression for the error in the weighted mean. Instead of that, we have used Eq. A.7, that includes both the contribution from the errors on each individual value and the dispersion of values around the weighted mean.

A.3 Maximum Likelihood technique

A maximum likelihood technique has been used to calculate the intrinsic dispersion in a set of measurements in Sec. 3.3.5 and Sec. 4.3. The only additional assumption is that the distribution of values can be well represented by a Gaussian. Under this assumption, we just have to calculate the minimum value of the function

$$S = -2\,\ln \mathcal{L} \tag{A.8}$$

where

$$\mathcal{L} = \prod_{i=1}^{N} \frac{1}{\sqrt{2\,\pi\,(\sigma_p^2 + \sigma_i^2)}} \exp\left[\frac{-(x_i - \langle x_p \rangle)^2}{2\,(\sigma_p^2 + \sigma_i^2)} \right] \tag{A.9}$$

is the likelihood function, x_i and σ_i are the individual values and their associated errors, and x_p and σ_p are the expectation values of the mean and intrinsic deviation of the parent population.

A.4 Measuring and comparing fractions of absorbed objects

In this section it is described in detail the method that we used to calculate fractions of objects with a defined property (e.g. absorption) and their corresponding 1σ errors after correction for the spurious detections expected from the selected confidence value (e.g. see Sec. 3.3.2 and Sec. 4.5).

Suppose that we have a sample of *N* objects, and that we detect a selected property, for example absorption, in *n* of them. The probability of *n* detections in a sample of *N* objects is the binomial probability formula

$$P(n, N) = \begin{pmatrix} N \\ n \end{pmatrix} p^n \, (1-p)^{N-n} \tag{A.10}$$

where *p* is the probability of detection. This probability depends on the number of objects in the sample which are indeed absorbed, *f*, and on the selected confidence level, that will allow for a fraction of spurious detections, f_{spu},

$$p = f + f_{spu} \tag{A.11}$$

Using Bayes' theorem the probability distribution of *f*, $P(f; n, N, f_{spu})$, is

$$P(f; n, N, f_{spu}) = \frac{(f + f_{spu})^n \, (1 - f - f_{spu})^{N-n}}{\int_0^1 \, df \, (f + f_{spu})^n \, (1 - f - f_{spu})^{N-n}} \tag{A.12}$$

normalising Eq. A.10.

The fraction that we want to calculate will be the mode (maximum value) of the probability distribution of *f*. The corresponding 1σ errors can be obtained integrating the above expression from the mode in the two directions until the desired probability is obtained. It is also possible to calculate the confidence of detection of the selected property integrating the *P(f)* distribution from *f*=1 down to the value where the integral is equal to the selected probability.

If we want to compare values of *f* obtained for different subsamples of objects we have to use a slightly different approach. Let us suppose that we have a sample of *M* type-1 AGN with *m* of them being absorbed, and another sample of *N* type-2 AGN with *n* of them being absorbed. If we assume that both samples are drawn from the same parent population, then

$$P(n, m; N, M) = \begin{pmatrix} N + M \\ n + m \end{pmatrix} p^{n=m} \, (1-p)^{M+N-m-n} \tag{A.13}$$

Under this assumption, the probability of obtaining m or more absorbed objects out of M, and n or less out of N is given by

$$\sum_{i \leq n} \sum_{j \geq m} P(i, j; N, M) \tag{A.14}$$

If this probability is small we can reject the hypothesis that the fractions are the same.

Appendix B

Detection efficiency function of AXIS sources

As we explained in Sec. 3.1.1, in order to interpret the results of the spectral analysis presented in Chapter 3, it is important to account for any biases present in the data. To do this we need to calculate the detection efficiency function of our sources. However, the fact that we carried out source detection on different energy bands with different sensitivities to X-ray photons simultaneously, the selection of fields covering a wide range of exposure times (from ~ 10 to ~ 100 ksec), and the quality filters applied to the spectra (especially the selection of spectra with MOS+pn counts ≥ 50) make the calculation of the efficiency of source detection difficult. We expect it to be a function of the X-ray flux, but it is important to know whether it also depends on the spectral shape of the sources.

We have conducted simulations to calculate the efficiency of detection as a function of the X-ray photon index, Γ for a power law spectrum, and X-ray flux S: $\mathrm{W}(\Gamma, S)$. For a given number of sources with spectral parameters Γ and S, $\mathrm{W}(\Gamma, S)$ gives the fraction of simulated objects that were detected (and their spectra fulfilled the quality filters applied to our data, see Sec. 3.1), and with best fit spectral parameters being the same as the input (simulated) ones. This function can be used to correct observed source properties, for example the dependence of the mean spectral slope, $\langle\Gamma\rangle$, with X-ray flux, from all the effects listed above. In order to calculate this function we defined a grid in the Γ-S plane covering the range of values measured for our objects (Γ from 0.5 to 3; S from 10^{-16} to $10^{-12}\,\mathrm{erg\,cm^{-2}\,s^{-1}}$).

We have simulated the same number of spectra on each grid cell. For these simulations we have used the list of detected sources before applying the quality filters, i.e., 2145 sources have been simulated on each cell in the Γ-S grid. The input parameters of each simulated spectrum were the exposure time, response matrices and Galactic absorption of each real source, and the values of Γ and S at each grid cell. We used a power law spectrum, `model A` (see Sec. 2.6), to simulate all the spectra, therefore excess absorption is not included in the simulations. Once all the spectra were simulated, we applied the same quality filters that we used for the real data.

We found that there are two possible contributions to the final number of sources that

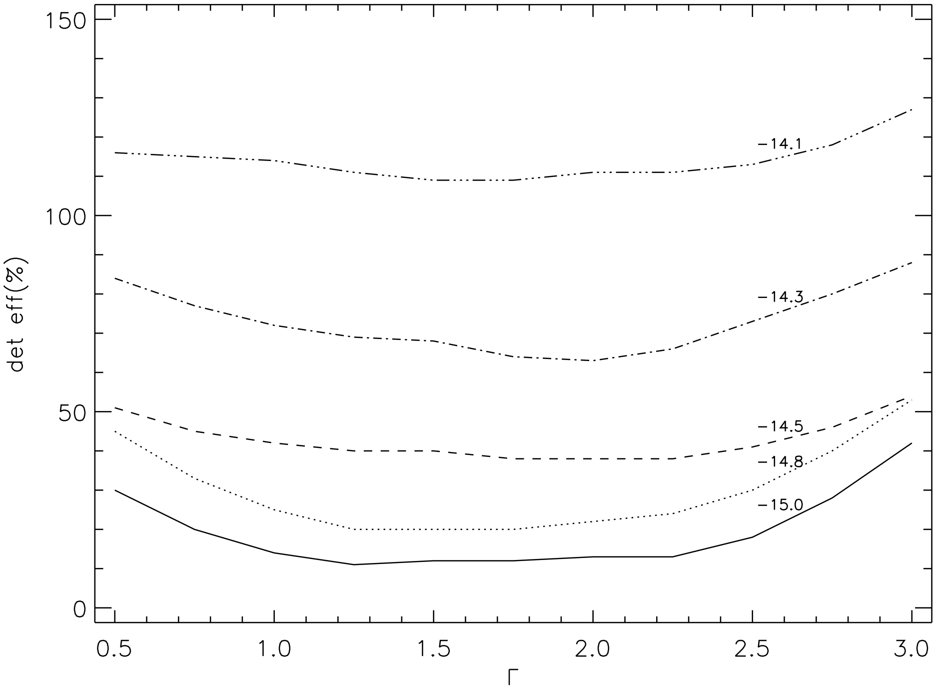

Figure B.1: *Dependence of the detection efficiency function of* `AXIS` *sources as a function of* Γ *for different values of flux, obtained from simulations. Some values of the efficiency function were found to be above 100% because fitted parameters may differ from input ones (see text for details).*

will appear at a given grid cell (Γ, S):

1. The number of simulated sources at the grid cell (Γ, S) that, after fitting, remain at the same grid cell, $N_{det}(\Gamma, S)$.
2. The number of sources simulated at different grid cells (Γ', S') that were detected with best fit spectral parameters (Γ, S), $N_{det}(\Gamma', S')$.

This means that our source detection efficiency function, at each grid cell, is defined as

$$W(\Gamma, S) = \frac{N_{det}(\Gamma, S) + N_{det}(\Gamma', S')}{N_{sim}} \tag{B.1}$$

where N_{sim} is the number of sources that were simulated at the grid cell (Γ, S) (it is the same for all the grid cells).

The values of the source detection efficiency function as a function of Γ are plotted in Fig. B.1 for different fluxes. We found that, at fluxes below $\sim 10^{-14}\,\mathrm{erg\,cm^{-2}\,s^{-1}}$, the efficiency of detection decreases significantly from Γ=0.5 to Γ=2, and then, starts to increase up to Γ=3. The rise of efficiency at high values of Γ could be due to the sharp

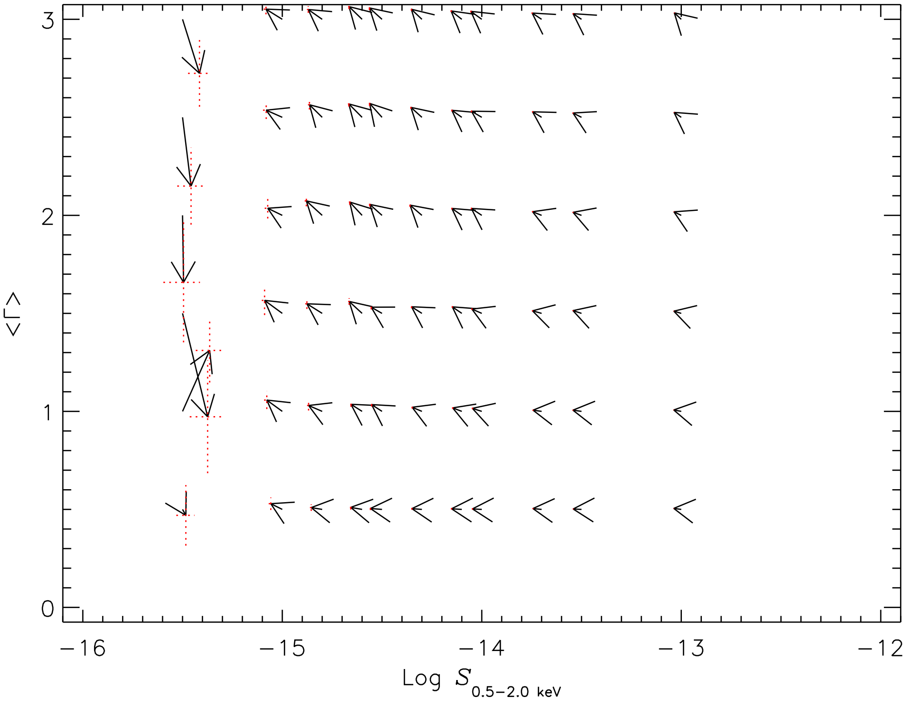

Figure B.2: *Representation of the average movements in the* Γ-S *plane obtained from simulations. The starting point of each arrow indicates the input values of* Γ *and* S *in the simulations that fulfil the quality filters; the end points are observed (fitted) average values for the sources from that bin which were detected.*

increase in the effective areas of the EPIC detectors at low energies, combined with the increase in the relative contribution to the total counts at these energies for the steeper spectral slopes. It is interesting to note that, although we have shown that the detection efficiency increases for Γ values above 2.5, we have not detected these super-soft sources in our sample, hence, they must be rare. The reason why the efficiency function is higher for objects with hard ($\Gamma \sim 0.5$) spectral slopes (notice that the effective area of the X-ray detectors drops rapidly at energies below ~1 keV) is that a source with flat (i.e. hard) spectral slope has to be much brighter than one with steep (i.e. soft) ($\Gamma \sim 2$) spectrum in order to have the same 0.5-2 keV flux [254]. Therefore, we will receive more counts in the 0.2-12 keV band from flatter objects, which means that we will detect them better and will pass more easily our spectral quality filters.

Our simulations showed that there are movements of objects in the Γ-S plane, i.e., fitted parameters may differ from the input (simulated) ones. It is necessary to study how important this effect is, and whether there are systematic shifts (for example a tendency to detect the sources with lower values of Γ at faint fluxes). Hence, we have calculated for each grid cell average values of Γ and S from all the sources simulated at that cell that were detected (no matter at which grid cell they were detected) in the same way as we did for the real sample. The results, shown in Fig. B.2, confirm the existence of shifts in the Γ-S plane which are more important at the faintest fluxes: on average, the measured Γ values tend to be softer, and the observed 0.5-2 keV fluxes are lower. However, for fluxes $\geq 10^{-15}\,\mathrm{erg\,cm^{-2}\,s^{-1}}$, these movements are not significant and tend to soften instead of harden the measured average spectra, contrary to the effect seen in Sec. 3.3.1. We can therefore exclude these selection effects as being at the root of the spectral hardening of X-ray sources towards fainter fluxes.

Appendix C

Variability analysis of *Lockman Hole* sources

C.1 Correction of count rates for calibration drifts

In order to study flux and spectral variability in our sample of *Lockman Hole* sources (Chapter 4 and Chapter 5), we have compared the observed count rate of each object obtained on each *XMM-Newton* observation. However, the *XMM-Newton* observations in the *Lockman Hole* field span a broad range of the mission lifetime, and therefore, changes might be expected in the calibration of the data. Particularly in the instrumental spectral response and systematic variations in the background modelling with time. That could introduce systematic differences in the measured count rates of the same source between observations. In addition, pn observations were obtained with different blocking filters. A change in the blocking filter affects more the soft X-rays and therefore the measured 0.2-12 and 0.5-2 keV count rates.

In order to estimate how much of the measured variability in our sources is due to the effects listed before, we have calculated for each revolution r the average deviation of the measured count rates in that revolution from their mean flux over all revolutions for the subset of sources detected in that revolution. If there are no variations in the calibration, we would expect this value to be very close to unity, since variability is not expected to be correlated with time for different sources. We have called this value Ω^r and it is defined as,

$$\Omega^r = \frac{1}{N(r)} \sum_{i=1}^{N(r)} \frac{c_i^r}{\langle c_i \rangle} \tag{C.1}$$

The sum is over the number of sources detected on each revolution r, *N(r)*, c_i^r is the count rate of source i in revolution r and $\langle c_i \rangle$ is the mean unweighted count rate of the source over all revolutions where it was detected.We found that the errors in the count rates were dominated by the quality of the observations (the errors in the background modelling and fitting of the source parameters in the `SAS` source detection task `emldetect`), and do

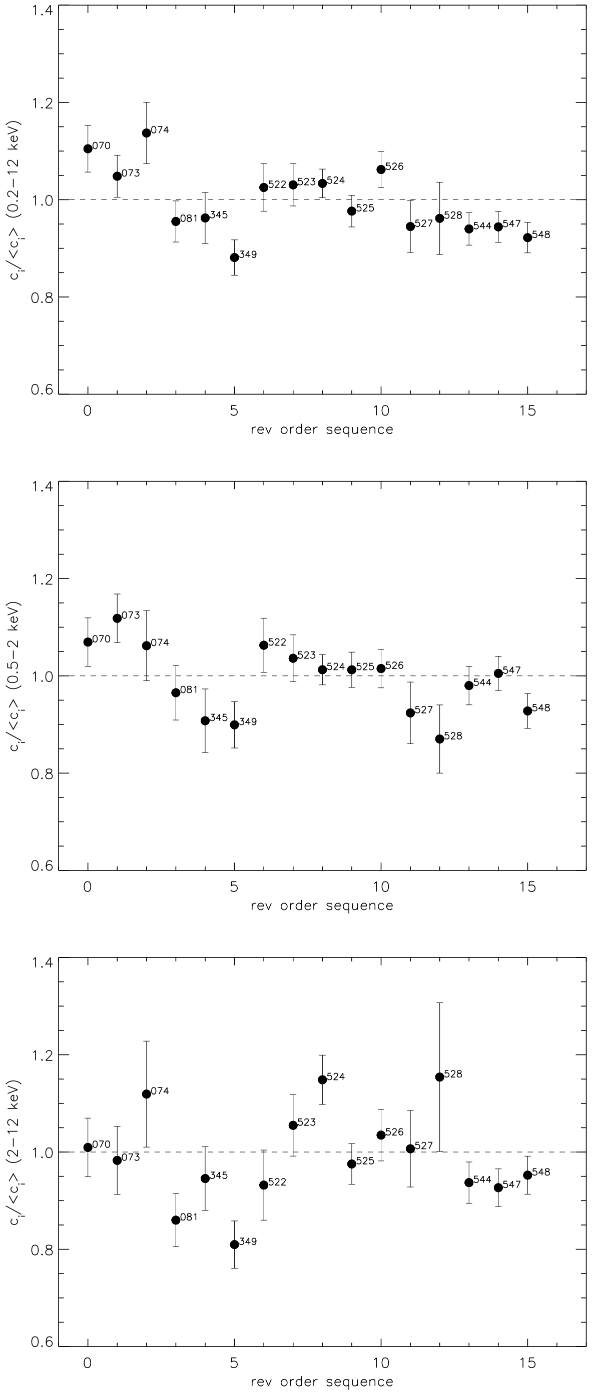

Figure C.1: *Corrections of the count rates for each revolution that we used to correct the measured flux of our objects from systematic variations during the live time of the mission and from variations from using different blocking filters for the observations. From top to bottom corrections for the 0.2-12, 0.5-2 and 2-12 keV count rates. Errors correspond to the 1σ confidence interval.*

not depend strongly on the values of the count rates themselves, in the sense that sources with larger count rates do not tend to have smaller errors. Because of this, the use of the weighted mean is not necessary in this case, and therefore we used the unweighted mean to calculate the average flux of each source and the mean dispersion of the count rates of the sources from their mean values for each revolution. However our mean values could be significantly affected by outliers due to flux variability of the sources. In order to avoid this, we applied a sigma-clipping (3σ) before calculating average values[1].

The 1σ errors in Ω^r will be $\sigma(\Omega^r)/\sqrt{n(r)}$ where $n(r)$ is the number of points in revolution r after sigma-clipping and $\sigma(\Omega^r)$ is

$$[\sigma(\Omega^r)]^2 = \frac{1}{n(r)-1}\sum_{i=1}^{n(r)}\left(\frac{c_i^r}{\langle c_i\rangle} - \Omega^r\right)^2 \tag{C.2}$$

We calculated values of Ω^r for the measured 0.2-12 keV count rates that we used to study source flux variability, and for 0.5-2 keV and 2-12 keV count rates that we used to carry out the study of spectral variability. The values of Ω^r and their corresponding 1σ errors that we obtained for each revolution and energy band are shown in Fig. C.1.

The corrected count rates and their corresponding 1σ errors for each revolution were obtained as

$$(c_i^r)^{corr} = \frac{c_i^r}{\Omega^r} \tag{C.3}$$

$$\Delta(c_i^r)^{corr} = ((c_i^r)^{corr})^2 \times \sqrt{\left(\frac{\Delta c_i^r}{c_i^r}\right)^2 + \left(\frac{\Delta\Omega^r}{\Omega^r}\right)^2} \tag{C.4}$$

It is evident from Fig. C.1 that all the values are very close to unity, which means that we did not find calibration drifts between revolutions in any of the three energy bands, and therefore these corrections are very small in all cases.

C.2 Simulations of variability in *Lockman Hole* sources

In Chapter 5 we show the distribution of intrinsic variability amplitude that we found in our sample of objects. However measured values might differ from intrinsic values due to a number of effects, such as not enough quality in the light curves. In order to take into account all possible effects, we carried out simulations to calculate the distribution of intrinsic variability amplitude in our sample of objects after correcting for these effects.

In order to simplify the notation we will refer to the intrinsic amplitude of flux variability, σ_{intr}^i, as S_i while S_o we be used to refer to the corresponding measured amplitude, σ_{intr}^o (see Sec. 5.2.1). We defined a 3D parameter space (S_i, S_o, CR), where S_i is the intrinsic amplitude of flux variability, S_o is the observed amplitude as measured following the procedure described in Chapter 5 (see Sec. 5.2.1), and CR is 0.2-12 keV count rate.

We defined the grid in count rates such that the full range of count rates of our data is covered by simulations, from 0.001 to 0.481 counts s^{-1}, while S_i values covered the range

---

[1] Sigma-clipping only removed a small (~a few) number of points from each revolution, therefore we still have enough number of points to calculate reliable mean values for each revolution and energy band.

from 0 to 4 (fraction of variability over the total count rate). As we will see later, the maximum simulated value of S_i had to be chosen high enough to ensure that we obtain the correct distribution of intrinsic amplitudes within the covered range by our sources (below $S_o^{max} \sim 0.7$).

For each grid point (S_i, *CR*), and for each of the 120 sources in our sample for which we could study flux variability, we simulated a light curve. Simulated light curves have the same number of points than the real data and mean count rate *CR*. Count rates and their corresponding statistical errors are correlated as we show in Fig. C.3 where we plotted the values obtained on each revolution for all sources (we did not see variations in the correlation between different revolutions). The correlation in logarithmic scale is linear, i.e., $\ln(\Delta CR) = \alpha \times \ln(CR) + \beta$. From this expression the analytical form of the correlation between ΔCR and CR is a power law with

$$\Delta CR = CR^{\alpha} \times e^{\beta} \tag{C.5}$$

The values that we obtained from the best fit were α=0.66 and β=-3.61. Using this correlation we obtained for each simulated count rate CR the corresponding statistical error, σ_{stat}. The values (count rates) of each point in the light curves, *cr*, were assumed to follow a Gaussian distribution of mean equal to the mean count rate, *CR*, and dispersion $\sigma^2 = \sigma_{stat}^2 + (S_i \times CR)^2$, where σ_{stat} is the statistical count rate error that corresponds to a count rate value CR.

Finally, for each *cr* value we obtained the corresponding statistical error from Eq. C.5. We then obtained for each simulated light curve the measured values of the intrinsic amplitude, S_o, following the same procedure as for the real data.

For each set of values (S_i, *CR*) we computed the function $N(S_o|S_i, CR)$ that gives for each value S_o the number of sources with that observed amplitude. Then we calculated the function $N(S_o|S_i)$, that gives for each S_i the number of sources in the simulations for each value of S_o, weighted with the distribution of CR, as

$$N(S_o|S_i) = \sum P(CR) \times N(S_o|S_i, CR) \tag{C.6}$$

where $P(CR)$ is the distribution of count rates in our sources which is shown in Fig. C.3. The count rates were obtained as the arithmetic mean of the corrected count rates of all the points in the light curves. The total number of sources in the simulations with observed values S_o is

$$N(S_o) = \sum N(S_o|S_i) \tag{C.7}$$

This number can be used to obtain the probability distribution of S_i values for a given S_o as

$$P(S_i|S_o) = \frac{N(S_o|S_i)}{N(S_o)} \tag{C.8}$$

Then the probability distribution of S_i will be

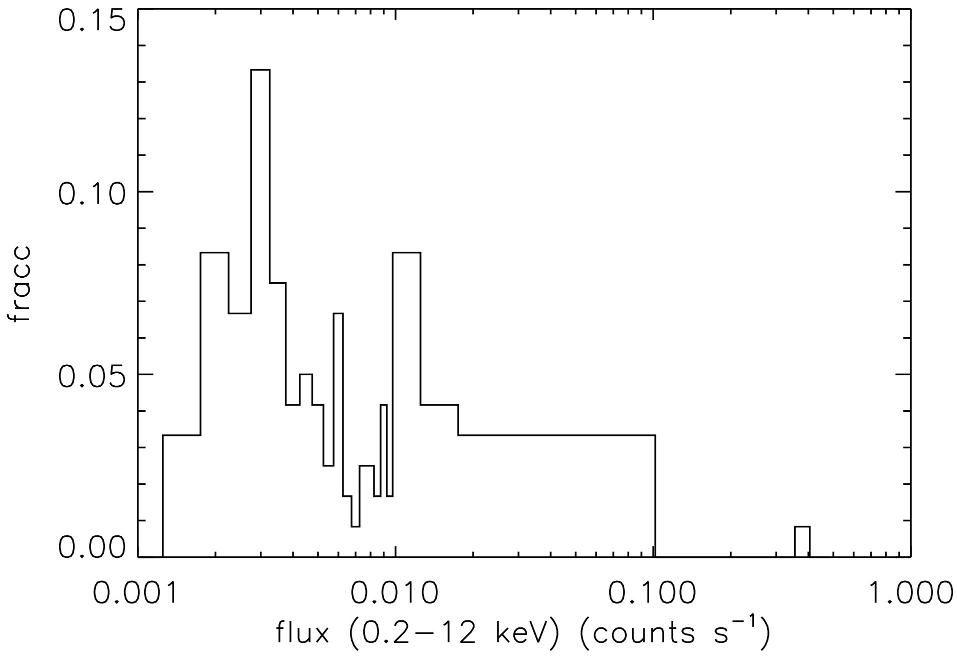

Figure C.2: *Distribution of 0.2-12 keV count rates (corrected for calibration uncertainties) in our sample of sources for which we studied flux variability.*

$$P(S_i) = \sum P(S_i|S_o) \times P(S_o) \tag{C.9}$$

where $P(S_o)$ is the distribution of S_o values observed in our sources (see Fig 5.2).

In order to get the correct distribution of $P(S_i)$ we need to simulate up to a value of S_i for which all values of S_o are above the maximum observed variance $\sigma_{intr} = 0.7 \equiv S_o^{max}$, otherwise the normalisation of $P(S_i)$ will be wrong. However during the simulations we found a number of sources for which we obtained values of S_o below 0.7 independently of how large was the simulated S_i. This is shown in Fig. C.4 where the fraction of these cases is plotted as a function of simulated S_i (solid line). Although this fraction decreases rapidly for low S_i (below ∼2) it remains ∼constant for the highest simulated values.

We identified these anomalous cases with sources with a small number of bins in the light curves.

Fig. C.5 (left) shows for each source, identified in the x-axis with its corresponding ./M. *XMM-Newton* identification number (first column in Table 4.8), the fraction of simulations (for all values of (S_i, CR)) for which $S_o \leq S_o^{max}$ (∼0.7). We see that only a small number of sources have a fraction of $S_o \leq S_o^{max}$ (∼0.7) above 10%. Fig. C.5 (right) shows the distribution of the number of bins in the light curves of our objects (solid line). The corresponding distribution for the sources for which the fraction of simulations with $S_o \leq S_o^{max} \geq 10\%$ is indicated with a dashed-line. Our results show that, selecting a value of

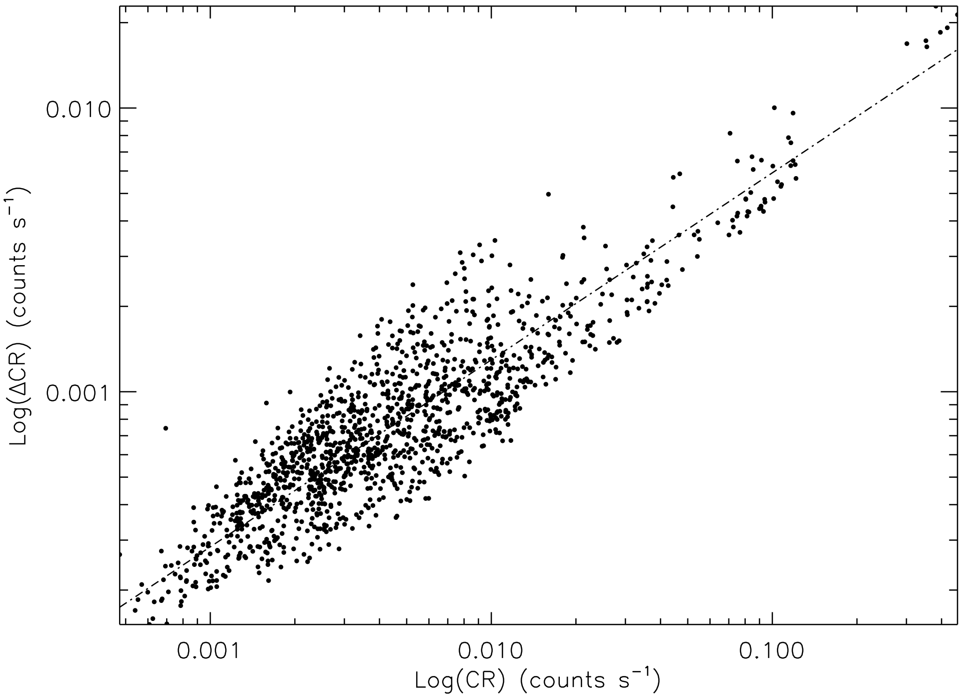

Figure C.3: *Correlation between ΔCR and CR for the sources in our sample. The values were obtained from the 0.2-12 keV energy band. The solid line represents the power law best fit to the points.*

the fraction of 10% we pick up most of the "problematic" light curves withough reducing significantly the number of light curves appropriate for the analysis presented in Chapter 5. In addition we found that these "problematic" cases correspond to the sources with lower number of bins in the light curves.

As we need to simulate values of S_i where the fraction of simulations with $S_o \leq S_o^{max}$ is low, we have not used sources with less than 5 points in their light curves in the calculation of the distributions $P(S_i)$ and $P(S_o)$.

This implies that the number of sources for which we can obtain the distribution of S_i is 103, instead of the original sample of 120 sources having at least 2 points in their light curves. By doing this selection we can be confident that we can represent the expected distribution of S_i, $P(S_i)$, using simulations of S_i values up to ~ 4.

A fraction of the simulated light curves were found to have negative mean count rates, and therefore in these cases the measured amplitudes of variability, S_o, were also negative as $S_o = \sigma_Q / \langle CR \rangle (\equiv \sigma_{intr}$; see Eq. 5.5) with $\langle CR \rangle$ being the mean unweighted count rate of the simulated light curve. Our simulations showed that the fraction of simulated light curves with negative mean count rates did not vary significantly with the simulated count rates, CR, but it was a strong function of S_i. This can be seen in Fig. C.6 where we plotted

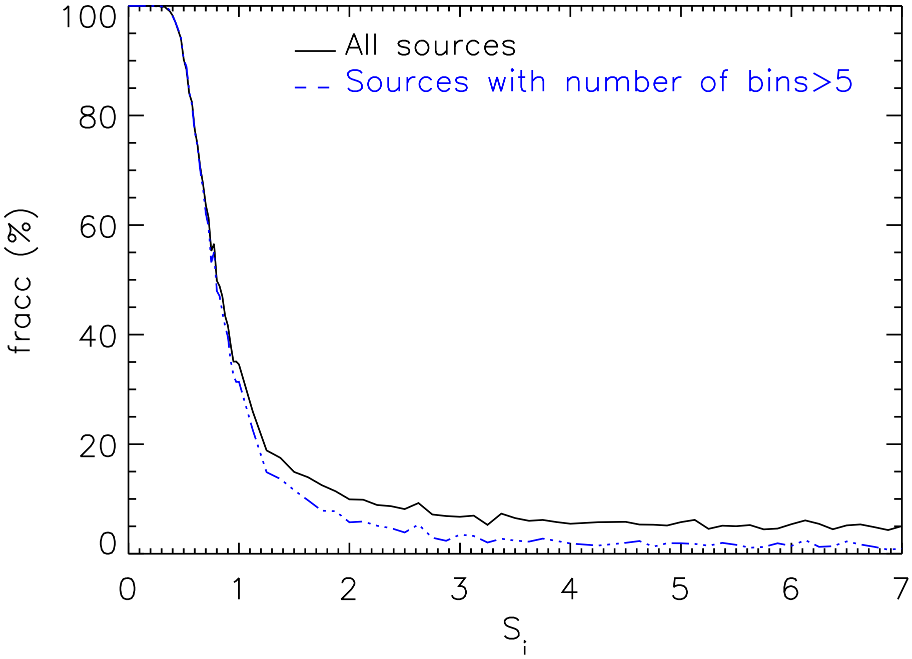

Figure C.4: *Fraction of simulations that give S_o values below S_o^{max} as a function of simulated S_i for all CR, when all sources are used in the simulations and when only sources with at least 5 points in their light curves are used.*

this fraction as a function of S_i and CR. We see that using only observations with $S_i \leq 4$ the maximum fraction of simulated light curves with negative S_o is ~5% for S_i=4.

This result is expected as for larger values of S_i the Gaussian distribution that we are using to obtain simulated count rates becomes broader, while the mean does not move significantly from zero, and hence the probability of obtaining negative average values increases. In all these cases we used the absolute values of the mean count rates to calculate the values of S_o.

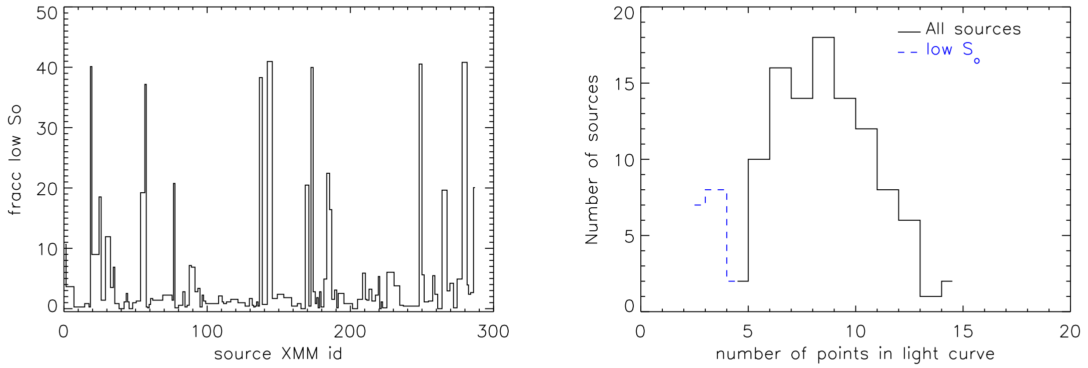

Figure C.5: *Left: For each source, represented in the x-axis with its corresponding XMM-Newton identification number (first column in Table 4.8), fraction of simulations (for all simulated values of (S_i, CR)) where $S_o \leq S_o^{max}$ (∼0.7). Right: Distribution of number of bins in the light curves of our sources. The corresponding distribution for the objects where the fraction of simulations with $S_o \leq S_o^{max}$ was higher than 10% is indicated with a dashed-line.*

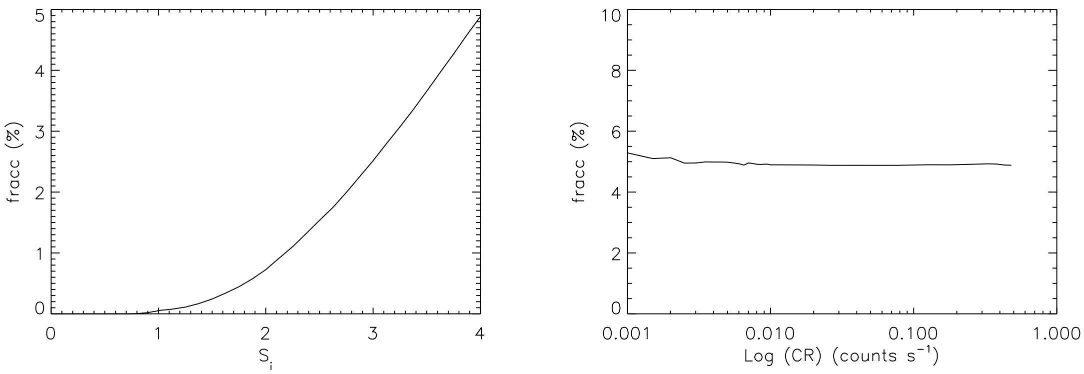

Figure C.6: *Fraction of simulated light curves with negative mean count rates as a function of S_i (intrinsic amplitude; left) and CR (0.2-12 keV count rate; right).*

Appendix D

Stacking of X-ray spectra

This Appendix describes in detail the recipes we used to obtain co-added spectra for our sources. Sec. D.1 explains how to obtain MOS spectra and co-added spectra from different observations of the same object. We co-added spectra to increase the signal to noise ratio of the data used in the analyses presented in Chapter 3 and Chapter 4. Sec. D.2 explains how to co-add spectra of different objects. This recipe was used in Sec. 4.18 to obtain the shape of the integrated emission of our *Lockman Hole* objects and compare it with that of the extragalactic X-ray background.

D.1 Stacking of spectra of the same object

In order to increase the signal to noise ratio of the data used in the analysis presented in Chapter 3 and Chapter 4, we combined M1 and M2 spectral products. In addition, for objects with more than one set of spectral products available, i.e. sources with more than one observation, all MOS and pn spectra were co-added. Because of their different responses pn and MOS data were not combined. In order to account for the differences between the effective exposure times of the spectra and also for the effect of using different blocking filters in observations of the same source (the filters affect in a different way the X-ray spectra at low energies) we weighted the spectral products of each individual observation with the exposure times and backscales (areas used to extract source and background spectra) of the observation. This is specially important to obtain co-added spectra for the *Lockman Hole* sources, because as we see in Table. 4.1 different blocking filters were used for the observations.

Suppose that we want to obtain the co-added spectrum for a source with two different observations. The spectrum from each observation has counts $C_1(I)$ and $C_2(I)$ on each channel I, exposure times ts_1 and ts_2, backscales bs_1 and bs_2, and response files rsp_1 and rsp_2[1]. Suppose the corresponding background spectra have counts $B_1(I)$ and $B_2(I)$ on each channel I, exposure times tb_1 and tb_2, and backscales bb_1 and bb_2. Source and

---

[1] The instrument response is usually represented with a single file, rsp, containing both the ancillary response file `ARF` and the redistribution matrix file `RMF` (see Sec. 2.5).

background co-added spectra, $C(I)$ and $B(I)$, are obtained adding the counts on each channel I,

$$C(I) = \sum_I C_1(I) + C_2(I) \tag{D.1}$$

$$B(I) = \sum_I B_1(I) + B_2(I) \tag{D.2}$$

The exposure times of the co-added source and background spectra are $ts = ts_1 + ts_2$ and $tb = tb_1 + tb_2$ while the backscales are

$$bs = \frac{bs_1 \times ts_1 + bs_2 \times ts_2}{ts} \tag{D.3}$$

and

$$bb = \frac{bb_1 \times tb_1 + bb_2 \times tb_2}{tb} \tag{D.4}$$

The response matrix of the co-added spectrum, rsp, is obtained with a weighted sum (using the exposure times) of the response matrices from each observation,

$$rsp = \frac{ts_1 \times rsp_1 + ts_2 \times rsp_2}{ts_1 + ts_2} \tag{D.5}$$

The same procedure has been used to stack M1 and M2 spectra.

D.2 Computing the contribution to the background of a set of sources

In Sec. 4.18 we compared the shape of the integrated emission of our *Lockman Hole* sources with that of the cosmic X-ray background. In order to do that we stacked all MOS and pn spectra of our sources. We kept MOS and pn data separately because of their different instrumental responses.

The MOS and pn co-added spectra were obtained with the following procedure: suppose we want to add two spectra having counts $C_1(I)$ and $C_2(I)$, exposure times ts_1 and ts_2, backscales bs_1 and bs_2 and response matrices rsp_1 and rsp_2, and that the corresponding background extraction regions have counts $B_1(I)$ and $B_2(I)$, exposure times tb_1 and tb_2 and backscales bb_1 and bb_2.

Source and background co-added spectra, $C(I)$ and $B(I)$, are obtained as in previous section, adding the counts on each channel I,

$$C(I) = \sum_I C_1(I) + C_2(I) \tag{D.6}$$

$$B(I) = \sum_I B_1(I) + B_2(I) \tag{D.7}$$

The total backscale of the co-added spectrum will be in this case $bs = bs_1 + bs_2$ and the total exposure time $ts = (ts_1 \times bs_1 + ts_2 \times bs_2)/(bs_1 + bs_2)$. The total backscale of the co-added background spectrum will be $bb = bb_1 + bb_2$ and the total exposure time $tb = (tb_1 \times bb_1 + tb_2 \times bb_2)/(bb_1 + bb_2)$. Finally, the combined response matrix, rsp, will be

$$rsp = \frac{(ts_1 \times bs_1) \times rsp_1 + (ts_2 \times bs_2) \times rsp_2}{(ts_1 \times bs_1 + ts_2 \times bs_2)} \tag{D.8}$$

This procedure can be trivially extended to stack any number of sources.

Note that we cannot use the method described in Sec. D.1 because in this case we are accumulating counts from different sky regions where we have our sources and therefore, to obtain the staked spectra we are accumulating counts in an increasing solid angle. This means that instead of averaging backscales we have to add them, and instead of adding the exposure times we have to calculate a mean exposure time, in this case weighted with the backscale values.

Bibliography

[1] **M. Akiyama**. AGN Population at $10^{-13} ergs^{-1} cm^{-2}$: Results from Optical Identification of ASCA Surveys. In *ASP Conf. Ser. 234: X-ray Astronomy 2000*, pages 539–+, 2001.

[2] **M. Akiyama, Y. Ueda, K. Ohta, T. Takahashi, and T. Yamada**. Optical Identification of the ASCA Medium Sensitivity Survey in the Northern Sky: Nature of Hard X-Ray-Selected Luminous Active Galactic Nuclei. *ApJS*, 148:275–315, October 2003.

[3] **O. Almaini, A. Lawrence, T. Shanks, A. Edge, B. J. Boyle, I. Georgantopoulos, K. F. Gunn, G. C. Stewart, and R. E. Griffiths**. X-ray variability in a deep, flux-limited sample of QSOs. *MNRAS*, 315:325–336, June 2000.

[4] **O. Almaini, T. Shanks, B. J. Boyle, R. E. Griffiths, N. Roche, G. C. Stewart, and I. Georgantopoulos**. A deep ROSAT survey. XII. The X-ray spectra of faint ROSAT sources. *MNRAS*, 282:295–303, September 1996.

[5] **R. Antonucci**. Unified models for active galactic nuclei and quasars. *ARA&A*, 31:473–521, 1993.

[6] **R. R. J. Antonucci and J. S. Miller**. Spectropolarimetry and the nature of NGC 1068. *ApJ*, 297:621–632, October 1985.

[7] **K. A. Arnaud**. XSPEC: The First Ten Years. In **G. H. Jacoby and J. Barnes**, editors, *ASP Conf. Ser. 101: Astronomical Data Analysis Software and Systems V*, pages 17–+, 1996.

[8] **K. A. Arnaud, G. Branduardi-Raymont, J. L. Culhane, A. C. Fabian, C. Hazard, T. A. McGlynn, R. A. Shafer, A. F. Tennant, and M. J. Ward**. EXOSAT observations of a strong soft X-ray excess in MKN 841. *MNRAS*, 217:105–113, November 1985.

[9] **X. Barcons**. Confusion noise and source clustering. *ApJ*, 396:460–468, September 1992.

[10] **X. Barcons, F. J. Carrera, and M. T. Ceballos**. The warm absorber of the type 1 Seyfert galaxy H1419+480. *MNRAS*, 346:897–904, December 2003.

[11] **X. Barcons, F. J. Carrera, M. G. Watson, R. G. McMahon, B. Aschenbach, M. J. Freyberg, K. Page, M. J. Page, T. P. Roberts, M. J. L. Turner, D. Barret, H. Brunner, M. T. Ceballos, R. Della Ceca, P. Guillout, G. Hasinger, T. Maccacaro, S. Mateos, C. Motch, I. Negueruela, J. P. Osborne, I. Pérez-Fournon, A. Schwope, P. Severgnini, G. P. Szokoly, N. A. Webb, P. J. Wheatley, and D. M. Worrall**. The XMM-Newton serendipitous survey . II. First results from the AXIS high galactic latitude medium sensitivity survey. *A&A*, 382:522–536, February 2002.

[12] **X. Barcons, S. Mateos, and M. T. Ceballos**. On the intensity of the extragalactic X-ray background. *MNRAS*, 316:L13–L16, July 2000.

[13] **X. et al. Barcons**. (to be submitted). *A&A*, 2006.

[14] **A. J. Barger, L. L. Cowie, W. N. Brandt, P. Capak, G. P. Garmire, A. E. Hornschemeier, A. T. Steffen, and E. H. Wehner**. X-Ray, Optical, and Infrared Imaging and Spectral Properties of the 1 Ms Chandra Deep Field North Sources. *AJ*, 124:1839–1885, October 2002.

[15] **A. J. Barger, L. L. Cowie, R. F. Mushotzky, and E. A. Richards**. The Nature of the Hard X-Ray Background Sources: Optical, Near-Infrared, Submillimeter, and Radio Properties. *AJ*, 121:662–682, February 2001.

[16] **P. Barr and R. F. Mushotzky**. Limits of X-ray variability in active galactic nuclei. *Nature*, 320:421–423, April 1986.

[17] **L. Bassani, M. Dadina, R. Maiolino, M. Salvati, G. Risaliti, R. della Ceca, G. Matt, and G. Zamorani**. A Three-dimensional Diagnostic Diagram for Seyfert 2 Galaxies: Probing X-Ray Absorption and Compton Thickness. *ApJS*, 121:473–482, April 1999.

[18] **F. E. Bauer, D. M. Alexander, W. N. Brandt, D. P. Schneider, E. Treister, A. E. Hornschemeier, and G. P. Garmire**. The Fall of Active Galactic Nuclei and the Rise of Star-forming Galaxies: A Close Look at the Chandra Deep Field X-Ray Number Counts. *AJ*, 128:2048–2065, November 2004.

[19] **F. E. Bauer, C. Vignali, D. M. Alexander, W. N. Brandt, G. P. Garmire, A. E. Hornschemeier, P. Broos, L. Townsley, and D. P. Schneider**. The AGN source population in the Chandra Deep Field-North Survey: constraints from X-ray spectroscopy and variability. *Astronomische Nachrichten*, 324:175–+, 2003.

[20] **J. Bechtold, A. Siemiginowska, J. Shields, B. Czerny, A. Janiuk, F. Hamann, T. L. Aldcroft, M. Elvis, and A. Dobrzycki**. Chandra Survey of Radio-quiet, High-Redshift Quasars. *ApJ*, 588:119–127, May 2003.

[21] **F. Bertola, C. S. Boschetti, S. Ciroi, E. Corbelli, E. M. Corsini, L. Danese, M. D'Onofrio, A. Marconi, A. Pizzella, P. Rafanelli, and P. Salucci**. Super-

massive black holes in the center of disk galaxies. *Memorie della Societa Astronomica Italiana*, 74:324–+, 2003.

[22] **P. R. Bevington and D. K. Robinson**. *Data reduction and error analysis for the physical sciences*. New York: McGraw-Hill, |c1992, 2nd ed., 1992.

[23] **W.-H. Bian and Y.-H. Zhao**. Black Hole-Bulge Relation for Narrow-Line Objects. *PASJ*, 55:143–148, February 2003.

[24] **A. J. Blair, G. C. Stewart, I. Georgantopoulos, B. J. Boyle, R. E. Griffiths, T. Shanks, and O. Almaini**. A deep ROSAT survey - XV. The average QSO spectrum and its evolution. *MNRAS*, 314:138–144, May 2000.

[25] **E. Boldt and D. Leiter**. Optical characteristics of young quasars as sources of the cosmic X-ray background. *ApJ*, 276:427–433, January 1984.

[26] **T. Boller, W. N. Brandt, and H. Fink**. Soft X-ray properties of narrow-line Seyfert 1 galaxies. *A&A*, 305:53–+, January 1996.

[27] **W. N. Brandt, D. M. Alexander, A. E. Hornschemeier, G. P. Garmire, D. P. Schneider, A. J. Barger, F. E. Bauer, P. S. Broos, L. L. Cowie, L. K. Townsley, D. N. Burrows, G. Chartas, E. D. Feigelson, R. E. Griffiths, J. A. Nousek, and W. L. W. Sargent**. The Chandra Deep Field North Survey. V. 1 Ms Source Catalogs. *AJ*, 122:2810–2832, December 2001.

[28] **H. et al. Brunner**. (to be submitted). *A&A*, 2007.

[29] **M. Brusa, A. Comastri, M. Mignoli, F. Fiore, P. Ciliegi, C. Vignali, P. Severgnini, F. Cocchia, F. La Franca, G. Matt, G. C. Perola, R. Maiolino, A. Baldi, and S. Molendi**. The HELLAS2XMM survey. III. Multiwavelength observations of hard X-ray selected sources in the PKS 0312-77 field. *A&A*, 409:65–78, October 2003.

[30] **A. Caccianiga, P. Severgnini, V. Braito, R. Della Ceca, T. Maccacaro, A. Wolter, X. Barcons, F. J. Carrera, I. Lehmann, M. J. Page, R. Saxton, and N. A. Webb**. The XMM-Newton HBS28 sample: Studying the obscuration in hard X-ray selected AGNs. *A&A*, 416:901–915, March 2004.

[31] **I. Cagnoni, R. della Ceca, and T. Maccacaro**. A Medium Survey of the Hard X-Ray Sky with the ASCA Gas Imaging Spectrometer: The (2–10 keV) Number Counts Relationship. *ApJ*, 493:54–+, January 1998.

[32] **S. Campana, A. Moretti, D. Lazzati, and G. Tagliaferri**. The Deepest X-Ray Look at the Universe. *ApJ*, 560:L19–L22, October 2001.

[33] **F. J. Carrera, J. Ebrero, S. Mateos, M. T. Ceballos, A. Corral, X. Barcons, M. J. Page, S. R. Rosen, M. G. Watson, J. Tedds, R. della Ceca, H. Brunner, G. Lamer, F. E. Bauer, and Y. Ueda**. The XMM-Newton serendipitous

survey IV: the AXIS X-ray source counts and angular clustering; (submitted to A&A). *A&A*, 2006.

[34] **F. J. Carrera, M. J. Page, and J. P. D. Mittaz**. XMM-Newton spectra of hard spectrum Rosat AGN: X-ray absorption and optical reddening. *A&A*, 420:163–172, June 2004.

[35] **W. Cash**. Parameter estimation in astronomy through application of the likelihood ratio. *ApJ*, 228:939–947, March 1979.

[36] **R. Cen**. The Intergalactic Medium and Soft X-Ray Background. In **S. P. Brumby**, editor, *American Institute of Physics Conference Series*, pages 58–+, 1999.

[37] **L.-W. Chen, A. C. Fabian, and K. C. Gendreau**. ASCA and ROSAT observations of the QSF3 field: the X-ray background in the 0.1-7 keV band. *MNRAS*, 285:449–471, March 1997.

[38] **L. Chevallier, S. Collin, A.-M. Dumont, B. Czerny, M. Mouchet, A. C. Gonçalves, and R. Goosmann**. The role of absorption and reflection in the soft X-ray excess of Active Galactic Nuclei. I. Preliminary results. *A&A*, 449:493–508, April 2006.

[39] **P. Ciliegi, M. Elvis, B. J. Wilkes, B. J. Boyle, and R. G. McMahon**. The Cambridge-Cambridge ROSAT Serendipity Survey - IV. The X-ray properties. *MNRAS*, 284:401–415, January 1997.

[40] **S. Collin-Souffrin**. Line and continuum radiation from the outer region of accretion discs in active galactic nuclei. I - Preliminary considerations. *A&A*, 179:60–70, June 1987.

[41] **N. R. Collins, S. B. Kraemer, D. M. Crenshaw, J. Ruiz, R. Deo, and F. C. Bruhweiler**. Physical Conditions in the Narrow-Line Region of Markarian 3. I. Observational Results. *ApJ*, 619:116–133, January 2005.

[42] **A. Comastri, M. Brusa, P. Ciliegi, M. Mignoli, C. Vignali, P. Severgnini, R. Maiolino, F. Fiore, F. La Franca, G. Matt, G. C. Perola, A. Baldi, and S. Molendi**. X-ray Bright Optically Quiet Galaxies: the Case of P3. In *ASP Conf. Ser. 258: Issues in Unification of Active Galactic Nuclei*, pages 199–+, 2002.

[43] **A. Comastri, F. Fiore, C. Vignali, G. Matt, G. C. Perola, and F. La Franca**. The BeppoSAX High Energy Large Area Survey (HELLAS) - III. Testing synthesis models for the X-ray background. *MNRAS*, 327:781–787, November 2001.

[44] **A. Comastri, G. Setti, G. Zamorani, and G. Hasinger**. The contribution of AGNs to the X-ray background. *A&A*, 296:1–+, April 1995.

[45] **A. Corral, X. Barcons, F. J. Carrera, M. T. Ceballos, and S. Mateos**. Simultaneous X-ray and optical spectroscopy of the Seyfert galaxy Mrk 993. *A&A*, 431:97–102, February 2005.

[46] **R. G. Cruddace, G. R. Hasinger, and J. H. Schmitt**. The application of a maximum likelihood analysis to detection of sources in the ROSAT data base. In **F. Murtagh and A. Heck**, editors, *Astronomy from Large Databases*, pages 177–182, 1988.

[47] **B. Czerny and M. Elvis**. Constraints on quasar accretion disks from the optical/ultraviolet/soft X-ray big bump. *ApJ*, 321:305–320, October 1987.

[48] **A. De Luca and S. Molendi**. The 2-8 keV cosmic X-ray background spectrum as observed with XMM-Newton. *A&A*, 419:837–848, June 2004.

[49] **R. Della Ceca, T. Maccacaro, A. Caccianiga, P. Severgnini, V. Braito, X. Barcons, F. J. Carrera, M. G. Watson, J. A. Tedds, H. Brunner, I. Lehmann, M. J. Page, G. Lamer, and A. Schwope**. Exploring the X-ray sky with the XMM-Newton bright serendipitous survey. *A&A*, 428:383–399, December 2004.

[50] **J. W. den Herder, A. C. Brinkman, S. M. Kahn, G. Branduardi-Raymont, K. Thomsen, H. Aarts, M. Audard, J. V. Bixler, A. J. den Boggende, J. Cottam, T. Decker, L. Dubbeldam, C. Erd, H. Goulooze, M. Güdel, P. Guttridge, C. J. Hailey, K. A. Janabi, J. S. Kaastra, P. A. J. de Korte, B. J. van Leeuwen, C. Mauche, A. J. McCalden, R. Mewe, A. Naber, F. B. Paerels, J. R. Peterson, A. P. Rasmussen, K. Rees, I. Sakelliou, M. Sako, J. Spodek, M. Stern, T. Tamura, J. Tandy, C. P. de Vries, S. Welch, and A. Zehnder**. The Reflection Grating Spectrometer on board XMM-Newton. *A&A*, 365:L7–L17, January 2001.

[51] **T. di Matteo, A. Esin, A. C. Fabian, and R. Narayan**. On the origin of the hard X-ray background. *MNRAS*, 305:L1–L5, May 1999.

[52] **J. M. Dickey and F. J. Lockman**. H I in the Galaxy. *ARA&A*, 28:215–261, 1990.

[53] **J. M. Dickey and F. J. Lockman**. H I in the Galaxy. *ARA&A*, 28:215–261, 1990.

[54] **R. A. Edelson, T. Alexander, D. M. Crenshaw, S. Kaspi, M. A. Malkan, B. M. Peterson, R. S. Warwick, J. Clavel, A. V. Filippenko, K. Horne, K. T. Korista, G. A. Kriss, J. H. Krolik, D. Maoz, K. Nandra, P. T. O'Brien, S. V. Penton, T. Yaqoob, P. Albrecht, D. Alloin, T. R. Ayres, T. J. Balonek, P. Barr, A. J. Barth, R. Bertram, G. E. Bromage, M. Carini, T. E. Carone, F.-Z. Cheng, K. K. Chuvaev, M. Dietrich, D. Dultzin-Hacyan, C. M. Gaskell, I. S. Glass, M. R. Goad, S. Hemar, L. C. Ho, J. P. Huchra, J. Hutchings, W. N. Johnson, D. Kazanas, W. Kollatschny, A. P. Koratkar, O. Kovo, A. Laor, G. M. MacAlpine, P. Magdziarz, P. G. Martin, T. Matheson, B. McCollum, H. R. Miller, S. L. Morris, V. L. Oknyanskij, J. Penfold, E. Perez, G. C. Perola, G. Pike, R. W. Pogge, R. L. Ptak, B.-C. Qian, M. C. Recondo-Gonzalez, G. A. Reichert, J. M. Rodriguez-Espinoza, P. M. Rodriguez-Pascual, E. L. Rokaki,**

J. Roland, A. C. Sadun, I. Salamanca, M. Santos-Lleo, J. C. Shields, J. M. Shull, D. A. Smith, S. M. Smith, M. A. J. Snijders, G. M. Stirpe, R. E. Stoner, W.-H. Sun, M.-H. Ulrich, E. van Groningen, R. M. Wagner, S. Wagner, I. Wanders, W. F. Welsh, R. J. Weymann, B. J. Wilkes, H. Wu, J. Wurster, S.-J. Xue, A. A. Zdziarski, W. Zheng, and Z.-L. Zou. Multiwavelength Observations of Short-Timescale Variability in NGC 4151. IV. Analysis of Multiwavelength Continuum Variability. *ApJ*, 470:364–+, October 1996.

[55] **M. Elvis**. A Structure for Quasars. *ApJ*, 545:63–76, December 2000.

[56] **M. Elvis, E. J. Schreier, J. Tonry, M. Davis, and J. P. Huchra**. Two optically dull galaxies with strong nuclear X-ray sources. *ApJ*, 246:20–27, May 1981.

[57] **A. C. Fabian**. The obscured growth of massive black holes. *MNRAS*, 308:L39–L43, October 1999.

[58] **A. C. Fabian and X. Barcons**. The origin of the X-ray background. *ARA&A*, 30:429–456, 1992.

[59] **A. C. Fabian, I. M. George, S. Miyoshi, and M. J. Rees**. Reflection-dominated hard X-ray sources and the X-ray background. *MNRAS*, 242:14P–16P, January 1990.

[60] **A. C. Fabian, M. J. Rees, L. Stella, and N. E. White**. X-ray fluorescence from the inner disc in Cygnus X-1. *MNRAS*, 238:729–736, May 1989.

[61] **H. Falcke**. The Black Hole in the Galactic Center. In **R. E. Schielicke**, editor, *Astronomische Gesellschaft Meeting Abstracts*, pages 6–+, 1999.

[62] **X. Fan, M. A. Strauss, D. P. Schneider, R. H. Becker, R. L. White, Z. Haiman, M. Gregg, L. Pentericci, E. K. Grebel, V. K. Narayanan, Y.-S. Loh, G. T. Richards, J. E. Gunn, R. H. Lupton, G. R. Knapp, Ž. Ivezić, W. N. Brandt, M. Collinge, L. Hao, D. Harbeck, F. Prada, J. Schaye, I. Strateva, N. Zakamska, S. Anderson, J. Brinkmann, N. A. Bahcall, D. Q. Lamb, S. Okamura, A. Szalay, and D. G. York**. A Survey of z>5.7 Quasars in the Sloan Digital Sky Survey. II. Discovery of Three Additional Quasars at z>6. *AJ*, 125:1649–1659, April 2003.

[63] **B. L. Fanaroff and J. M. Riley**. The morphology of extragalactic radio sources of high and low luminosity. *MNRAS*, 167:31P–36P, May 1974.

[64] **L. Ferrarese, H. C. Ford, and W. Jaffe**. Evidence for a Massive Black Hole in the Active Galaxy NGC 4261 from Hubble Space Telescope Images and Spectra. *ApJ*, 470:444–+, October 1996.

[65] **F. Fiore, F. La Franca, P. Giommi, M. Elvis, G. Matt, A. Comastri, S. Molendi, and I. Gioia**. The contribution of faint active galactic nuclei to the hard X-ray background. *MNRAS*, 306:L55–L60, July 1999.

[66] **F. Fiore, F. La Franca, C. Vignali, A. Comastri, G. Matt, G. C. Perola, M. Cappi, M. Elvis, and F. Nicastro**. Spectroscopic identification of ten faint hard X-ray sources discovered by Chandra. *New Astronomy*, 5:143–153, May 2000.

[67] **F. Fiore, A. Laor, M. Elvis, F. Nicastro, and E. Giallongo**. The Variability Properties of X-Ray-Steep and X-Ray-Flat Quasars. *ApJ*, 503:607–+, August 1998.

[68] **C. Gabriel, M. Denby, D. J. Fyfe, J. Hoar, A. Ibarra, E. Ojero, J. Osborne, R. D. Saxton, U. Lammers, and G. Vacanti**. The XMM-Newton SAS - Distributed Development and Maintenance of a Large Science Analysis System: A Critical Analysis. In *ASP Conf. Ser. 314: Astronomical Data Analysis Software and Systems (ADASS) XIII*, pages 759–+, 2004.

[69] **P. Gandhi and A. C. Fabian**. X-ray background synthesis: the infrared connection. *MNRAS*, 339:1095–1102, March 2003.

[70] **K. C. Gendreau, X. Barcons, and A. C. Fabian**. Deep hard X-ray source counts from a fluctuation analysis of ASCA SIS images. *MNRAS*, 297:41–48, June 1998.

[71] **K. C. Gendreau, R. Mushotzky, A. C. Fabian, S. S. Holt, T. Kii, P. J. Serlemitsos, Y. Ogasaka, Y. Tanaka, M. W. Bautz, Y. Fukazawa, Y. Ishisaki, Y. Kohmura, K. Makishima, M. Tashiro, Y. Tsusaka, H. Kunieda, G. R. Ricker, and R. K. Vanderspek**. ASCA Observations of the Spectrum of the X-Ray Background. *PASJ*, 47:L5–L9, April 1995.

[72] **I. Georgantopoulos, A. Georgakakis, A. Akylas, G. C. Stewart, O. Giannakis, T. Shanks, and S. Kitsionas**. The XMM-Newton/2dF survey - IV. The X-ray spectral properties of the hard sources. *MNRAS*, 352:91–100, July 2004.

[73] **I. Georgantopoulos, G. C. Stewart, A. J. Blair, T. Shanks, R. E. Griffiths, B. J. Boyle, O. Almaini, and N. Roche**. ASCA observations of deep ROSAT fields - I. The nature of the X-ray source populations. *MNRAS*, 291:203–210, October 1997.

[74] **I. Georgantopoulos, G. C. Stewart, T. Shanks, B. J. Boyle, and R. E. Griffiths**. A deep ROSAT survey - V. The extragalactic populations at faint fluxes. *MNRAS*, 280:276–284, May 1996.

[75] **I. M. George and A. C. Fabian**. X-ray reflection from cold matter in active galactic nuclei and X-ray binaries. *MNRAS*, 249:352–367, March 1991.

[76] **I. M. George, T. J. Turner, R. Mushotzky, K. Nandra, and H. Netzer**. ASCA Observations of the Ionized Gas in the Seyfert Galaxy NGC 3783. *ApJ*, 503:174–+, August 1998.

[77] **A. M. Ghez**. The Supermassive Black Hole at the Center of the Milky Way. In **L. C. Ho**, editor, *Coevolution of Black Holes and Galaxies*, pages 53–+, 2004.

[78] **R. Giacconi, J. Bechtold, G. Branduardi, W. Forman, J. P. Henry, C. Jones, E. Kellogg, H. van der Laan, W. Liller, H. Marshall, S. S. Murray, J. Pye, E. Schreier, W. L. W. Sargent, F. Seward, and H. Tananbaum**. A high-sensitivity X-ray survey using the Einstein Observatory and the discrete source contribution to the extragalactic X-ray background. *ApJ*, 234:L1–L7, November 1979.

[79] **R. Giacconi, H. Gursky, F. R. Paolini, and B. B. Rossi**. Evidence for X-rays from sources outside the Solar System. *Phys. Rev. Lett.*, 9:439–443, December 1962.

[80] **R. Giacconi, P. Rosati, P. Tozzi, M. Nonino, G. Hasinger, C. Norman, J. Bergeron, S. Borgani, R. Gilli, R. Gilmozzi, and W. Zheng**. First Results from the X-Ray and Optical Survey of the Chandra Deep Field South. *ApJ*, 551:624–634, April 2001.

[81] **R. Giacconi, A. Zirm, J. Wang, P. Rosati, M. Nonino, P. Tozzi, R. Gilli, V. Mainieri, G. Hasinger, L. Kewley, J. Bergeron, S. Borgani, R. Gilmozzi, N. Grogin, A. Koekemoer, E. Schreier, W. Zheng, and C. Norman**. Chandra Deep Field South: The 1 Ms Catalog. *ApJS*, 139:369–410, April 2002.

[82] **M. Gierliński and C. Done**. Is the soft excess in active galactic nuclei real? *MNRAS*, 349:L7–L11, March 2004.

[83] **R. Gilli**. The X-ray background and the deep X-ray surveys. *Advances in Space Research*, 34:2470–2477, 2004.

[84] **R. Gilli, M. Salvati, and G. Hasinger**. Testing current synthesis models of the X-ray background. *A&A*, 366:407–417, February 2001.

[85] **P. Gondoin, B. Aschenbach, C. Erd, D. H. Lumb, S. Majerowicz, D. Neumann, and J. L. Sauvageot**. In-orbit calibration of the XMM-Newton telescopes. In *Proc. SPIE Vol. 4140, p. 1-12, X-Ray and Gamma-Ray Instrumentation for Astronomy XI, Kathryn A. Flanagan; Oswald H. Siegmund; Eds.*, pages 1–12, December 2000.

[86] **R. W. Goodrich, S. Veilleux, and G. J. Hill**. Infrared spectroscopy of Seyfert 2 galaxies: A look through the obscuring Torus? *ApJ*, 422:521–536, February 1994.

[87] **G. L. Granato and L. Danese**. Thick Tori around Active Galactic Nuclei - a Comparison of Model Predictions with Observations of the Infrared Continuum and Silicate Features. *MNRAS*, 268:235–+, May 1994.

[88] **G. L. Granato, L. Danese, and A. Franceschini**. Thick Tori around Active Galactic Nuclei: The Case for Extended Tori and Consequences for Their X-Ray and Infrared Emission. *ApJ*, 486:147–+, September 1997.

[89] **P. Grandi, G. Tagliaferri, P. Giommi, P. Barr, and G. G. C. Palumbo**. X-ray luminosity and spectral variability of hard X-ray-selected active galactic nuclei. *ApJS*, 82:93–116, September 1992.

[90] **A. R. Green, I. M. McHardy, and H. J. Lehto**. On the nature of rapid X-ray variability in active galactic nuclei. *MNRAS*, 265:664–+, December 1993.

[91] **P. J. Green, J. D. Silverman, R. A. Cameron, D.-W. Kim, B. J. Wilkes, W. A. Barkhouse, A. LaCluyzé, D. Morris, A. Mossman, H. Ghosh, J. P. Grimes, B. T. Jannuzi, H. Tananbaum, T. L. Aldcroft, J. A. Baldwin, F. H. Chaffee, A. Dey, A. Dosaj, N. R. Evans, X. Fan, C. Foltz, T. Gaetz, E. J. Hooper, V. L. Kashyap, S. Mathur, M. B. McGarry, E. Romero-Colmenero, M. G. Smith, P. S. Smith, R. C. Smith, G. Torres, A. Vikhlinin, and D. R. Wik**. The Chandra Multiwavelength Project: Optical Follow-up of Serendipitous Chandra Sources. *ApJS*, 150:43–71, January 2004.

[92] **R. E. Griffiths, I. Georgantopoulos, B. J. Boyle, G. C. Stewart, T. Shanks, and R. della Ceca**. A ROSAT deep survey - VI. Active and passive X-ray galaxies. *MNRAS*, 275:77–88, July 1995.

[93] **R. E. Griffiths, T. Miyaji, and A. Knudson**. Galaxies at the detection limits of deep X-ray surveys. *Advances in Space Research*, 34:2486–2491, 2004.

[94] **R. E. Griffiths, S. S. Murray, R. Giacconi, J. Bechtold, P. Murdin, M. Smith, H. T. MacGillivray, M. Ward, J. Danziger, J. Lub, B. A. Peterson, A. E. Wright, M. J. Batty, D. L. Jauncey, and D. F. Malin**. The optical identification content of the Einstein Observatory deep X-ray survey of a region in Pavo. *ApJ*, 269:375–386, June 1983.

[95] **D. E. Gruber**. The Hard X-Ray Background. In **X. Barcons and A. C. Fabian**, editors, *The X-ray Background*, pages 44–+, 1992.

[96] **D. E. Gruber, J. L. Matteson, L. E. Peterson, and G. V. Jung**. The Spectrum of Diffuse Cosmic Hard X-Rays Measured with HEAO 1. *ApJ*, 520:124–129, July 1999.

[97] **D. Grupe, S. Mathur, B. Wilkes, and P. Osmer**. XMM-Newton Observations of High-Redshift Quasars. *AJ*, 131:55–69, January 2006.

[98] **M. Guainazzi, G. C. Perola, G. Matt, F. Nicastro, L. Bassani, F. Fiore, D. dal Fiume, and L. Piro**. The complex 0.1-200 keV spectrum of the Seyfert 1 Galaxy NGC 4593. *A&A*, 346:407–414, June 1999.

[99] **P. W. Guilbert and M. J. Rees**. 'Cold' material in non-thermal sources. *MNRAS*, 233:475–484, July 1988.

[100] **F. Haardt and L. Maraschi**. A two-phase model for the X-ray emission from Seyfert galaxies. *ApJ*, 380:L51–L54, October 1991.

[101] **F. Haardt and L. Maraschi**. X-ray spectra from two-phase accretion disks. *ApJ*, 413:507–517, August 1993.

[102] **F. Haardt, L. Maraschi, and G. Ghisellini**. X-Ray Variability and Correlations in the Two-Phase Disk-Corona Model for Seyfert Galaxies. *ApJ*, 476:620–+, February 1997.

[103] **T. T. Hamilton, D. J. Helfand, and X. Wu**. Faint X-ray source counts and the origin of the X-ray background. *ApJ*, 379:576–585, October 1991.

[104] **G. Hasinger**. ROSAT Deep Surveys. In **X. Barcons and A. C. Fabian**, editors, *The X-ray Background*, pages 229–+, 1992.

[105] **G. Hasinger**. ROSAT deep surveys. *Advances in Space Research*, 13:241–, December 1993.

[106] **G. Hasinger, B. Altieri, M. Arnaud, X. Barcons, J. Bergeron, H. Brunner, M. Dadina, K. Dennerl, P. Ferrando, A. Finoguenov, R. E. Griffiths, Y. Hashimoto, F. A. Jansen, D. H. Lumb, K. O. Mason, S. Mateos, R. G. McMahon, T. Miyaji, F. Paerels, M. J. Page, A. F. Ptak, T. P. Sasseen, N. Schartel, G. P. Szokoly, J. Trümper, M. Turner, R. S. Warwick, and M. G. Watson**. XMM-Newton observation of the Lockman Hole. I. The X-ray data. *A&A*, 365:L45–L50, January 2001.

[107] **G. Hasinger, R. Burg, R. Giacconi, M. Schmidt, J. Trumper, and G. Zamorani**. The ROSAT Deep Survey. I. X-ray sources in the Lockman Field. *A&A*, 329:482–494, January 1998.

[108] **S. S. Holt, R. F. Mushotzky, E. A. Boldt, P. J. Serlemitsos, R. H. Becker, A. E. Szymkowiak, and N. E. White**. X-ray spectral constraints on the broad-line cloud geometry of NGC 4151. *ApJ*, 241:L13–L17, October 1980.

[109] **A. E. Hornschemeier, F. E. Bauer, D. M. Alexander, W. N. Brandt, W. L. W. Sargent, C. Vignali, G. P. Garmire, and D. P. Schneider**. The weak outnumbering the mighty: normal galaxies in deep Chandra surveys. *Astronomische Nachrichten*, 324:12–15, 2003.

[110] **A. E. Hornschemeier, W. N. Brandt, G. P. Garmire, D. P. Schneider, A. J. Barger, P. S. Broos, L. L. Cowie, L. K. Townsley, M. W. Bautz, D. N. Burrows, G. Chartas, E. D. Feigelson, R. E. Griffiths, D. Lumb, J. A. Nousek, L. W. Ramsey, and W. L. W. Sargent**. The Chandra Deep Survey of the Hubble Deep Field-North Area. II. Results from the Caltech Faint Field Galaxy Redshift Survey Area. *ApJ*, 554:742–777, June 2001.

[111] **A. E. Hornschemeier, W. N. Brandt, G. P. Garmire, D. P. Schneider, P. S. Broos, L. K. Townsley, M. W. Bautz, D. N. Burrows, G. Chartas, E. D. Feigelson, R. Griffiths, D. Lumb, J. A. Nousek, and W. L. W. Sargent**. X-Ray Sources in the Hubble Deep Field Detected by Chandra. *ApJ*, 541:49–53, September 2000.

[112] **Y. Ishisaki, Y. Ueda, A. Yamashita, T. Ohashi, I. Lehmann, and G. Hasinger**. ASCA Deep Survey in the Lockman Hole Field. *PASJ*, 53:445–457, June 2001.

[113] **F. Jansen, D. Lumb, B. Altieri, J. Clavel, M. Ehle, C. Erd, C. Gabriel, M. Guainazzi, P. Gondoin, R. Much, R. Munoz, M. Santos, N. Schartel, D. Texier, and G. Vacanti**. XMM-Newton observatory. I. The spacecraft and operations. *A&A*, 365:L1–L6, January 2001.

[114] **J. S. Kaastra, K. C. Steenbrugge, A. J. J. Raassen, R. L. J. van der Meer, A. C. Brinkman, D. A. Liedahl, E. Behar, and A. de Rosa**. X-ray spectroscopy of NGC 5548. *A&A*, 386:427–445, May 2002.

[115] **S. Kaspi, W. N. Brandt, H. Netzer, I. M. George, G. Chartas, E. Behar, R. M. Sambruna, G. P. Garmire, and J. A. Nousek**. High-Resolution X-Ray Spectroscopy and Modeling of the Absorbing and Emitting Outflow in NGC 3783. *ApJ*, 554:216–232, June 2001.

[116] **E. Kendziorra, E. Bihler, W. Grubmiller, B. Kretschmar, M. Kuster, B. Pflueger, R. Staubert, H. W. Braeuninger, U. G. Briel, N. Meidinger, E. Pfeffermann, C. Reppin, D. Stoetter, L. Strueder, P. Holl, J. Kemmer, H. Soltau, and C. von Zanthier**. PN-CCD camera for XMM: performance of high time resolution/bright source operating modes. In *Proc. SPIE Vol. 3114, p. 155-165, EUV, X-Ray, and Gamma-Ray Instrumentation for Astronomy VIII, Oswald H. Siegmund; Mark A. Gummin; Eds.*, pages 155–165, October 1997.

[117] **E. Kendziorra, M. Colli, M. Kuster, R. Staubert, N. Meidinger, and E. Pfeffermann**. Operational aspects of the pn-CCD camera for XMM and ABRIXAS. In *Proc. SPIE Vol. 3765, p. 204-214, EUV, X-Ray, and Gamma-Ray Instrumentation for Astronomy X, Oswald H. Siegmund; Kathryn A. Flanagan; Eds.*, pages 204–214, October 1999.

[118] **R. L. Kinzer, G. V. Jung, D. E. Gruber, J. L. Matteson, and L. E. Peterson**. Diffuse Cosmic Gamma Radiation Measured by HEAO 1. *ApJ*, 475:361–+, January 1997.

[119] **M. G. F. Kirsch, B. Altieri, B. Chen, F. Haberl, L. Metcalfe, A. M. Pollock, A. M. Read, R. D. Saxton, S. Sembay, and M. J. Smith**. XMM-Newton (cross)-calibration. In **G. Hasinger and M. J. L. Turner**, editors, *Proceedings of the SPIE, Volume 5488, pp. 103-114 (2004).*, pages 103–114, October 2004.

[120] **J. Kormendy and D. Richstone**. Inward Bound—The Search For Supermassive Black Holes In Galactic Nuclei. *ARA&A*, 33:581–+, 1995.

[121] **R. Krivonos, A. Vikhlinin, E. Churazov, A. Lutovinov, S. Molkov, and R. Sunyaev**. Extragalactic Source Counts in the 20-50 keV Energy Band from the Deep Observation of the Coma Region by INTEGRAL IBIS. *ApJ*, 625:89–94, May 2005.

[122] **J. H. Krolik and M. C. Begelman**. Molecular tori in Seyfert galaxies - Feeding the monster and hiding it. *ApJ*, 329:702–711, June 1988.

[123] **A. Kushino, Y. Ishisaki, U. Morita, N. Y. Yamasaki, M. Ishida, T. Ohashi, and Y. Ueda**. Study of the X-Ray Background Spectrum and Its Large-Scale Fluctuation with ASCA. *PASJ*, 54:327–352, June 2002.

[124] **M. Kuster, S. Benlloch, E. Kendziorra, and U. G. Briel**. Time resolution capability of the XMM EPIC pn-CCD in different readout modes. In *Proc. SPIE Vol. 3765, p. 673-682, EUV, X-Ray, and Gamma-Ray Instrumentation for Astronomy X, Oswald H. Siegmund; Kathryn A. Flanagan; Eds.*, pages 673–682, October 1999.

[125] **A. Laor**. Massive Thin Accretion Discs - Part Three - Comparison with the Observations. *MNRAS*, 246:369–+, October 1990.

[126] **A. Laor**. Line profiles from a disk around a rotating black hole. *ApJ*, 376:90–94, July 1991.

[127] **A. Laor and H. Netzer**. Massive thin accretion discs. I - Calculated spectra. *MNRAS*, 238:897–916, June 1989.

[128] **A. Lawrence and I. Papadakis**. X-ray variability of active galactic nuclei - A universal power spectrum with luminosity-dependent amplitude. *ApJ*, 414:L85–L88, September 1993.

[129] **I. Lehmann, G. Hasinger, H. Boehringer, H. Brunner, M. Brusa, A. Comastri, M. Elvis, A. Finoguenov, F. Fiore, A. Franceschini, R. Gilli, R. Griffiths, C. D. Impey, O. Le Fevre, S. Lilly, V. Mainieri, G. Matt, I. Matute, T. Miyaji, S. Molendi, S. Paltani, D. Sanders, N. Scoville, L. Tresse, M. Urry, G. Vettolani, and G. Zamorani**. Evolution of AGN in the cosmic web: The XMM-Newton Cosmos Survey. *American Astronomical Society Meeting Abstracts*, 205:–+, December 2004.

[130] **I. Lehmann, G. Hasinger, M. Schmidt, R. Giacconi, J. Trümper, G. Zamorani, J. E. Gunn, L. Pozzetti, D. P. Schneider, T. Stanke, G. Szokoly, D. Thompson, and G. Wilson**. The ROSAT Deep Survey. VI. X-ray sources and Optical identifications of the Ultra Deep Survey. *A&A*, 371:833–857, June 2001.

[131] **K. M. Leighly**. A Comprehensive Spectral and Variability Study of Narrow-Line Seyfert 1 Galaxies Observed by ASCA. I. Observations and Time Series Analysis. *ApJS*, 125:297–316, December 1999.

[132] **A. P. Lightman and T. R. White**. Effects of cold matter in active galactic nuclei - A broad hump in the X-ray spectra. *ApJ*, 335:57–66, December 1988.

[133] **F. J. Lockman, K. Jahoda, and D. McCammon**. The structure of galactic HI in directions of low total column density. *ApJ*, 302:432–449, March 1986.

[134] **M. S. Longair**. *High energy astrophysics. Vol.1: Particles, photons and their detection.* High Energy Astrophysics, by Malcolm S. Longair, pp. 436. ISBN 0521387736. Cambridge, UK: Cambridge University Press, March 1992., March 1992.

[135] **D. H. Lumb, R. S. Warwick, M. Page, and A. De Luca**. X-ray background measurements with XMM-Newton EPIC. *A&A*, 389:93–105, July 2002.

[136] **S. L. Lumsden and D. M. Alexander**. The infrared luminosity of the torus and the visibility of scattered broad line emission in Seyfert 2 galaxies. *MNRAS*, 328:L32–L36, December 2001.

[137] **Y. E. Lyubarskii**. Flicker noise in accretion discs. *MNRAS*, 292:679–+, December 1997.

[138] **T. Maccacaro, I. M. Gioia, A. Wolter, G. Zamorani, and J. T. Stocke**. The X-ray spectra of the extragalactic sources in the Einstein extended medium sensitivity survey. *ApJ*, 326:680–690, March 1988.

[139] **P. Madau, G. Ghisellini, and A. C. Fabian**. The Unified Seyfert Scheme and the Origin of the Cosmic X-Ray Background. *MNRAS*, 270:L17+, September 1994.

[140] **V. Mainieri, J. Bergeron, G. Hasinger, I. Lehmann, P. Rosati, M. Schmidt, G. Szokoly, and R. Della Ceca**. XMM-Newton observation of the Lockman Hole. II. Spectral analysis. *A&A*, 393:425–438, October 2002.

[141] **R. Maiolino, A. Comastri, R. Gilli, N. M. Nagar, S. Bianchi, T. Böker, E. Colbert, A. Krabbe, A. Marconi, G. Matt, and M. Salvati**. Elusive active galactic nuclei. *MNRAS*, 344:L59–L64, October 2003.

[142] **R. Maiolino, A. Marconi, and E. Oliva**. Dust in active nuclei. II. Powder or gravel? *A&A*, 365:37–48, January 2001.

[143] **R. Maiolino and G. H. Rieke**. Low-Luminosity and Obscured Seyfert Nuclei in Nearby Galaxies. *ApJ*, 454:95–+, November 1995.

[144] **A. Malizia, L. Bassani, J. B. Stephen, G. Malaguti, and G. G. C. Palumbo**. High-Energy Spectra of Active Galactic Nuclei. II. Absorption in Seyfert Galaxies. *ApJS*, 113:311–+, December 1997.

[145] **M. A. Malkan and W. L. W. Sargent**. The ultraviolet excess of Seyfert 1 galaxies and quasars. *ApJ*, 254:22–37, March 1982.

[146] **J. Manners, O. Almaini, and A. Lawrence**. The X-ray variability of high-redshift QSOs. *MNRAS*, 330:390–398, February 2002.

[147] **A. Markowitz and R. Edelson**. An RXTE Survey of Long-Term X-Ray Variability in Seyfert 1 Galaxies. *ApJ*, 547:684–692, February 2001.

[148] **A. Markowitz and R. Edelson**. An Expanded Rossi X-Ray Timing Explorer Survey of X-Ray Variability in Seyfert 1 Galaxies. *ApJ*, 617:939–965, December 2004.

[149] **A. Markowitz, R. Edelson, and S. Vaughan**. Long-Term X-Ray Spectral Variability in Seyfert 1 Galaxies. *ApJ*, 598:935–955, December 2003.

[150] **F. E. Marshall, E. A. Boldt, S. S. Holt, R. B. Miller, R. F. Mushotzky, L. A. Rose, R. E. Rothschild, and P. J. Serlemitsos**. The diffuse X-ray background spectrum from 3 to 50 keV. *ApJ*, 235:4–10, January 1980.

[151] **N. Marshall, R. S. Warwick, and K. A. Pounds**. The variability of X-ray emission from active galaxies. *MNRAS*, 194:987–1002, March 1981.

[152] **S. Mateos, X. Barcons, F. J. Carrera, M. T. Ceballos, A. Caccianiga, G. Lamer, T. Maccacaro, M. J. Page, A. Schwope, and M. G. Watson**. X-ray spectra of XMM-Newton serendipitous medium flux sources. *A&A*, 2005.

[153] **S. Mateos, X. Barcons, F. J. Carrera, M. T. Ceballos, G. Hasinger, I. Lehmann, A. C. Fabian, and A. Streblyanska**. XMM-Newton observations of the Lockman Hole IV: spectra of the brightest AGN. *A&A*, 2005.

[154] **J. C. Mather, E. S. Cheng, D. A. Cottingham, R. E. Eplee, D. J. Fixsen, T. Hewagama, R. B. Isaacman, K. A. Jensen, S. S. Meyer, P. D. Noerdlinger, S. M. Read, L. P. Rosen, R. A. Shafer, E. L. Wright, C. L. Bennett, N. W. Boggess, M. G. Hauser, T. Kelsall, S. H. Moseley, R. F. Silverberg, G. F. Smoot, R. Weiss, and D. T. Wilkinson**. Measurement of the cosmic microwave background spectrum by the COBE FIRAS instrument. *ApJ*, 420:439–444, January 1994.

[155] **G. Matt and A. C. Fabian**. Spectral Constraints on SEYFERT-2 Galaxies as Major Contributors to the Hard 3-100-KEV X-Ray Background. *MNRAS*, 267:187–+, March 1994.

[156] **G. Matt, G. C. Perola, and L. Piro**. The iron line and high energy bump as X-ray signatures of cold matter in Seyfert 1 galaxies. *A&A*, 247:25–34, July 1991.

[157] **G. Matt, G. C. Perola, L. Piro, and L. Stella**. Iron K-alpha line from X-ray illuminated relativistic disks. *A&A*, 257:63–68, April 1992.

[158] **D. McCammon and W. T. Sanders**. The soft X-ray background and its origins. *ARA&A*, 28:657–688, 1990.

[159] **J.E. McClintock and R.A. Remillard**. *Black hole binaries.* In Compact Stellar X-ray Sources, Edited by Walter Lewin and Michiel van der Klis, pp. 157-214. ISBN-13: 9780521826594, ISBN-10: 0521826594. Cambridge, UK: Cambridge University Press, April 2006., 2006.

[160] **I. M. McHardy, L. R. Jones, M. R. Merrifield, K. O. Mason, A. M. Newsam, R. G. Abraham, G. B. Dalton, F. Carrera, P. J. Smith, M. Rowan-Robinson, G. A. Wegner, T. J. Ponman, H. J. Lehto, G. Branduardi-Raymont, G. A. Luppino, G. Efstathiou, D. J. Allan, and J. J. Quenby**. The origin of the cosmic soft X-ray background - Optical identification of an extremely deep ROSAT survey. *MNRAS*, 295:641–+, April 1998.

[161] **J. P. D. Mittaz, F. J. Carrera, E. Romero-Colmenero, K. O. Mason, G. Hasinger, R. McMahon, H. Andernach, R. Bower, J. Burgos-Martin, J. I. González-Serrano, and D. Wonnacott**. X-ray spectra of the RIXOS source sample. *MNRAS*, 308:233–256, September 1999.

[162] **T. Miyaji and R. E. Griffiths**. Faint-Source Counts from Off-Source Fluctuation Analysis on Chandra Observations of the Hubble Deep Field-North. *ApJ*, 564:L5–L8, January 2002.

[163] **T. Miyaji, G. Hasinger, and M. Schmidt**. Soft X-ray AGN luminosity function from it ROSAT surveys. I. Cosmological evolution and contribution to the soft X-ray background. *A&A*, 353:25–40, January 2000.

[164] **T. Miyaji, G. Hasinger, and M. Schmidt**. Soft X-ray AGN luminosity function from ROSAT surveys. II. Table of the binned soft X-ray luminosity function. *A&A*, 369:49–56, April 2001.

[165] **T. Miyaji, Y. Ishisaki, Y. Ogasaka, Y. Ueda, M. J. Freyberg, G. Hasinger, and Y. Tanaka**. The cosmic X-ray background spectrum observed with ROSAT and ASCA. *A&A*, 334:L13–L16, June 1998.

[166] **E. C. Moran, A. V. Filippenko, and R. Chornock**. "Hidden" Seyfert 2 Galaxies and the X-Ray Background. *ApJ*, 579:L71–L74, November 2002.

[167] **A. Moretti, S. Campana, D. Lazzati, and G. Tagliaferri**. The Resolved Fraction of the Cosmic X-Ray Background. *ApJ*, 588:696–703, May 2003.

[168] **R. Morrison and D. McCammon**. Interstellar photoelectric absorption cross sections, 0.03-10 keV. *ApJ*, 270:119–122, July 1983.

[169] **R. F. Mushotzky**. The X-ray spectrum and time variability of narrow emission line galaxies. *ApJ*, 256:92–102, May 1982.

[170] **R. F. Mushotzky, L. L. Cowie, A. J. Barger, and K. A. Arnaud**. Resolving the extragalactic hard X-ray background. *Nature*, 404:459–464, March 2000.

[171] **R. F. Mushotzky, C. Done, and K. A. Pounds**. X-ray spectra and time variability of active galactic nuclei. *ARA&A*, 31:717–761, 1993.

[172] **K. Nandra, J. Clavel, R. A. Edelson, I. M. George, M. A. Malkan, R. F. Mushotzky, B. M. Peterson, and T. J. Turner**. New Constraints on the

Continuum Emission Mechanism of Active Galactic Nuclei: Intensive Monitoring of NGC 7469 in the X-Ray and Ultraviolet. *ApJ*, 505:594–606, October 1998.

[173] **K. Nandra, I. M. George, R. F. Mushotzky, T. J. Turner, and T. Yaqoob**. ASCA Observations of Seyfert 1 Galaxies. II. Relativistic Iron K alpha Emission. *ApJ*, 477:602–+, March 1997.

[174] **K. Nandra and K. A. Pounds**. GINGA Observations of the X-Ray Spectra of Seyfert Galaxies. *MNRAS*, 268:405–+, May 1994.

[175] **K. Nandra, K. A. Pounds, G. C. Stewart, I. M. George, K. Hayashida, F. Makino, and T. Ohashi**. Compton reflection and the variable X-ray spectrum of NGC 5548. *MNRAS*, 248:760–772, February 1991.

[176] **F. Nicastro, L. Piro, A. De Rosa, M. Feroci, P. Grandi, F. Fiore, M. Elvis, F. Haardt, J. Kaastra, A. Malizia, L. Maraschi, G. Matt, G. C. Perola, and P. O. Petrucci**. A Long Observation of NGC 5548 by BeppoSAX: The High-Energy Cutoff, Intrinsic Spectral Variability, and a Truly Warm Absorber. *ApJ*, 536:718–728, June 2000.

[177] **F. Nicastro, A. Zezas, J. Drake, M. Elvis, F. Fiore, A. Fruscione, M. Marengo, S. Mathur, and S. Bianchi**. Chandra Discovery of a Tree in the X-Ray Forest toward PKS 2155-304: The Local Filament? *ApJ*, 573:157–167, July 2002.

[178] **D. E. Osterbrock**. *Astrophysics of gaseous nebulae and active galactic nuclei.* Research supported by the University of California, John Simon Guggenheim Memorial Foundation, University of Minnesota, et al. Mill Valley, CA, University Science Books, 1989, 422 p., 1989.

[179] **D. E. Osterbrock and R. W. Pogge**. The spectra of narrow-line Seyfert 1 galaxies. *ApJ*, 297:166–176, October 1985.

[180] **M. J. Page, I. M. McHardy, K. F. Gunn, N. S. Loaring, K. O. Mason, T. Sasseen, A. Newsam, A. Ware, J. Kennea, K. Sekiguchi, and T. Takata**. X-ray and optical properties of X-ray sources in the 13hr XMM-Newton/Chandra deep survey. *Astronomische Nachrichten*, 324:101–104, 2003.

[181] **F. Panessa and L. Bassani**. Unabsorbed Seyfert 2 galaxies. *A&A*, 394:435–442, November 2002.

[182] **M. Paolillo, E. J. Schreier, R. Giacconi, A. M. Koekemoer, and N. A. Grogin**. Prevalence of X-Ray Variability in the Chandra Deep Field-South. *ApJ*, 611:93–106, August 2004.

[183] **A. Pappa, I. Georgantopoulos, G. C. Stewart, and A. L. Zezas**. The X-ray spectra of optically selected Seyfert 2 galaxies: are there any Seyfert 2 galaxies with no absorption? *MNRAS*, 326:995–1006, September 2001.

[184] **G. C. Perola, G. Matt, M. Cappi, D. Dal Fiume, F. Fiore, M. Guainazzi, T. Mineo, S. Molendi, F. Nicastro, L. Piro, and G. Stirpe**. X-ray spectral components from a broad band BeppoSAX observation of the Seyfert galaxy IC 4329A. *A&A*, 351:937–944, November 1999.

[185] **G. C. Perola, G. Matt, F. Fiore, P. Grandi, M. Guainazzi, F. Haardt, L. Maraschi, T. Mineo, F. Nicastro, and L. Piro**. BeppoSAX observations of Mrk 509 and MCG +8-11-11. *A&A*, 358:117–124, June 2000.

[186] **G. C. Perola, L. Piro, A. Altamore, F. Fiore, A. Boksenberg, M. V. Penston, M. A. J. Snijders, G. E. Bromage, J. Clavel, A. Elvius, and M. H. Ulrich**. New results on the X-ray emission and its correlation with the ultraviolet in NGC 4151. *ApJ*, 306:508–521, July 1986.

[187] **G. C. Perola, S. Puccetti, F. Fiore, N. Sacchi, M. Brusa, F. Cocchia, A. Baldi, N. Carangelo, P. Ciliegi, A. Comastri, F. La Franca, R. Maiolino, G. Matt, M. Mignoli, S. Molendi, and C. Vignali**. The HELLAS2XMM survey. VI. X-ray absorption in the 1df AGN sample through a spectral analysis. *A&A*, 421:491–501, July 2004.

[188] **B. M. Peterson**. Variability of Active Galactic Nuclei. In *Advanced Lectures on the Starburst-AGN*, pages 3–+, 2001.

[189] **E. Piconcelli, M. Cappi, L. Bassani, G. Di Cocco, and M. Dadina**. An XMM-Newton study of the hard X-ray sky. *A&A*, 412:689–705, December 2003.

[190] **E. Piconcelli, M. Cappi, L. Bassani, F. Fiore, G. Di Cocco, and J. B. Stephen**. Exploring the spectral properties of faint hard X-ray sources with XMM-Newton. *A&A*, 394:835–849, November 2002.

[191] **E. A. Pier and J. H. Krolik**. Radiation-pressure-supported obscuring tori around active galactic nuclei. *ApJ*, 399:L23–L26, November 1992.

[192] **E. A. Pier and J. H. Krolik**. Infrared Spectra of Obscuring Dust Tori around Active Galactic Nuclei. II. Comparison with Observations. *ApJ*, 418:673–+, December 1993.

[193] **F. Pompilio, F. La Franca, and G. Matt**. The X-ray background and the evolution of AGN. *A&A*, 353:440–446, January 2000.

[194] **D. Porquet, J. N. Reeves, P. O'Brien, and W. Brinkmann**. XMM-Newton EPIC observations of 21 low-redshift PG quasars. *A&A*, 422:85–95, July 2004.

[195] **K. A. Pounds, K. Nandra, G. C. Stewart, I. M. George, and A. C. Fabian**. X-ray reflection from cold matter in the nuclei of active galaxies. *Nature*, 344:132–+, March 1990.

[196] **K. A. Pounds, R. S. Warwick, J. L. Culhane, and P. A. J. de Korte**. The soft X-ray spectrum of NGC 4151. *MNRAS*, 218:685–694, February 1986.

[197] **W. H. Press, S. A. Teukolsky, W. T. Vetterling, and B. P. Flannery**. *Numerical recipes in FORTRAN. The art of scientific computing.* Cambridge: University Press, |c1992, 2nd ed., 1992.

[198] **F. A. Primini, S. S. Murray, J. Huchra, R. Schild, R. Burg, and R. Giacconi**. The CfA Einstein Observatory extended deep X-ray survey. *ApJ*, 374:440–455, June 1991.

[199] **R. Protassov, D. A. van Dyk, A. Connors, V. L. Kashyap, and A. Siemiginowska**. Statistics, Handle with Care: Detecting Multiple Model Components with the Likelihood Ratio Test. *ApJ*, 571:545–559, May 2002.

[200] **E. M. Puchnarewicz, K. O. Mason, F. A. Cordova, J. Kartje, A. A. Brabduardi, E. M. Puchnarewicz, K. O. Mason, F. A. Cordova, J. Kartje, G. Branduardi-Raymont, J. P. D. Mittaz, P. G. Murdin, and J. Allington-Smith**. Optical properties of active galaxies with ultra-soft X-ray spectra. *MNRAS*, 256:589–623, June 1992.

[201] **A. Rasmussen, S. M. Kahn, F. Paerels, J. den Herder, and C. de Vries**. Observational limits to highly ionized absorption systems in the intergalactic medium for z below 0.15. *AAS/High Energy Astrophysics Division*, 7:–+, March 2003.

[202] **J. Reeves**. XMM-Newton Observations of AGN Iron Line profiles. In **S. Collin, F. Combes, and I. Shlosman**, editors, *ASP Conf. Ser. 290: Active Galactic Nuclei: From Central Engine to Host Galaxy*, pages 35–+, 2003.

[203] **M. Revnivtsev, M. Gilfanov, R. Sunyaev, K. Jahoda, and C. Markwardt**. The spectrum of the cosmic X-ray background observed by RTXE/PCA. *A&A*, 411:329–334, December 2003.

[204] **C. S. Reynolds**. An X-ray spectral study of 24 type 1 active galactic nuclei. *MNRAS*, 286:513–537, April 1997.

[205] **G. Risaliti and M. Elvis**. *A Panchromatic View of AGN*, pages 187–+. ASSL Vol. 308: Supermassive Black Holes in the Distant Universe, August 2004.

[206] **G. Risaliti, M. Elvis, and F. Nicastro**. Ubiquitous Variability of X-Ray-absorbing Column Densities in Seyfert 2 Galaxies. *ApJ*, 571:234–246, May 2002.

[207] **G. Risaliti, R. Maiolino, and M. Salvati**. The Distribution of Absorbing Column Densities among Seyfert 2 Galaxies. *ApJ*, 522:157–164, September 1999.

[208] **H.-W. Rix, G. Rieke, M. Rieke, and N. P. Carleton**. Probing intermediate Seyfert galaxies by Pa(beta) spectroscopy. *ApJ*, 363:480–487, November 1990.

[209] **E. Romero-Colmenero, G. Branduardi-Raymont, F. J. Carrera, L. R. Jones, K. O. Mason, I. M. McHardy, and J. P. D. Mittaz**. ROSAT PSPC spectra of X-ray-selected narrow-emission-line galaxies. *MNRAS*, 282:94–98, September 1996.

[210] **P. Rosati, P. Tozzi, R. Giacconi, R. Gilli, G. Hasinger, L. Kewley, V. Mainieri, M. Nonino, C. Norman, G. Szokoly, J. X. Wang, A. Zirm, J. Bergeron, S. Borgani, R. Gilmozzi, N. Grogin, A. Koekemoer, E. Schreier, and W. Zheng**. The Chandra Deep Field-South: The 1 Million Second Exposure. *ApJ*, 566:667–674, February 2002.

[211] **R. R. Ross and A. C. Fabian**. The effects of photoionization on X-ray reflection spectra in active galactic nuclei. *MNRAS*, 261:74–82, March 1993.

[212] **R. R. Ross, A. C. Fabian, and S. Mineshige**. The spectra of accretion discs in active galactic nuclei. *MNRAS*, 258:189–197, September 1992.

[213] **M. Ruiz, G. H. Rieke, and J. D. Sheilds**. Near-Infrared Spectroscopy of Seyfert Galaxies. *Bulletin of the American Astronomical Society*, 26:1356–+, December 1994.

[214] **D. B. Sanders, E. S. Phinney, G. Neugebauer, B. T. Soifer, and K. Matthews**. Continuum energy distribution of quasars - Shapes and origins. *ApJ*, 347:29–51, December 1989.

[215] **P. A. G. Scheuer**. Fluctuations in the X-ray background. *MNRAS*, 166:329–338, February 1974.

[216] **M. Schmidt, G. Hasinger, J. Gunn, D. Schneider, R. Burg, R. Giacconi, I. Lehmann, J. MacKenty, J. Trumper, and G. Zamorani**. The ROSAT deep survey. II. Optical identification, photometry and spectra of X-ray sources in the Lockman field. *A&A*, 329:495–503, January 1998.

[217] **G. Setti and L. Woltjer**. Active Galactic Nuclei and the spectrum of the X-ray background. *A&A*, 224:L21–L23, October 1989.

[218] **P. Severgnini, A. Caccianiga, V. Braito, R. Della Ceca, T. Maccacaro, A. Wolter, K. Sekiguchi, T. Sasaki, M. Yoshida, M. Akiyama, M. G. Watson, X. Barcons, F. J. Carrera, W. Pietsch, and N. A. Webb**. XMM-Newton observations reveal AGN in apparently normal galaxies. *A&A*, 406:483–492, August 2003.

[219] **N. I. Shakura and R. A. Sunyaev**. Black holes in binary systems. Observational appearance. *A&A*, 24:337–355, 1973.

[220] **P. Shastri, B. J. Wilkes, M. Elvis, and J. McDowell**. Quasar X-ray spectra revisited. *ApJ*, 410:29–38, June 1993.

[221] **G. A. Shields**. Thermal continuum from acretion disks in quasars. *Nature*, 272:706–708, April 1978.

[222] **D. C. Shih, K. Iwasawa, and A. C. Fabian**. The continuum variability of MCG-6-30-15: a detailed analysis of the long 1999 ASCA observation. *MNRAS*, 333:687–696, July 2002.

[223] **D. N. Spergel, L. Verde, H. V. Peiris, E. Komatsu, M. R. Nolta, C. L. Bennett, M. Halpern, G. Hinshaw, N. Jarosik, A. Kogut, M. Limon, S. S. Meyer, L. Page, G. S. Tucker, J. L. Weiland, E. Wollack, and E. L. Wright**. First-Year Wilkinson Microwave Anisotropy Probe (WMAP) Observations: Determination of Cosmological Parameters. *ApJS*, 148:175–194, September 2003.

[224] **J. A. Stevens, M. J. Page, R. J. Ivison, F. J. Carrera, J. P. D. Mittaz, I. Smail, and I. M. McHardy**. Submillimetre photometry of X-ray absorbed quasi-stellar objects: their formation and evolutionary status. *MNRAS*, 360:610–618, June 2005.

[225] **A. Streblyanska, G. Hasinger, A. Finoguenov, X. Barcons, S. Mateos, and A. C. Fabian**. XMM-Newton observations of the Lockman Hole. III. A relativistic Fe line in the mean X-ray spectra of type-1 and type-2 AGN. *A&A*, 432:395–400, March 2005.

[226] **L. Strüder, U. Briel, K. Dennerl, R. Hartmann, E. Kendziorra, N. Meidinger, E. Pfeffermann, C. Reppin, B. Aschenbach, W. Bornemann, H. Bräuninger, W. Burkert, M. Elender, M. Freyberg, F. Haberl, G. Hartner, F. Heuschmann, H. Hippmann, E. Kastelic, S. Kemmer, G. Kettenring, W. Kink, N. Krause, S. Müller, A. Oppitz, W. Pietsch, M. Popp, P. Predehl, A. Read, K. H. Stephan, D. Stötter, J. Trümper, P. Holl, J. Kemmer, H. Soltau, R. Stötter, U. Weber, U. Weichert, C. von Zanthier, D. Carathanassis, G. Lutz, R. H. Richter, P. Solc, H. Böttcher, M. Kuster, R. Staubert, A. Abbey, A. Holland, M. Turner, M. Balasini, G. F. Bignami, N. La Palombara, G. Villa, W. Buttler, F. Gianini, R. Lainé, D. Lumb, and P. Dhez**. The European Photon Imaging Camera on XMM-Newton: The pn-CCD camera. *A&A*, 365:L18–L26, January 2001.

[227] **G. P. Szokoly, J. Bergeron, G. Hasinger, I. Lehmann, L. Kewley, V. Mainieri, M. Nonino, P. Rosati, R. Giacconi, R. Gilli, R. Gilmozzi, C. Norman, M. Romaniello, E. Schreier, P. Tozzi, J. X. Wang, W. Zheng, and A. Zirm**. The Chandra Deep Field-South: Optical Spectroscopy. I. *ApJS*, 155:271–349, December 2004.

[228] **P. Tozzi, P. Rosati, M. Nonino, J. Bergeron, S. Borgani, R. Gilli, R. Gilmozzi, G. Hasinger, N. Grogin, L. Kewley, A. Koekemoer, C. Norman, E. Schreier, G. Szokoly, J. X. Wang, W. Zheng, A. Zirm, and R. Giacconi**. New Results from the X-Ray and Optical Survey of the Chandra Deep Field-South: The 300 Kilosecond Exposure. II. *ApJ*, 562:42–51, November 2001.

[229] **J. Tr*ü*mper**. . *Adv. Space Res.*, 27:1404, November 1983.

[230] **M. Türler, S. Paltani, T. J.-L. Courvoisier, M. F. Aller, H. D. Aller, A. Blecha, P. Bouchet, M. Lainela, I. M. McHardy, E. I. Robson, J. A. Stevens, H. Teräsranta, M. Tornikoski, M.-H. Ulrich, E. B. Waltman,**

W. Wamsteker, and M. C. H. Wright. 30 years of multi-wavelength observations of 3C 273. *A&AS*, 134:89–101, January 1999.

[231] **M. J. L. Turner, A. Abbey, M. Arnaud, M. Balasini, M. Barbera, E. Belsole, P. J. Bennie, J. P. Bernard, G. F. Bignami, M. Boer, U. Briel, I. Butler, C. Cara, C. Chabaud, R. Cole, A. Collura, M. Conte, A. Cros, M. Denby, P. Dhez, G. Di Coco, J. Dowson, P. Ferrando, S. Ghizzardi, F. Gianotti, C. V. Goodall, L. Gretton, R. G. Griffiths, O. Hainaut, J. F. Hochedez, A. D. Holland, E. Jourdain, E. Kendziorra, A. Lagostina, R. Laine, N. La Palombara, M. Lortholary, D. Lumb, P. Marty, S. Molendi, C. Pigot, E. Poindron, K. A. Pounds, J. N. Reeves, C. Reppin, R. Rothenflug, P. Salvetat, J. L. Sauvageot, D. Schmitt, S. Sembay, A. D. T. Short, J. Spragg, J. Stephen, L. Strüder, A. Tiengo, M. Trifoglio, J. Trümper, S. Vercellone, L. Vigroux, G. Villa, M. J. Ward, S. Whitehead, and E. Zonca**. The European Photon Imaging Camera on XMM-Newton: The MOS cameras : The MOS cameras. *A&A*, 365:L27–L35, January 2001.

[232] **T. J. Turner, I. M. George, K. Nandra, and R. F. Mushotzky**. ASCA Observations of Type 2 Seyfert Galaxies. II. The Importance of X-Ray Scattering and Reflection. *ApJ*, 488:164–+, October 1997.

[233] **T. J. Turner, I. M. George, K. Nandra, and D. Turcan**. On X-Ray Variability in Seyfert Galaxies. *ApJ*, 524:667–673, October 1999.

[234] **T. J. Turner and K. A. Pounds**. The EXOSAT spectral survey of AGN. *MNRAS*, 240:833–880, October 1989.

[235] **Y. Ueda, M. Akiyama, K. Ohta, and T. Miyaji**. Cosmological Evolution of the Hard X-Ray Active Galactic Nucleus Luminosity Function and the Origin of the Hard X-Ray Background. *ApJ*, 598:886–908, December 2003.

[236] **Y. Ueda, T. Takahashi, H. Inoue, T. Tsuru, M. Sakano, Y. Ishisaki, Y. Ogasaka, K. Makishima, T. Yamada, K. Ohta, and M. Akiyama**. A population of faint galaxies that contribute to the cosmic X-ray background. *Nature*, 391:866–+, February 1998.

[237] **C. M. Urry and P. Padovani**. Unified Schemes for Radio-Loud Active Galactic Nuclei. *PASP*, 107:803–+, September 1995.

[238] **A. Vecchi, S. Molendi, M. Guainazzi, F. Fiore, and A. N. Parmar**. The BeppoSAX 1-8 keV cosmic background spectrum. *A&A*, 349:L73–L76, September 1999.

[239] **C. Vignali, W. N. Brandt, D. P. Schneider, and S. Kaspi**. X-Ray Lighthouses of the High-Redshift Universe. II. Further Snapshot Observations of the Most Luminous z $\sim$4 Quasars with Chandra. *AJ*, 129:2519–2530, June 2005.

[240] **C. Vignali, A. Comastri, M. Cappi, G. G. C. Palumbo, M. Matsuoka, and H. Kubo**. Probing the Hard X-Ray Properties of High-Redshift Radio-Quiet Quasars with ASCA. *ApJ*, 516:582–590, May 1999.

[241] **A. Vikhlinin, W. Forman, C. Jones, and S. Murray**. ROSAT Extended Medium-Deep Sensitivity Survey: Average Source Spectra. *ApJ*, 451:564–+, October 1995.

[242] **R. S. Warwick and T. P. Roberts**. The extragalactic X-ray background at 0.25 keV. *Astronomische Nachrichten*, 319:59–+, 1998.

[243] **M. G. Watson, J.-L. Augueres, J. Ballet, X. Barcons, D. Barret, M. Boer, T. Boller, G. E. Bromage, H. Brunner, F. J. Carrera, M. S. Cropper, M. Denby, M. Ehle, M. Elvis, A. C. Fabian, M. J. Freyberg, P. Guillout, J.-M. Hameury, G. Hasinger, D. A. Hinshaw, T. Maccacaro, K. O. Mason, R. G. McMahon, L. Michel, L. Mirioni, J. P. Mittaz, C. Motch, J.-F. Olive, J. P. Osborne, C. G. Page, M. Pakull, B. H. Perry, M. Pierre, W. Pietsch, J. P. Pye, A. M. Read, T. P. Roberts, S. R. Rosen, J.-L. Sauvageot, A. D. Schwope, K. Sekiguchi, G. C. Stewart, I. Stewart, I. Valtchanov, M. J. Ward, R. S. Warwick, R. G. West, N. E. White, and D. M. Worrall**. The XMM-Newton Serendipitous Survey. I. The role of XMM-Newton Survey Science Centre. *A&A*, 365:L51–L59, January 2001.

[244] **M. C. Weisskopf, H. D. Tananbaum, L. P. Van Speybroeck, and S. L. O'Dell**. Chandra X-ray Observatory (CXO): overview. In *Proc. SPIE Vol. 4012, p. 2-16, X-Ray Optics, Instruments, and Missions III, Joachim E. Truemper; Bernd Aschenbach; Eds.*, pages 2–16, July 2000.

[245] **N. E. White**. The X-ray evolution of galaxies: implications for future X-ray observatories. *Advances in Space Research*, 34:2632–2636, 2004.

[246] **B. J. Wilkes and M. Elvis**. Quasar energy distributions. I - Soft X-ray spectra of quasars. *ApJ*, 323:243–262, December 1987.

[247] **R. J. Williams, S. Mathur, and R. W. Pogge**. Chandra Observations of X-Ray-weak Narrow-Line Seyfert 1 Galaxies. *ApJ*, 610:737–744, August 2004.

[248] **M. A. Worsley, A. C. Fabian, X. Barcons, S. Mateos, G. Hasinger, and H. Brunner**. The (un)resolved X-ray background in the Lockman Hole. *MNRAS*, 352:L28–L33, August 2004.

[249] **M. A. Worsley, A. C. Fabian, F. E. Bauer, D. M. Alexander, G. Hasinger, S. Mateos, H. Brunner, W. N. Brandt, and D. P. Schneider**. The unresolved hard X-ray background: the missing source population implied by the Chandra and XMM-Newton deep fields. *MNRAS*, 357:1281–1287, March 2005.

[250] **T. Yaqoob, I. M. George, and T. J. Turner**. Iron-K Line Diagnostics from Chandra Grating Observations of AGN. In *Two Years of Science with Chandra,*

Abstracts from the Symposium held in Washington, DC, 5-7 September, 2001, meeting abstract., September 2001.

[251] **T. Yaqoob and R. S. Warwick**. The X-ray spectral variability of NGC 4151. *MNRAS*, 248:773–786, February 1991.

[252] **T. Yaqoob, R. S. Warwick, F. Makino, C. Otani, J. L. Sokoloski, I. A. Bond, and M. Yamauchi**. Further probing of the X-ray source in NGC 4151 - New constraints on the nuclear geometry. *MNRAS*, 262:435–448, May 1993.

[253] **F. Yuan and R. Narayan**. On the Nature of X-Ray-Bright, Optically Normal Galaxies. *ApJ*, 612:724–728, September 2004.

[254] **G. Zamorani, I. M. Gioia, T. Maccacaro, and A. Wolter**. Effects of Galactic absorption on soft X-ray surveys. *A&A*, 196:39–43, May 1988.

[255] **G. Zamorani, M. Mignoli, G. Hasinger, R. Burg, R. Giacconi, M. Schmidt, J. Trümper, P. Ciliegi, C. Gruppioni, and B. Marano**. The ROSAT deep survey. V. X-ray sources and optical identifications in the Marano field. *A&A*, 346:731–752, June 1999.